REMOTE SENSING OF RADIATIVE FLUXES AND HEATING RATES
FROM SATELLITE INSTRUMENT MEASUREMENTS

Thesis By

Daniel Robert Feldman

In Partial Fulfillment of the Requirements for the

Degree of

Doctor of Philosophy

CALIFORNIA INSTITUTE OF TECHNOLOGY

Pasadena, California

2008

(Defended on April 25, 2008)

Acknowledgements.

My parents, George and Virginia, and my sisters, Sarah and Kiera were always gracious in providing help and support throughout the last 6 years. James the cat and Pele the dog also provided comfort and inspiration. Finally, my significant other, Neena Kadaba, was always there for the ups and the downs. I owe you all more than you know.

Abstract.

Weather and climate models are required to calculate radiative fluxes and shortwave heating and longwave cooling rate profiles on a large scale. Heating and cooling rates describe the effect that different configurations of temperature, radiatively active gases, and clouds have on the rates of interlayer energy exchange and affect circulation patterns. Meanwhile, a suite of satellite-based instruments from the NASA Earth Observing System's A-Train provide an unprecedented set of measurements that can be used to produce quantities that can also yield radiative fluxes and heating and cooling rates. This work explores the extent to which passive-infrared hyperspectral measurements such as those made by the Atmospheric Infrared Sounder impart information towards infrared cooling rates. Several novel methods are explored for interpreting and retrieving cooling rates using spectral measurements.

For scenes with optically thick clouds, however, passive visible and infrared measurements will have limited power in describing heating and cooling rates. Vertical cloud information can be obtained from several A-Train instruments: the Microwave Limb Sounder Ice Water Content product provides data on the profiles of ice clouds in the upper troposphere and this work explores how this data can be used to describe the cloud radiative effect. Recently, active-sounding measurements from CloudSat have offered an unrivalled description of cloud profiles which can be used to compute fluxes and heating rates. Preliminary CloudSat products are evaluated and a case study of heating rate analysis is presented in which CloudSat products are used to determine Tropical Tropopause Layer radiation balance.

The radiative processes that affect the far-infrared (wavelengths of 15–100 μm) are described in a limited fashion by the current suite of A-Train measurements, and yet these spectral regions have a large impact on cooling rates in the troposphere. The extra information

gained by the introduction of a set of spectrally resolved far-infrared measurements is discussed for clear and cloudy scenes.

Finally, this work discusses future directions for analyzing heating rates derived from remote sensing measurements, and challenges and opportunities for future research.

Table of Contents.

List of Figures and Tables.

Chapter 1

Chapter 2

Chapter 3

Chapter 4

Chapter 5

Chapter 6

Chapter 7

Chapter 8

Chapter 9

Abbreviations.

AER:	Atmospheric Environmental Research, Inc.
AIRS:	Atmospheric Infrared Sounder
AMSR:	Advanced Microwave Scanning Radiometer
AMSU:	Advanced Microwave Sounding Unit
ARM:	Atmospheric Radiation Measurement program
AR4:	Fourth Assessment Report
AVE:	Aura Validation Experiment
CALIPSO:	Cloud-Aerosol Lidar and Infrared Pathfinder Satellite Observations
CAM:	Community Atmosphere Model
CCM3:	Community Climate Model, Version 3
CER:	Cloud Effective Radius
CERES:	Clouds and the Earth's Radiant Energy System
CHARTS:	Code for Highly-Accelerated Radiative Transfer with Scattering
CLARREO:	CLimate Absolute Radiance and Refractivity Observatory
CO_2:	Carbon Dioxide
CRE:	Cloud Radiative Effect
CWC:	Cloud Water Content
CWP:	Cloud Water Path
DISORT:	Discrete Ordinate Radiative Transfer
ECMWF:	European Centre for Medium-Range Weather Forecasting
EOS:	Earth Observing System
ERA:	ECMWF Re-Analysis
ERBE:	Earth Radiation Budget Experiment

FAT: Fixed-Anvil Temperature

FIR: Far-Infrared

FIRS: Far-Infrared Spectrometer

FIRST: Far-Infrared Spectroscopy of the Troposphere

GCM: Global Circulation Model

H_2O: Water vapor

HITRAN: HIgh resolution TRANsmission molecular absorption database

hPa: Hectopascals (100 Pascals)

IPCC: Intergovernmental Panel on Climate Change

IRIS-D: Infrared Interferometer Spectrometer, Version D

ISCCP: International Satellite Cloud Climatology Program

IWC: Ice Water Content

LBLRTM: Line-by-Line Radiative Transfer Model

LHS: Left-Hand Side

LW: Longwave

LWC: Liquid Water Content

MCMC: Markov Chain Monte Carlo

MIR: Mid-Infrared

MLS: Microwave Limb Sounder

MODIS: MODerate resolution Imaging Spectrometer

MODTRAN: MODerate resolution TRANsmittance code

MPACE: Mixed-Phase Arctic Climate Experiment

MW: Microwave

NASA: National Aeronautics and Space Administration

NCAR: National Center for Atmospheric Research

NEDT: Noise-Effective Delta Temperature

NER: Noise-Effective Radiance

NRC: National Research Council

NWP: Numerical Weather Prediction

O_3:   Ozone

PDF: Probability Distribution Function

PPMV: Parts Per Million by Volume

RGB: Red-Green-Blue

RHS: Right-Hand Side

RRTM: Rapid Radiative Transfer Model

RTM: Radiative Transfer Model

SAFIRE-A: Spectroscopy of the Atmosphere Using Far-Infrared Emission/Airborne

SAW: Sub-Arctic Winter conditions

SGP: Southern Great Plains

SRF: Spectral Response Function

SSB: Space Studies Board

SW: Shortwave

T: Temperature

Tcir: Cloud-Induced Radiance

TES: Tropospheric Emission Spectrometer

TRMM: Tropical Rainfall Measuring Mission

TTL: Tropical Tropopause Layer

TRP: Tropical conditions

UARS: Upper Atmosphere Research Satellite

UTC: Upper Tropospheric Clouds

VMR: Volume Mixing Ratio

Summary.

This dissertation covers several different topics related to using remote sensing data to infer information about radiative fluxes and heating rates. It is organized in nine chapters that address several aspects of this topic, though not from a monolithic perspective.

The first chapter presents a broad introduction and a motivation for the subsequent research in the context of current- and future-satellite-borne instrumentation. This research is being performed in order to be supportive of climate models in the context of a large number of available satellite-based measurements

The second chapter provides a short overview of radiative transfer which is of direct relevance to the determination of radiative fluxes and heating rates. This chapter contains a description of some of the theoretical and practical aspects of this topic but is by no means exhaustive. The reader is encouraged to review standard radiative transfer textbooks and the references cited in this chapter for a more complete treatment of this field. For those readers seeking a rigorous foundation to the theory of radiative transfer, the paper by *Mishchenko et al.* [2006] is recommended because it links fundamental concepts of radiative transfer to Maxwell's equations. The end of this chapter broaches the topic of retrieval theory as it pertains to using satellite instrument measurements to derive products that are scientifically meaningful.

The third chapter introduces the topic of cooling rate retrievals, which has received limited treatment in the published literature despite its relevance to circulation models. This chapter explores this novel retrieval approach in a limited framework that indicates that this retrieval approach is numerically stable and feasible.

Several practical questions are raised in the third chapter regarding the assessment of heating and cooling rate profile knowledge, and so the fourth chapter develops a methodology for comparing different observing systems in terms of their abilities to constrain cooling rate profiles

under clear conditions. This methodology allows for scientific analysis to be performed in terms of heating and cooling rates. Heating and cooling rate analysis has direct relevance to climate models, but it is simplified as compared to analysis according to the larger number of atmospheric state parameters required to calculate the heating and cooling rates.

The fifth chapter builds upon the results of the previous work and explores using passive spectroscopy to perform a direct cooling rate retrieval and the extent to which this method can be applied in the presence of clouds.

Subsequent chapters explore practical aspects of inferring fluxes and heating rates from a variety of measurements. Chapter 6 analyzes the Ice Water Content profile product of the Earth Observing System's Aura-based Microwave Limb Sounder and how that product can be used to describe the top-of-atmosphere cloud radiative effect.

Chapter 7 provides an overview of CloudSat-derived heating and cooling rate products and how to assess their quality. This chapter focuses on determining the level of zero clear-sky radiative heating in the Tropical Tropopause Layer because this level is relevant to stratospheric water vapor transport and is a case where heating and cooling rates dominate vertical transport.

In the course of this research, the absence of spectral measurements at wavelengths longer than 15 μm became increasingly conspicuous, even though this spectral region is quite important to determining tropospheric cooling rates. Therefore, Chapter 8 addresses some aspects of far-infrared measurements, and analyzes spectra from a prototyped balloon-borne instrument in the context of the currently orbiting satellite instruments.

The final chapter provides thoughts on directions for the future of this research and addresses some of the new frontiers towards which future efforts may reasonably be expended.

Chapter One. Introduction.

1.1   Overview

Now that global warming has captured the world's attention, it is incumbent on the scientific community to present a clear, concise, and consistent prediction of the likely consequences of climate change for the general public. Atmospheric science is of increasing interest to general audiences due to rising popular concern about the societal risks associated with climate change. Several assessment reports from the Intergovernmental Panel on Climate Change (IPCC) have provided estimates of the many dimensions of anthropogenically induced climate change, and science, with its predictive models, has played an important role in driving policy debates about what types of societal change may be required to mitigate greenhouse warming. Therefore, confidence in model predictions is of the highest importance to a society concerned about global warming, and one essential route for establishing trust in the current generation of climate models is to require that they agree substantially with the set of measurements that currently exist.

The research presented in this thesis focuses on one method for analyzing measurements in the context of model calculations by utilizing remote sensing measurements to understand the radiative energy exchange between different levels of the atmosphere between the surface and an altitude of approximately 50 km. We focus on this region because the atmosphere above 50 km contributes very little to processes relevant to climate change. In numerical weather prediction and climate modeling, estimating radiative energy exchange over these 50 km is required, and these computer codes have to perform thousands of calculations to this effect at every time-step of integration. Because these instruments fly aboard satellite platforms several hundred kilometers above the Earth's surface, care must be taken to understand how different types of measurements impart information towards this interlayer radiative energy exchange, a quantity that is conventionally referred to as the calculation of heating and cooling rate profiles.

This chapter will provide some context for the subsequent research by offering a very brief overview of climate model discrepancies, a description of some of the currently-operational earth observing measurements, and why the scientific community is interested in understanding heating and cooling rates.

1.2   Climate Model Discrepancies

Several different institutions have engaged in the massive effort required to produce and run a global circulation model that can predict climate change. These models project future climate patterns that the Earth will experience over the next approximately 100 years under a broad range of natural and anthropogenic scenarios.
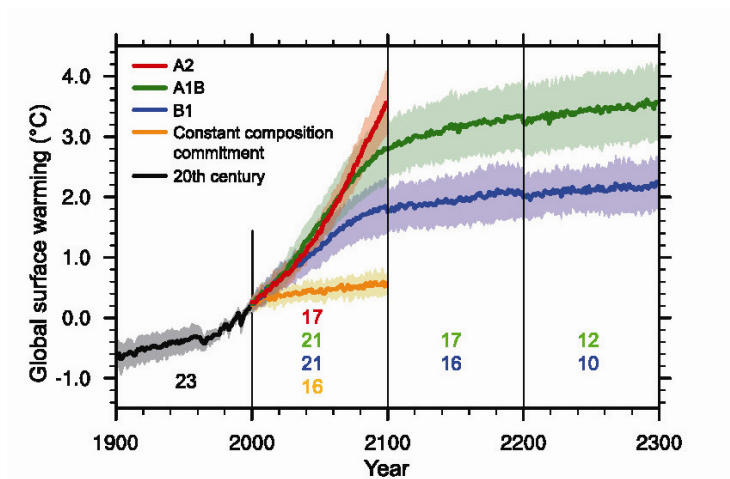
Figure 1.1: From the IPCC Fourth Assessment Report. Model-predicted surface warming relative to the period from 1980-1999 for several IPCC emission scenarios (A2, A1B, and B1) for a simulation of 21st century climate with stabilization being implemented in 2100. Shading denotes the ±1 σ range for individual model annual means.

They also present one method for testing and analyzing how different processes interact and allow the public and policy-makers to formulate decisions regarding the expected changes in the earth-atmosphere system that will likely be associated with increased carbon dioxide levels.

These scenarios range from business-as-usual (A2) carbon dioxide emission to some emission reduction (A1B) to drastic emission cuts (B1). Shading in the figure describes the standard deviation of the 18 different model runs about the solid line of the mean. The standard deviation is often taken to be representative of the uncertainty in the trajectory of the global average surface temperature rise associated with anthropogenic carbon emission. Besides global average surface temperature, there are a large number of features of the climate system that can be analyzed from a general circulation model (GCM) run, including precipitation and cloud cover. Even more drastic differences between models can be seen when comparing other fields [*IPCC*, 2007]. Additionally, discrepancies between different climate model results are difficult to rectify because their sources are often very obscure.

The differences in climate model results have received serious scientific scrutiny but the discrepancies persist. Moreover, these differences have been used to delay pro-active changes in anthropogenic emissions policies. This is understandable because many climate processes are subtle but ultimately are important for determining the response of the earth system to natural and anthropogenic forcings. Disentangling the sources of these discrepancies and discriminating between climate model results are non-trivial tasks, but they must be addressed by the scientific community.

However, uncertainty in model performance and therefore in climate change predictions can be reduced dramatically by the presence of a far-reaching set of reliable measurements. Circulation models can and do benefit from a comprehensive suite of measurement data so that they can be trained properly on observations. Numerical weather prediction, for example, routinely ingests many disparate datasets including balloon observations, surface station measurements, and satellite radiance data [i.e., *Lorenc*, 1986; *Andersson et al*., 1994; *Courtier et al*., 1994; *Courtier et al.,* 1998]. Climate models are typically trained on a set of measurements and run in a constrained way before running unconstrained over long time-scales to predict future scenarios. While the set of measurements used to refine models is hardly comprehensive or

contiguous, recent advances in instrumentation have allowed atmospheric scientists to analyze processes from a global perspective with data that are of a caliber allowing for tenable comparisons between measurements and climate models. Still, modeling atmospheric and oceanic circulation for hundreds to thousands of years requires massive computational power and a host of parameterizations, and there are many sources of significant uncertainty that arise in this effort.

1.3   Current and Future State of NASA Observing Systems
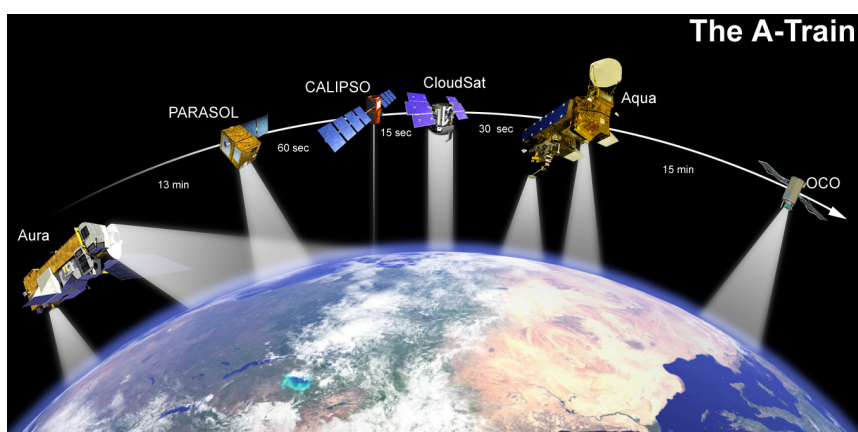
Figure 1.2: An artist's rendition of the several satellite platforms that comprise the Earth Observing System (EOS) A-Train with their separations indicated in terms of local equator-crossing time lag. From http://www-airs.jpl.nasa.gov/Technology/HistoricalContext/

Over the last two decades, NASA has designed, built, launched, and maintained the Earth Observing System [*Asrar and Dozier*, 1994]. This program consists of a satellite constellation flying in polar sun-synchronous orbit that has provided an absolutely unprecedented set of measurements of the atmospheric system. The constellation has been dubbed the A-Train and operates on an inclination angle of 98°, with most of the platforms having a local equator crossing between 1:00 pm and 2:00 pm solar time. The flotilla includes, among others, the Aqua platform

which went online in August 2002, the Aura platform which began collecting data in September 2004, and the CloudSat and CALIPSO platforms that commenced measurements in June 2006.

A great diversity of instruments exists on board these formation-flying platforms, including active and passive sounders. These instruments utilize many different spectral regions, including visible, near-infrared, infrared, and microwave wavelengths. They produce global coverage maps of a wide variety of quantities ranging from surface properties, to trace gas composition, to cloud coverage, to aerosol distribution, to surface and top-of-atmosphere energy balance. These datasets represent a comprehensive effort to provide information to the scientific community that specifies aspects of the earth-atmosphere system in a stable, well-calibrated fashion. They have enabled increased scientific understanding of a wide variety of processes, and the comprehensive picture that these instruments offer about the planet allows the community to address profound scientific questions that were totally inaccessible given the previous generation of satellite instruments. At the same time, due to the tens of megabytes of data that are produced every second from the various satellite instruments aboard the A-Train, it has been difficult to address the wealth of data with full scientific scrutiny.

The Data Age of earth observing from satellites has arrived but significant uncertainties remain in many earth-atmosphere processes. This is partly due to the continued difficulty associated with the integration of model results with the voluminous datasets. Despite the large number of measurements, models require a still larger specification of fields because these models utilize fine spatial gridding, narrow time-step incrementing, and complete vertical distribution of radiatively and dynamically active quantities. Moreover, many of the satellite instruments provide an incomplete picture of the fields that are required to run a model and the picture provided by the remote sensing data is often subject to systematic biases because certain classes of scenes observed by these instruments are difficult to interpret. Moreover, different mission requirements for these satellite instruments have led to widely varying viewing geometries, even for equipment aboard the same platform.

There have been numerous measurement-model comparisons published as a result of A-Train measurements, but one model-measurement comparison that has received limited attention concerns the radiative energy exchange between different levels of the atmosphere. While circulation models are required to calculate these values and satellite instruments provide a partial description of inputs necessary to make these calculations, only a very limited amount of research has been focused on the reconciliation of heating and cooling rates produced by models and those that may be described by measurements.

1.4   Importance of Fluxes and Heating Rates

At the top of the atmosphere, the Earth is approximately in radiative equilibrium in that there is no net gain or loss of radiative energy on time-scales relevant to weather prediction and climate change. However, the distribution of fluxes is governed by a wide variety of processes, as shown in the figure below.
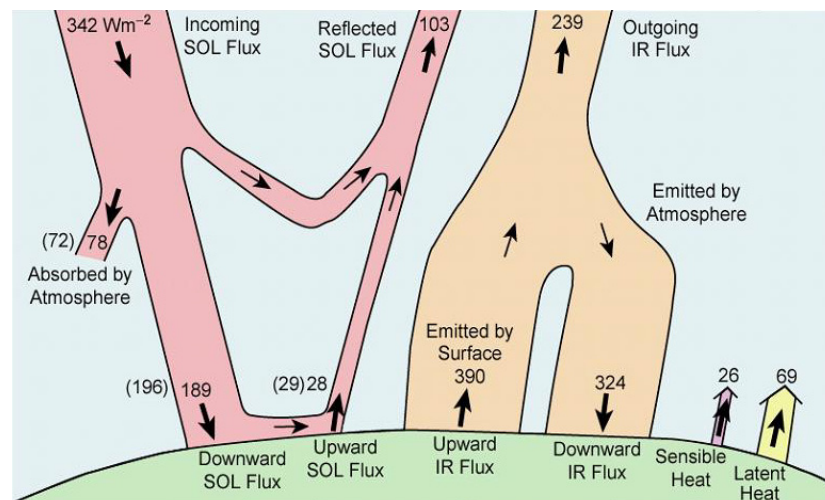
Figure 1.3: One-dimensional cartoon of the earth's radiation budget depicting energy fluxes in the atmosphere in W/m^2 from *Liou* [2002].

While a significant amount of shortwave radiation is reflected back to space, some is also absorbed between the top-of-atmosphere and the surface which leads to a decrease in surface

insolation of between 72 and 78 W/m². Meanwhile, the absorption and emission of the

atmosphere at longer wavelengths decreases the longwave radiation that is emitted at the top-of-

atmosphere by approximately 151 W/m². Clearly, the atmosphere is an active player in the

earth's energy balance, which is manifested through heating and cooling rates.

Weather and climate models are required to calculate heating rates because these models

seek to represent circulation through numerical integration of the primitive equations (e.g.,

Trenberth [1992]). This set of differential equations represents a form of several conservation

equations on a spherical shell under the assumption that vertical velocities are much smaller than

horizontal velocities. The primitive equations can be represented in several different forms, one

of which describes these relationships in pressure coordinates in the vertical and Cartesian

coordinates in the horizontal. Accordingly, the geostrophic momentum equations are given by:

$$\frac{Du}{Dt} - fv = -\frac{\partial \phi}{\partial x} + F_f \qquad (1.1a)$$

and

$$\frac{Dv}{Dt} + fu = -\frac{\partial \phi}{\partial y} + F_f \qquad (1.1b)$$

where D represents the total derivative, t represents time, f is the Coriolis force, v is the

meridional velocity, u is the zonal velocity, ϕ is the geopotential, F_f is a description of

frictional losses, x is the zonal coordinate, and y is the meridional coordinate. The hydrostatic

equation can be represented as:

$$-\frac{\partial \phi}{\partial p} - \frac{RT}{p} = 0 \qquad (1.2)$$

where p is the pressure coordinate, R is the gas constant, and T is the temperature. The

continuity equation can be displayed as:

$$\frac{\partial u}{\partial x} + \frac{\partial v}{\partial y} + \frac{\partial \omega}{\partial p} = 0 \tag{1.3}$$

where ω is the vertical velocity. Finally, the thermodynamic equation, which represents

conservation of energy, is denoted as:

$$\frac{\partial T}{\partial t} + u\frac{\partial T}{\partial x} + v\frac{\partial T}{\partial y} + \omega\left(\frac{\partial T}{\partial p} + \frac{RT}{pC_p}\right) = \frac{J}{C_p} \tag{1.4a}$$

where J is the heat flow per mass and C_p is the specific heat at constant pressure. Eq. (1.4)

describes the change in temperature with time arising from the net balance of incoming and

outgoing solar and infrared radiation, and represents a substantial fraction of the computational

cost associated with implementing circulation model calculations [*Dongarra et al.*, 2006]. The

decomposition of the RHS of Eq. (1.4a) into solar and infrared terms yields heating rate and

cooling rates respectively such that:

$$\frac{J}{C_p} = \theta' \tag{1.4b}$$

Heating and cooling rates represent the radiative drivers of circulation and are calculated on a

large scale by the supercomputers that execute numerical weather prediction and predict near-

and long-term climate change. Figure 1.4 indicates a schematic representation of how radiation is

implemented in a circulation model.

Heating and cooling rates refer specifically to the instantaneous rate of change of

temperature that arises from the divergence of radiative energy. For the lowest 50 km of the

terrestrial atmosphere, this radiative divergence is significant over length scales of hundreds of

meters in the vertical coordinate but insignificant on horizontal length scales of tens of

kilometers, except in the case of extremely heterogeneous clouds.
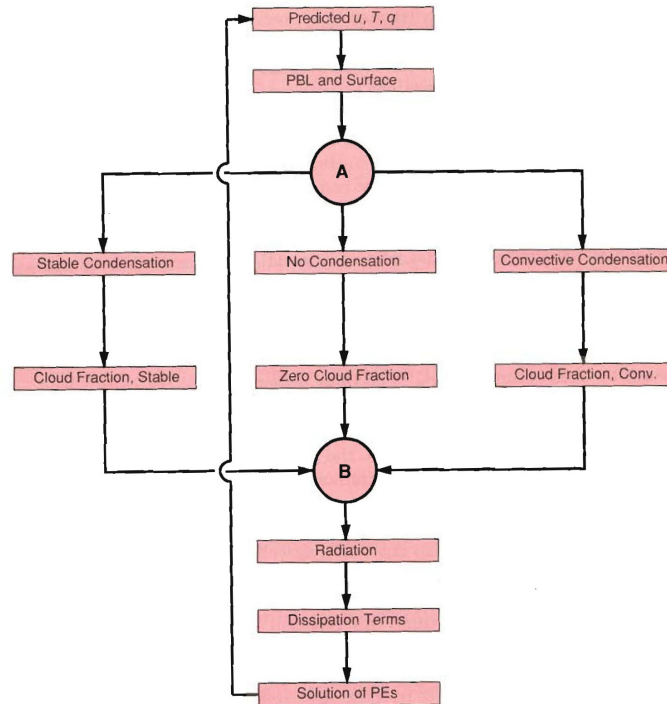
Figure 1.4: Diagram of procedures employed in an atmospheric circulation model. From Chapter 10 in *Trenberth* [1992].

Therefore, the vertical profile of heating and cooling rates is of interest to the modeling community and calculations to this end are performed in large quantities. Given that radiative flux is defined as the power per unit surface area, the heating rate profile $\theta'(z)$ is given by:

$$\theta'(z) = \frac{1}{C_p \rho(z)} \frac{dF(z)}{dz} \tag{1.5}$$

where C_p is the constant-pressure heat capacity, $\rho(z)$ is the atmospheric density profile, and

$F(z)$ is the net radiative flux for a certain layer over a certain spectral interval. Several different atmospheric constituents are responsible for the heating and cooling rate vertical structure on Earth. Because radiative flux divergence requires the significant absorption or emission in a layer, only constituents with significant absorption features in spectral regions that are important for the earth's radiative energy balance (in the vicinity of the solar or terrestrial Planck function maximum) contribute to heating and cooling rates.
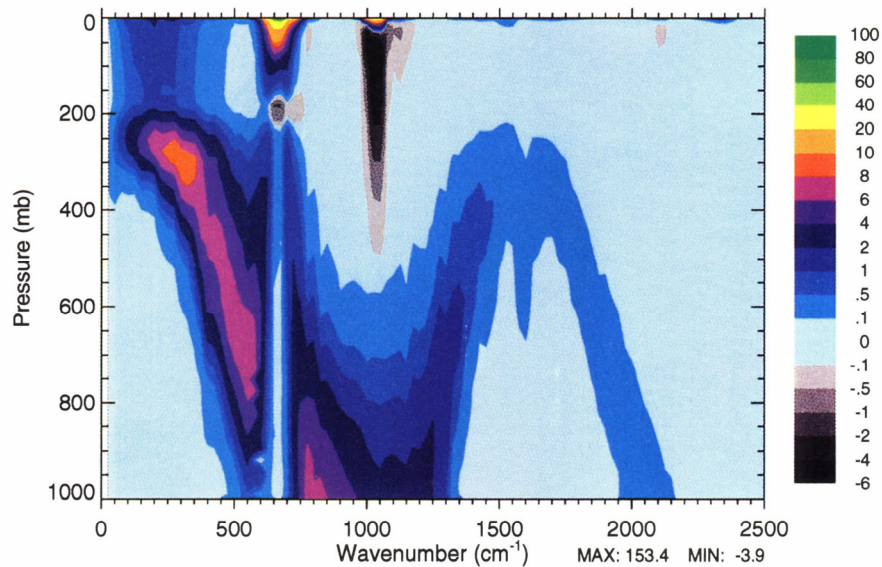
Figure 1.5: Spectral cooling rate profile as depicted in *Clough et al.* [1995] for H_2O, CO_2 (at a constant volume mixing ratio (VMR) of 355 ppmv), and O_3 as a function of pressure for the Mid-Latitude Summer atmosphere [*Anderson et al.*, 1986]. Data are smoothed over a 25 cm^{-1} bandpass and color-scale indicated values of mK/day.

For gases: water vapor (H_2O), carbon dioxide (CO_2), and ozone (O_3) dominate the heating and cooling rate profile budgets and small contributions are made by methane and nitrous oxide. Figure 1.5 indicates the spectral distribution of cooling rate profiles and gives an indication of which spectral regions contribute to infrared heating and cooling in the troposphere. Also, the same figure can be replotted in log-pressure coordinates to describe infrared cooling in the stratosphere. The H_2O rotational bands between 100 and 650 cm^{-1} lead to strong upper-tropospheric cooling and a small amount of stratospheric cooling. The CO_2 ν_2 band between 650 and 700 cm^{-1} leads to very strong stratospheric cooling and a small amount of tropopausal heating. The O_3 ν_3 band leads to strong tropopausal infrared heating and stratospheric cooling. H_2O continuum absorption leads to cooling across altitudes and spectral regions, but is most significant in its contribution to cooling in the boundary layer by affecting the spectral region from 800 to 1200 cm^{-1} (excepting the O_3 band coverage).
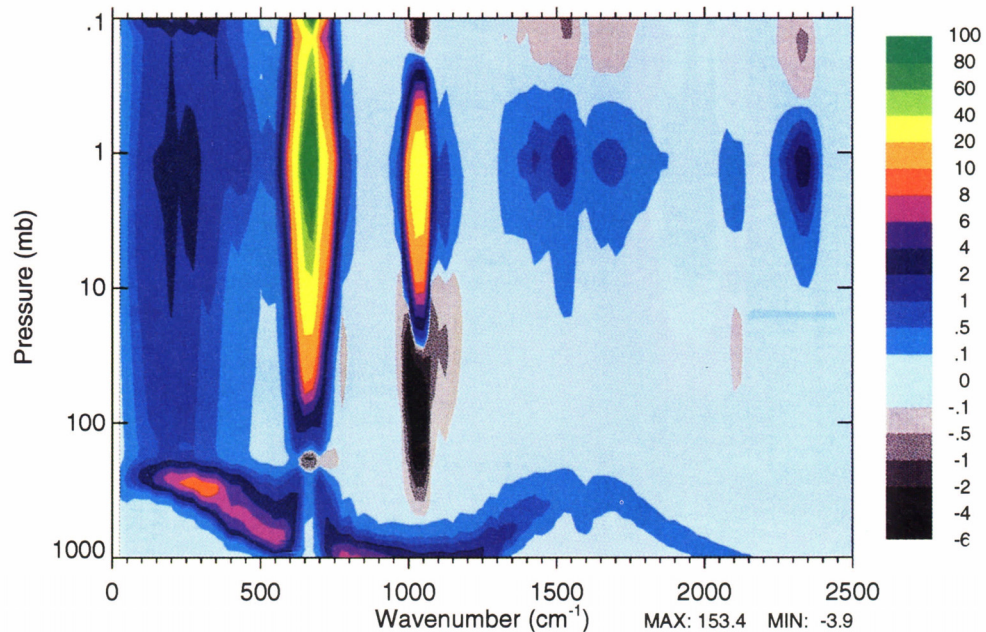
Figure 1.6: Spectral cooling rate profile as depicted in *Clough et al.* [1995] for H_2O, CO_2 (at a constant VMR of 355 ppmv), and O_3 as a logarithmic function of pressure for the Mid-Latitude Summer atmosphere [*Anderson et al.*, 1986]. Data are smoothed over a 25 cm^{-1} bandpass and color-scale indicated values of mK/day.

Shortwave clear-sky heating rates are dominated by a small number of atmospheric constituents, though all species contribute to heating and none to cooling at wavelengths shorter than 3 μm. In the upper stratosphere, electronic transitions of oxygen are the primary source of solar heating. In the middle and lower stratosphere, ozone contributes substantially to stratospheric heating through the Hartley and Huggins bands, and it contributes to tropospheric heating through the much weaker Chappuis band. Also, several different CO_2 and H_2O bands in the near-infrared portion of the spectrum contribute to tropospheric solar heating. Figure 1.7 depicts longwave cooling, shortwave heating, and net heating rate profiles for the Mid-Latitude Summer atmosphere [*Anderson et al.*, 1986]. The broadband integrated shortwave and longwave heating rates indicate that heating and cooling are on the order of 1–3 K/day in the troposphere, achieving a minimum in both heating and cooling near the tropopause. Both heating and cooling rates increase drastically in the mid- and upper-stratosphere, attaining a maximum in the stratopause region.
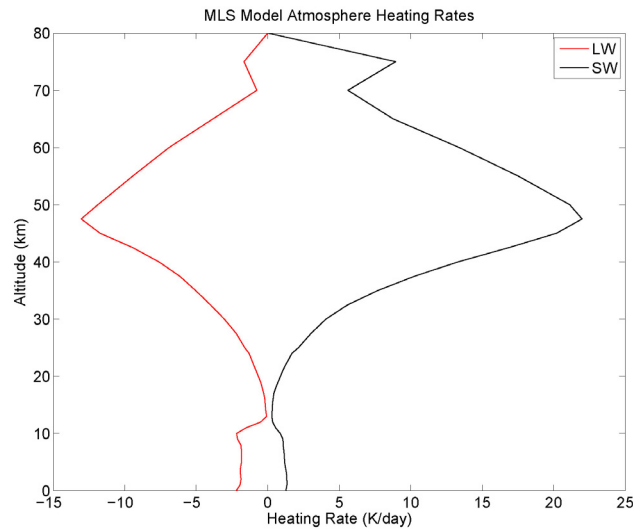
Figure 1.7: Calculated shortwave and longwave heating rates for the Mid-Latitude Summer atmosphere [*Anderson et al.*, 1986].

In non clear-sky scenes, clouds can dramatically affect heating and cooling rate profiles. Aerosols can also affect shortwave heating rate profiles, but they generally have a more limited impact on longwave cooling rates because infrared aerosol optical depth is generally small compared to its clear-sky counterpart.   Radiative fluxes can exhibit sharp changes near cloud boundaries, leading to shortwave cloud-top heating, longwave cloud-top cooling, and longwave cloud-base heating. Heating rates can be over 100 °K/day for certain cloud types, and such large values immediately impact circulation at cloud boundaries. Figure 1.8 shows examples of heating rates in the presence of three cloud types, indicating the importance of clouds for heating and cooling rate calculations. These profiles exhibit characteristic IR heating at the base of the cloud, wild fluctuations from heating to cooling within the cloud, and strong IR cooling at the top of the cloud.

The qualitative behavior of the heating and cooling rate profiles is quite different from clear-sky conditions both for those layers adjacent to clouds and for layers several kilometers away.
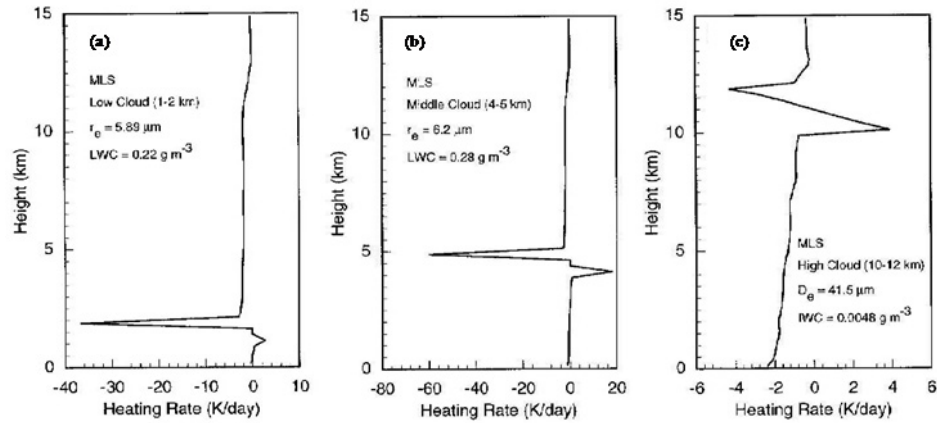
Figure 1.8: Infrared heating rates calculated for a Mid-Latitude Summer Atmosphere [*Anderson et al.*, 1986] plotted in the presence of (a) a low-level liquid cloud, (b) a mid-level liquid cloud, and (c) a high-level cirrus cloud. From *Fu* [1997].

The extremely large values of radiative heating and cooling rates associated with clouds have immediate implications for the evolution of convection and upward mass transport in certain regimes [*Ackerman et al.*, 1988], but given the difficulty associated with describing cloud vertical distribution from remote sensing, many details remain uncertain.

Another reason that it is important to have a thorough understanding of heating and cooling rates is that this knowledge is crucial for deriving improved understanding of the net-surface radiation budget from satellite-based measurements (i.e., *Liou* [2002], Section 7.4.6). The surface radiation budget is strongly related to many processes that have immediate societal relevance such as precipitation [*Kiehl and Trenberth*, 1997] and the melting of ice [*Kay et al.,* 2008]. Whereas the top-of-atmosphere net radiation budget can be determined through a variety of methods, and extensive satellite campaigns have been devoted towards long-term, accurate measurements of net shortwave and longwave radiation (see Chapter 6's discussion of the earth radiation budget measurements), the determination of the net surface energy budget is much less certain [*Cess et al.*, 1991; *Darnell et al.*, 1983; *Gupta et al.*, 1999]. However, since heating and cooling rate profiles are directly related to net flux divergence, any retrieval of net surface flux requires some knowledge of the heating and cooling rates.

To illustrate the importance of accuracy in heating rate calculations, it is instructive to refer to the results of *Iacono et al.* [2000]. In this work, the authors compared the performance of the National Center for Atmospheric Research (NCAR) Community Climate Model, Version 3 (CCM3) in two instances: one with an older radiative transfer model and the other with a revised and updated radiative transfer scheme (the Rapid Radiative Transfer Model-Global RRTMG) that boasted several improvements over the previous version. RRTMG was developed utilizing a large number of datasets based on measurements from the Atmospheric Radiation Measurement program with the specific intent of addressing some of the outstanding issues related to flux biases in the radiative transfer in GCMs. In particular, the new code computed stratospheric energy balance with greater accuracy, provided a more reasonable treatment of cloud cover, and addressed the water vapor continuum (see Chapter 2) more realistically. The subsequent figures dramatically illustrate the importance of heating and cooling rates, both for climate models and numerical weather prediction. First, Figure 1.9 shows the change in the initial zonally-averaged cooling rates arising from the radiative transfer model update.
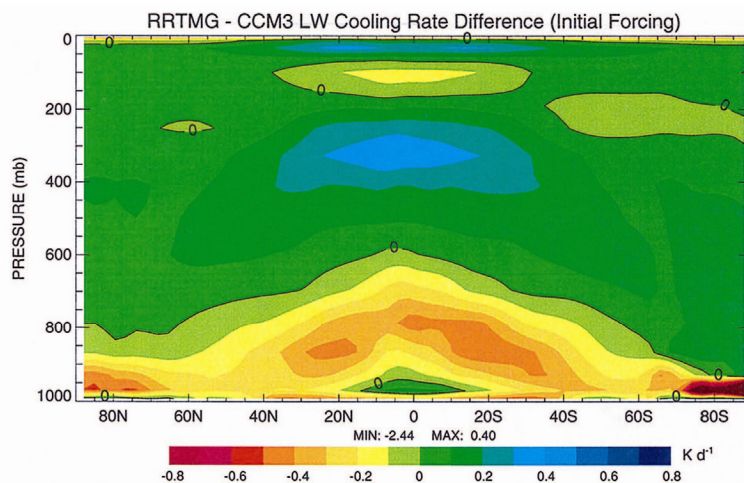
Figure 1.9: Zonal average, initial cooling rate difference between the updated radiative transfer scheme (RRTMG) and the original scheme (CCM3) as shown in *Iacono et al.,* [2000].

The distribution of radiative cooling is altered dramatically by the new radiation scheme: cooling in the lower troposphere is decreased by about 0.4–0.6 K/day (25–50%). Cooling near the

surface in polar regions decreases by around 80%, whereas cooling in the tropical upper

troposphere increases by about 0.4 K/day, which represents nearly a 100% increase.
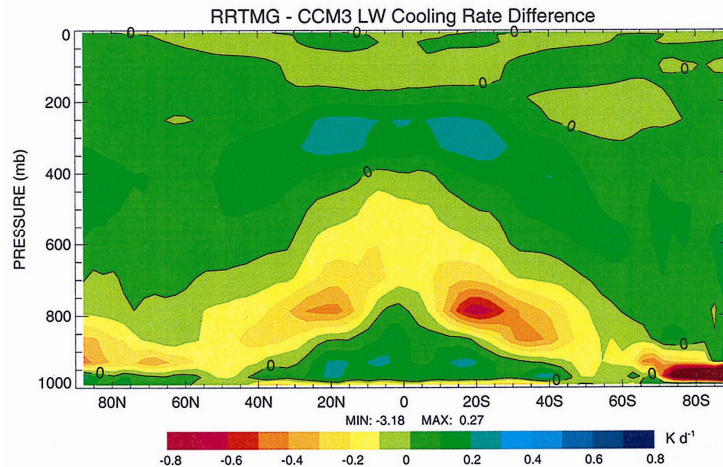
Figure 1.10: Zonal average, annual mean, cooling rate difference between the updated radiative transfer scheme (RRTMG) and the original scheme (CCM3) with two 5-year CCM3 simulations as shown in *Iacono et al.* [2000].

After a 5-year climate model simulation, the difference in cooling rates between the two model

runs changes as shown in the Figure 1.10: RRTMG shows decreased cooling now in the middle

troposphere with a small amount of increased cooling in the tropics near the surface and in the

upper troposphere.
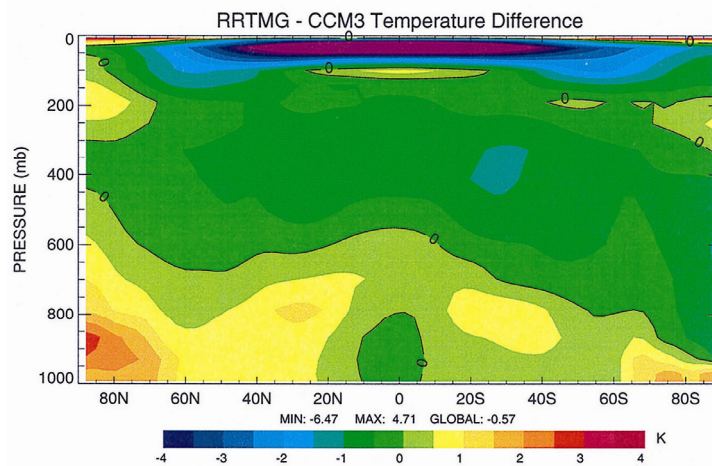
Figure 1.11: Annual mean, zonal average temperature difference as a result of using RRTMG vs. CCM3 longwave radiation models with a 5-year CCM3 simulation as shown in *Iacono et al.* [2000].

In response to the modified radiation scheme, the temperature and water vapor fields are also significantly affected. The stratospheric temperature is also quite sensitive to cooling rate calculations, and the upper tropospheric temperatures at lower latitudes, along with lower tropospheric polar temperatures, are affected due to an improved water vapor continuum model.
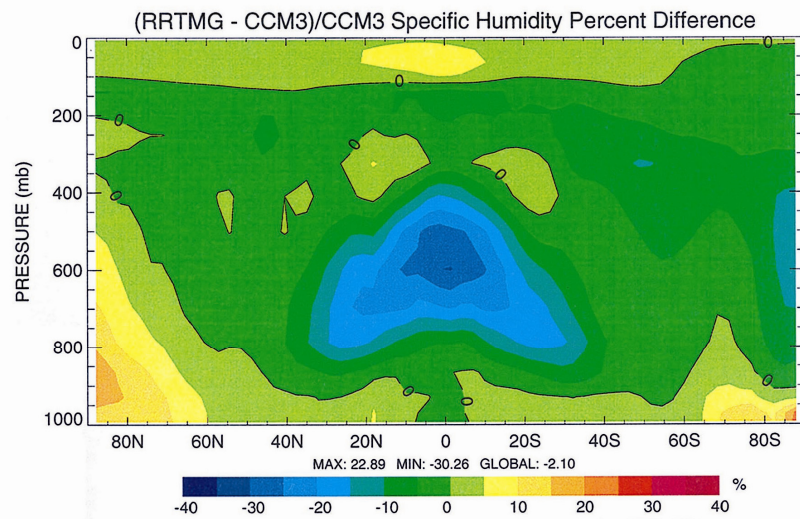
Figure 1.12: Annual mean, zonal average specific humidity difference as a result of using RRTMG vs. CCM3 longwave radiation models with a 5-year CCM3 simulation as shown in *Iacono et al.* [2000].

Lower- to middle-tropospheric water vapor at low latitudes decreases by around 20–30%, whereas polar tropospheric water vapor increases by 10–30% as the result of the change in radiation scheme. These changes largely arise because the modification in radiative cooling alters the distribution between latent, radiative, and sensible heating, which leads to constituent changes.

Finally, weather forecast models are also dependent upon accurate radiative transfer modeling. Figure 1.13 demonstrates that, with the exception of the 500 mbar level, forecast prediction improves as a result of the more advanced treatment of longwave cooling rates.

Unfortunately, some variables in the primitive equations are more amenable to validation than others, and radiative heating and cooling rate profiles have been particularly difficult to

measure *in situ* directly. The reasons for the difficulty with experimental validation are several:

First, heating and cooling rate profiles can exhibit dramatic temporal variability, especially in the

presence of clouds, and validation measurement campaigns are therefore not likely to provide

insight regarding discrepancies between model-produced heating rates (which are only

descriptive in a statistical sense) and those derived from the measurements.
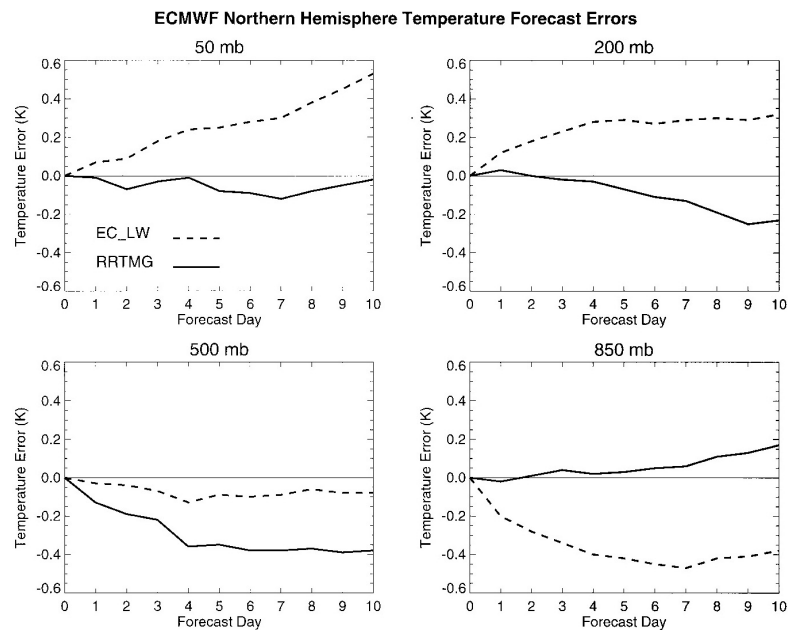
Figure 1.13: Ten-day temperature forecast errors for the Northern Hemisphere average over 12 months as computed by the ECMWF weather forecast model using the ECMWF operational LW model (EC_LW) and the RRTMG model. Errors are displayed for 50, 200, 500, and 850 mbar as shown in *Iacono et al.* [2000].

Second, determining heating and cooling rates requires the determination of net solar and infrared

flux values; from a measurement perspective, it must be recognized that the signal being derived

is a small signal that results from the difference of two much larger signals. Therefore, extremely

stringent requirements must be imposed upon any flux/heating rate measurement campaign in

order to produce results that are reasonable [*Taylor* 2000]. Several authors (i.e., *Valero et al.*

[1982]; *Mlynczak et al.* [2006a]) have explored the implementation of net flux measurements on

aerial vehicles in support of radiative heating and cooling rate determination, but there have only

been limited radiative flux measurements and no comprehensive validation campaigns for verifying atmospheric net flux values have been undertaken. Finally, while extensive research has been focused on measurement-model intercomparisons for many of the standard model outputs, there has been only limited research into methods for the comparison of measured heating rates with those derived from models (which usually are not standard outputs).

Because of the importance of heating and cooling rate profiles, this thesis explores several topics related to heating and cooling rate calculations and the utilization of remote sensing data for such calculations. This work has been inspired by a paper by *Liou and Xue* [1988] which began the discussion of using remote sensing measurements to retrieve cooling rate profiles (see Appendix A for details). This thesis explores some aspects of the efforts to marry model calculations with measurements within the heating and cooling rate context. Several chapters of this work are moderately theoretical in that they develop heating and cooling rate retrieval concepts for notional instruments. Later chapters, however, rely entirely upon the constraints imposed by existing instrumentation and explore how these measurements can be employed for the analysis of heating and cooling rates. The final chapter discusses future prospects for this relatively unexplored topic and offers some limited recommendations for measurement and model comparisons. Ultimately, as such comparisons become more sophisticated, researchers may be able to undertake the analysis of heating and cooling rates from measurements and models as an important diagnostic tool for exploring whether processes that affect the atmospheric energy balance are being described properly.

Chapter Two. Radiative Transfer.

2.1   Abstract

Most earth-observing satellite instruments measure photons, though the set of wavelengths utilized varies widely. Interpretation of these measurements to confirm agreement and to reduce differences between measurements and models is difficult without first understanding how those photons propagate through the atmosphere.   The theory of radiative transfer provides a robust foundation for deriving information about these constituents from electromagnetic remote sensing. It rests on the notion of establishing a model that correctly describes the physics and accurately simulates the range of measurements that a satellite will record during its mission lifetime. By taking actual satellite measurements and ancillary knowledge of the system, one can, after establishing appropriate mathematical stability, derive scientifically meaningful information about the surface and atmosphere.

2.2   Introduction

Many remote sensing instruments collect and measure photons and thus are sensitive to the fundamental quantity of radiative transfer: radiance. It can be shown that the radiant energy incident upon a satellite is a function of wavelength, time of exposure, and the instrumental footprint relative to the area subtended by its field-of-view. Radiance therefore is defined as the specific intensity of radiant energy in terms of wavelength-specific energy per time per area and per solid angle. The *Fundamental Equation of Radiative Transfer* is a differential equation that describes how monochromatic electromagnetic radiance interacts with matter in local thermodynamic equilibrium in a plane-parallel atmosphere:

$$\mu \frac{dI_\nu(\tau_\nu,\mu,\phi)}{d\tau_\nu} = I_\nu(\tau_\nu,\mu,\phi) - J_\nu(\tau_\nu,\mu,\phi) \qquad (2.1)$$

where μ is the cosine of the viewing angle, $I_\nu(\tau_\nu,\mu,\phi)$ is the monochromatic radiance at

wavenumber ν, ϕ is the azimuth viewing angle, $J_\nu(\tau_\nu,\mu,\phi)$ is the source function, and τ_ν is

the monochromatic optical depth coordinate. The optical depth is related to the fractional

attenuation of the incident radiance and is given by the following equation:

$$\tau_\nu = \int_z^\infty \sigma_\nu(z')n(z')dz' \qquad (2.2)$$

where σ_ν is the absorption cross section per molecule, n is the molecular number density, and z

is the vertical coordinate. Transmission refers to the ratio of the number of photons at a specific

wavelength that propagate through the medium of interest to the total number of incident photons.

Transmission between two layers in the atmosphere is of critical importance to future discussion

in this paper and is a direct function of optical path, which is the difference in optical depth

between two layers of the atmosphere:

$$T_\nu(z_1,z_2,\mu) = \exp\left(-\frac{|\tau_\nu(z_1)-\tau_\nu(z_2)|}{\mu}\right). \qquad (2.3)$$

The Fundamental Equation of Radiative Transfer is deceptively simple in that it seems to suggest

that solving this equation in order to analyze satellite-instrument measurements can be achieved

with elementary integration techniques. However, there are many factors that complicate formal

solution techniques which require numerical solutions in all but the most elementary (and

generally idealized) cases.

First, Eq. (2.2) requires a moderately thorough understanding of molecular absorption.

This phenomenon is only achieved where the photons incident to the layer of interest have

energies (i.e., wavelengths) that correspond to allowed energy transition values for the molecules.

Isolated molecules have quantized electronic, vibrational, and rotational transitions. Information about the location and strength of lines is contained in line-list databases which catalog millions of different transitions for about 30 species that may reasonably produce a spectral signature. One such line-list is the HIgh Resolution Transmission (HITRAN) molecular absorption database [*Rothman et al.*, 2005]. In such a list, the location of lines and their temperature-dependent strengths are tabulated en masse. However, spectral observations show lines with broad absorption characteristics that are not consistent with the millions of very narrow absorptions that would be observed according to the line placements listed in HITRAN. This discrepancy arises due to well-known Doppler and pressure line broadening phenomena which arise because systems of molecules exhibit absorption behavior in the vicinity of the quantized absorption lines. Figure 2.1 shows that shortwave (SW) radiation of wavelengths between 0.1 and 4 μm is derived almost exclusively from the sun, whereas longwave (LW) radiation of wavelengths between 4 and 100 μm arises from terrestrial emission, implying that the two wavelengths regimes can be treated independently.
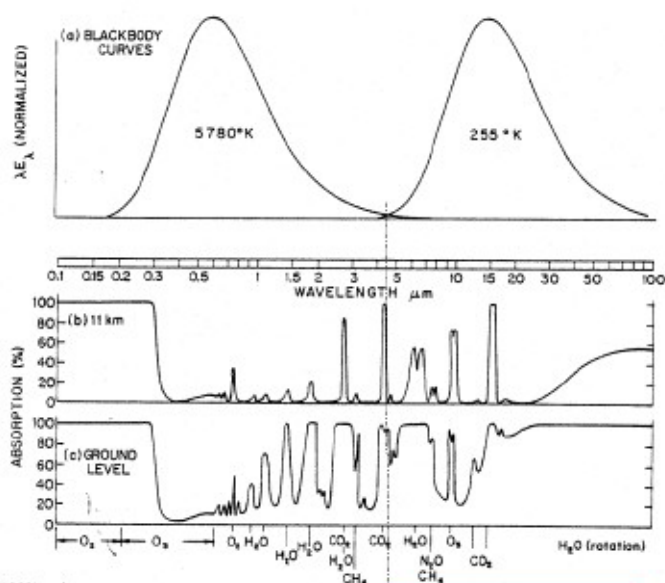
Figure 2.1: Upper panel shows emission-peak normalized solar and terrestrial blackbody spectra as a function of wavelength. Lower panel shows relatively broadband transmission from the top-of-atmosphere to 11 km and from the top-of-atmosphere to the ground level.

Also, this figure shows that several trace gases such as O_2, O_3, H_2O, CO_2, and CH_4 strongly absorb radiation at wavelengths throughout the shortwave and longwave.

The fundamental equation of radiative transfer becomes considerably more complicated where the source function term is non-negligible. In these cases, emission and scattering imply that propagation of light through the medium of interest at the viewing angle of interest may be a function of more than just the absorbing properties of that medium. For wavelengths of light between 3 and 100 μm, Planck emission of the molecules in the layer of interest will contribute to measured radiance as follows:

$$B_v(\theta(z)) = \frac{2hc^2v^3}{\exp\left(\frac{hcv}{k\theta(z)}\right) - 1} \tag{2.4}$$

where $\theta(\tau_v)$ is the temperature corresponding to the layer of the atmosphere at z, h is Planck's constant, c is the speed of light, and k is Boltzmann's constant. Scattering involves the angular rearrangement of photons from the direction of initial propagation to other directions sometimes with accompanying absorption. For the purposes of this work, changes in wavelength as a result of scattering processes (Raman scattering) will not be considered, as their contribution to radiative energy exchange is negligible. Another aspect of scattering that tends to increase the complexity of radiative transfer solutions is the vectorized nature of radiation. That is, the incident photons have an electric vector of a specific orientation relative to the direction of propagation which is not necessarily conserved during scattering processes. Stokes parameters describe the polarization of an electromagnetic vector in several components, and a phase matrix (analogous to the phase function) must be included to describe how incident radiance of a certain intensity and polarization will change both intensity and polarization as a result of the scattering event. For the purposes of this research, polarization is only indirectly relevant insofar as satellite

instrument measurements must either be corrected to consider polarization or polarized radiation measurements can be useful in discerning various atmospheric state properties.

In the presence of scattering, the source function adds significant complexity to the solution of this Eq. (2.1) and is often described as follows:

$$J_\nu\left(\tau_\nu(z),\mu,\phi\right)=\frac{\omega_o}{4\pi}\int_0^{2\pi}\left[\int_{-1}^1 P_\nu\left(\tau_\nu(z),\mu,\phi,\mu',\phi'\right)*I_\nu(\tau_\nu(z),\mu,\phi)d\mu'\right]d\phi'+B_\nu\left(\tau_\nu(z)\right) \qquad (2.5)$$

where ω_o is the single-scattering albedo, which refers to the ratio of scattering to extinction, $P_\nu\left(\tau_\nu(z),\mu,\phi,\mu',\phi'\right)$ is the phase function for a given incident zenith and azimuth angles (μ,ϕ) at zenith and azimuth scattering angles (μ',ϕ') which functionally describes how incident radiance is rearranged angularly, and $B_\nu(\tau_\nu)$ is the blackbody emission from Eq. (2.4). The last two terms in Eq. (2.5) describe the contribution of solar radiation and the contribution of radiance reflected from the surface and incident upon the layer. A description of the phase function depends on the composition of the scattering medium (either molecules or larger particles such as aerosols or hydrometeors). It also strongly depends on the ratio of the size of the scatterers to the wavelength of incident radiation which is known as the size parameter. Where the wavelength of incident photons is much smaller than the particle size, simple ray-tracing can be utilized to describe the phase function. Where the wavelength of the photons is of comparable size to the scattering medium, treatment of the phase function is considerably more complex and requires a detailed understanding of particle geometry and composition. For spherical particles, Mie scattering [*Mie*, 1908] calculations produce phase functions in a computationally efficient and accurate manner, though scattering is much more complicated when particles are non-spherical. Where the wavelength of the incident radiation is much larger than the scattering media, Rayleigh scattering [*Strutt*, 1899] provides an accurate description of the phase function and is computationally efficient. Figure 2.2 shows a diagram that depicts the relationship between the

size of the scattering medium and the wavelength of incident photons as described above with

several examples of scattering media included.
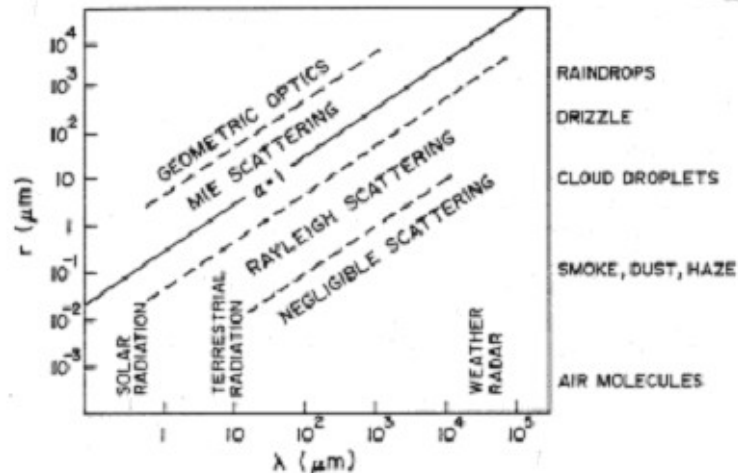
Figure 2.2: Diagram depicting scattering regimes as a function of scattering medium radius (x-axis) and incident particle wavelength (y-axis) as adapted from *Wallace and Hobbs* [1977].

Solutions to the equation of radiative transfer depend strongly on the problem being addressed

and the wavelengths being measured. Several sections of this chapter will discuss solution

techniques for radiative transfer at different sets of wavelengths.

Ultimately, the interpretation of measured spectra requires accurate and computationally

efficient methods for solving the radiative transfer equation so that spectra, such as those shown

in the figure below, can be scientifically meaningful. The figure on the left shows a large number

of spectral lines arising from different molecular absorption/emission lines which change the

Planck function emitted by the surface. The same information can be transformed by inverting

Planck function of the radiance for the temperature. The new brightness temperature ordinate

indicates the temperature of the layer of the atmosphere to which the channel's radiance value is

most sensitive. The current generation of satellite instruments can record tens to hundreds of

high-spectral resolution spectra each second, and all of this voluminous data can be scientifically

meaningful given appropriate interpretation.
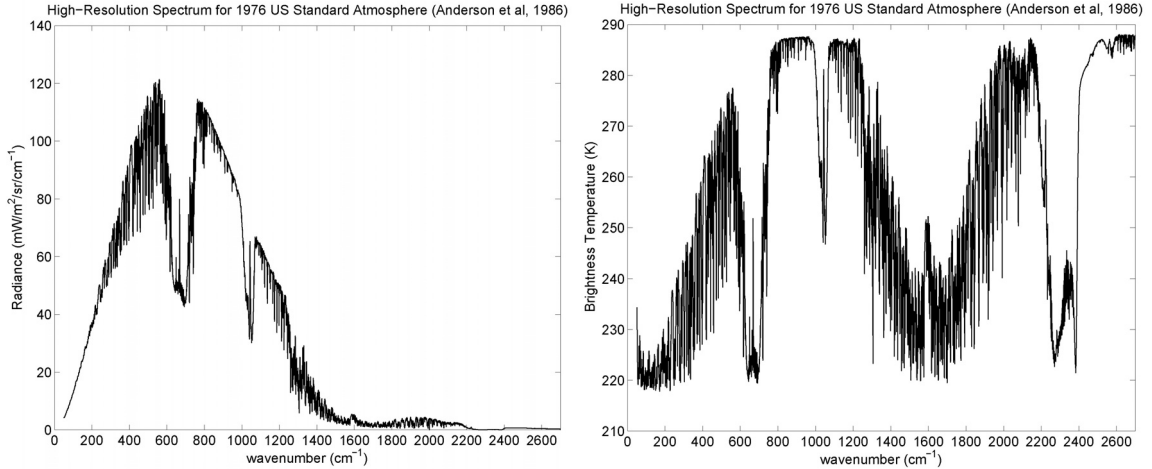
Figure 2.3: High-resolution clear-sky spectra calculated from the Line-by-Line Radiative Transfer Model (see *Clough et al.* [2005] for details) using the 1976 US Standard Atmosphere [*Anderson et al.*, 1986]. The left panel indicates the spectra in radiance units and the right panel indicates the same spectrum in brightness temperature units.

Therefore, analytic and numerical solutions to the radiative transfer equation are exceedingly useful, though the exact means of the solution depends on the wavelengths under consideration.

2.3   LW Radiative Transfer Basics

In the absence of scattering and where the source function is the Planck function, Eq. (2.1) is a linear, first-order differential equation that is azimuthally independent and can be solved by means of an integrating factor to yield the following expression for upwelling radiance, which is valid under clear-sky conditions in the longwave:

$$I_v(z_{meas}, \mu) = \varepsilon_{v,surf} B_v(\theta_{surf}) T_v(0, z_{meas}, \mu) + \int_0^{z_{meas}} B_v(\theta(z')) \frac{\partial T_v(0, z', \mu)}{\partial z'} dz' \quad (2.6)$$

where $\varepsilon_{v,surf}$ is the monochromatic surface emissivity. Eq. (2.6) allows for the calculation of top-of-atmosphere (TOA) radiance at a given wavelength when the temperature profile and transmission profile at the wavelength of interest is known. The latter quantity requires knowledge of the concentration of the species that contribute to absorption at the wavelength of

interest in order to produce absorption coefficients for Eq. (2.2). For downwelling radiance, the following expression replaces Eq. (2.6):

$$I_\nu(z_{meas}, \mu) = H_\nu^{sun} T_\nu(\infty, z_{meas}, \mu) + \int_\infty^{z_{meas}} B_\nu(\theta(z')) \frac{\partial T_\nu(\infty, z', \mu)}{\partial z'} dz' \qquad (2.7)$$

where H_ν^{sun} represents the top-of-atmosphere downwelling thermal radiation from the sun.

When clouds are present, LW radiative transfer can be more complicated and is usually described by including a cloud in an atmospheric layer and modeling its transmission and reflection properties. The following expression, after *Kulawik et al.* [2006] describes how radiance (which here is implicitly wavelength- and zenith angle-dependent) can be calculated:

$$I^{TOA} = I_1^\uparrow T_c' T_3 + (1 - T_c') B_c T_3 + I_3^\uparrow \qquad (2.8)$$

where I^{TOA} is the TOA radiance, $I_1^\uparrow$ is the upwelling radiance incident on the bottom of the cloud deck, T_3 is the clear-sky transmittance between the cloud-deck and the detector, B_c is the Planck emission at the temperature of the cloud deck, $I_3^\uparrow$ is the emission of the atmosphere above the cloud-deck that reaches the detector, and T_c' is the effective cloud transmittance given by:

$$T_c' = T_c - R_c \frac{I_3^\downarrow - B_c}{I_1^\uparrow - B_c} \qquad (2.9)$$

where T_c is the transmission through the cloud, R_c is the cloud reflectance, and $I_3^\downarrow$ is the downward emission from above the cloud deck that reaches the cloud's upper boundary. Calculating the cloud transmission and reflection functions is not a trivial task but has been addressed in detail in the literature. Particularly, the Discrete Ordinate Radiative Transfer (DISORT) method [*Stamnes et al.*, 1988] and the doubling-adding method [*Twomey,* 1966; *Hansen*, 1971] are efficient techniques to produce accurate solutions to the radiative transfer equation where scattering is non-negligible.

Unfortunately, the efforts to describe cloud properties as they relate to longwave radiative transfer is not as easily amenable to parameterization as it is for clear-sky conditions (see *L'Ecuyer et al.* [2006] and *Cooper et al.* [2006] for a more detailed discussion on this matter). Often, however, one-dimensional radiative transfer can be reasonably achieved by describing clouds in terms of a cloud water content profile, a cloud phase profile (either liquid or ice), and a cloud effective radius profile. The latter term provides a simple though effective parameterization of cloud optical properties, including single-scattering albedo and a description of the angular asymmetry in the phase function in terms of the geometric mean of the size distribution of hydrometeors at a specific level [*Hu and Stamnes,* 1993; *Fu et al.*, 1997].

Longwave radiative transfer is generally straightforward from a computational perspective because the source function is dominated by Planck emission. Several vibrational-rotational bands of H_2O, CO_2, O_3, and CH_4 produce the dominant spectral features observed in TOA spectra. Many radiative transfer computer codes have been written independently and most tend to agree [*Kratz et al.,* 2005], though one of the principal sources of discrepancy between different radiative transfer codes is the model for the water vapor continuum. Continuum absorption, which accounts for effects at wavelengths far from a line center in the presence of multiple absorption lines, has been especially difficult to implement in radiative transfer models. Theoretical models [*Tipping and Ma*, 1995] provide a robust foundation but have not been as accurate as semi-empirical models [*Tobin*, 1996; *Clough et al.*, 2005]. In fact, it is extremely challenging to account for the subtle interactions which must be described in order to model absorptions at wavelengths that are very far (25 cm^{-1} or more) from the line center. A change in the continua models may result in outgoing longwave radiation (OLR) changes of 10–30 W/m^2.

2.4   SW Radiative Transfer Basics

For wavelengths of light between 0.1 and 4 μm, radiative transfer can be considerably complicated and computationally expensive. Under all but the most trivial cases, the source function must be considered explicitly and surface reflection must be modeled explicitly. Finally, Planck emission is negligible. The source function for shortwave radiation can be modeled as following:

$$J_\nu\left(\tau_\nu(z),\mu,\phi\right)=\frac{\omega_o}{4\pi}\int_0^{2\pi}\left[\int_{-1}^{1}P_\nu\left(\tau_\nu(z),\mu,\phi,\mu',\phi'\right)*I_\nu\left(\tau_\nu(z),\mu,\phi\right)d\mu'\right]d\phi'+$$
$$\frac{\omega_o}{4\pi}F_\oplus P_\nu\left(\tau_\nu(z),\mu,\phi,-\mu_o,\phi_o\right)$$

(2.10)

where $F_\oplus$ is the solar function. For SW radiative transfer, the solar source function is scattered in the forward direction allowing for the phase function to be described using the δ-Eddington approximation, which models the function as a Dirac-δ function followed by terms describing the phase-function side-lobes. Integrating the radiative transfer equation requires explicit treatment of the phase function, and reasonable and computationally efficient methods for doing this strongly depend on the specifics of the radiative transfer problem being addressed. Books by *Chandrasekhar* [1950], *Goody and Yung* [1989], *Thomas and Stamnes* [1998], and *Liou* [2002] provide extensive discussions of solution methods to the radiative transfer equation which may be necessary for the proper interpretation of shortwave radiance measurements.

2.5   Microwave Radiative Transfer Basics

Microwave radiative transfer can be understood as a direct extension of some of the principles of longwave radiative transfer. Wavelengths in this spectral region range from millimeters to centimeters and are considerably longer than those which are important for the

earth's energy balance. There are relatively few absorption lines to be measured, especially when compared to the number of lines that are sampled by shortwave and longwave spectrometers. Additionally, treatment of scattering in non-precipitating scenes is simplified by the fact that size parameter is much smaller in the microwave than at infrared or visible wavelengths, and so Rayleigh scattering is a valid assumption for particle sizes up to 100 μm.

Otherwise, microwave radiative transfer is similar to infrared radiative transfer (e.g., *Read et al.,* 2006]), but these longer wavelengths can be very useful for atmospheric characterization. Cloud optical depths can be much lower in the microwave relative to visible optical depths, allowing for the characterization of water vapor and cloud properties for most cloudy scenes. At the same time, microwave detection by itself can be insufficient for detecting optically thin clouds and achieving high vertical resolution in the description of gaseous profiles. These tasks are generally achievable using visible and infrared wavelengths.

2.6   Flux and Heating Rate Calculations

One-dimensional radiative heating/cooling rate profiles are a function of pressure for each spectral interval. For circulation model calculations, the ultimate quantities of interest are the total shortwave heating rate profile and the total longwave cooling rate profile which represent the integration of spectral heating/cooling rate profile information generally over the 3000–50000 cm^{-1} and 100–3000 cm^{-1} bands, respectively. The value of the radiative heating/cooling rate for a given pressure layer is directly proportional to the radiative flux divergence for that layer:

$$\theta'_{\bar{v}}(z) = \frac{1}{C_p \rho(z)} \frac{dF_{\bar{v}}^{net}(z)}{dz} \tag{2.11}$$

where $\theta'_{\bar{v}}(z)$ is the spectral heating/cooling rate of the layer, $\rho(z)$ is the density of the layer, C_p is the heat capacity, and $F_{\bar{v}}^{net}(z)$ is the net (upward-downward) flux for the layer over the spectral interval denoted $\bar{v}$. For the longwave, the heating rate profile is generally negative, so the convention is to reverse the sign and use the term "cooling rate profile" instead.

The calculation of heating/cooling rate profiles is ubiquitous, so a large amount of research has been devoted to addressing the accuracy and computational efficiency of these values. For the clear sky in local thermodynamic equilibrium, the derivation of the net flux divergence follows from a solution to the Fundamental Equation of Radiative Transfer because the source function is the Planck function as described in Section 2.3. For the calculation of heating/cooling rates, radiance calculations must be converted into flux:

$$F_{\bar{v}}^{\downarrow\uparrow}(z) = \int_0^1 I_{\bar{v}}^{\downarrow\uparrow}(\mu, z)\, \mu \, d\mu \tag{2.12}$$

where the $\downarrow\uparrow$ superscript refers to separate upwelling and downwelling components for radiance and flux. As an analog to spectral transmittance, the concept of flux transmittance allows for the representation of flux in similar terms as the solution to the radiative transfer equation in terms of radiance without having constantly to declare the angular integration:

$$T_{\bar{v}}^f(z', z) = \int_0^1 T_{\bar{v}}(\mu, z', z)\, \mu \, d\mu \tag{2.13}.$$

The preceding equation allows for the expression of upwelling and downwelling flux in a form that is similar to the radiative transfer equation solution for upwelling and downwelling radiance:

$$F_{\bar{v}}^{\uparrow}(z) = \varepsilon_{\bar{v}} B_{\bar{v}}\big[\theta(z_{surf})\big] T_{\bar{v}}^f(z_{surf}, z) + \int_{z_{surf}}^{z} B_{\bar{v}}[\theta(z')] \frac{\partial T_{\bar{v}}^f(z', z)}{\partial z'} \, dz' \tag{2.14}$$

$$F_{\bar{v}}^{\downarrow}(z) = \int_{z}^{\infty} B_{\bar{v}}[\theta(z')] \frac{\partial T_{\bar{v}}^f(z, z')}{\partial z'} \, dz' \quad . \tag{2.15}$$

Consequently, the net flux divergence is the derivative of the net flux (upwelling minus downwelling) and is given by:

$$
\theta'_{\bar{v}}(z) = \frac{2\pi}{C_p \rho(z)} \varepsilon_{\bar{v}} B_{\bar{v}}\left[\theta\left(z_{surf}\right)\right] \frac{\partial T_{\bar{v}}^f\left(z_{surf}, z\right)}{\partial z} +
$$
$$
\frac{2\pi}{C_p \rho(z)} \int_{z_{surf}}^{z} B_{\bar{v}}\left[\theta\left(z'\right)\right] \frac{\partial^2 T_{\bar{v}}^f\left(z', z\right) dz'}{\partial z' \partial z} - \qquad (2.16)
$$
$$
\frac{2\pi}{C_p \rho(z)} \int_{z}^{\infty} B_{\bar{v}}\left[\theta\left(z'\right)\right] \frac{\partial^2 T_{\bar{v}}^f\left(z, z'\right)}{\partial z' \partial z} dz'
$$

In practice, cooling rate profile calculation is performed with an emphasis on computational efficiency. With a given atmospheric state (temperature, H_2O, CO_2, O_3, CH_4, N_2O, and cloud optical depth profiles), band-model programs are utilized to estimate interlayer transmittance. In particular, the correlated-*k* method [*Lacis and Oinas*, 1991] has proven to be computationally efficient and reasonably accurate with respect to the much more computationally intensive line-by-line integration in producing interlayer band-average transmittance. The resulting transmittance values are then used to solve for band-averaged radiance. Radiance-to-flux conversion requires integrating radiance over zenith angle and is achieved formally and exactly through exponential integrals [*Goody and Yung*, 1988]. However, the computational expense of exponential integrals motivates the usage of limited-point quadrature instead. Gauss-Jacobi quadrature [*Abramowitz and Stegun*, 1964] is an optimal means for the calculation of flux transmittance, and the utilization of three-point quadrature produces little discrepancy as compared to complete angular integration. Many fast radiative transfer models even use the diffusivity approximation (1-point quadrature) to calculate flux transmittance. Quadrature methods tend to produce some error in the layer exchange terms only with low optical depth bands. The discretized calculation of upwelling and downwelling fluxes at layer boundaries (levels) is given by:

$$F_{\bar{v}}^{\uparrow}(z_i) = \varepsilon_{\bar{v}} B_{\bar{v}}\left[\theta(z_{surf})\right] T_{\bar{v}}^{f}(z_{surf}, z_i) + \sum_{k=i}^{N-1} B_{\bar{v}}\left[\theta(z_{k+1/2})\right] * \left[T_{\bar{v}}^{f}(z_i, z_{k+1}) - T_{\bar{v}}^{f}(z_i, z_k)\right] \qquad (2.17)$$

$$F_{\bar{v}}^{\downarrow}(z_i) = \sum_{k=i}^{N-1} B_{\bar{v}}\left[\theta(z_{k+1/2})\right] * \left[T_{\bar{v}}^{f}(z_i, z_{k+1}) - T_{\bar{v}}^{f}(z_i, z_k)\right] \qquad . \qquad (2.18)$$

Finite-difference derivatives of net flux produce flux divergence, which is scaled to produce the cooling rate profile. Evaluation of analytic derivatives with respect to altitude for cooling rate profile calculation is generally avoided due to the inconsistency between the vertical coordinate scheme needed for accurate radiative transfer calculations and the Lipschitz condition [*Jeffreys*, 1988] which is necessary for derivative stability.

The band models are typically evaluated over the fewest bands while minimizing the variation of the Planck function across the band and minimizing overlap between absorptions from different species. For the longwave, 10–15 bands are generally sufficient for accuracy of 1 W/m^2 for fluxes at all levels, 0.1 K/day for tropospheric cooling rates, and 0.3 K/day for lower-stratospheric cooling rates relative to line-by-line calculations [*Clough et al.*, 2005]. Shortwave heating rates are calculated in a similar fashion to cooling rates except that solutions to the radiative transfer equation are achieved through the inclusion of scattering of the solar source function. The δ-Eddington approximation is utilized to characterize a strongly forward-peaked phase function. Accurate, though computationally expensive radiative transfer in the presence of scattering is achieved through the use of DISORT which allows for the integration of radiance at several viewing angles (streams). The two-stream approximation [*Schuster*, 1905] eases some of the computational expense with slightly inferior accuracy [*Liou*, 1974]. Currently, the multiple-stream heating rate calculations are radiometrically accurate to approximately 2 W/m^2, while the two-stream approach is only accurate to 3 W/m^2 relative to line-by-line models. In terms of heating rates, the two-stream approximation has an accuracy of 0.1 K/day in the troposphere and 0.3 K/day in the stratosphere [*Clough et al.*, 2005].
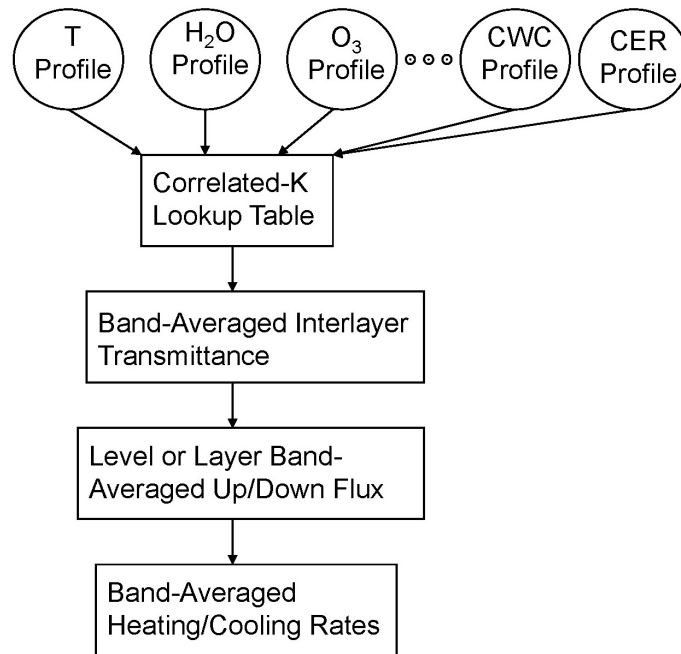
Figure 2.4: Flow-chart detailing the computational processes involved in producing heating/cooling rate profiles with a correlated-k method from standard atmospheric state inputs including temperature, water vapor, ozone, and cloud optical depth profiles.

For several decades, atmospheric modelers have calculated radiative heating and cooling rates but have had much more limited computational resources as compared to the present. Consequently, approximate methods have been widely utilized. One such approach, Newtonian cooling, allows for the estimation of cooling rates near the surface and in the stratosphere by multiplying the Planck radiation of a layer times a parameterized change in flux transmittance over that layer. This approach is reasonably accurate (around 90%) where its application is warranted and has the benefit of being analytical. Unfortunately, it is also inapplicable for cooling rate calculations spanning the free troposphere and lower stratosphere and will not suffice where clouds are present. In light of the availability of computational resources that can be used to achieve accurate heating and cooling rate calculations, these approximations will not be utilized in this research.

2.7   Description of Inverse Theory

Inverse theory provides a complement to forward model calculations and facilitates the interpretation of data in terms of the quantities of interest that underlie the measurement. Inverse theory is applied to a wide variety of scientific and engineering disciplines ranging from medicine to seismology, and it is a central aspect of remote sensing because of the ambiguity sometimes associated with the measurements. Satellite instrument measurements are derived from the convolution of the quantity of interest with a function that describes how that signal propagates through the atmosphere to the detector several hundred kilometers above the earth's surface. From a satellite platform, it is generally non-trivial to interpret the measurements in terms of the quantities of interest.

A general representation of the inverse problem starts with defining y, the measurement, as a function of a forward model F acting upon the atmospheric state x as shown by the following:

$$y = F(x) \tag{2.19}$$

where F contains a description of the physics that map the quantities of interest from state space to measurement space. In general, $F(x)$ is a nonlinear function of x, but can be linearized in the vicinity of a state x_o and expressed in a discrete form:

$$\mathbf{y} - \mathbf{y}_o = \mathbf{K}(\mathbf{x} - \mathbf{x}_o) + \varepsilon \tag{2.20}$$

where $\mathbf{y}$ is the discrete measurement vector as determined by the remote sensing instrument, $\mathbf{y}_o$ is the measurement vector as computed by the forward model F using a pre-supposed state vector $\mathbf{x}_o$, $\mathbf{x}$ is the true state vector, ε represents the total error in the equation (as discussed below), and $\mathbf{K}$ is the Jacobian with elements defined by the following:

$$K_{jk} = \frac{\partial F_j(\mathbf{x})}{\partial x_k} \qquad . \qquad (2.21)$$

Here, $\mathbf{K}$ represents the linearization of the discretized forward model. For historical reasons, it is also called the weighting function matrix. The weighting function matrix rows are of particular importance to profile retrieval methods using wavelengths for which the transmittance between the surface and the satellite is very low. Under these circumstances, the altitude of the peak of the weighting function row for a certain channel corresponds to that layer which contributes most significantly to the channel radiance measured at the top of the atmosphere. The following figure provides a representation of a few representative rows of a weighting function matrix with arbitrary abscissa units. Each row indicates a spectral channel's vertical sensitivity to temperature profile perturbations.
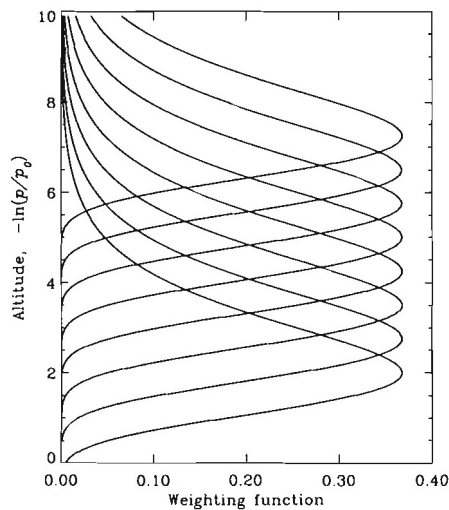
Figure 2.5: A set of synthetic temperature weighting functions representing a typical nadir sounder measuring thermal emission. From *Rodgers* [2000].

Because these weighting functions exhibit relatively narrow peaks, the satellite measurements are almost entirely determined by the contribution from the composition of a region in the atmosphere within a fraction of a scale height.

Solving for $\mathbf{x}$ in terms of $\mathbf{y}$ and $\mathbf{K}$ has been the focus of much discussion in the field of

remote sensing [*Twomey,* 1977; *Milman*, 1999; *Rodgers*, 2000]. In general, Eq. (2.20) is ill-posed and such a problem involves either implicit or explicit regularization which can be done in a variety of different ways (e.g., *Hansen* [1994]; *Tarantola* [2005]). Additionally, the appropriate criteria for a successful retrieval are not always clear. *Twomey* [1963] proposed that realistic state vector profiles should be smooth, which can be defined in a number of different ways. The retrieval algorithm can also be formulated to minimize the expected error in the calculated state, or it can produce a result that is the most likely given the measurement and the *a priori* information on the state [*Rodgers,* 2000]. This latter method offers several benefits: it presents a balance between the *a priori* and measurement information while making solutions to the problem numerically well conditioned. Finally, estimation of *a posteriori* statistics is generally straightforward using the techniques prescribed by *Rodgers* [2000].

A brief overview is presented here. Starting with Bayes' theorem [*Bayes*, 1763], which relates the conditional and *a priori* probabilities of random variables, the probabilistic relationship between the retrieval, the measurement, and the *a priori* information can be described by:

$$P(\mathbf{x}|\mathbf{y}) = \frac{P(\mathbf{y}|\mathbf{x})P(\mathbf{x})}{P(\mathbf{y})} \tag{2.22}$$

where $P(\mathbf{x}|\mathbf{y})$ is the conditional probability of the atmospheric state $\mathbf{x}$ given the measurement $\mathbf{y}$, $P(\mathbf{y}|\mathbf{x})$ is the conditional probability of the measurement $\mathbf{y}$ given atmospheric state $\mathbf{x}$, $P(\mathbf{x})$ is the *a priori* probability associated with the atmospheric state, and $P(\mathbf{y})$ is the *a priori* probability associated with the measurement. Assuming Gaussian statistics, it can be shown (e.g., *Rodgers* [2000]) that the following relationship exists:

$$-2\ln P(\mathbf{x}|\mathbf{y}) = [\mathbf{y} - \mathbf{Kx}]^T \mathbf{S}_\varepsilon^{-1} [\mathbf{y} - \mathbf{Kx}] + [\mathbf{x} - \mathbf{x}_a]^T \mathbf{S}_a^{-1} [\mathbf{x} - \mathbf{x}_a] + const \tag{2.23}$$

where $\mathbf{S}_\varepsilon$ is the covariance matrix associated with experimental error, and $\mathbf{S}_a$ is *a priori* covariance matrix of the state vector. The concept of the covariance matrix is very useful for retrieving quantities based on remote sensing measurements. A covariance matrix both describes the spread of individual variables about their mean values and the relationship between sets of variables as they vary about their mean values. The covariance matrix $\mathbf{S}(\mathbf{X}, \mathbf{Y})$ is given by the following:

$$\mathbf{S}(\mathbf{X}, \mathbf{Y}) = E\big((\mathbf{X} - \boldsymbol{\mu})(\mathbf{Y} - \mathbf{v})\big) \tag{2.24}$$

where E is the expectation operator, $\mathbf{X}$ and $\mathbf{Y}$ are sets of random variables, $E(\mathbf{X}) = \boldsymbol{\mu}$ and $E(\mathbf{Y}) = \mathbf{v}$. This quantity is frequently carried through the analysis of remote sensing data because a large number of random variables contribute to the retrieved quantities. It is therefore important to estimate how these quantities are related both from a physical perspective and from the perspective that several variables may produce indiscernible measurement differences and will thus be correlated mathematically as the result of the retrieval.

In many cases, it is desired to have an estimate of the retrieval state in lieu of a distribution, and this estimate is some function of $P(\mathbf{x}|\mathbf{y})$. For example, the following is called the maximum *a posteriori* method and produces vector estimate according to the posterior distribution [*DeGroot*, 1970]:

$$\hat{\mathbf{x}} = \int P(\mathbf{x}|\mathbf{y}) \mathbf{x} \, d\mathbf{x} \tag{2.25}$$

where $\hat{\mathbf{x}}$ is the estimate of the atmospheric state retrieval. By equating terms, it is also possible to show that the covariance matrix associated with this estimate $\hat{\mathbf{S}}$ is given by the following:

$$\hat{\mathbf{S}} = \left(\mathbf{K}^T \mathbf{S}_\varepsilon^{-1} \mathbf{K} + \mathbf{S}_a^{-1}\right)^{-1} \tag{2.26}$$

The previous discussion was predicated on the assumption that the forward model was moderately non-linear. This assumption is appropriate where the weighting function matrix is valid to within the range of atmospheric states spanned by the *a priori* estimate and the retrieval estimate. Where the linearity assumption does not hold, more complicated retrieval techniques are warranted, adding considerable difficulty to retrieval efforts.

A discussion of inverse theory requires a discussion of the sources of possible errors that may arise. In the case of satellite instrument measurements, the large quantities of measurement data must be treated carefully and error budgets tabulated in order to avoid improper interpretation. Errors in the retrieval algorithm can be broadly divided into four categories: smoothing error arising from improper representation of the quantities targeted for retrieval relative to their underlying state, forward model parameter errors arising from the retrieval's incomplete representation of the atmospheric state by not including quantities that have bearing on the measurement, systematic forward model error due to improper physics, and retrieval error arising from an improper conversion from the measurement to the retrieval. These sources of error are represented in Eq. (2.27):

$$\hat{\mathbf{x}} - \mathbf{x} = (\mathbf{A} - \mathbf{I}_n)(\mathbf{x} - \mathbf{x}_a) + \mathbf{G}_y \mathbf{K}_b (\mathbf{b} - \hat{\mathbf{b}}) + \mathbf{G}_y \Delta \mathbf{f}(\mathbf{x}, \mathbf{b}, \hat{\mathbf{b}}) + \mathbf{G}_y \mathbf{e} \qquad (2.27)$$

where $\hat{\mathbf{x}}$ is the retrieved state vector, $\mathbf{x}$ is the true state vector, and $\mathbf{A}$ is the averaging kernel matrix which denotes the ability of the retrieval to resolve perturbations in the true state and is given by:

$$\mathbf{A} = \frac{\partial \hat{\mathbf{x}}}{\partial \mathbf{x}} \qquad . \qquad (2.28)$$

An example of the averaging kernel matrix is shown in the following figure which indicates that for a thermal sounder, perturbations in $\mathbf{x}$ are well-resolved in the middle of the troposphere but poorly resolved near the surface and in the upper stratosphere.
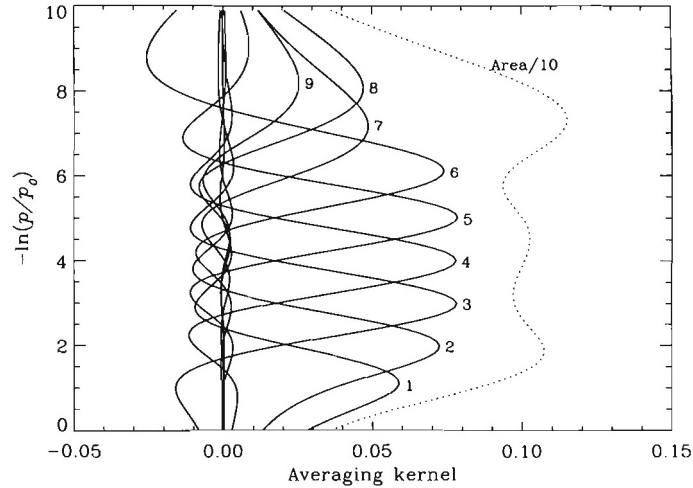
Figure 2.6: Averaging kernels for a standard nadir temperature retrieval (in solid) and the total area denoting the vertical sensitivity of the entire retrieval. From *Rodgers* [2000].

From Eq. (2.27), $\mathbf{I}_n$ is the identify matrix of size n and $\mathbf{G}_y$ is the gain matrix which describes how measurement uncertainties propagate into the retrieval:

$$\mathbf{G}_y = \frac{\partial \hat{\mathbf{x}}}{\partial \mathbf{y}} \qquad . \qquad (2.29)$$

$\mathbf{K}_b$ is the weighting function matrix for non-retrieved forward model parameters, $\mathbf{b}$ is the set of non-retrieved forward model parameters, $\hat{\mathbf{b}}$ is an estimate of forward model parameters that are most appropriate for the retrieval, $\Delta\mathbf{f}\left(\mathbf{x}, \mathbf{b}, \hat{\mathbf{b}}\right)$ is the difference between the calculated and the true forward model calculation, and $\mathbf{e}$ describes the remaining sources of error including measurement error and retrieval error. The first, second, and fourth terms on the RHS of Eq. (2.27) can be reasonably estimated in the course of the retrieval algorithm, while the third term describing forward model errors is difficult to address except through extensive model improvement efforts.

In order to test the feasibility of using a set of measurements to reduce uncertainty in a set of atmospheric state parameters, a retrieval sensitivity test can be used. This approach involves establishing a retrieval environment which simulates measurements and tests whether these

measurements can be used to interpret the retrieval quantities properly. The sensitivity test

begins with an atmospheric state that is specified by a model atmosphere (i.e., *Anderson et al*.

[1986]) and calculates a synthetic measurement using that model atmosphere as a set of inputs to

the forward model.   Noise is then added to the synthetic measurement that is consistent with the

instrument being used in the retrieval. The model atmosphere is then perturbed in a manner that

is consistent with the *a priori* covariance of the atmospheric state to produce a conception of the *a*

priori state. The difference between the synthetic measurement with noise and the spectrum

associated with the *a priori* state forms the input to the retrieval algorithm. The retrieval

algorithm then attempts to reproduce the original model atmosphere and the retrieval results are

compared in state and measurement space. The resulting comparison indicates numerical

stability and the sensitivity that the retrieval will exhibit to aspects of the atmospheric state. The

following flow-chart indicates the steps associated with this retrieval sensitivity test.
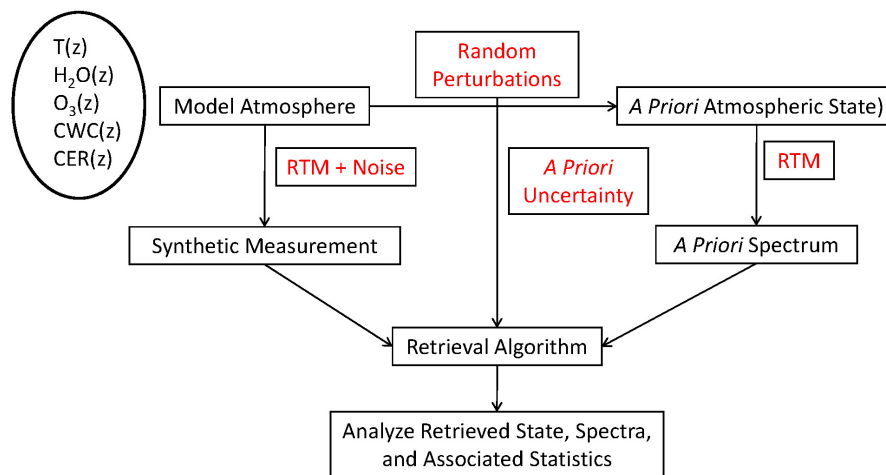
Figure 2.7: Flowchart for a synthetic retrieval sensitivity test in order to test the numerical stability of the retrieval algorithm and its dependence on *a priori* knowledge.

Another concept that is central to remote sensing data handling is information content

analysis. This will be discussed in more detail in later chapters, but this concept refers

qualitatively to the factor by which the understanding of a set of quantities as a result of making a

measurement changes. *Shannon* [1948] quantified this concept by introducing the notion of the

entropy of a probability distribution function. This describes the number of distinct internal states of a system (conventionally in thermodynamic terms) and can be evaluated by the following expression:

$$S = -k \sum_i P(x_i) \ln P(x_i)$$ (2.30)

where S is the entropy of the system, k is a numerical scaling factor that depends on the information content units, and $P(x_i)$ refers to the probability density of the system being in state x_i. The information content refers to the change in entropy and is given by

$$h = S_2 - S_1$$ (2.31)

where h is the information content associated with the measurement and S_2 and S_1 refer to the entropy of the states before and after the measurement respectively. Where a state can be described by a multivariate Gaussian distribution with m elements, the entropy can be expressed as the following:

$$S(P(\mathbf{x})) = m \ln\left(\sqrt{2\pi e}\right) + \frac{1}{2} \ln|\mathbf{S_x}|$$ (2.32)

where $\mathbf{x}$ is the vector describing the quantity of interest in a retrieval, m is the length of the vector, and $\mathbf{S_x}$ is the covariance associated with the vector. Therefore, the information content in nats becomes:

$$h = \frac{1}{2} \ln|\mathbf{S_2}\mathbf{S_1}^{-1}|$$ (2.33)

which can be evaluated during the course of a retrieval algorithm with minimal computational cost.

In subsequent chapters, this work will explore the analysis of remote sensing data to provide estimates of radiative fluxes, heating, and cooling rates. Briefly, this topic can be

understood in terms of deriving the best estimate of a function of the state vector, which in this case refers to the temperature, water vapor, ozone, and cloud profiles. While some higher-order retrieval products are derived from non-linear operators, most retrieval schemes that derive products that are functions of the state vector do so only by passing the retrieved state vector through a linear operator (e.g., column-integrated water-vapor concentration, average retrieval value). The case of the heating/cooling rate calculation as part of a retrieval cannot, in general, be considered to be a case where a linear operator acts on the retrieved state vector because the radiative transfer model cannot be regarded as a linear operator for all atmospheric states. However, assuming the operator acting upon the state vector is linear within the expected uncertainty in the retrieved state vector, it is reasonable to design the retrieval in terms of the following

$$\hat{\mathbf{z}}(\mathbf{x}) = \int P(\mathbf{x}|\mathbf{y}) \mathbf{z}(\mathbf{x}) d\mathbf{x} \tag{2.34}$$

where $\hat{\mathbf{z}}$ is the estimate of the function of the atmospheric state (i.e., the heating/cooling rate profile), and $\mathbf{z}(\mathbf{x})$ represents the radiative transfer model evaluated at state $\mathbf{x}$. Ultimately, this approach allows for an alternative consideration of the measurements with a greater emphasis placed on heating and cooling rate profiles. As shown in Figure 2.8 different approaches to deriving heating/cooling rate profiles are possible.
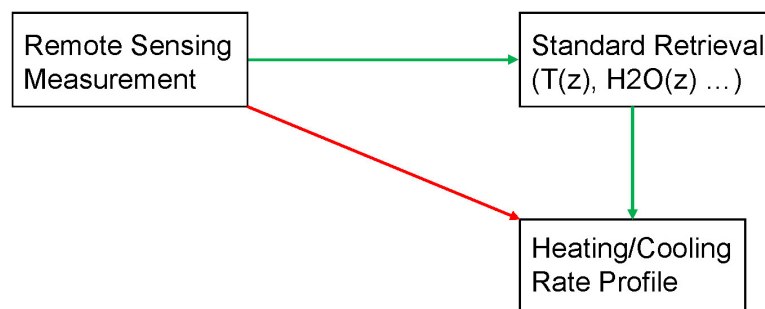
Figure 2.8: Diagram depicting routes for analysis of measurement data in order to derive heating and cooling rate profile data.

These approaches may lead to different covariance matrices with respect to the heating/cooling rate profile. The diagram in Figure 2.8 outlines two different approaches for understanding heating and cooling rates from measurements. Subsequent chapters will explore the estimation of these quantities in greater detail. Moreover, given that the retrieval of information from a remote sensing measurement is generally ill-posed, external information is often required to interpret the data properly. Different constraints, regularization, and retrieval techniques may allow for improved heating/cooling rate characterization. Subsequent chapters will explore some aspects of how remote sensing measurements can be used to describe heating and cooling rate profiles.

Chapter Three. Cooling Rate Retrievals: A Case Study.

3.1   Abstract

We expand upon methods for retrieving thermal infrared cooling rate profiles, originally developed by *Liou and Xue* [1988] through application to the inversion of the stratospheric cooling rate produced by carbon dioxide (CO_2) and a formal description of the associated error budget. Specifically, we infer lower- and mid-stratospheric cooling rates from the CO_2 ν_2 band on the basis of selected spectral channels and available data from the Atmospheric Infrared Sounder (AIRS). In order to establish the validity of our results, we compare our retrievals to those calculated from a forward radiative transfer program using retrieved temperature data from spectra taken by the Scanning High-Resolution Interferometer Sounder (S-HIS) on two aircraft campaigns: the Mixed-Phase Arctic Cloud Experiment (MPACE) and the Aura Validation Experiment (AVE), both in fall 2004. Reasonable and consistent comparisons are illustrated, revealing that spectral radiance data taken by high-resolution infrared sounders can be used to determine the vertical distribution of radiative cooling due to CO_2.

3.2   Introduction

Conventional clear-sky infrared cooling rates are calculated ubiquitously, and the accuracy of these calculations has been shown to affect forecast and general circulation model (GCM) performance [*Iacono et al*., 2000]. Numerical weather prediction models calculate radiative heating and cooling efficiently but are burdened by the computational requirement of estimating the atmospheric state from a suite of different instruments. In this light, novel approaches for the treatment of heating and cooling may be warranted. The largest infrared cooling takes place in the stratosphere, and this atmospheric region is strongly influenced by radiative interactions. The

interaction between solar heating and infrared cooling has been analyzed with satellite instrument measurements [*Mlynczak et al.*, 1999]. However, since the infrared cooling rate profile is dependent upon both individual layer atmospheric state vector values and their relationship to the broad structure of the atmospheric state, we seek to understand whether high-resolution infrared spectra can offer a better description of the infrared cooling rate profile beyond the atmospheric state standard products. The retrieval of infrared cooling rates from top-of-atmosphere (TOA) radiance data is a novel concept, and it may improve upon the understanding of the vertical distribution of infrared radiative cooling if successfully implemented. The approach of this retrieval will differ from atmospheric state retrievals in that we retrieve in the context of a spectral interval's description of the radiative cooling of an absorption band at a certain level, as opposed to a channel's description of an atmospheric state quantity at that level.

We chose to demonstrate the feasibility of a cooling rate profile retrieval with the CO_2 ν_2 band, as measured by the AIRS instrument [*Aumann et al.*, 2003], for several reasons. First, this band is a major contributor to clear-sky cooling in the stratosphere and mesosphere [*Kiehl and Solomon*, 1986]. Second, CO_2 is well mixed and the cooling rate profile varies minimally over an observation granule. Third, AIRS is a proven instrument with extensive spatial coverage, excellent signal-to-noise ratio, and well-quantified stability [*Aumann et al.*, 2005]. Finally, clouds, which greatly affect cooling rate profile values, are a minimal presence in the stratosphere, so the retrieval of CO_2 cooling rates can be greatly simplified.

Calculations of the radiative cooling of CO_2 in the stratosphere are straightforward with known atmospheric state quantities, but uncertainties in some of these quantities, most notably the temperature structure, propagate into cooling rate errors in ways that have not been fully explored. A formal understanding of the cooling rate error budget through observation is therefore warranted in order to determine to what extent our method can improve cooling rate profile determination.

3.3   Theoretical Basis

The derivation of the cooling rate profile from observed radiance data was first developed theoretically by *Liou and Xue* [1988] in order to measure the strong tropospheric cooling produced by the rotational band of water vapor in the far infrared. The spectral cooling rate profile is defined by:

$$\theta'(\nu,z) = \frac{1}{\rho(z)C_p} \frac{dF^{net}(\nu,z)}{dz} \tag{3.1}$$

where $\theta'(\nu,z)$ is the cooling rate, $\rho(z)$ is the atmospheric density profile, C_p is the heat capacity of air at constant pressure, and $F^{net}(\nu,z)$ is the net flux at height z for wavenumber ν. Conventionally, the cooling rate profile is calculated for the entire infrared (0–3000 cm^{-1}) by integrating Eq. (3.1) with respect to wavenumber. The contribution to the total infrared cooling rate of a spectral region at a particular level is given by the cumulative spectral cooling rate function which is defined as:

$$\Theta'(\nu,z) = \frac{\int_0^\nu \theta'(\nu,z)d\nu}{\int_0^{\nu_{max}} \theta'(\nu,z)d\nu}. \tag{3.2}$$

As shown in Figure 3.1, a change in color at a certain level on the horizontal axis implies appreciable spectral contribution to the total cooling rate value at that level.

A formal relationship between the infrared cooling rate profile and measured radiance values for a spectral band was established in *Liou and Xue* [1988] and is given by:

$$\int_0^\infty K(\nu,\mu,z)\,\dot\theta(z)\,dz = \alpha(\nu,\mu)\bar{I}(\bar\mu) + \beta(\nu,\mu)I(\nu,\mu) = y(\nu,\mu), \tag{3.3}$$

where $K(\nu,\mu,z) = C_p\,\rho(z)T(\nu,\mu,z)$ forms the weighting function matrix, $T(\nu,\mu,z)$ is the transmittance function, $I(\nu,\mu)$ is the TOA radiance, the coefficients $\alpha(\nu,\mu)$ and $\beta(\nu,\mu)$ can

be determined numerically, and $\bar{I}(\bar{\mu})$ is the mean spectral radiance as measured at a zenith angle,

$\bar{\mu}$, computed from the mean value theorem (see *Liou and Xue* [1988] for derivation).
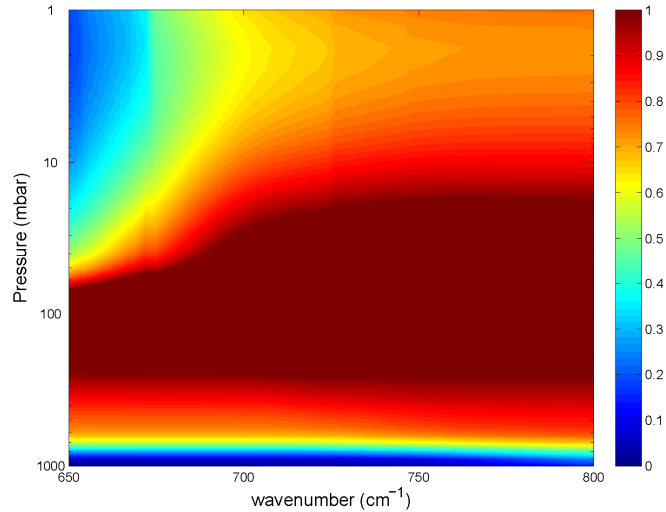
Figure 3.1: Spectral cumulative cooling rate contribution function for mid-latitude summer conditions. As opposed to the standard spectral cooling rate plot, this plot is useful for discerning the differential contribution of certain spectral regions to the total IR cooling rate.

In this chapter, the values of $\alpha(v,\mu)$ and $\beta(v,\mu)$ are computed numerically from two

executions of our radiative transfer model at slightly different atmospheric states. These terms

relate radiances to spectrally integrated and spectrally independent TOA fluxes. Equation (3.3)

demonstrates that the cooling rate profile cannot be measured in a forward sense with a remote

spectrometer, but it is possible to derive information about cooling from TOA radiance

measurements using inverse theory based on the Fredholm equation of the first kind denoted in Eq.

(3.3).

Assuming that the functional relationship between the measurements and the retrieval is

well behaved in the solution region, Eq. (3.3) can be analyzed using a linear Bayesian estimation

technique to retrieve the cooling rate profile. With Gaussian statistics for the measurement and *a*

priori error, the retrieved state can be expressed as a balance between the expected amount of

information about the retrieval quantity as given by the measurement metric $y(v,\mu)$ with the

knowledge that constrains the retrieval to a certain solution space. The *a priori* covariance matrix

of the cooling rate profile, which is utilized to constrain the retrieval, is calculated empirically,

given expected state vector change uncertainties. For the cooling rate profile *a priori* constraint, the

long range covariances between cooling rate profile components are smoothed according to a scale-

height correlation that is derived from near off-diagonal components of the empirical covariance

matrix. The error covariance matrix, which describes expected errors in the measurement metric, is

assumed to be diagonal with diagonal elements derived from the expected deviation in

measurements derived from Eq. (3.3). For this type of retrieval error analysis, it can be shown

(*Rodgers* [2000]) that the *a posteriori* covariance for the cooling rate profile can be determined

from the combination of the measurement error projected onto the data space and the prior error.

In terms of computing the net flux divergence at several atmospheric levels, radiance

measurements at different viewing angles provide improved information over a single spectra, but

the degree and manner in which angular information can be utilized needs further exploration.

We have generalized the retrieval method of *Liou and Xue* [1988] for more complicated scenarios

with cross-track spatial variability where the viewing geometry does not easily lend itself to

meaningful spatial resolution. Various measurements may be utilized according to the viewing

geometry of the instrument being considered, but for scanning instruments, radiance values taken

at different viewing angles describe unique atmospheric states, thereby requiring knowledge of

the atmospheric state spatial covariance. The utilization of angular radiance values represents a

balance between the information that can be derived from the radiance at a single viewing angle

and the lack of correlation between different atmospheric states from different viewing angles.

The measurement metric through which the cooling rate profile is retrieved, $\mathbf{y}$, must be

modified to include an optimal amount of the cross-track angular scan, as determined by error

budget considerations described above. As such, $\mathbf{y}$, vectorized according to wavenumber, is

defined as:

$$\mathbf{y} = [\mathbf{y}(\mu_o) \quad \cdots \quad \mathbf{y}(\mu_n)] \,, \tag{3.4a}$$

$$\mathbf{y}(\mu_i) = \int_0^\infty (\rho(z) C_p \mathbf{T}(\mu_i, z)) \dot{\theta}(z) dz \,, \tag{3.4b}$$

where $\mathbf{T}(\mu_i, z)$ is the transmittance as a function of viewing angle and height vectorized by wavenumber, and the i subscript refers to a discrete viewing angle in a cross-track scan. The metric $\mathbf{y}$ must be defined in such a way as to maximize the information content that can be derived about the integrand. We utilize new angular weighting terms $\gamma(\mu_i)$ to relate cross-track radiances to the left-hand side of Eq. (3.3). The formal measurement error covariance matrix then becomes the sum of two terms: The first is derived from the radiometric uncertainty multiplied by the angular weighting terms, and the second term arises from an understanding of the *a priori* covariance of the cooling rate profile at the viewing angle μ_i with respect to the cooling rate profile of the footprint of interest at viewing angle μ_o.

3.4   Methodology

For radiance and transmittance calculations, we use Modtran™ 5, Version 2, Release 1 [*Berk et al.*, 1989], which is a pre-release product offering spectral resolution as high as 0.1 cm^{-1}. The results of this program are routinely verified using the Line-by-Line Radiative Transfer Model version 9.3 (LBLRTM) and RADSUM 2.4 calculations [*Clough and Iacono*, 1995; *Clough et al.*, 2005] and generally agree to within 0.05 K/day between 800 and 5 mbar.

Forward model radiances are convolved with the pre-launch AIRS Spectral Response Function (SRF) information [*Strow et al.*, 2003] to simulate AIRS channel measurements. For Noise-effective Radiance (NeR), we use values derived from in-orbit calibration algorithms as included in the Level 1B data set [*Pagano et al.*, 2003]. We have calculated the cooling rate weighting functions for the AIRS instrument and found significant lower- and middle-stratospheric

coverage from the 649 to 800 cm^{-1} region, as shown in Figure 3.2. In this figure, the normalized

cooling rate weighting functions for 453 AIRS channels with about 1 cm^{-1} FWHM per channel

cover a large portion of the CO_2 v_2 band spectral interval, and their cooling rate weighting functions

cover from the surface to 1 mbar.
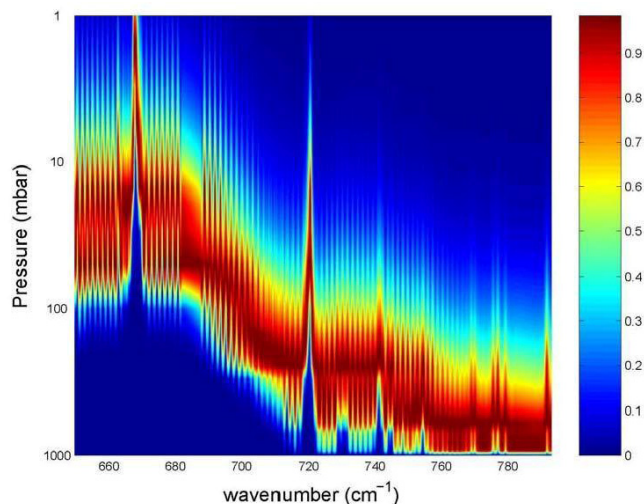
Figure 3.2: Normalized cooling rate weighting functions for mid-latitude summer (MLS) conditions for AIRS instrument from 649 to 800 cm^{-1}.

3.5   Cross Comparison

Direct validation of cooling rate profile retrievals requires data from *in situ* vertically

ascending or descending hemispheric radiometers that span the spectral region of interest and that

have the same overpass time as the remote sounder. In the absence of such a dedicated mission,

only a cross comparison between data sets is possible. We do this by analyzing other sets of

coincidental spectra and deriving atmospheric state information, and then inputting that data into the

forward model to calculate the cooling rate profile.

We utilize data from Scanning High-Resolution Interferometer Sounder (S-HIS) taken

during AVE over the Gulf of Mexico and the southeastern United States during October 2004

[*AVE*, 2005; *Revercomb*, 1998]. These data include zenith and nadir soundings at altitudes from

10–20 km aboard a NASA WB-57 aircraft coincidental with Aqua and Aura overpasses. The

instrument model for S-HIS is given by a sinc function with an FWHM of 0.96 cm^{-1}. S-HIS

measurement noise is calculated using spectra of the instrument's calibration black-body.

We have calculated the cooling rate profile in the 649 to 800 cm^{-1} region by using the

forward model with a retrieved temperature and CO_2 profile from the S-HIS zenith and nadir

spectra. The retrieved atmospheric state is calculated using a linear Bayesian update. The *a priori*

cooling rate profile is calculated from AIRS L2 standard retrieval product data with an assumed

uniform CO_2 profile of 379 ppmv. Uncertainties in the *a priori* and measured profiles were derived

empirically from L2 estimated errors in state vector components. The calculation of the uncertainty

in the retrieved cooling rate profile is described above. The error covariance matrix is calculated

according to radiometric error estimation and cross-track temperature changes in the L2 granule

data. A comparison of the measured, *a priori*, and retrieved profiles is shown in Figure 3.3a and

suggests that our methods may be utilized for a more extensive analysis of the CO_2 cooling rate

profile.
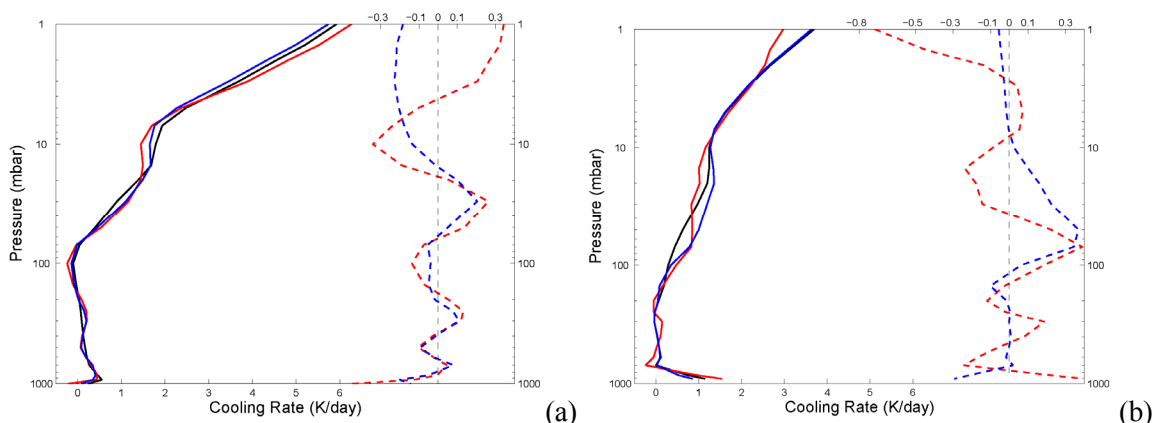
Figure 3.3: Deviation from *a priori* cooling rate profile from 649–800 cm^{-1} for AIRS retrieved and S-HIS calculated cooling rate profiles. Black solid line: *a priori* cooling rate profile (lower axis); black dashed line: zero line for difference from *a priori*; blue solid and dashed lines: cooling rate profile and deviation respectively from *a priori* calculated from S-HIS zenith and nadir measurements; red solid and dashed lines: cooling rate profile and deviation respectively from *a priori* retrieved with AIRS L1B spectra from coincidental footprint and at 45° in the cross-track scan. (a): AVE Flight: 10/31/2004, 24.8 N, 271.8 E. (b): MPACE flight: 10/10/2004, 62.7 N, 214.4 E.

Because there is greater uncertainty in stratospheric cooling processes in polar regions, we also performed a cross-comparison test using data from the MPACE mission near Fairbanks, Alaska, aboard a Proteus aircraft flying at 11 km [*Verlinde et al.*, 2007]. As shown in Figure 3.3b, the agreement between retrieved and measured cooling rate profiles is insufficient in the free troposphere, largely due to the difficulties associated with temperature retrievals at high latitudes and large discrepancies between skin temperature and emissivity values. In this case, the lack of appropriate *a priori* information seems to be quite serious.

3.6   Discussion

The concept of a direct retrieval of radiative cooling profiles in the infrared is relatively uncharted territory and this research presents several exciting opportunities for future work. We have expanded on *Liou and Xue* [1988] so that real data are used, and two cross-comparison experiments lend confidence to the methods that we utilize. Stratospheric cooling rates caused by CO_2 are assumed to be known currently to within a few tenths of a K/day, but the uncertainty has yet to be formally quantified in light of temperature uncertainties. Our retrievals are generally precise to within 0.1 K/day in the lower and middle-stratosphere. Unfortunately, the AIRS instrument does not cover the entire CO_2 ν_2 band, and scaling between partial band and total band cooling needs to be explored further.

The stratospheric temperature decrease in winter and springtime polar regions is of great scientific interest because of the interaction between radiative and dynamic effects in this region. The total stratospheric cooling rate profile meridional variation near the polar region has been explored briefly [*Hicke et al.*, 1999] using a cross comparison with *in situ* data. The results of this work indicate that changes in the cooling rate profile of the lower stratosphere in polar regions will be detectable if the retrieval can be precise to around 0.1 K/day.

A thorough analysis of stratospheric radiative cooling rates to measure the trends in radiative cooling due to changing stratospheric climate and CO_2 concentrations will require a robust input data set that resolves temperature profiles from the tropopause to the middle stratosphere. It will also require the development of computationally efficient methods for calculating the angular weighting terms $\gamma(\mu_i)$ and a thorough understanding of the effects of errors in these values on retrieved cooling rate profiles. Ultimately, an operational algorithm for the ingestion of radiance information into cooling rate calculations for GCMs is a monumental task, and we have explored some theoretical and practical aspects for employing direct retrieval methods to this end.

Chapter Four. Heating Rate Error Analysis: Clear Sky.

4.1   Abstract

This work investigates how remote sensing of the quantities required to calculate clear-sky cooling rate profiles propagates into cooling rate profile knowledge. The formulation of a cooling rate profile error budget is presented for clear-sky scenes given temperature, water vapor, and ozone profile uncertainty. Using linear propagation of error analysis, an expression for the cooling rate profile covariance matrix is given. Some of the features of the cooling rate covariance matrix are discussed, and it is found that non-zero error correlations in the temperature, water vapor, and ozone retrieval profiles must be considered to produce an unbiased estimate of cooling rate profile variance and the covariance structure. Hence, the exclusion of the details of this error correlation leads to an underestimation of the cooling rate profile uncertainty. This work then examines the assumptions made in the course of deriving the expression for the cooling rate covariance matrix by using ERA-40 Reanalysis data. It is established that the assumptions of linear error propagation and Gaussian statistics are generally tenable. Next, the information content of thermal infrared spectra with respect to clear-sky cooling rate profiles is investigated. Several formerly and currently operational spectrometers are compared with different spectral coverage, resolution, and signal-to-noise ratio. Among operational spectrometers, IASI is found to have the ability to provide the greatest amount of information on the cooling rate profile. Also, it may be scientifically useful to develop far-infrared missions in terms of cooling rate profile analysis.

4.2   Introduction

Heating and cooling rate profiles are influenced by absorption, emission, and scattering by atmospheric state constituents such as water vapor (H_2O), carbon dioxide (CO_2), ozone (O_3), oxygen (O_2), methane (CH_4), nitrous oxide (N_2O), and liquid and ice clouds. Aerosols have a strong influence on radiative heating in the visible and near infrared portions of the spectrum but only have a small impact on the infrared cooling rates where aerosol optical depth is high. Heating and cooling rate profile calculations are ubiquitous in the course of general circulation model (GCM) runs which utilize correlated-*k* (or other band-model) methods. These algorithms provide computational efficiency and achieve reasonable accuracy with respect to line-by-line calculations for the same inputs of temperature, water vapor, ozone, and cloud optical depth profiles. An in-depth discussion of heating rate profile calculation, both from a theoretical and practical standpoint, can be found in texts such *Goody and Yung* [1989] and *Liou* [2002].

Radiometric accuracy with respect to line-by-line models is crucial to many aspects of model performance because diabatic heating affects circulation. *Morcrette*, [1990] found that an improved radiative transfer algorithm resulted in substantial changes to the distribution of radiative energy in the ECMWF forecast model, while *Iacono et al*. [2000] explored how the introduction of an improved correlated-k algorithm to the CCM3 model changed the resulting cooling rates and fluxes, partially ameliorating the model's cold bias at high latitudes. In general, line-by-line codes are in good agreement with each other [*Kratz et al*., 2005], though comparisons of GCM heating rate calculations still exhibit discrepancies related to band-model parameterizations [*Ellingson and Fouquart*, 1991; *Baer et al*., 1996; *Collins et al*., 2006].

Meanwhile, large-scale retrieval efforts from satellite-borne instruments produce the inputs necessary to calculate fluxes and heating rate profiles. These products include temperature, water vapor, ozone profiles, and other trace gas descriptions, along with some

description of cloud cover (e.g., *Qu et al.* [2001]; *Susskind et al.* [2003]; *Barnet et al.* [2003]; *Li et al.* [2005]). Several authors have explored the determination of fluxes such as OLR and total surface downwelling flux (more easily measurable quantities) from remote sensing products (e.g., *Zhang et al.* [1995]; *Zhang et al.* [2004]). Nevertheless, there have been only a few papers focused on how well suited these products are for determining heating and cooling rates. *Mlynczak et al.* [1999] provided a comprehensive assessment of stratospheric radiative balance by using remote sensing data. Efforts to utilize International Satellite Cloud Climatology Program data to calculate monthly radiative fluxes and heating rates and the associated sensitivity of such calculations were explored by *Bergman and Hendon* [1998]. More recently, there has been renewed focus on assessing heating rates using data from ground validation sites [*Fueglistaler and Fu*, 2006; *McFarlane et al.*, 2007]. Also, heating rates derived from operational analysis temperature, water vapor, and ozone data, in combination with cloud profiling radar data, are currently being released as a standard product associated with the CloudSat mission [*L'Ecuyer*, 2007]. If properly implemented, the patterns of heating rates derived from remote sensing data can be compared with those calculated by models in a state space that summarizes the interlayer radiative energy exchange as it pertains to the primitive equations. In principle, if all of the inputs to the heating rate calculation are known with certainty, the radiometric accuracy of the band-model with respect to line-by-line calculations is the only appreciable source of error. However, remote sensing retrievals produce an imperfect estimation of the true quantity being retrieved, and it is important to assess how these imperfections relate to heating and cooling rate knowledge.

In order to bridge the gap between satellite-based remote-sensing measurements and the heating and cooling rates on which circulations models rely, preliminary efforts to address the correspondence between radiances and cooling rates have been made [*Liou and Xue*, 1988; *Feldman et al.*, 2006], though formal error analyses have been undertaken sparingly. Those papers discuss methods for retrieving cooling rates from radiance data, and the latter paper

utilizes several AIRS spectra [*Aumann et al*., 2003] to demonstrate feasibility. Given the existence of several different instruments for atmospheric sounding, it is reasonable to explore metrics for understanding which instruments best constrain heating/cooling rates. To this end, it is necessary to produce a formal error budget and discuss the hyperspectral instrument parameters that most effectively reduce uncertainty in heating/cooling rate knowledge. Therefore, this chapter focuses on establishing straightforward, computationally efficient methods for making appropriate estimation of the cooling rate covariance matrix so that the skill of standard retrieval products and methods can be evaluated in the context of cooling rates. While shortwave heating rates are also important to circulation models, this chapter will generally focus on tropical longwave cooling rates associated with different temperature, water vapor, and ozone profiles due to timely scientific interest (i.e., *Hartmann et al*. [2001]; *Sherwood et al*. [2001]; *Gettelman et al*. [2004]).

The concept of information content is broadly applied throughout this chapter. Formally originating with *Fisher* [1925] and elaborated substantially by *Shannon* [1948], information content is a useful concept for describing the change in knowledge as the result of a measurement of a set of quantities that may or may not be independent. The information content of a set of measurements is equivalent to the same number of measurements of independent equal probability binary events. Another interpretation of information content is that it describes the number of different states that can be distinguished by a measurement. When used properly, information content is an absolute currency for the evaluation of retrieval system design that produces a reliable metric with which optimization can occur on many fronts simultaneously.

This chapter is organized as follows. In Section 4.2, we discuss the basic molecular bands and their cooling rates using the template of the Tropical Model Atmosphere [*Anderson et al*., 1986]. Next, we move on to describe sources of uncertainty in determining cooling rate profiles and cooling rate variability in the tropics. In Section 4.3, formal error propagation analysis is applied to the study of cooling rates given expected *a priori* and *a posteriori* uncertainties in the

clear-sky inputs. This propagation of error analysis is then applied to reanalysis data to demonstrate the efficacy of this approach in determining cooling rate covariance matrices. Finally, Section 4.4 provides context for the treatment of the intersection between cooling rate profiles and remote sensing measurements by presenting a comparison of the cooling rate information content associated with several past and current spectrometers.

4.3   Sample Case and Sources of Uncertainty

This chapter utilizes radiative transfer codes from the AER suite (http://rtweb.aer.com): for line-by-line radiative transfer calculations to produce radiance, the Line-by-Line Radiative Transfer Model, LBLRTM [*Clough et al.*, 1992; 1995; 2005] version 9.3 is used; for line-by-line flux and heating-rate calculations, RADSUM version 2.4 is used; and for correlated-k calculations, the Rapid Radiative Transfer Model (RRTM) including longwave (version 3.01) and shortwave (version 2.5) modules are used [*Iacono et al.*, 2000; *Mlawer et al.*, 1997]. For heating rate profile calculations, RRTM is accurate to within 0.1 K/day in the troposphere and to within 0.3 K/day in the stratosphere relative to line-by-line calculations (see *Mlawer et al.*, [1997] for details).

A sample cooling rate profile calculated with RRTM is shown in Figure 4.1. Here, nine spectral bands are presented along with the total IR cooling rate profile given the Tropical Model Atmosphere. The three far-infrared bands covering 10–630 cm^{-1} show significant upper tropospheric cooling which arises from the rotational band of water vapor. In fact, these far-infrared bands, for which no global satellite-based direct measurements currently exist, account for upwards of 90% of cooling in the upper troposphere in the tropics. The two bands from 630-820 cm^{-1} are dominated by the ν_2 band of CO_2 which contributes significantly to stratospheric cooling rates.
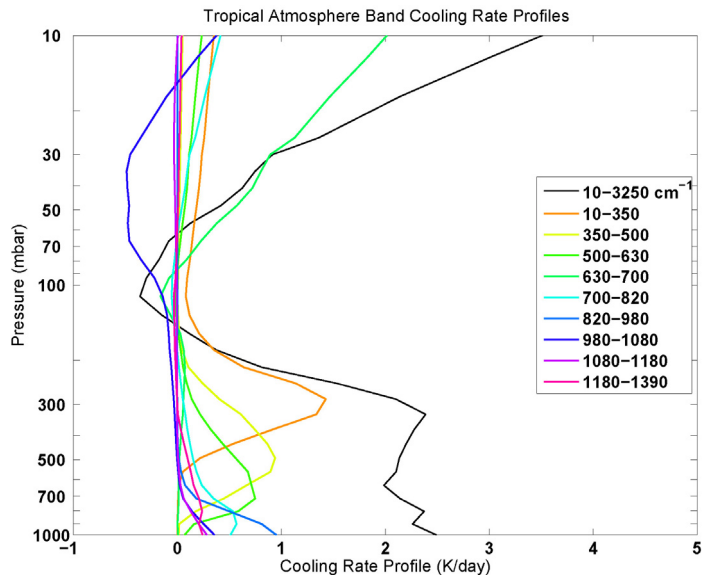
Figure 4.1: Total and band-averaged IR cooling rate profiles for the Tropical Atmosphere on a log-pressure scale.

The two spectral bands from 820–980 cm^{-1} and 1080–1180 cm^{-1} show cooling in the window bands which is strongly influenced by water vapor continuum absorption. The 985–1085 cm^{-1} spectral region is affected by the ν_3 band of O_3 and the 1070–1180 cm^{-1} region is influenced by the ν_1 band of O_3 [*Clough and Kneizys*, 1966]. Both of these bands produce IR heating in the lower stratosphere which arises from a rapid vertical change in O_3 concentration and a corresponding drop in interlayer transmittance. These bands also lead to IR cooling in the mid- and upper-stratosphere with radiation to space.

A demonstration of the zonal, meridional, and temporal variability in total IR cooling rate profiles due to the corresponding variability in the temperature, water vapor, and ozone fields gives an indication of the appropriate scale for *a priori* values and constraints for cooling rate profile analysis. For this purpose, data from the year 2000 of the European Centre for Medium Range Weather Forecasts (ECMWF) 40-year reanalysis (ERA-40) [*Uppala et al.*, 2005] have been utilized as inputs to RRTM, which happens to be essentially the same radiative transfer code that the ERA-40 program utilizes internally. The reanalysis reports temperature, water vapor, and ozone at 23 sigma levels ranging from the surface to around 1 mbar at six-hour intervals. As seen

in Figure 4.2a, the total IR cooling rate profile at low latitudes is several K/day in the troposphere, decreases to much less than 1 K/day in the tropopause region, and rises rapidly in the stratosphere to around 10 K/day near the stratopause. For higher latitudes, cooling rates are more uniform from the free troposphere to the lower stratosphere and rise rapidly in the mid- and upper-stratosphere. Figure 4.2b shows the temporal standard deviation of the cooling rate profile across a zonal band located at the equator over using re-analysis data from January 2000 with tropospheric variability ranging from several tenths of a K/day in the troposphere to around 0.1 K/day at the tropopause and to around 0.5 K/day in the middle stratosphere.
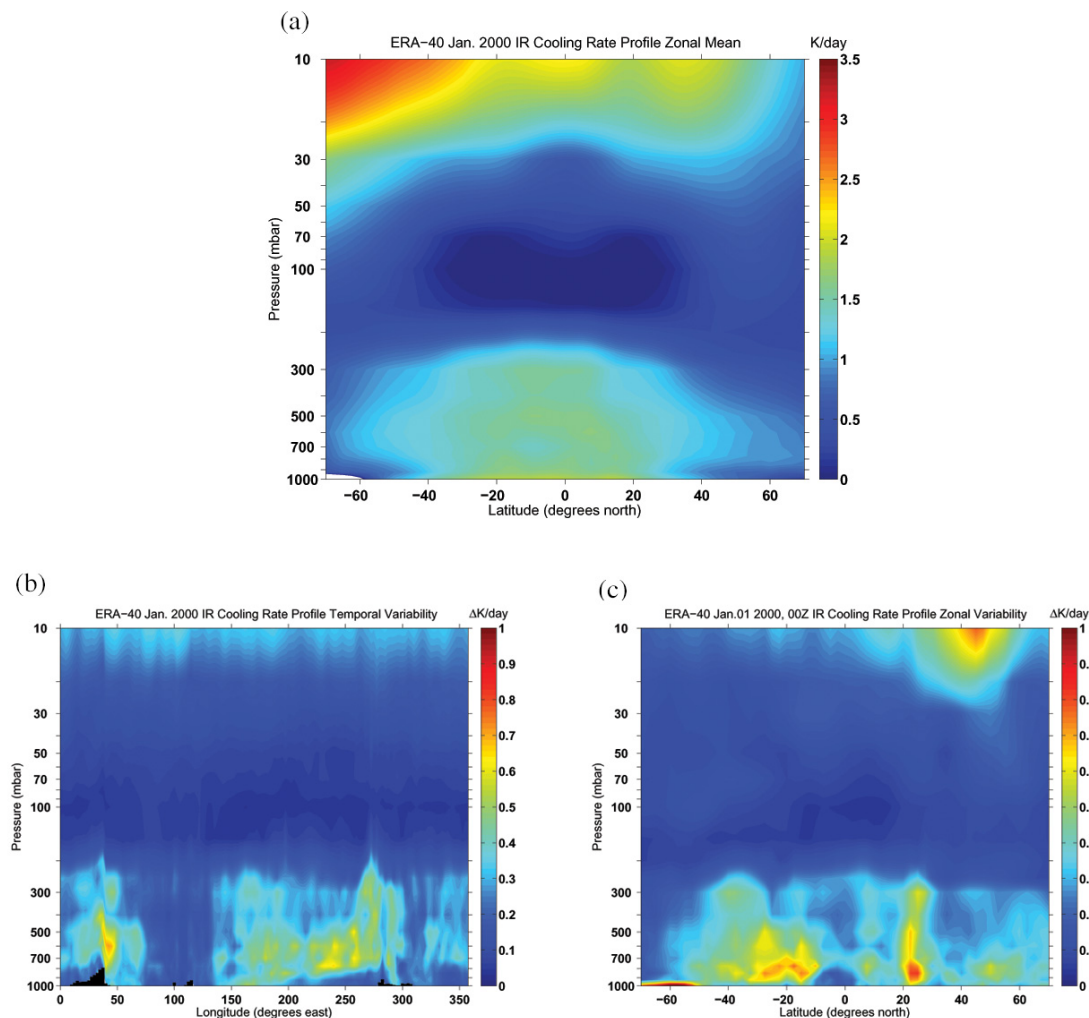
Figure 4.2: (a) Contours of clear-sky total IR cooling rate profile values from monthly-averaged ERA-40 re-analysis data for Jan. 2000. (b) Meridional cross section of temporal variability in clear-sky total IR cooling rate at the equator using 6-hour ERA-40 re-analysis data for Jan. 2000. (c) Same as (b) but displaying a zonal cross-section of temporal variability.

Figure 4.2c displays a meridional cross-section of the temporal variability in the cooling rate profile and shows comparable magnitude to Figure 4.2b.

A cooling rate profile calculation requires knowledge of the inter-layer transmission profile in the band of interest along with the temperature profile. For clear-sky calculations, uncertainty arises from the lack of knowledge of the temperature profile, from the vertical distribution of absorbing/emitting species, and from spectroscopic uncertainty which is largely limited to continua models. The water vapor continuum has been shown to be very significant for the determination of cooling rate profiles at many different altitudes [*Iacono et al.*, 2000]. However, the incorporation of a state-of-the-art, semi-empirical model [*Mlawer et al.*, 2003] into many modern cooling rate calculations largely removes this as a source of systematic error.

4.4   Error Propagation and Covariance Matrices

Operational heating and cooling rate calculation algorithms generally do not include formal error estimates as a result of the uncertainty in input parameters such as the temperature, water vapor, ozone, and cloud profiles. Finite-difference uncertainty estimation is sometimes employed for gross error statistics [*Mlynczak et al.*, 1999]. However, formal error estimates can establish how uncertainties in atmospheric state descriptors such as temperature, water vapor, ozone, and cloud profiles propagate into uncertainties both in spectral and broadband cooling rate profiles. This calculation will involve the mapping of the atmospheric state covariance matrix onto the cooling rate covariance matrix. For this mapping, we recognize that a deviation in an atmospheric state value in one layer will tend to impact the cooling rate profile at that layer *and* at neighboring layers also. Figure 4.3 shows the result of a perturbation in a single atmospheric layer of the temperature value or the water vapor or ozone concentration.
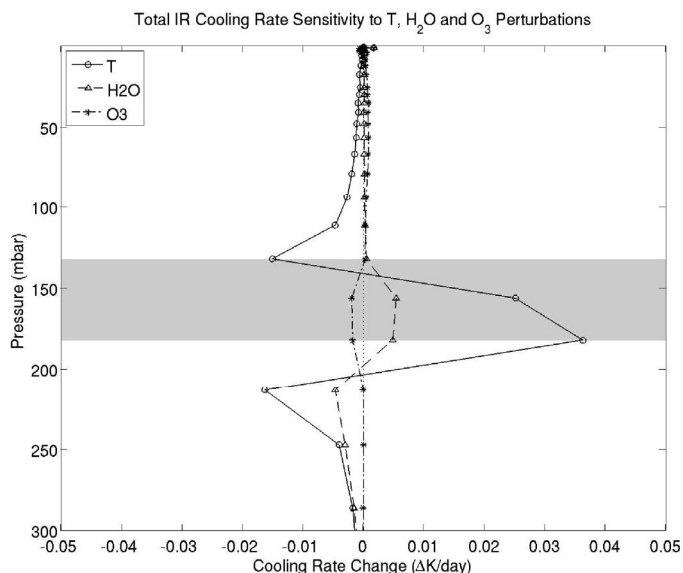
Figure 4.3: Change in Tropical Model Atmosphere total IR cooling rate profile arising from separate perturbations in the layer from 132 to 182 mbar of +1 K in temperature and +5% in H_2O and O_3 volume mixing ratio. Gray shading indicates the perturbation layer.

Here, the results of three separate perturbations to the atmospheric state for the layer from 14 to 16 km (182–132 mbar) are shown: the temperature is increased by 1 K, the water vapor value is increased by 5%, and the ozone value is increased by 5%. Note that as a result of a positive perturbation in the temperature and water vapor in a certain layer, the cooling rate in that layer increases, and the cooling rate in adjacent layers will generally decrease as a result of increased emission from the perturbation layer. Also, for increases in water vapor, the optical path of the perturbed layer increases, thereby decreasing the cooling to space of the layers below the perturbed layer. A positive perturbation in ozone in the troposphere will lead to different results: this perturbation will lead to increased IR *heating* in that layer, and it will decrease IR heating in the upper troposphere/lower stratosphere (UTLS), even if the perturbation layer is not-necessarily near the UTLS. This behavior arises because ozone IR heating in the UTLS results from the rapid increase of O_3 with height. In a spectral region that is otherwise free of significant absorptions between the surface and the UTLS, a typical O_3 profile leads to a change of inter-layer

transmittance from the O_3 ν_3 and ν_1 bands. Any positive increase in the O_3 concentration will lead to increased IR heating in the perturbation layer. However, the response of the total IR cooling rate profile to similar perturbations at other layers will lead to qualitatively and quantitatively different results depending on which bands contribute to the cooling and whether cooling-to-space dominates.

Clearly the propagation of uncertainties in conventional atmospheric state parameters such as the T, H_2O, and O_3 profiles as they pertain to the cooling rate covariance structure is non-trivial. We seek to characterize the cooling rate covariance matrix because it is a useful concept as applied to the retrieval of profile quantities from remote sensing data: it describes how errors are correlated between different entries of the profile. In order to account for the extent to which uncertainties in atmospheric state parameters at all layers impact knowledge of the cooling rate at the layer of interest, we start with linear error propagation for a function of several normally distributed random variables:

$$[\Delta f]^2 = \sum_{i=1}^{n}\sum_{j=1}^{n} \frac{\partial f}{\partial x_i} \frac{\partial f}{\partial x_j} \mathrm{cov}(x_i, x_j) \qquad (4.1)$$

where *cov* refers to the covariance function to describe the error correlations in a quantity f that is a function of several variables for which there is non-zero covariance among input variables $(x_1,...x_n)$ [*Taylor et al.*, 1994].

To calculate the diagonal of the cooling rate profile covariance matrix, we apply Eq. (4.1) to the cooling rate value in each layer:

$$[\Delta \theta'(z)]^2 = \sum_{i=1}^{n}\sum_{j=1}^{n} \frac{\partial \theta'(z)}{\partial x_i} \frac{\partial \theta'(z)}{\partial x_j} \mathrm{cov}(x_i, x_j) \qquad (4.2)$$

where $(x_1,...x_n)$ represent all of the atmospheric state inputs that are relevant to cooling rate profile calculations at each layer, and $\theta'(z)$ refers to either the spectral or broadband cooling rate

at height z. In order to calculate the off-diagonal elements of the cooling rate profile covariance matrix, we note the following relationship between the variance of a sum of two quantities:

$$\text{var}(x+y) = \text{var}(x) + \text{var}(y) + 2\,\text{cov}(x,y) \tag{4.3}$$

from which we find:

$$\text{cov}\big[\theta'(z_i), \theta'(z_j)\big] = \frac{1}{2}\Big\{\text{var}\big[\theta'(z_i) + \theta'(z_j)\big] - \text{var}\big[\theta'(z_i)\big] - \text{var}\big[\theta'(z_j)\big]\Big\} \tag{4.4}$$

where the first term on the RHS of the above equation is given by:

$$\text{var}\big[\theta'(z_i) + \theta'(z_j)\big] = \sum_{k=1}^{n}\sum_{m=1}^{n} \frac{\partial\big[\theta'(z_i) + \theta'(z_j)\big]}{\partial x_k} \frac{\partial\big[\theta'(z_i) + \theta'(z_j)\big]}{\partial x_m} \text{cov}(x_k, x_m) \tag{4.5}$$

and the other terms on the RHS of Eq. (4.4) were derived from Eq. (4.2). In this formulation, it should be noted that $\theta'(z_i)$ and $\theta'(z_j)$ can refer to cooling rates associated with different layers and different spectral regions. With Eqs. (4.2) and (4.4), we can populate a covariance matrix with respect to the cooling rate profile given the covariance matrix of the atmospheric state parameters. In order to implement Eq. (4.2) numerically, finite difference perturbations are applied to the T, H_2O, and O_3 profiles separately to produce cooling rate profile difference values (Jacobians). The implementation of the derivative terms in Eq. (4.5) simply requires summing the finite-difference values calculated for Eq. (4.2).

An application of this formal error budget analysis to cooling rate profile calculations is demonstrated with the RRTM calculation of band cooling rate profile errors for the Tropical Model Atmosphere [*Anderson et al.*, 1986]. Here, the standard deviation in the temperature profile is 3 K in each layer (spaced approximately 1 km apart), and that of the water vapor and ozone profiles is 20% of their respective values in each layer. The purpose of this exercise is to characterize cooling rate variability from T, H_2O, and O_3 variability and set reasonable *a priori* constraints on the cooling rate from an assumed climatology for subsequent analysis. The *a*

priori covariance of the temperature, water vapor, and ozone profiles is assumed to be based on a first-order autoregressive process such that adjacent layer errors are correlated [*Rodgers*, 2000]. Consequently, each element of this covariance matrix is given by:

$$\text{cov}(x_i, x_j) = \sigma(x_i)\sigma(x_j)\exp\left(-\frac{|z_i - z_j|}{H}\right) \quad\quad (4.6)$$

where x_i and x_j refer to different layer quantities, $\sigma(x_i)$ refers to the standard deviation in x_i, z_i and z_j refer to the altitude of each layer, and H is the atmospheric pressure scale height.

The true covariance matrix of H_2O and O_3 will undoubtedly be of a quantitatively different nature because such profile quantities as T and H_2O are undoubtedly correlated to some extent. For the purposes of illustrating the mapping of T, H_2O, and O_3 covariance matrices to the cooling rate covariance matrix, however, we assume in the *a priori* sense that the T-H_2O, T-O_3, and H_2O-O_3 covariances are exactly zero. From Figure 4.4a, it can be seen that this propagation of uncertainty analysis leads to some predictable and some surprising results.

From a qualitative point of view, we find that uncertainty in the distribution of water vapor contributes most substantially to the total cooling rate profile uncertainty in the troposphere as shown with the contributions from the far-infrared. In the stratosphere, uncertainty in the total IR cooling rate profile arises from uncertainty in the O_3 v_3 and v_1 bands and the CO_2 v_2 band cooling; the former term is determined by O_3 and T profile uncertainty while the latter term is determined only by T profile uncertainty. In the tropopause region, the total IR cooling rate uncertainty is largely comprised of the O_3 v_3 and v_1 bands and the CO_2 v_2 band cooling uncertainty, and water vapor uncertainty (from the rotational band and the v_3 band) is not the dominant contributor.

Another very important consideration from this analysis is to note the results shown in Figures 4.4a–d with respect to uncertainty estimation. All figures show the estimation of total IR

and also band-averaged cooling rate profile uncertainty. First, Figure 4.4a shows error estimation derived from Eq. (4.2) and (4.4), with off-diagonal covariance matrix components determined from Eq. (4.6). Figure 4.4b shows this estimation derived from formal uncertainty propagation as described above with no off-diagonal covariance matrix components (zero covariance between layers for T, H_2O, and O_3). Figure 4.4c shows the estimation of variability using 1000 Monte Carlo perturbations of the T, H_2O, and O_3 profiles assuming that the probability distribution functions (PDFs) of all variables are Gaussian. In these Monte Carlo simulations, the layer of the perturbation of the T, H_2O, and O_3 values is chosen from a uniformly distributed random number and the magnitude and sign of the perturbation are determined by a normally distributed random variable scaled by the estimated error in the perturbation layer. The correlation matrix derived from the covariance matrix is used to scale a profile of non-zero perturbations of the T, H_2O, and O_3 profiles so the simulation is authentic to the assumed covariance structure.

From Figures 4.4a and 4.4b, it can be seen that the off-diagonal components of the T, H_2O, and O_3 covariance matrices tend to increase the derived variability in the cooling rate profile which implies that, for remote sensing to be useful for cooling rate constraint, it is important to retain the details of the retrieval product error correlation structure. Also, the latter two panels show that the cooling rate error budget can be estimated through Monte Carlo simulations, though in practice fewer than 1000 simulations are required to describe the cooling rate profile uncertainties.   That is, Figure 4.4d shows the variability estimation using 40 Monte Carlo simulations which is qualitatively similar to the estimation shown in Figure 4.4c. It should be noted that the uncertainty shown in these four panels is much greater than the typical error that would be expected in the reanalysis results. Nevertheless, the purpose of these figures is to demonstrate different methods for estimating cooling rate uncertainty *given* T, H_2O, and O_3 uncertainty and the associated covariance matrix.   Also relevant to this discussion is the sensitivity of the derived cooling uncertainty to the covariance terms of the T, H_2O, and O_3 covariance matrices.
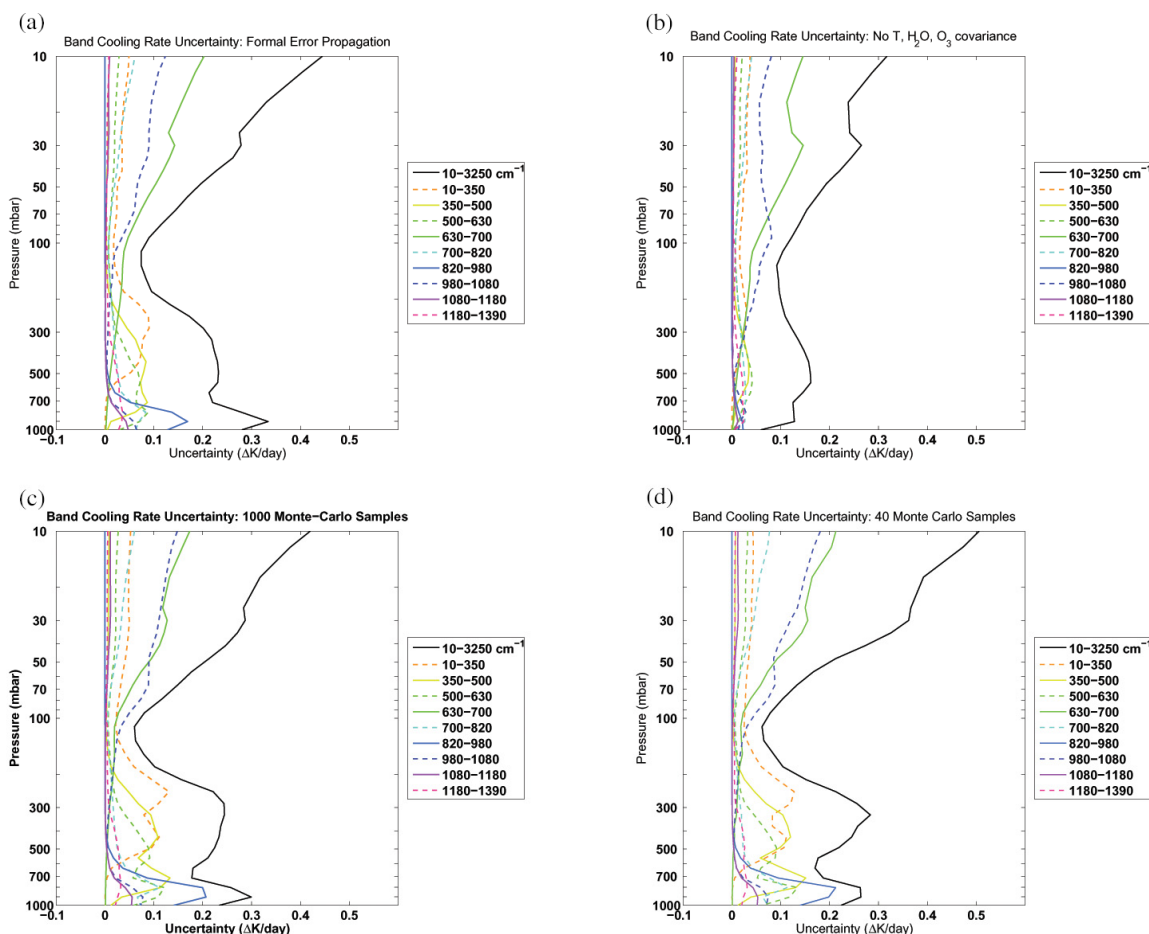
Figure 4.4: (a) Error estimation for the total and band-averaged IR cooling rate profile using formal error propagation as described in Eq. (4.2) and (4.4) with T uncertainty at 3K/km and H_2O and O_3 uncertainty at 20% vmr/km where T, H_2O, and O_3 errors co-vary according to Eq. (4.6). (b) Same as (a) but T, H_2O, and O_3 errors are uncorrelated. (c) Error bars estimated from 1000 Monte Carlo perturbations to the T, H_2O, and O_3 profiles. (d) Same as (c) but using 40 Monte Carlo perturbations.

Particularly, we examined the sensitivity of the results shown in Figure 4.4a to the parameter H in Eq. (4.6). We found, for example, that a decrease in H by a factor of two, leads to an increase in the resulting cooling rate uncertainty at all levels by approximately 10 percent.

It should also be noted that this formal error propagation analysis for quantities that are derived directly from retrieval results can be applied to many other aspects of satellite instrument data analysis, especially with respect to higher-level retrievals using Bayesian geophysical inversions which directly apply to circulation models. Specifically, this analysis is also

applicable to the understanding of cooling rate profiles under cloudy conditions with respect to the knowledge of cloud optical depth profiles.

Whereas Figures 4.4a–d show cooling rate profile standard deviations, the cooling rate covariance matrix in Figure 4.5a illustrates the propagation of temperature, water vapor, and ozone profile covariance into the covariance for the total IR cooling rate profile. The figure shows that the off-diagonal covariance matrix components generally decrease exponentially with vertical separation, and that the long-range, weak covariance between cooling rates at different layers in the troposphere arises from the assumed long-range, weak covariance in the water vapor profile. Cooling rate profile variance in the stratosphere is much greater than in the troposphere due to stratospheric temperature and ozone uncertainty. The small off-diagonal covariance matrix elements of the cooling rate profile in the stratosphere are caused by the larger altitude spacing between layers in the stratosphere which also leads to small off-diagonal covariance matrix components for stratospheric T and O_3 profiles.
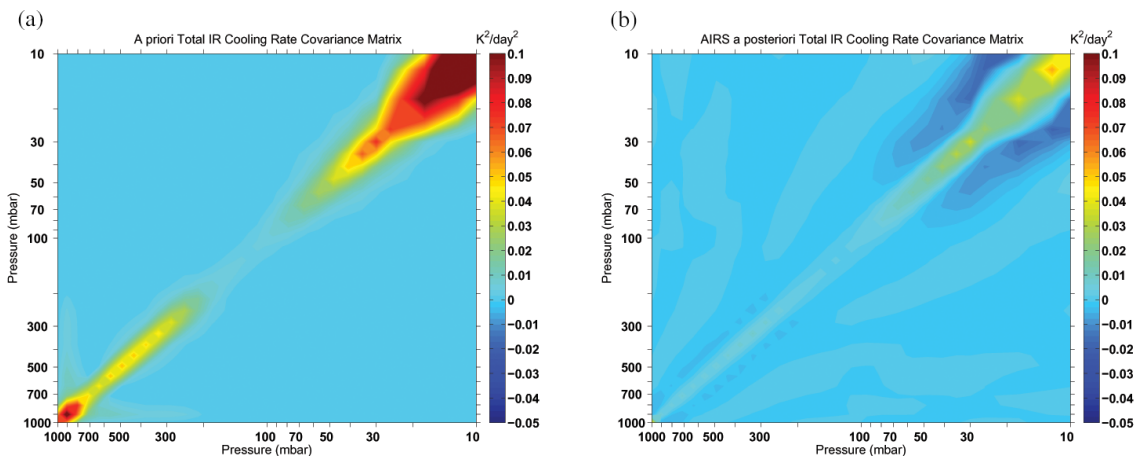
Figure 4.5: Total IR cooling rate covariance matrices with the Tropical Model Atmosphere for (a) *a priori* uncertainty of T at 3K/km, and H_2O and O_3 uncertainty at 20% vmr/km, where T, H_2O, and O_3 errors co-vary according to Eq. (4.6). (b) *A posteriori* uncertainty with a standard retrieval of T, H_2O, and O_3 profiles using the AIRS instrument model.

Figure 4.5b shows that the introduction of thermal sounder retrieval information produces an *a posteriori* covariance matrix that is qualitatively and quantitatively different from the *a*

priori covariance matrix because the sounder measurement significantly improves understanding of those quantities required for the cooling rate profile calculation. First, the variance at all layers is significantly reduced after the measurement. This is to be expected since the T, H_2O, and O_3 profiles are better constrained after the measurement. Second, the limited number of degrees of freedom of the signal with respect to the temperature, water vapor, and ozone profiles is also evidenced in the *a posteriori* cooling rate covariance. That is, the retrieval has limited vertical resolution and thus imparts a set of independent pieces of information that is generally smaller than the number of retrieval quantities. The result is that the retrieved profile quantities tend to oscillate about the true profile quantities, and the cooling rate covariance matrix associated with such T, H_2O, and O_3 profile retrievals has negative covariance values in the near-range off-diagonal components. This negative covariance tends to reduce the effective vertical resolution of cooling rates that are derived from the spectrometer retrievals. If, for example, one is interested in the vertical structure of the cooling rate in the boundary layer, the vertical width of the T, H_2O, and O_3 retrieval averaging kernels will frustrate efforts for meaningful cooling rate analysis. Depending on the way in which cooling rates are utilized, vertical resolution may or may not be necessary. The comparison of vertically integrated tropospheric cooling resulting from different water vapor distributions may allow for degraded vertical resolution which can be accomplished by passing the high-resolution covariance matrix through a vertically averaging operator. On the other hand, circulation models generally require high vertical resolution for heating/cooling rates, so analysis of cooling rates from sounder retrievals as compared to circulation model cooling rates should be undertaken at high resolution.

The formulation of the cooling rate covariance matrix herein rests on several assumptions which need to be addressed. First, because significant cooling arises from the layer at which the atmosphere transitions between optical thickness and transparency in a certain band, the nonlinear nature of the radiative transfer equation may render the linear error analysis less meaningful. The issue here is whether this error propagation is valid for small changes in the clear-sky cooling rate

inputs, and what magnitude of T, H_2O, and O_3 profile uncertainty invalidates this linearity assumption. To estimate this, we investigate the behavior of the derivative terms in Eq. (4.2) by examining the change in a finite-difference derivative approximation with increasing differential step size.
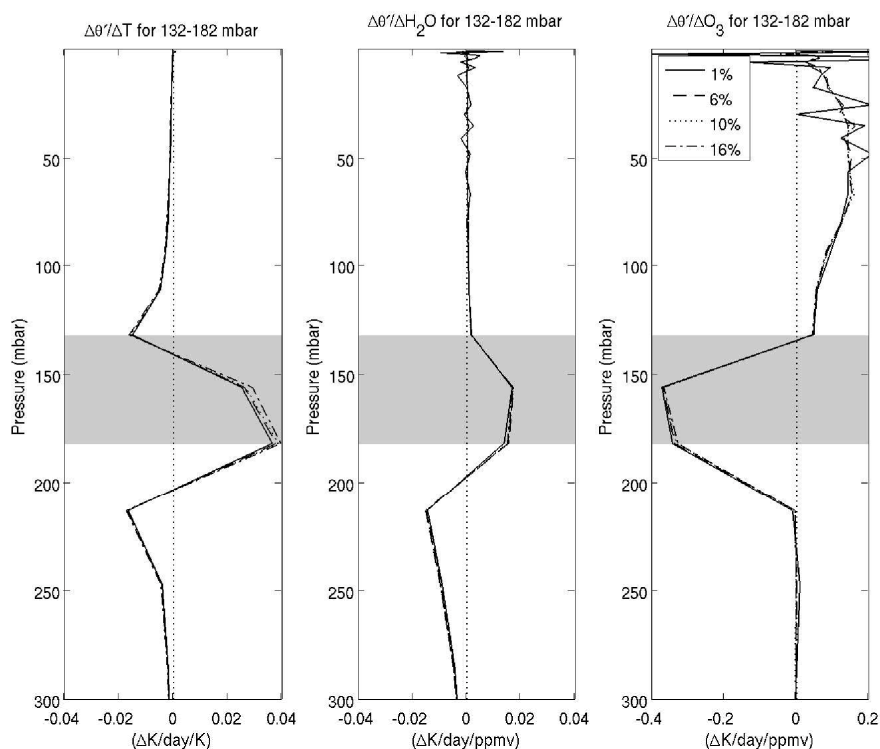
Figure 4.6: Finite-difference Jacobian of cooling rate profile change with respect to changes in T (left panel), H_2O (center panel), and O_3 (right panel) over the layer from 132–182 mbar. The linearity of the Jacobian is tested through different percentage change step sizes. These different step sizes are distinguished through the linestyles indicated by the legend in the right panel. The shaded gray indicates the layer being perturbed.

The three panels of Figure 4.6 show the change in cooling rate for different perturbations in the temperature, water vapor, and ozone at 150 mbar normalized by the perturbation step size. It can be seen from this figure that even for fairly large perturbations, the normalized response of the clear-sky cooling rate profile does not change significantly (though RRTM has difficulty resolving the effects of small perturbations on stratospheric cooling rates). Even the nonlinearity shown in the T perturbation panel only becomes evident for changes on the order of 10% which

represents a perturbation of over 20 K. Perturbations in other layers in the atmosphere are similar to the results in Figure 4.6 in that the finite-difference Jacobians are nearly independent of step-size.

The other important assumption in the derivation of a cooling rate covariance matrix is whether Gaussian statistics can be utilized. Since many of the physical quantities relevant to cooling rate profiles can be reasonably represented with Gaussian statistics, and because error propagation in these instances can be described analytically, it is convenient to make an assumption that the probability distribution functions (PDFs) of all variables associated with the calculation of the cooling rate profile are normal. This may be reasonable given the low number of parameters required to constrain a Gaussian PDF, but this assumption can also be tested. If the PDFs of the input variables are non-Gaussian, covariance matrix estimation from the approach described above may be difficult. The lack of an analytic expression (e.g., Eq. (4.1)) for meaningful error bars of functions with non-Gaussian inputs has led to diverse approaches, some of which focus on Monte Carlo distribution sampling (e.g., *Palacios and Steel* [2006]; *Posselt et al.* [2006]). Indeed, the error estimation in Figure 4.4a was qualitatively accomplished with a limited number of Monte Carlo samples as shown in Figure 4.4d.

Testing the assumptions made in the course of the cooling rate covariance matrix formulation using real data or a realistic data set is important to establishing the utility of error propagation as it applies to cooling rate profiles. The ERA-40 reanalysis data fields provide a convenient, straightforward, and realistic set to calculate sample covariance matrices of T, H_2O, and O_3 profiles and also to sample cooling rate covariance matrices. The PDFs of temperature exhibit qualitatively Gaussian behavior, though water vapor and ozone exhibit much different distributions that can be better characterized as lognormal. The resulting PDFs of cooling rates at various layers are also qualitatively Gaussian with some positive skewness. An example of the PDFs of temperature, water vapor, ozone, and cooling rate at 150 mbar is shown in Figure 4.7.
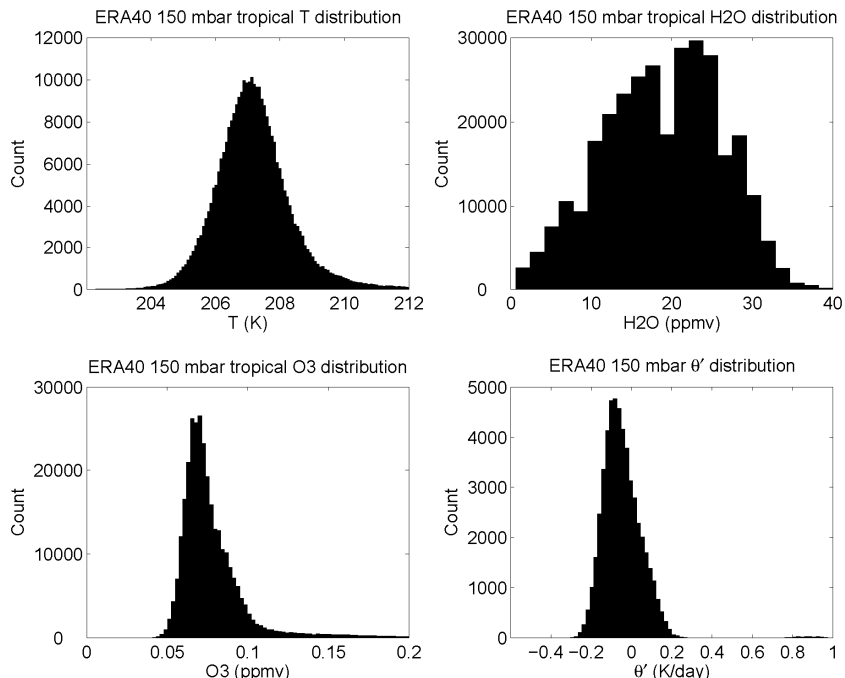
Figure 4.7: Sample probability distribution functions of the temperature (upper left panel), water vapor (upper right panel), ozone (lower left panel), and cooling rate (lower right panel) at 150 mbar from the ERA-40 data set for January 2000 for the region bounded by (20S , 20N) and (150E, 210E).

In order to estimate the cooling rate covariance matrix, it is more appropriate to utilize the covariance of the logarithm of H_2O and O_3 and the change in cooling rate profile with respect to changes in the logarithm of H_2O and O_3.
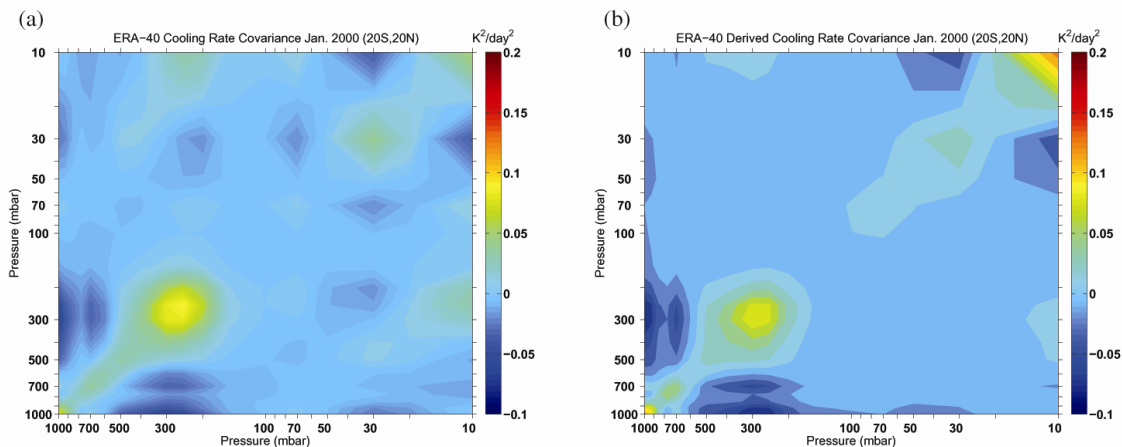
Figure 4.8: Clear-sky total IR cooling rate covariance matrix from ERA-40 reanalysis for the region bounded by (20S , 20N) and (150E, 210E) for January 2000 calculated from (a) ensemble cooling rate calculations and (b) error propagation analysis using calculated variability in T, H_2O, and O_3 fields.

In Figure 4.8a, a cooling rate profile covariance matrix is calculated from an ensemble of clear-sky cooling rate profiles from all time steps of the ERA-40 in January 2000 from 20S to 20N and 150E to 210E. Figure 4.8b shows the cooling rate covariance matrix derived with Eqs. (4.2–5) using calculated T, $\log(H_2O)$, and $\log(O_3)$ covariance matrices. That is, we are calculating the covariance matrix of T, $\log(H_2O)$, and $\log(O_3)$ from a large set of reanalysis profiles using error propagation as discussed above to produce a cooling rate covariance matrix. The results are compared to the covariance matrix derived empirically from the cooling rate profile calculations performed with the same set of T, H_2O, and O_3 profiles. The two covariance matrices describe variability and are qualitatively similar, though the latter (empirically derived) has substantially more structure. The discrepancy arises primarily due to the non-Gaussian PDFs of the input quantities. Clearly, the series of assumptions necessary to create the cooling rate covariance matrix from Eq. (4.2) and Eq. (4.4), including Gaussian statistics and the validity of the linear error estimation for slightly or moderately non-linear regimes, must be utilized with some caution.

4.5   Spectrometer Information Content Comparison

Given a proper formulation for the cooling rate profile covariance matrix as a function of the atmospheric state covariance matrix, an information content analysis can be performed to assess the relative merits of traditional retrieval techniques using data from past, current, and future observing systems. Also, information content analysis facilitates discussion of the value of the traditional treatment of cooling rates and other approaches to the analysis of spectra. In the previous section, we developed methods for calculating the error budget for the cooling rate profile both from prior knowledge and from knowledge gained by data from remote-sensing

instruments. It is sensible to use a measure such as information content to compare these two

states of knowledge.

According to *Shannon* [1948], the information content can also be described by the

entropy of the probability distribution functions associated with the *a priori* and *a posteriori*

states. Given an assumption of Gaussian statistics for the quantity of interest, the entropy, and

thus the information content can be directly related to the covariance matrix of the suite of

physical variables estimated in the retrieval (e.g., T, H_2O, O_3 profiles):

$$S(P_a) = \frac{1}{2} \ln(|\mathbf{S}_a|) \tag{4.7}$$

where P_a is the prior state and $\mathbf{S}_a$ is its associated covariance matrix. The information content

h, in bits, is given by the difference in entropy from the prior to the posterior state:

$$h = -\frac{1}{2} \ln\left(\left|\hat{\mathbf{S}} * \mathbf{S}_a^{-1}\right|\right) \tag{4.8}$$

where $\hat{\mathbf{S}}$ is the posterior covariance matrix.

We estimate the information content for the cooling rate profile derived from current

thermal sounder measurements according to instrumental spectral coverage, noise, and resolution.

The purpose of this analysis is to understand and compare how different instrument

characteristics are able to impart knowledge towards the determination of the cooling rate profile.

First, this analysis compares the cooling rate profile information, in bits, derived from standard

optimal-estimation atmospheric state retrievals [*Rodgers*, 2000] for the temperature, H_2O, and O_3

profiles. While it is recognized that most operational retrieval techniques employ more advanced

approaches to the inversion, a linear error analysis is chosen for simplicity. Additionally, the *a*

posteriori covariance matrix estimation for non-linear retrieval is similar to the linear case.

For these cases, the suite of physical quantities retrieved consists of a vector of the

concatenated profiles of the temperature and the logarithm of the H_2O, and O_3 profiles. We

assume that the *a priori* covariance matrix for the gaseous profiles is given as a modification of Eq. (4.6), noting that a Taylor expansion approximation of the variance of a function is:

$$\text{var}[f(x)] \approx (f'(x))^2 * \text{var}(x) \tag{4.9}$$

which implies that for the transformation:

$$\begin{cases} y_i = \log(x_i) \\ y_j = \log(x_j) \end{cases} \tag{4.10a}$$

where x_i and x_j refer to gaseous profile concentration at different layers, that:

$$\begin{cases} \sigma(y_i) = \dfrac{\sigma(x_i)}{x_i} \\ \sigma(y_j) = \dfrac{\sigma(x_j)}{x_j} \end{cases} \tag{4.10b}$$

which leads to the following result for the H_2O and O_3 elements of the *a priori* covariance matrix:

$$\text{cov}(y_i, y_j) = \sigma(y_i)\sigma(y_j) \exp\left(-\frac{|z_i - z_j|}{H}\right) \quad . \tag{4.11}$$

The *a priori* covariance matrix is generally block-diagonal with respect to the different gaseous species in the absence of compelling *a priori* knowledge of the covariance between different profile quantities. That is, the retrieval of physical quantities can be implemented without constraining the covariance between different species, though the covariance matrix of the suite of physical values retrieved from the measurement will not, in general, be block-diagonal. For information content analyses, the role of the *a priori* constraint is central towards determining how the measurement translates to total knowledge about the quantity of interest. Since the *a priori* was not specified rigorously here, it should be noted that for higher assumed

values of prior uncertainty in T, H_2O, O_3 and correlations in those uncertainties, the information content associated with that measurement will also increase.

The thermal infrared sounders herein compared include the IRIS-D instrument aboard the Nimbus 4 platform [*Hanel et al.*, 1971], the AIRS instrument aboard the Aqua platform [*Aumann et al.*, 2003], the TES instrument aboard the Aura platform [*Beer et al.*, 2001], the IASI instrument aboard the MetOp platform [*Chalon et al.*, 2001], and the FIRST instrument — a newly-developed instrument that has been tested from a balloon platform [*Mlynczak et al.*, 2006b]. All instruments are infrared spectrometers: AIRS, TES, and IASI measure most of the mid-infrared out to approximately 650 cm^{-1}, while IRIS-D covers a portion of the far-infrared with measurements out to 400 cm^{-1} and FIRST measures nearly the entire far-infrared out to 50 cm^{-1}. Each information content calculation requires the utilization of an instrument line shape (ILS). All but one of the instruments herein considered are Fourier Transform Spectrometers (FTS) and the ILS for the FTS instruments is specified as an upapodized sinc-function parameterized by the maximum optical path length of each scan and the integrated field of view. The specification of the ILS for the AIRS instrument, the only grating instrument included in the comparison, is defined by the post-launch characterization of channel centroids and spectral response characteristics [*Gaiser et al.*, 2003]. The approximate noise characteristics of the instruments listed in Table 4.1 show the range of the Noise-Effective Delta Temperature (NEDT) for each instrument.

A posteriori covariance of T, H_2O, and O_3 profiles is estimated according to a linear Bayesian atmospheric state retrieval approach detailed by *Rodgers* [2000] and is given by the following:

$$\hat{\mathbf{S}} = \left(\mathbf{K}^T \mathbf{S}_\varepsilon^{-1} \mathbf{K} + \mathbf{S}_a^{-1} \right)^{-1} \qquad (4.12)$$

where $\mathbf{S}_\varepsilon$ is the measurement covariance matrix, T and -1 denote the matrix transpose and

inverse respectively, and $\mathbf{K}$ is the weighting function matrix with components given by:

$$K(i,j) = \frac{\partial R_i}{\partial x_j} \qquad (4.13)$$

where R_i refers to the radiance in the ith channel, and x_j is an input to the line-by-line radiative

transfer model. The measurement covariance matrix is derived from an estimation of

measurement error, which is generally acquired through a detailed calibration procedure. For this

demonstration, static measurement error models were used which assume that the noise is limited

to a non-spectrally correlated detector signal. That is, the off-diagonal elements of the

measurement covariance matrix are set to zero. While not all spectral errors are uncorrelated, it is

reasonable to assume that in the course of the processing of raw detector data to geolocated,

calibrated radiance data that a significant part of the calibration fluctuations and other spectrally

correlated errors can be corrected. The *a posteriori* covariance matrix from Eq. (4.12) is then re-

entered into the cooling rate covariance matrix formulation calculated with Eqs. (4.2) and (4.4)

and from this, the cooling rate information content is calculated.

Table 4.1 shows the information content of several clear-sky sounders for three model

atmospheres [*Anderson et al.*, 1986] where h_{TRP} denotes information content for the Tropical

Model Atmosphere, h_{MLS} denotes information content for the Mid-Latitude Summer Model

Atmosphere, and h_{SAW} denotes information content for the Sub-Arctic Winter Model Atmosphere.

These results indicate some optimal qualities for remote sensing data for cooling rate profile

determination. First, it is expected that older instruments such as IRIS-D, with relatively low

spectral resolution and high instrument noise, will contain some information regarding the

cooling rate profile, but that newer instruments will have improved performance. Second, the

amount of information that a thermal sounder can derive about the cooling rate profile is also

proportional to the thermal contrast between the surface and the atmosphere. Therefore, cooling

rate profiles can be determined better when viewing tropical atmospheres as opposed to wintertime polar ones. Third, the balance between signal-to-noise ratio and spectral resolution tends to favor the AIRS instrument (which has a superior signal-to-noise ratio). Fourth, IASI, with comparable channel coverage and noise, yet increased spectral resolution, should provide more information regarding the cooling rate profile as compared to AIRS.

Table 4.1.

Instrument	Temporal Span	Spectral Coverage (cm^{-1})	NEDT (K)	Spectral Resolution (cm^{-1})	h_{TRP} (bits)	h_{MLS} (bits)	h_{SAW} (bits)
IRIS-D (Nimbus 4)	1970–71	400–1600	2–4	2.8	9.8	8.4	6.4
AIRS (Aqua)	2002– Present	650–1400, 1900–2700	0.1–0.6	1–2	17.1	11.5	12.6
TES (Aura)	2004– Present	650–1325, 1900–2250	1–4	0.12	13.2	10.5	8.0
IASI	2006– Present	650–2700	0.3–0.5	0.5	21.8	19.9	18.3
FIRST	Prototype	50–2000	1.1	0.6	17.5	18.3	11.4

Finally, the descriptive ability of upper tropospheric water vapor bands that the FIRST instrument exhibits strongly suggests that far-infrared measurements do not represent a completely redundant description as compared to what is derived from the 6.3 μm H_2O band. In fact, if only the mid-infrared portion of the FIRST instrument is used for the analysis listed in Table 1, h_{TRP} is 16.2 bits, h_{MLS} is 16.9 bits, and h_{SAW} is 10.3 bits. Moreover, it is expected that errors in the

spectroscopic databases in the far-infrared will contribute to mid-tropospheric cooling rate profile biases, and large-scale measurements in this spectral region should reveal discrepancies.

4.6 Discussion

In this chapter, we have addressed the formulation of a cooling rate profile error budget for clear-sky scenes. This is particularly important for cooling rate analysis from remote sensing data so that the errors associated with the retrieval of standard physical quantities are retained. We start with formal linear propagation of error analysis to derive an expression for the diagonal and off-diagonal components of the cooling rate profile covariance matrix. From this, we find that knowledge of the structure of error correlations in the T, H_2O, and O_3 profiles is important to the estimation of the cooling rate profile error budget in that higher error correlation tends to increase cooling rate uncertainty. While this knowledge may not always be available, it is necessary for the proper assessment of the cooling rate error budget.

Next, we explore the assumptions made in the course of deriving an expression for the cooling rate covariance matrix, which are borne out by using a large set of T, H_2O, and O_3 profiles from the ERA-40 reanalysis data set. Namely, we test the extent to which linear error propagation can be assumed, and Gaussian PDFs for radiative transfer model input variables can be utilized. There is qualitative agreement between the cooling rate profile covariance matrix derived from an ensemble of radiative transfer calculations and that derived from the covariance matrices of temperature, water vapor, and ozone profiles, though some *ad hoc* second-order corrections may be required.

Subsequently, we address how the formal retrieval of temperature, water vapor, and ozone profiles using thermal infrared spectra impart information towards understanding the clear-sky cooling rate profiles. Several spectrometers were compared with different spectral coverage,

resolution, and signal-to-noise ratio. Among operational spectrometers, IASI was found to have the ability to provide the greatest amount of information to the cooling rate profile; also, it was found that it may be scientifically useful to develop far-infrared missions in terms of cooling rate profile analysis. In the absence of operational far-infrared satellite-borne spectrometer, the implicit information contained in mid-infrared spectra about long-wavelength processes will have to suffice.

This chapter has not directly discussed the characterization of cooling rate errors and their correlations in GCMs and reanalysis data. However, with the uncertainties in T, H_2O, and O_3 profiles, the cooling rate error propagation described herein can be applied. Straightforward statistical tests can be employed to test the significance of discrepancies between cooling rates derived from satellite-based products and those calculated in circulation models.

One major frontier in the characterization of the cooling rate profile error budget is how uncertainties in cloud cover and overlap impact the error budget formulation in this chapter. Thermal IR spectra may be able to provide partial information regarding cloud-covered scenes, but most of that information will be imparted towards cooling rate profiles above the cloud decks. The cooling rate profiles arising from the new generation of active remote sensing instruments in the A-Train including CloudSat [*Stephens et al.*, 2002] and CALIPSO [*Winker et al.*, 2003] should be able to provide large amounts of information on the cooling rate profile. Since different cloud vertical distributions produce differential changes in H_2O rotational band cooling and in O_3 v_3 and v_1 IR heating (e.g., *Hartmann et al.* [2001]) which may affect such processes as stratosphere-troposphere exchange [*Gettelman et al.*, 2004; *Fueglistaler and Fu*, 2006], cloud water content and optical depth profiles will impart unprecedented information on heating/cooling rate profiles at high vertical resolution. The work of *L'Ecuyer* [2001] may prove to be very useful for addressing the cooling rate error budget in the presence of clouds, and the advent of the 2B-FLXHR product associated with CloudSat [*L'Ecuyer*, 2008] presents a comprehensive assessment of cloud radiative impacts throughout the atmospheric column.

Significant IR radiative heating generally occurs at cloud bases and cooling occurs at cloud tops with rates as high as 100 K/day for sharp cloud boundaries. Therefore, it is expected that error budget determination for cooling rates in all-sky scenes will require that more attention be focused on the linearity and Gaussian PDF assumptions utilized here.

Finally, methods for determining shortwave heating rate profiles have not been discussed, though they are of course necessary to the determination of the layer-by-layer radiative energetic budget. The formal error propagation discussion herein is directly relevant to clear-sky heating rate error budget analyses.

Chapter Five. Retrieval of Heating and Cooling Rates.

5.1   Abstract

The utilization of passive remote sensing data to retrieve radiative heating and cooling rates is revisited in detail and explored in terms of extracting the maximum information contained in the measurement related to the heating/cooling rate profile. This chapter first presents a formal discussion of heating and cooling rate estimation even in the presence of non-linearities. Next, it addresses methods for configuring a retrieval technique so that the algorithm better constrains heating and cooling rates. A clear-sky retrieval example is presented and the resulting heating and cooling rate profiles are discussed. This chapter then examines the extent to which hyperspectral infrared data may be useful for describing heating and cooling rates where clouds are present. It is found that data such as that provided by the AIRS instrument are strongly influenced by clouds, but the measurements provide a minimal constraint on heating and cooling rate profiles. Collocated microwave measurements from AMSR-E may offer an additional weak constraint on heating/cooling rates, though cloud vertical profiles from active sounding measurements provide much stronger heating/cooling rate profile constraints. Finally, we discuss computational cost considerations with respect to heating/cooling rate analysis.

5.2   Introduction

Many products are derived from hyperspectral infrared satellite instrument measurements that are of scientific importance. The immense number of spectra recorded by space-based instruments such as those in the Earth Observing System (EOS) A-Train [*Asrar and Dozier*, 1994] contains both clear-sky signals related to such quantities as the temperature, water vapor, ozone profiles, and partial descriptions of cloud cover. The spectra form an integral part of

standard product retrievals and have proven to be incredibly useful for assessing Earth system

processes. Additionally, these spectra contain subtle signals related to quantities that can be

derived from the retrieval products; in particular, they describe such quantities as radiative

heating and cooling rate profiles. Conventionally, spectra are analyzed over the course of the

generation of standard products which are related to heating and cooling rate profiles. In

particular, the temperature, water vapor, and ozone profiles are routinely retrieved from TOA

spectra, and these quantities are sufficient for calculating clear-sky heating and cooling rate

profiles with a broadband radiative transfer model (RTM). Additionally, these instruments

provide a limited but potentially useful description of cloud cover which is also necessary for

RTM calculations. However, the information content of the spectra with respect to the heating or

cooling rate profile from different instruments given standard atmospheric state retrieval methods

is not necessarily the maximum amount of information that can be derived regarding these

quantities of interest. From a qualitative perspective, it is apparent that certain standard retrieval

products are more important than others in terms of describing heating/cooling rate profile details.

For instance, the joint influence of surface temperature and the tropopausal ozone strongly impact

the infrared heating that occurs in the vicinity of the tropopause, yet this relationship is not

considered whatsoever in standard retrieval techniques.

Therefore, instead of retrieving standard atmospheric state quantities, several authors

(*Liou and Xue* [1988]; *Feldman et al*. [2006]) have proposed a direct retrieval technique in which

measurements are analyzed in terms of their descriptive power with respect to spectral and band

cooling rate profile knowledge. These previous efforts to retrieve cooling rate profiles directly

from radiance data are discussed in Appendix A and Chapter 3 and have relied on a series of

approximations that show numerical stability. Unfortunately, the technique proposed in

Appendix A requires the observation of a scene at several different viewing angles with a spectral

resolution of better than 5 cm^{-1} for wavelengths from 5 to 100 μm. These specifications are not

achieved by the current generation of satellite instruments, and it will be difficult to motivate such

instrument development prior to a comprehensive demonstration of the widespread scientific utility of a novel viewing geometry and spectral coverage. Therefore, other methods must be explored that formally process the information contained in the spectra regarding the IR cooling rate profile. Given the cooling rate covariance formulation and associated information content studies described in Chapter 4 [*Feldman et al.*, 2008], it is possible to address cooling rate profile information systematically. As cloud coverage on the Earth is very extensive, a discussion of cooling rates requires an examination of the impact of clouds on spectra and cooling rates. The presence of clouds erodes some of the information contained in visible and infrared spectra, especially at significant cloud optical depth. Heating and cooling rate behavior in the troposphere and lower stratosphere in the presence of clouds can be substantially different from clear-sky heating and cooling, so the assumptions which allow for estimation of clear-sky heating and cooling rates from remote sensing spectra must be re-examined.

This chapter explores several aspects of the formal utilization of remote sensing measurements to understand heating and cooling rate profiles. First, we expand upon several of the issues raised by *Feldman et al.* [2008] regarding the estimation of heating and cooling rates. This includes addressing heating and cooling rate covariance even where clouds are present and the non-linearities associated with the radiative transfer model are severe. Second, the retrieval of heating and cooling rate profiles is discussed and compared with standard retrieval techniques. Armed with these new methods for relating remote sensing measurements to heating and cooling rate profiles, we develop an example using a synthetic retrieval in clear-sky conditions and demonstrate how existing measurements may be used to describe clear-sky heating and cooling rate profiles. Finally, we discuss how it may be possible to utilize these methods in order to characterize these quantities for scenes where clouds are present.

5.3   Heating and Cooling Rate Estimation from Measurements

The heating/cooling rate profile is a strong function of some of the quantities that are retrieved from hyperspectral measurements. Consequently, the analysis of heating rates from remote sensing measurements begins with the recognition that the heating rate profile can be a product derived from standard atmospheric state retrievals. This is useful because it allows for the modification of the retrieval algorithm so that it is oriented towards heating and cooling rates rather than towards standard atmospheric state variables.

Standard retrieval algorithms utilize the difference between the synthetic measurement and the spectrum associated with the *a priori* atmospheric state in conjunction with the *a priori* state covariance matrix to produce an atmosphere that is more consistent with the synthetic measurement. One straightforward and commonly utilized approach is the maximum *a posteriori* retrieval technique that is described in detail by *Rodgers* [2000]. According to this technique, the estimate of the atmospheric state is given by:

$$d\hat{\mathbf{x}} = \left(\mathbf{K}^T\mathbf{S}_\varepsilon^{-1}\mathbf{K} + \mathbf{S}_a^{-1}\right)^{-1}\mathbf{K}^T\mathbf{S}_\varepsilon^{-1}d\mathbf{y} \tag{5.1}$$

where $d\hat{\mathbf{x}}$ is the *a posteriori* estimate of the difference between the actual atmospheric state and its *a priori* conception $\mathbf{x}_a$, $\mathbf{K}$ is the Jacobian of the measurement with respect to the atmospheric state, $\mathbf{S}_\varepsilon$ is the measurement covariance matrix, $\mathbf{S}_a$ is the *a priori* covariance matrix of atmospheric state, $d\mathbf{y}$ is the difference between the measurement, and $\mathbf{y}_a$ is the conception of the measurement produced by using the forward model with the *a priori* atmospheric state. *T* and *-1* refer to the transpose and inverse operators, respectively. The estimate of the *a posteriori* covariance matrix is given by:

$$\hat{\mathbf{S}} = \left(\mathbf{K}^T \mathbf{S}_\varepsilon^{-1} \mathbf{K} + \mathbf{S}_a^{-1} \right)^{-1} \qquad . \qquad (5.2)$$

The maximum *a posteriori* form for a product derived from a retrieval wherein the state and measurement variables exhibit Gaussian statistics is given by:

$$\hat{\mathbf{\theta}}' = \int \mathbf{\theta}'(\mathbf{x}) P(\mathbf{x}|\mathbf{y}) d\mathbf{x} \qquad (5.3)$$

where $\hat{\mathbf{\theta}}'$ is the estimate of the heating/cooling rate profile, $\mathbf{\theta}'(\mathbf{x})$ is the heating/cooling rate produced by the broadband radiative transfer model (RTM) for the atmospheric state $\mathbf{x}$, and $P(\mathbf{x}|\mathbf{y})$ is the posterior probability distribution function of $\mathbf{x}$ given the measurement $\mathbf{y}$. This clarifies the proper approach for estimating the heating/cooling rate profile given a set of measurements describing the atmospheric state parameters that are relevant to heating/cooling rate profile calculation. If the heating/cooling rate profile is a linear function of $\mathbf{x}$ throughout the state space in which $\mathbf{x}$ is presumed to occur, the expected value of $\mathbf{\theta}'$ is given by the heating/cooling rate calculated from the maximum *a posteriori* estimate of $\mathbf{x}$. That is, the following expression provides an estimate of the heating rate given an estimate of the underlying atmospheric state parameters:

$$\hat{\mathbf{\theta}}'_{linear} = \mathbf{\theta}'(\hat{\mathbf{x}}) \qquad (5.4)$$

where $\hat{\mathbf{\theta}}'_{linear}$ is the estimate of the heating/cooling rate profile assuming linearity and $\mathbf{\theta}'(\hat{\mathbf{x}})$ is the heating/cooling rate profile calculated from the maximum *a posteriori* retrieval of $\mathbf{x}$. Furthermore, the covariance associated the estimate of $\mathbf{\theta}'$ using the assumption that heating/cooling rate calculations are strictly linear in this case is given by

$$\hat{\mathbf{S}}(\mathbf{\theta}') = \mathbf{J}_{\mathbf{\theta}'}^T \hat{\mathbf{S}}(\mathbf{x}) \mathbf{J}_{\mathbf{\theta}'} \qquad (5.5)$$

where $\hat{\mathbf{S}}(\boldsymbol{\theta}')$ is the covariance of the heating/cooling rate profile, $\hat{\mathbf{S}}(\mathbf{x})$ is the *a posteriori*

covariance of $\mathbf{x}$, and $\mathbf{J}_{\boldsymbol{\theta}'}$ is the Jacobian of $\boldsymbol{\theta}'$ with respect to $\mathbf{x}$. This Jacobian is given by the

following expression:

$$\mathbf{J}_{\boldsymbol{\theta}'} = \frac{\partial\, \boldsymbol{\theta}'}{\partial\, \mathbf{x}} \qquad\qquad . \qquad (5.6)$$

Additionally, the cooling rate averaging kernel matrix, which describes the ability of a retrieval to

resolve the vertical structure of heating and cooling rate profiles, is given by the following

expression:

$$\mathbf{A}_{\boldsymbol{\theta}'} = \mathbf{J}_{\boldsymbol{\theta}'}\mathbf{A}_{\mathbf{x}}\mathbf{J}_{\boldsymbol{\theta}'}^{T} \qquad\qquad . \qquad (5.7)$$

where $\mathbf{A}_{\mathbf{x}}$ is given by the expression in Eq. (2.28).

Under certain circumstances, the approach taken in Eq. (5.4) may be reasonable,

especially for clear-sky cases where a large number of measurements, $\mathbf{y}$, constrain $\mathbf{x}$ sufficiently

such that the moderate nonlinearity associated with the heating/cooling rate calculations is small

compared to the prior estimation of the uncertainty in the heating/cooling rate profile.

However, for cases where the measurement $\mathbf{y}$ has limited descriptive power over $\mathbf{x}$,

(e.g., cloudy scenes), the estimation of the heating/cooling rate profile requires the application of

Eq. (5.3). In these cases, optimal estimation theory can be used to analyze the remote sensing

spectra in terms of atmospheric state parameters but may result in large *a posteriori* uncertainty in

these parameters. TOA hyperspectral measurements are generally not sensitive to cloud vertical

structure, even though this structure is central to the determination of the heating/cooling rate

profiles of the scene being sensed.

The practical implementation of Eq. (5.3) to estimate heating and cooling rates is non-

trivial because integration over the space spanned by $\mathbf{x}$ may potentially involve a very large

number of calls to the broadband radiative transfer model. Several different techniques are

available for sampling a space with many dimensions, including the Markov chain Monte Carlo (MCMC) sampling technique (e.g., [*Berg*, 2004]) and the Gibbs sampler [*Geman and Geman*, 1984], which is a special case of the MCMC approach. These techniques are able to sample the state space efficiently and allow for the evaluation of the integral in Eq. (5.2).

Unlike numerical integration based on Monte Carlo methods, numerical integration based on the Gibbs sampler generally avoids calculations where $P(\mathbf{x}|\mathbf{y})$ is very low and thus is more numerically efficient. Briefly, the Gibbs Sampler works as follows: It starts with a description of the probability of the underlying atmospheric state given the measurement that results from the assumption that the measurement and atmospheric state statistics can be described as Gaussian:

$$P(\mathbf{x}|\mathbf{y}) = \frac{1}{(2\pi)^{n/2}|\hat{\mathbf{S}}|^{1/2}} \exp\left(-\frac{1}{2}\left[(\mathbf{x}-\hat{\mathbf{x}})^T \hat{\mathbf{S}}^{-1}(\mathbf{x}-\hat{\mathbf{x}})\right]\right) \tag{5.8}$$

where T and -1 denote the matrix transpose and inverse operators respectively, $\hat{\mathbf{x}}$ is the retrieved atmospheric state, and $\hat{\mathbf{S}}$ is the estimate of the *a posteriori* covariance matrix. Next, the atmospheric state is initialized to the *a posteriori* state and a random integer j is chosen between 0 and L, where L is the length of $\mathbf{x}$. Element j of $\mathbf{x}$ is sampled and updated from a conditional distribution given fixed values for the other elements. To achieve this, a matrix of conditional coefficients must first be defined:

$$\mathbf{C} = \mathbf{I} - \left[diag\left(\hat{\mathbf{S}}^{-1}\right)\right]^{-1}\hat{\mathbf{S}}^{-1} \tag{5.9a}$$

where $\mathbf{I}$ is the identity matrix, and *diag* refers to an operator that sets all of the off-diagonal elements of a matrix to zero. The conditional coefficients are utilized in the following expression for a conditional distribution based on a multivariate normal:

$$\left(x_i|x_j \forall j \neq i\right) \sim N\left(\bar{x}_i + \sum_{j \neq i} C_{ij}\left(x_j - \bar{x}_j\right), \left[\left(\hat{\mathbf{S}}^{-1}\right)_{ii}\right]^{-1}\right) \tag{5.9b}$$

where C_{ij} represents the elements of the matrix in Eq. (5.9a) and N denotes a normal distribution (see *Gelman et al.* [2004] and Appendix A for a derivation). Another random integer is then chosen from **x** and the process is repeated several times. A cartoon of the process is shown below, where the Gibbs Sampler navigates two dimensions in order to sample two correlated quantities efficiently. After each set of sampling, the atmospheric state is entered into a broadband radiative transfer model in order to calculate heating and cooling rate profiles. To produce a diverse sampling of the atmospheric state, the Gibbs Sampler algorithm individually samples the conditional distribution for each element of **x** given fixed quantities for the other elements after which time a call is made to the radiative transfer algorithm. This sampling process then produces a set of calculated heating and cooling rate profiles which can be analyzed in terms of mean values, covariance matrices, or other statistics. In this way, the statistics associated with heating and cooling rate profiles can be estimated quickly even with uncertain cloud conditions that may lead to strongly non-linear dependencies between atmospheric state components and the heating/cooling rate calculation.

Nevertheless, even with the ability to estimate the heating or cooling rate profile from the retrieved atmospheric state and its associated covariance matrix, the imposition of additional constraints in the retrieval technique should be considered. The utilization of standard atmospheric state retrieval methods for the calculation of heating and cooling rate profile results may present errors as a result of not considering how various distributions of temperature, water vapor, and ozone lead to large fluctuations in the heating and cooling rate profiles.

There are several methods for imposing this constraint, but one of the most straightforward is to formulate a maximum *a posteriori* retrieval in a reduced state space that retains the relationship between the atmospheric state and heating/cooling rates (see *Rodgers* [2000], Section 10.3 for a detailed derivation). Accordingly,

$$d\,\boldsymbol{\theta}' = \mathbf{J}_{\boldsymbol{\theta}'}d\,\mathbf{x} \qquad (5.10).$$

The heating/cooling rate Jacobian matrix $\mathbf{J}_{\boldsymbol{\theta}'}$ can have a pseudo-inverse that assumes a large

number of possible forms. If we take the form of this pseudo-inverse $\mathbf{J}_{\boldsymbol{\theta}'}^{*}$, which minimizes

$d\,\mathbf{x}^{T}\mathbf{S}_{a}^{-1}d\,\mathbf{x}$ subject to $d\,\mathbf{x} = \mathbf{J}_{\boldsymbol{\theta}'}^{*}d\,\boldsymbol{\theta}'$, the result is:

$$\mathbf{J}_{\boldsymbol{\theta}'}^{*} = \mathbf{S}_{a}\mathbf{J}_{\boldsymbol{\theta}'}^{T}\left(\mathbf{J}_{\boldsymbol{\theta}'}\mathbf{S}_{a}\mathbf{J}_{\boldsymbol{\theta}'}^{T}\right)^{-1} \qquad . \qquad (5.11)$$

The quantity described in Eq. (5.11) should estimate the sensitivity of the atmospheric state

retrieval to the underlying heating/cooling rate profile and is non-trivial because the mapping

from heating/cooling rates to atmospheric state quantities is not unique. Once a proper

description of $\mathbf{J}_{\boldsymbol{\theta}'}^{*}$ is established, the retrieval can be formulated in heating/cooling rate space as

follows:

$$d\,\hat{\boldsymbol{\theta}}' = \left[\left(\mathbf{J}_{\boldsymbol{\theta}'}\mathbf{S}_{a}\mathbf{J}_{\boldsymbol{\theta}'}^{T}\right)^{-1} + \mathbf{J}_{\boldsymbol{\theta}'}^{*}{}^{T}\mathbf{K}^{T}\mathbf{S}_{\varepsilon}^{-1}\mathbf{K}\mathbf{J}_{\boldsymbol{\theta}'}^{*}\right]^{-1}\mathbf{J}_{\boldsymbol{\theta}'}^{*}{}^{T}\mathbf{K}^{T}\mathbf{S}_{\varepsilon}^{-1}d\,\mathbf{y} = \mathbf{G}_{\mathrm{MAP}}\,d\,\mathbf{y} \qquad . \qquad (5.12)$$

where $\mathbf{G}_{\mathrm{MAP}}$ is the heating/cooling rate gain matrix. Also, the retrieval can be represented in full

state space as follows:

$$d\,\hat{\mathbf{x}} = \mathbf{J}_{\boldsymbol{\theta}'}^{*}\left[\left(\mathbf{J}_{\boldsymbol{\theta}'}\mathbf{S}_{a}\mathbf{J}_{\boldsymbol{\theta}'}^{T}\right)^{-1} + \mathbf{J}_{\boldsymbol{\theta}'}^{*}{}^{T}\mathbf{K}^{T}\mathbf{S}_{\varepsilon}^{-1}\mathbf{K}\mathbf{J}_{\boldsymbol{\theta}'}^{*}\right]^{-1}\mathbf{J}_{\boldsymbol{\theta}'}^{*}{}^{T}\mathbf{K}^{T}\mathbf{S}_{\varepsilon}^{-1}d\,\mathbf{y} \qquad . \qquad (5.13)$$

This retrieval approach produces results that are better constrained than a standard retrieval that

does not consider how results will impact heating/cooling rate profiles. The retrieval covariance

matrix for this approach is given by the following:

$$\hat{\mathbf{S}}_{\boldsymbol{\theta}'} = \mathbf{J}_{\boldsymbol{\theta}'}\left[\left(\mathbf{J}_{\boldsymbol{\theta}'}^{*}\mathbf{G}_{\mathrm{MAP}}\mathbf{K} - \mathbf{I}\right)\mathbf{S}_{a}\left(\mathbf{J}_{\boldsymbol{\theta}'}^{*}\mathbf{G}_{\mathrm{MAP}}\mathbf{K} - \mathbf{I}\right)^{T} + \mathbf{J}_{\boldsymbol{\theta}'}^{*}\mathbf{G}_{\mathrm{MAP}}\mathbf{S}_{\varepsilon}\mathbf{G}_{\mathrm{MAP}}^{T}\mathbf{J}_{\boldsymbol{\theta}'}^{*}{}^{T}\right]\mathbf{J}_{\boldsymbol{\theta}'}^{T} \qquad (5.14)$$

Eqs. (5.12–5.14) are suitable for use within standard retrieval algorithms and produce retrieval

quantities that consider how the vertical distribution of atmospheric constituents affects heating

and cooling rate profiles. Still, the techniques described in this section require demonstration and can be understood in greater detail through the development of several example cases.

5.4   Treatment of Clear Spectra

In this and the subsequent section, we elaborate upon examples utilizing methods described above. In support of these efforts, we utilize several radiative transfer models developed by AER, Inc. [*Clough et al.*, 2005]. Line-by-line radiative transfer is calculated using the Line-by-Line Radiative Transfer Model (LBLRTM), version 11.1; fast broadband calculations are achieved with the Rapid Radiative Transfer Model (RRTM), longwave version 3.01 and shortwave version 2.5; line-by-line scattering calculations are performed with the Code for Highly-Accelerated Radiative Transfer with Scattering (CHARTS), version 2.0 [*Moncet et al.*, 1997].

The following example illustrates the benefits and shortcomings of using traditional retrieval approaches with infrared spectra to understand heating and cooling rate profiles. Starting with a clear-sky US Standard Atmosphere [*Anderson et al.*, 1986], we perform a synthetic retrieval of the surface temperature and the temperature, water vapor, and ozone profiles that indicates the extent to which the residual spectra can be processed properly to produce reasonable results. Accordingly, we start with the surface temperature and the temperature, water vapor, and ozone profiles from the model atmosphere, which we assign as the *a priori* atmospheric state. These values form the inputs to the line-by-line radiative transfer model which produces the spectrum associated with the *a priori.* We assume that the *a priori* standard deviation of each temperature value of the atmospheric state is 3 K and the *a priori* standard deviation of each water vapor and ozone value of the atmospheric state is 20% of its *a priori* value. The *a priori* covariance matrix of the temperature profile is assumed to be described by a first-order Markov process such that:

$$S_{ij} = \sigma_i \sigma_j \exp\left(-\frac{|z_i - z_j|}{H} \right) \qquad (5.15)$$

where S_{ij} is the covariance between elements i and j, σ_i is the standard deviation associated with element i, z_i is the altitude associated with element i, and H is the atmospheric scale height. The *a priori* covariance matrix is also assumed to be block-diagonal such that the temperature values with water vapor and ozone values are uncorrelated. The true underlying state is created by modifying the atmospheric state with perturbations that are consistent with the *a priori* covariance matrix. The synthetic measurement is created by calculating the spectrum associated with the true underlying state and adding noise consistent with the instrument being used. Finally, we attempt to retrieve the true underlying state given the *a priori* statistics, weighting functions, and the difference between the synthetic measurement and the radiative transfer model results arising from the *a priori* state.

With this approach, we can test how accurate the results of this synthetic test are in terms of surface temperature and the profiles of temperature, water vapor, and ozone as well as cooling rates. The following figure shows the outcome of a synthetic retrieval using the AIRS instrument [*Aumann et al.*, 2003] model as displayed in atmospheric state space. Note that the retrieval using the AIRS instrument has very limited sensitivity to water vapor above 15 km, and the resulting water vapor values above this level are determined almost exclusively by the *a priori* values. Also, the retrieval has limited sensitivity to tropospheric ozone.

One criterion for a successful retrieval is the ability to derive an atmospheric state that, through the forward model, produces a spectrum that agrees well with the measurement. The following figure shows the results of this synthetic retrieval experiment in measurement space. Clearly, the retrieval is able to incorporate the information contained in the spectra in order to update the atmospheric state so that it is more consistent with the observed spectra.
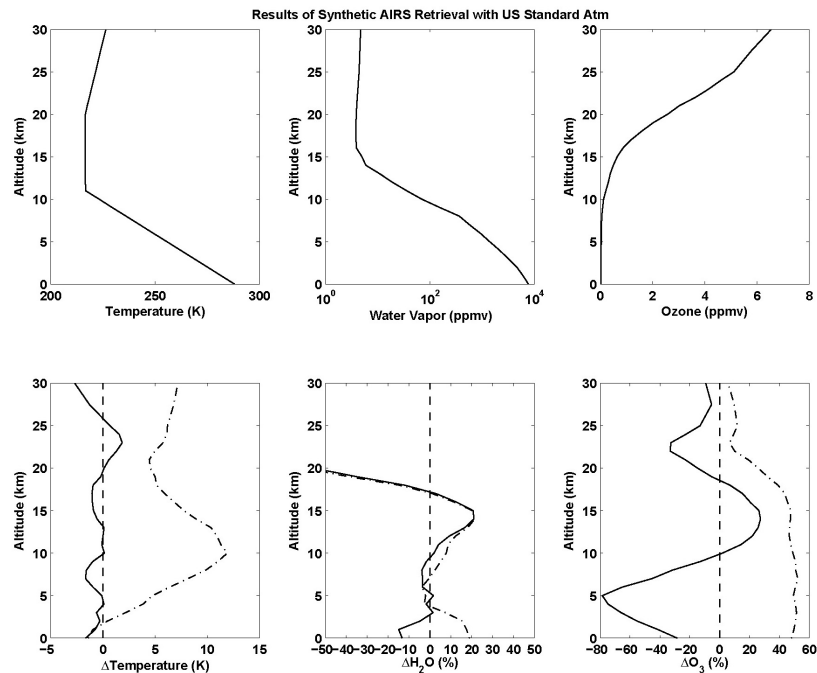
Figure 5.1: The top-left panel indicates the temperature profile of the US Standard Atmosphere. The top-middle panel shows the water vapor profile. The top-right panel displays the ozone profile. The bottom-left panel indicates the difference between *a priori* and retrieved temperature profiles relative to the true profile. The bottom-middle panel shows the profile differences for water vapor and the bottom-left panel exhibits the differences for ozone.
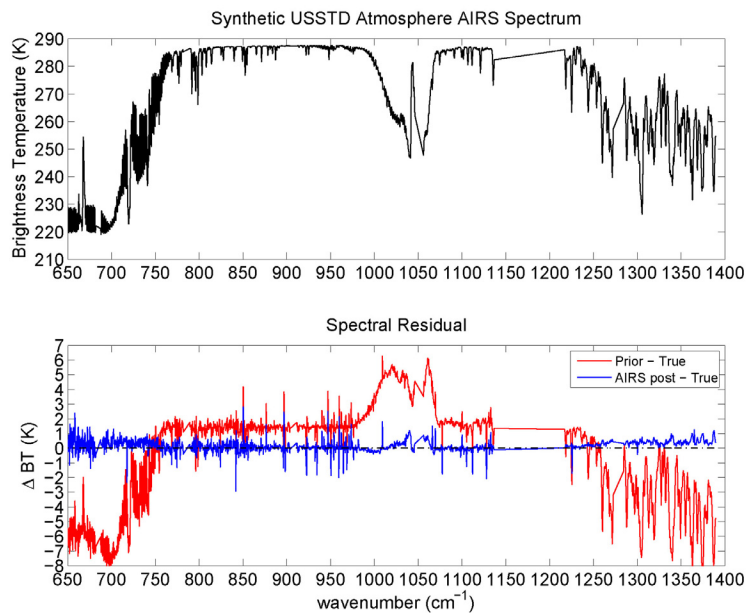
Figure 5.2: The top panel shows the AIRS spectrum calculated by LBLRTM [*Clough et al.*, 2005] for a US Standard Atmosphere [*Anderson et al.*, 1986]. The bottom panel shows a typical prior spectral residual (red) and the spectral residual associated with the retrieval (blue).

Nevertheless, while the result of the retrieval is a much-improved spectral residual, the resulting

profiles of temperature, water vapor, and ozone oscillate about the true underlying state, which

has implications for heating and, particularly, cooling rate calculations.
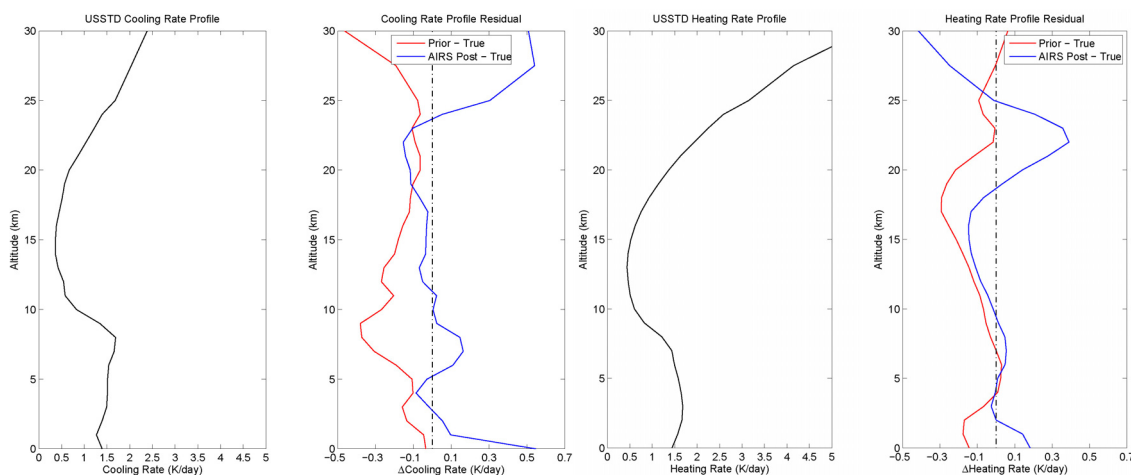
Figure 5.3: The leftmost panel shows the total infrared (10–3250 cm^{-1}) clear-sky cooling rate profile associated with the US Standard Atmosphere. The panel second to left shows the difference in cooling rate profiles associated with the synthetic retrieval. The panel second to right shows the clear-sky shortwave heating rate profile for a solar zenith angle of 30° from nadir. The right-most panel shows the difference in heating rate profiles associated with the synthetic retrieval.

The two panels of Figure 5.3 show that while a standard retrieval approach is able to produce

accurate temperature, water vapor, and ozone profiles which lead to calculated spectra that are

consistent with observations, the retrieval results do not necessarily yield an appreciably

improved cooling rate profile. The primary reason for this is that the oscillations in the profile

quantities are reasonable from the perspective of retrieving temperature, water vapor, and ozone

profiles, but they lead to more significant deviations in heating and cooling rate profiles.
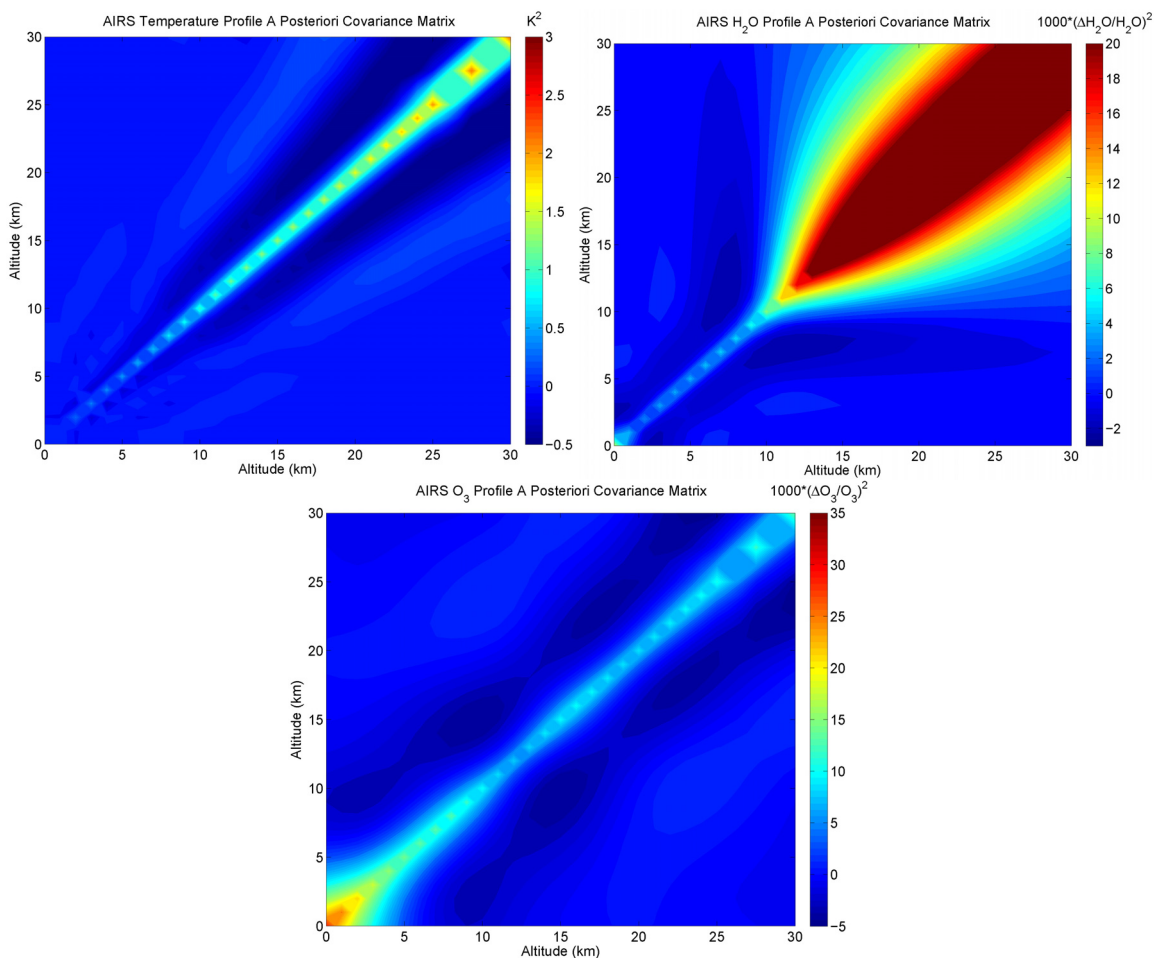
Figure 5.4: The upper-left panel indicates the temperature profile *a posteriori* covariance matrix with the example given in Section 5.2. The upper-right panel indicates the water vapor profile *a posteriori* covariance matrix, and the lower panel indicates the ozone profile *a posteriori* covariance matrix.

The *a posteriori* covariance matrices of the temperature, water vapor, and ozone profiles from this retrieval are shown in Figure 5.4 and indicate non-negligible off-diagonal components which lead to the cooling rate profile oscillations. According to *Feldman et al*. [2008], the covariance matrix of the cooling rate profile can be determined by calculating the Jacobian of the cooling rate profile with respect to the surface temperature and the temperature, water vapor, and the ozone profile.
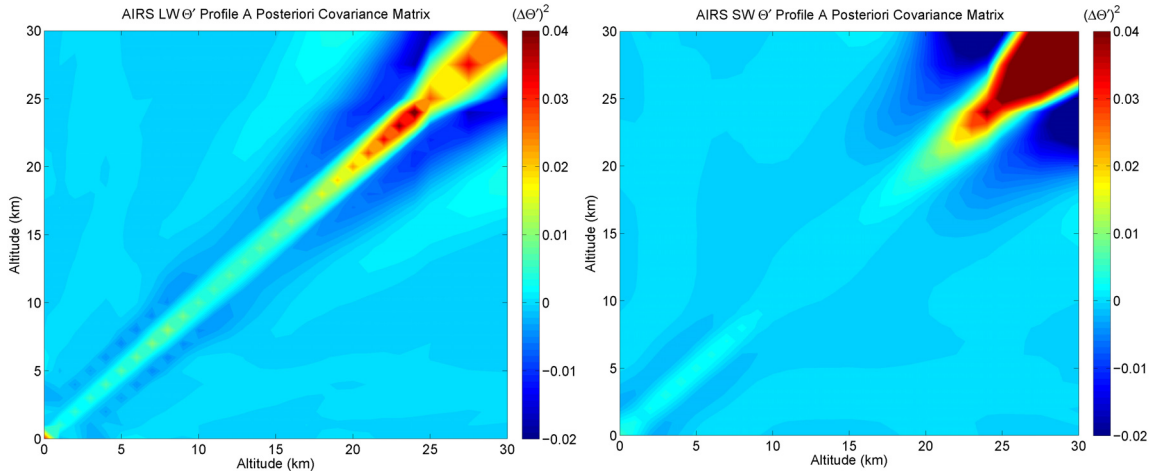
Figure 5.5: The left panel indicates the *a posteriori* cooling rate profile covariance matrix and the right panel indicates the heating rate profile covariance matrix, both calculated according to the description in *Feldman et al.* [2008].

The retrieval approach described in Eqs. (5.10–5.11) of Section 5.2 leads to heating and cooling profiles that differ from the standard retrieval approach shown in Figure 5.3. Figure 5.6 shows the differences between the standard retrieval approach and that retrieval configured with respect to the cooling rate profile. The retrieval that was reformulated to consider cooling rate profiles performs significantly better than the standard retrieval near the surface because it constrains the contrast between the surface temperature and the temperature at the lowest level which is much higher for the standard retrieval. Still, the reformulated retrieval does not perform as well as the standard retrieval near 10 kilometers and this largely arises from the ill-conditioning associated with the creation of the $\mathbf{J}_{\theta'}^{*}$ matrix. Nevertheless, the spectral residual associated with the retrieval as described in Eqs. (5.10–5.11) is qualitatively similar to that from the standard retrieval case.
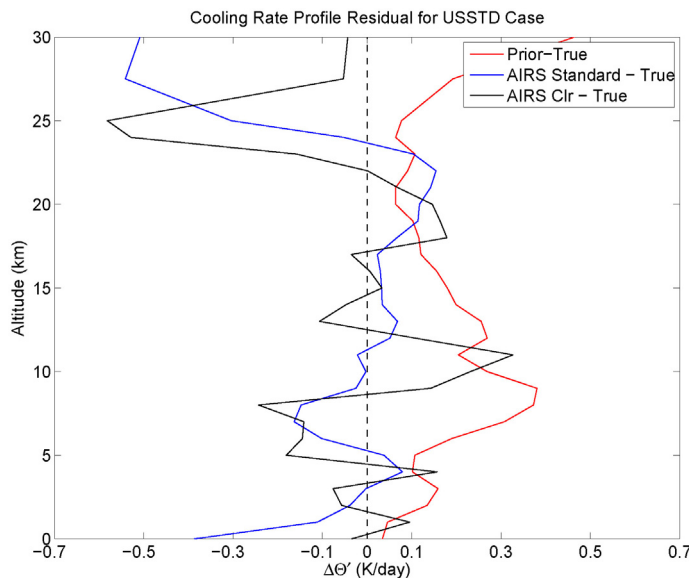
Figure 5.6: Comparison of cooling rate profiles derived for the clear-sky USSTD Atmosphere synthetic retrieval. The red line shows the difference between the total IR cooling rate profile associated with the *a priori* surface temperature, and temperature, water vapor, and ozone profiles. The blue line shows the cooling rate profile resulting from a maximum *a posteriori* estimate of the atmospheric state, while the black line shows the cooling rate profile associated with the cooling rate retrieval.
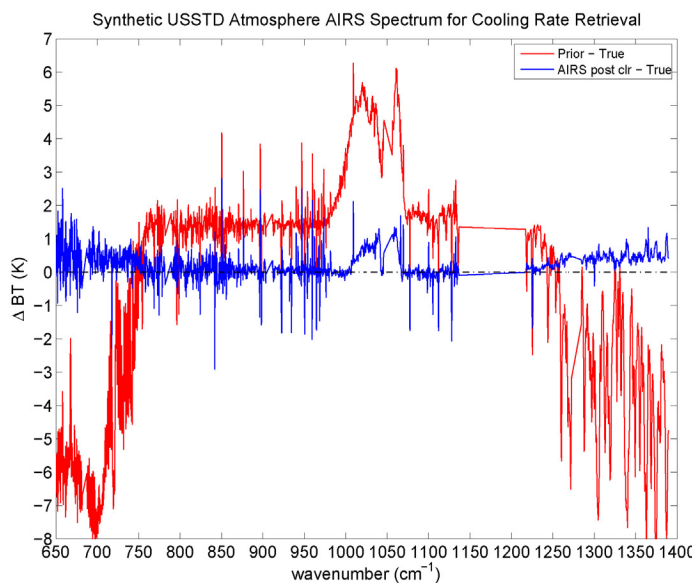
Figure 5.7: The residual spectrum associated with *a priori* state for the synthetic retrieval with the US Standard Atmosphere in red. The blue line indicates the residual associated with the retrieval using the cooling rate retrieval formulation.

Moreover, the estimation of the cooling rate uncertainty for the retrieval that is reformulated to consider cooling rates is qualitatively different from the covariance matrix arising from the standard retrieval formulation.
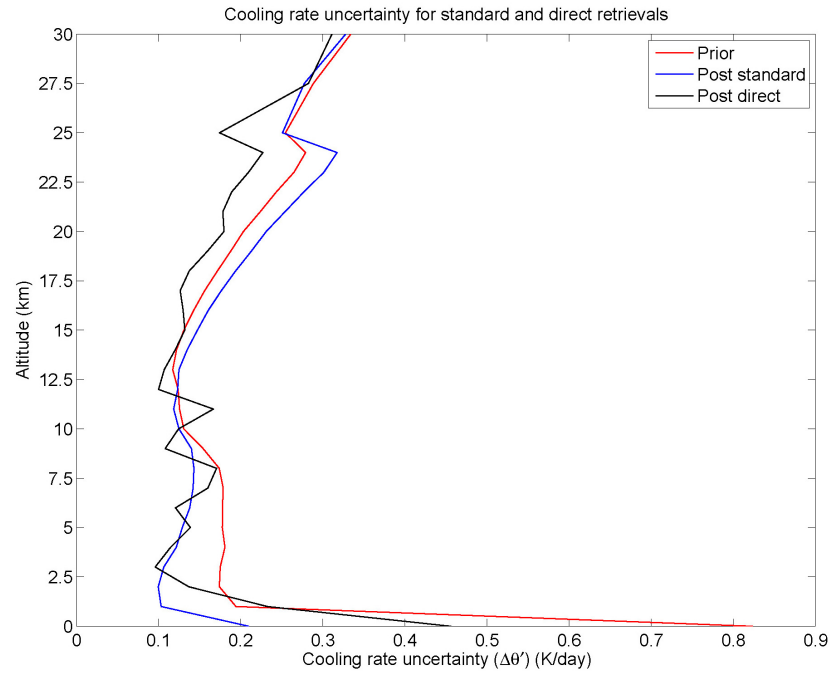
Figure 5.8: Cooling rate uncertainty (root of covariance matrix diagonal) comparison for clear-sky case for prior uncertainty and posterior uncertainty, according to a standard and direct retrieval approach.

Figures 5.6 and 5.8 show several different features that are interesting to note. First, the standard retrieval technique overestimates its retrieval ability with respect to boundary-layer cooling. Second, the direct retrieval technique performs comparably to the standard retrieval techniques in the free troposphere and tends to outperform the standard approach in the stratosphere. Third, the oscillations present in the estimation of the cooling rate uncertainty according to the direct retrieval technique suggest that the formulation of Eq. (5.11) requires further refinement. All of these details strongly suggest that the utilization of the standard retrieval approach to produce cooling rate profiles does not make use of all of the information contained in the spectra with respect to cooling rate profiles.

5.5   Treatment of Cloudy Spectra

The analysis of remote sensing spectra with respect to heating and cooling rate profiles in cloudy conditions is of scientific interest and warrants scientific scrutiny. As mentioned earlier, passive spectra only contain a partial description of the vertical distribution of cloud cover, yet this vertical distribution of clouds impacts heating and cooling rate profiles (i.e., *Chen, et al.* [2000]). Several authors [*Huffman et al.*, 1998; *Mather et al.*, 2007; *L'Ecuyer et al.*, 2008] have explored the ability of the active sounding instruments to provide additional information regarding heating/cooling rate profiles because radar and lidar have the ability to describe cloud vertical distribution under diverse conditions. Nevertheless, there are considerably more passive spectra available for the heating/cooling rate analysis as compared to active measurements because passive spectrometers such as AIRS provide comprehensive spatial coverage and have been operational since 2002.

The following figures show active and passive measurement characterization of a scene using CloudSat [*Stephens et al.*, 2002], CALIPSO [*Winker et al.*, 2003], and AIRS. Figure 5.9 depicts cloud profiles measured from CloudSat and CALIPSO at nadir for a tropical scene near Manus Island (147E, 2S) on January 5, 2007. The scenes depict various types of cloud cover including deep convective clouds (latitudes 0–4N), thin cirrus (latitudes 4–6N), and relatively clear conditions (latitudes 6–8N). At the same time, we can look at the near-collocation of AIRS infrared hyperspectral measurements to explore the passive spectral signature associated with the diverse cloud coverage of this scene. Clearly, most of the description of clouds in the IR passive spectra is contained in the brightness temperature values in the window channels (850–1210 cm^{-1} and 2450–2650 cm^{-1}) and the differential sensitivity of this band allows for some discrimination between different cloud types.
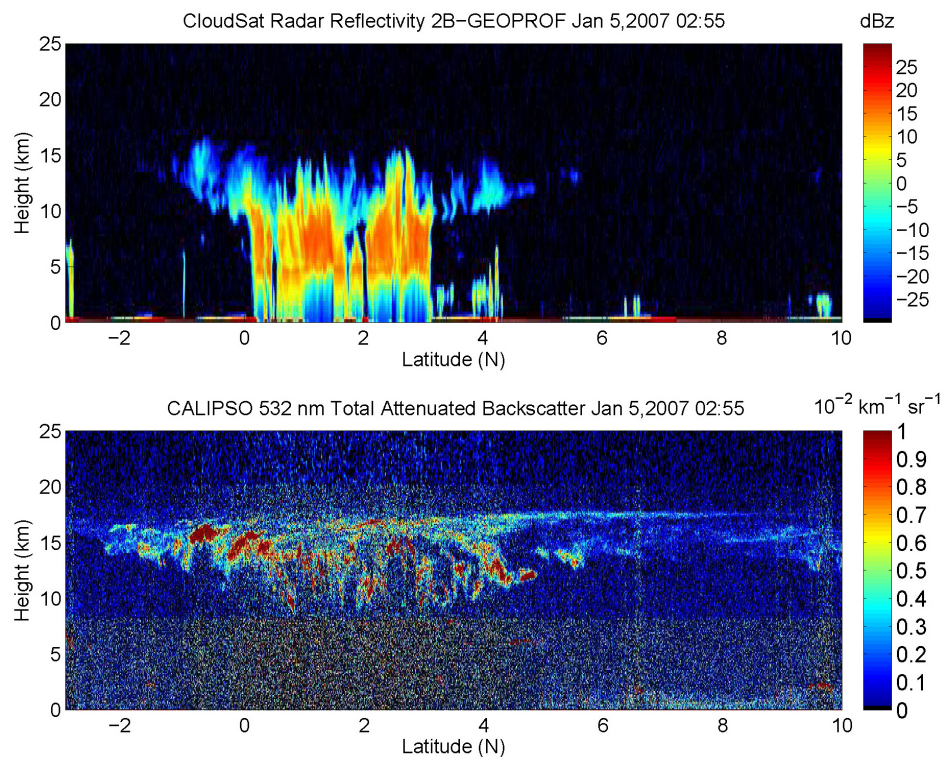
Figure 5.9: Top panel shows CloudSat Radar Reflectivity (2B-GEOPROF) product for a sample scene from January 5, 2007. Bottom panel depicts the same scene but shows the CALIPSO Total Attenuated Backscatter at 532 nm.

Also, the difference between cloud-cleared brightness temperature (derived from the cloud-clearing procedure described by *Susskind et al.* [2003]) and measured brightness temperature is the extent of the signal that the AIRS instrument measures with respect to clouds. Clearly, there are some deficiencies in describing diverse cloud cover using such passive spectra, not the least of which is the inability of the cloud-clearing algorithm to provide retrieval spectra for scenes with extensive cloud cover. Still, the brightness temperature spectral signatures associated with the diverse set of cloud coverage in this example show that cloud coverage information is contained within the spectra, though it may be difficult to retrieve.
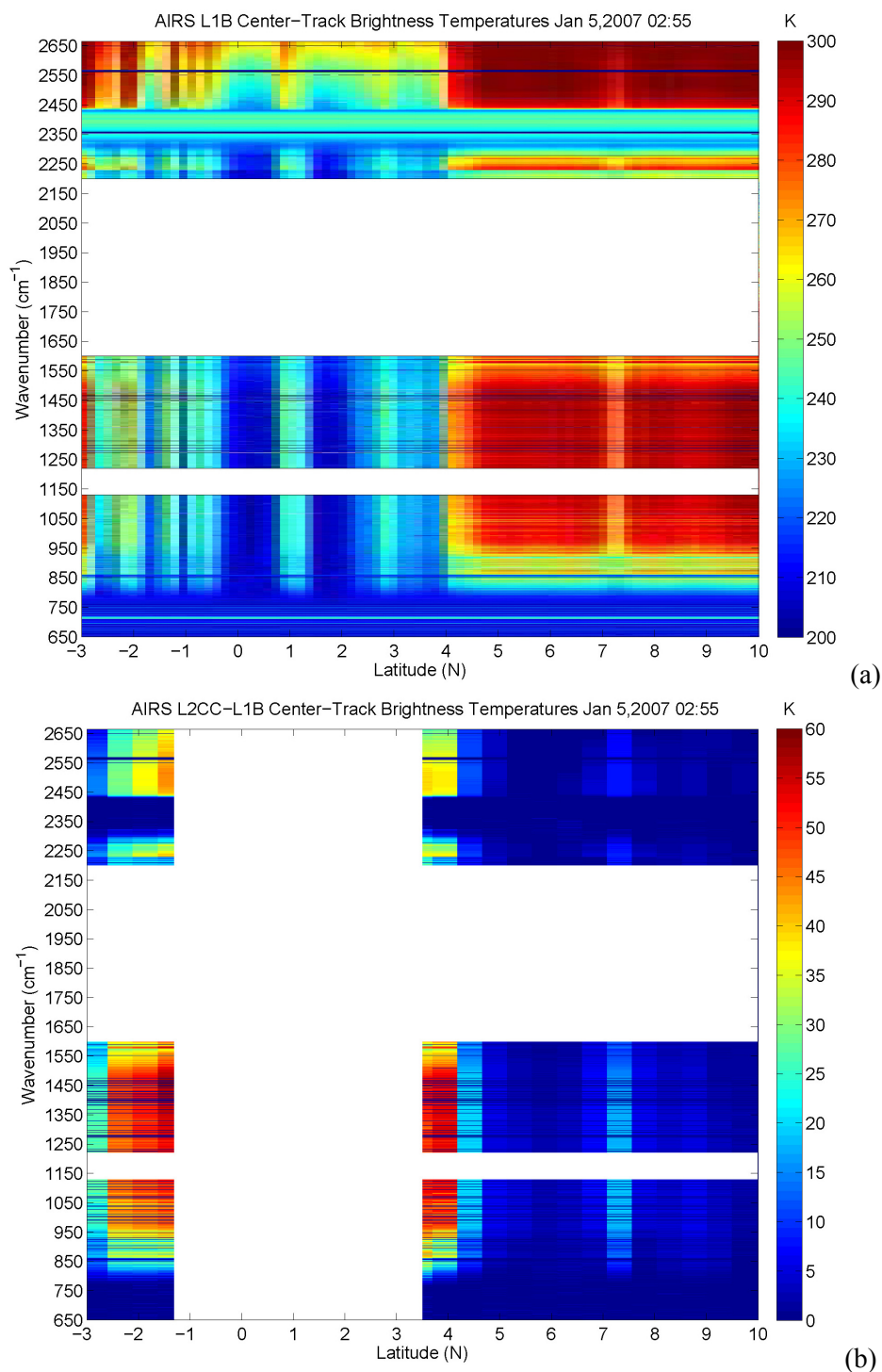
Figure 5.10: (a) Brightness temperature hyperspectral curtain of AIRS measurements for the nadir-viewing track of the scene described by the CloudSat and CALIPSO figures above. White spaces indicate no spectral measurements. (b) Same as (a) but the difference between cloud-cleared brightness temperature [*Susskind et al.*, 2003] and measured brightness temperature is displayed. Additional vertical white space indicates failure of cloud-clearing algorithm to produce spectra.

Given that AIRS passive infrared spectra are difficult to interpret in the presence of clouds, it may be useful to include coincidental measurements in other spectral regions. In particular, the Advanced Microwave Scanning Radiometer (AMSR-E) [*Kawanishi et al.*, 2003] provides an estimate of vertically integrated cloud water path that is nearly collocated with AIRS measurements over ocean scenes. Mid-IR spectra provide a fairly reliable estimate of cloud top height (i.e., [*Weisz et al.*, 2007]) and can characterize the distribution of gases above the cloud top. An additional constraint can be imposed on the determination heating and cooling rates where clouds are present, given the determination of cloud water path from AMSR-E. The constraints imposed by passive measurements on heating and cooling rates can be explored again through Gibbs sampling.

In the following figure, we explore varying the ice cloud vertical distribution subject to the constraint that the IR spectral residual associated with the change is less than 1 K across all channels. The purpose of this exercise is to test the ambiguity of cloudy-sky measurements with respect to clouds that occur below the cloud top but that may affect heating/cooling rates nonetheless. Therefore, with a Tropical Model Atmosphere, we test different values for cloud-top height and cloud-water content to determine the range of cooling rates that may be expected from AIRS measurements. Figure 5.11 indicates approximately the best possible description of the cooling rate profile from IR spectral measurements, though it does not contain estimates of the contribution of T, H_2O, and O_3 profile uncertainty on the cooling rate uncertainty.

From the figure, the cooling rate descriptive power of the passive spectra in cloudy conditions is reasonable where ice cloud cover is light to moderate. Where optically thick cloud cover is present (i.e., cloud water content greater than 0.01 g/m^3), AIRS passive spectra are unable to constrain cooling rates at the cloud top and for several kilometers below the cloud top. Furthermore, spectra that describe scenes with high, thick clouds will provide very little constraint on cooling rates at any level below the cloud top.

(a)

(b)
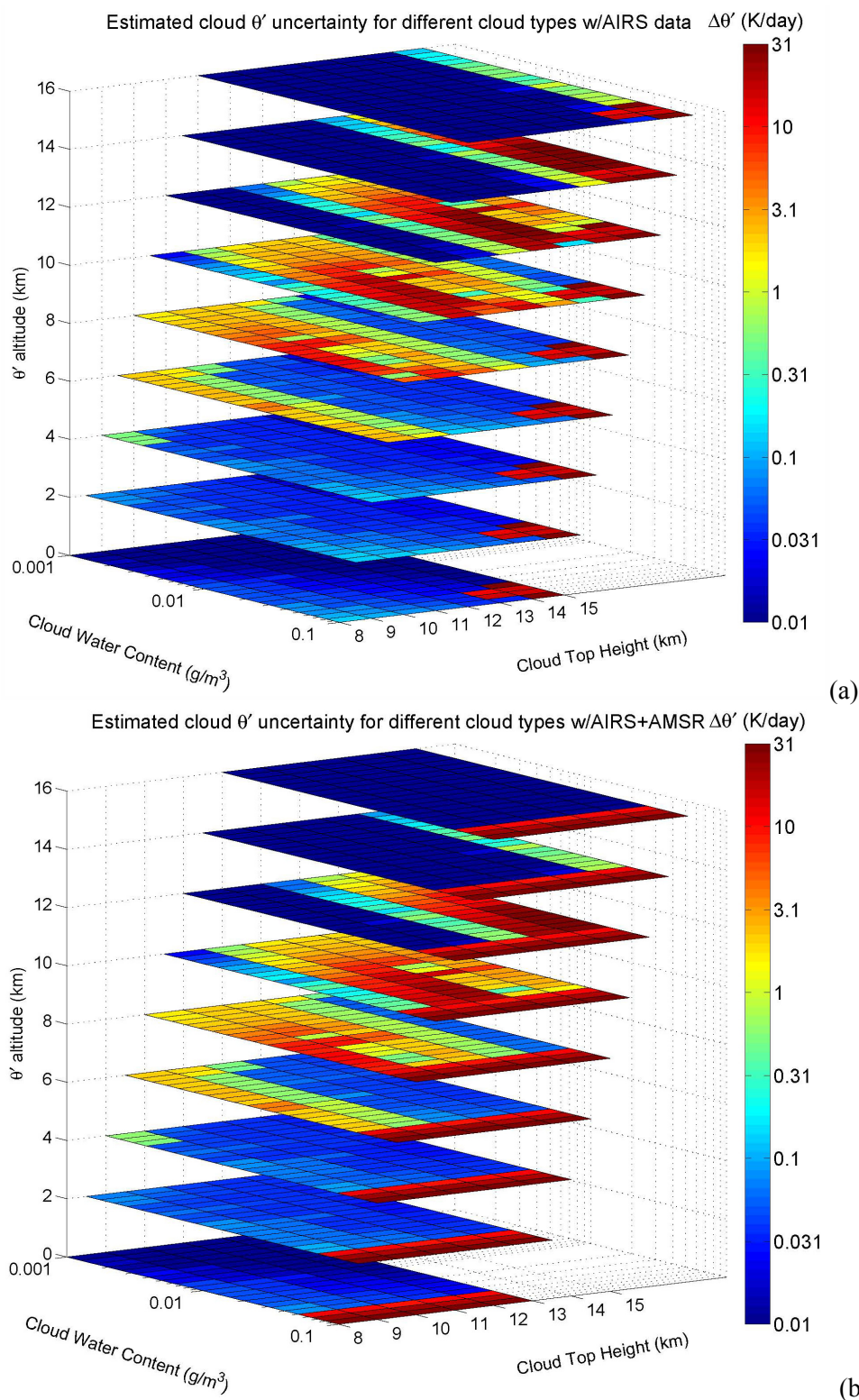
Figure 5.11: (a) Cooling rate profile uncertainty from clouds associated with AIRS spectra as a function of cloud-top height and cloud-water content for a 2-km thick ice cloud with $D_e = 41.5$ µm. (b) Same as (a) but with an additional cloud-water path constraint provided by AMSR-E measurements.

However, while these passive spectra are mostly insensitive to the atmospheric state below an optically-thick cloud, this figure demonstrates that the measurements do provide some constraint on allowable cloud configurations. According to this figure, the addition of a total cloud-water path constraint from AMSR (to within 40 g/m^2) does not provide a strong constraint on cooling rates beyond what is seen with the AIRS instrument. However, it may be fruitful to utilize Gibbs sampling to provide more formal estimates of passive measurement constraint on cooling rates.

Radar and lidar measurements from CloudSat and CALIPSO, respectively, provide a better constraint on cloud profile information, though these datasets are limited due to their lack of cross-track scanning capability. The value of these datasets should not be underestimated in terms of establishing retrieval techniques for cooling rates using passive spectra. Chapter 7 will discuss CloudSat and CALIPSO and selected mission products in greater detail.

5.6   Computational Cost Considerations

Because of the computational expense associated with radiative transfer calculations in models, we must look into computational considerations associated with a direct heating/cooling rate retrieval approach. First, a reasonable computational cost budget must be tabulated to compare the direct heating/cooling rate retrieval approach with the typical atmospheric state retrieval approach. This is accomplished by assessing the computational cost budget and estimating the cost that would reasonably be incurred in an operational algorithm for deriving heating/cooling rates from remote sensing data.

For the typical atmospheric state retrieval, significant computational cost is incurred in estimating the Jacobian matrix. For limited validation-type cases, full, physical radiative transfer models are utilized, but for most retrieval algorithms with missions utilizing hyperspectral instruments, the data-rate far exceeds the allotted computational resources if line-by-line codes

are to be used. Therefore, regression-based and lookup-table-based approaches are utilized.

Accordingly, significant up-front computational cost is incurred in creating a table of radiance

and Jacobian calculations that densely and completely sample the observation space that is

expected for the retrieval product [*Beer et al.*, 2004].

Marginal computational expense is incurred as a result of the retrieval approach described

in Eq. (5.13), in that the heating/cooling rate Jacobian matrix must be calculated in addition to the

atmospheric state Jacobian. For an *N*-layer atmosphere, this Jacobian would require on order of

$5*N$ calls to the broadband RTM in order to test heating/cooling rate sensitivity to T, H_2O, and

O_3, profiles in addition to cloud water and effective radius sensitivity. However, the estimation of

heating/cooling rate errors requires the calculation of this Jacobian, implying that the

computational cost of heating/cooling rate retrieval is only marginally more expensive than

standard retrieval techniques that do not produce heating/cooling rate error estimations. Even so,

it is important to explore how amenable the heating/cooling rate Jacobian is to parameterization.

This can be accomplished by examining heating/cooling rate Jacobians over a variety of different

atmospheric states and analyzing the percentage of variance captured by the first few principal

components.

For cloudy scenes, it would be scientifically fruitful to explore the computational costs of

using passive spectra to retrieve atmospheric state properties and cloud properties. Again, it is

expected that the heating/cooling rate Jacobian for these cases will incur a marginal

computational cost over the standard retrieval approaches.

5.7   Discussion

This chapter explores some of the details that must be considered when analyzing passive

remote sensing measurements to provide better understanding of heating and cooling rate profiles

with the goal of developing direct retrieval details. First, we present a method for formally

utilizing *a posteriori* atmospheric state retrieval statistics to estimate statistics associated with heating and cooling rate profiles for clear and cloudy scenes. Next, we broach the idea that additional constraints can be imposed on the retrieval process in order to provide improved estimates of clear-sky heating and cooling rates. Furthermore, we find that a combination of infrared and microwave measurements allows for a better description of heating and cooling rates in the presence of clouds.

Finally, we present a preliminary discussion of some computational issues associated with formulating remote sensing retrievals in favor of heating/cooling rate profiles. A small amount of additional computational cost is incurred in order to formulate heating/cooling rate constraints, but this cost is derived entirely from the heating/cooling rate Jacobian calculation which is necessary for the estimation of the heating/cooling rate error budget.

Significant additional work is warranted to explore the implementation of heating and cooling rate constraints into retrieval algorithms. However, results in the form of retrieved heating/cooling rate values will be very scientifically useful in that they can be readily compared with heating and cooling rates that are calculated by weather and climate models.

Chapter Six. Cloud Radiative Effect from MLS Products.

6.1   Abstract

The Ice Water Content (IWC) product from the Microwave Limb Sounder (MLS) measurements provides a novel view of the vertical distribution cloud water ice over the earth that has been largely inaccessible from previous satellite instrument datasets. This chapter provides an overview of the retrieval of IWC using MLS channels and shows how retrieval patterns compare with other descriptors of upper-tropospheric cloud ice, including ECMWF analysis. Because of the interest associated with the radiative effect of cirrus clouds, this chapter also explores the extent to which the IWC product can be utilized to examine the cloud radiative effect associated with cirrus clouds. Monthly-averaged data from the CERES instrument is then utilized to assess the contribution of cloud ice to the total cloud radiative effect (CRE). The CRE values from the analysis of MLS and CERES data are compared with what is derived from ECMWF analysis fields. It is found that the ECMWF IWC product is consistently lower than the MLS retrieved values from 100 to 200 mbar. However, the CRE derived from upper-tropospheric (UT) IWC is generally larger than the observed CRE from CERES. Even though it may be more difficult to analyze the radiative effect of the IWC product in isolation from underlying clouds, ice water information can be analyzed in conjunction with other existing products in order to uncover model problems that may be obscured by the apparent agreement in OLR products.

6.2   Introduction

The presence of clouds dramatically alters longwave and shortwave radiation budgets throughout the atmospheric column. In order to address this issue, the concept of cloud radiative

effect (CRE), also called cloud radiative forcing and initially described by *Ellis and Haar* [1976], gained popularity within the scientific community. Later, *Harrison et al.* [1990] utilized the Earth Radiation Budget Experiment measurement set [*Barkstrom*, 1984] to derive the cloud radiative effect from which they characterized the influence of clouds on the Earth-atmosphere system. From these and other works, an appropriate definition of radiative effect emerged as the difference between the TOA and /or surface broadband shortwave and longwave net flux over a model grid point or a measurement footprint for clear and cloudy conditions. Consequently, the LW CRE is given by:

$$CRE_{LW} = F_{LW}^{clear} - F_{LW}^{cloud} \qquad (6.1)$$

where F_{LW}^{clear} is the clear-sky net flux and F_{LW}^{cloud} is the all-sky net flux. Similarly, the SW CRE is given by:

$$CRE_{SW} = F_{SW}^{clear} - F_{SW}^{cloud} \qquad . \qquad (6.2)$$

The net CRE is given by:

$$CRE_{NET} = CRE_{LW} + CRE_{SW} \qquad (6.3)$$

with positive CRE indicating warming.   Clouds tend to heat tropical and mid-latitude atmospheres by absorbing IR surface flux and reemitting at colder temperatures while clouds also reflect incoming solar radiation back to space. Generally, the net radiative effect of clouds is small despite large changes in shortwave and longwave budgets. Especially in the tropics, observations and model results confirm the parity in longwave and shortwave effects, but since the LW CRE is positive and the SW CRE is negative, the total CRE is the difference of two large terms. The following figures are derived from the CERES instrument [*Wielicki et al.*, 1996] and illustrate SW, LW, and net CRE. *Cess et al.* [2001] found that the ratio of shortwave to longwave CRE varied from 1 to 1.1 in the tropics with significant interannual variability probably resulting

from variations in tropical circulation patterns as evidence by changes in CRE patterns associated with El Niño Southern Oscillation events [*Allan et al.*, 2002].
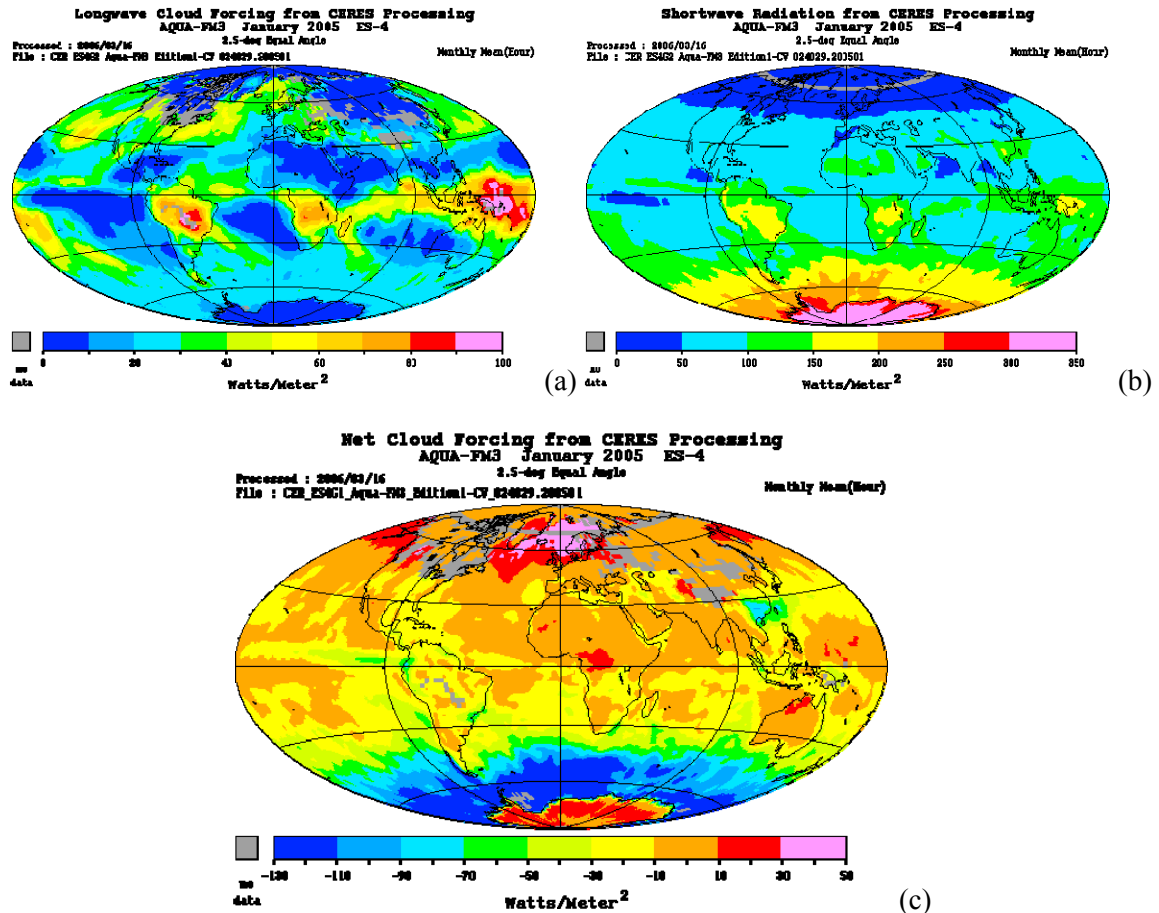
Figure 6.1: Monthly-averaged CRE derived from CERES instrument data in a manner that is consistent with the ERBE mission (ES-4 algorithm) for (a) LW measurements, (b) SW measurements, and (c) net LW + SW measurements.

Mace [2007] found that the utilization of various datasets from several instruments over an extended time period can reveal significant information about CRE details. That work utilized radar and lidar measurements at the Atmospheric Radiation Measurement program's Southern Great Plains site (ARM SGP) to determine how clouds contribute to net CRE. They found that the effects due to lower and upper clouds produce a small average net CRE with a vertical displacement between net heating and cooling regions. This displacement has a strong seasonal dependency but is not revealed solely in TOA flux measurements.

However, there are several potential feedbacks that are not revealed by studies that solely concern TOA net CRE. Depending on their vertical distribution, clouds heat and cool different layers of the atmosphere. For example, high clouds tend to warm the atmospheric column in the tropics relative to clear-sky conditions, while low clouds tend to enhance column cooling, especially at high latitudes. The following figure illustrates that despite the necessity of using measurements to estimate TOA energy balance and CRE, very different cloud configurations can produce similar TOA fluxes.
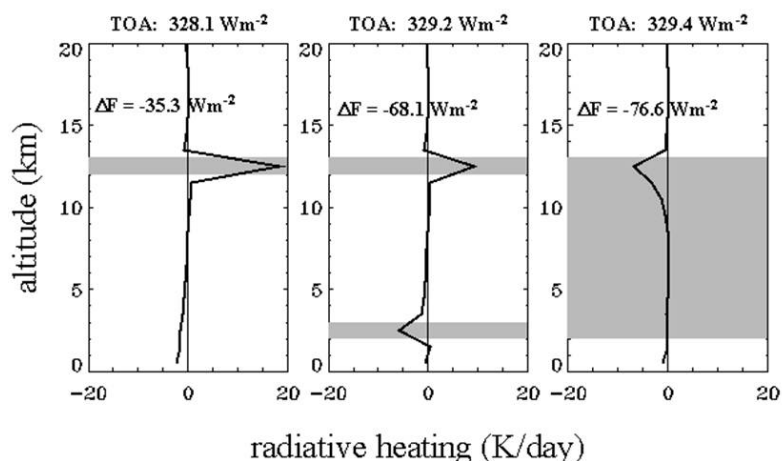
Figure 6.2: Different possible cloud profiles (shaded gray) and heating rates (black lines) associated for scenes with nearly the same TOA LW flux. The net column flux divergence is denoted in the figure as ΔF. Adapted from GCM simulations described in *Slingo and Slingo* [1988] and shown in *Stephens* [2002].

Given the ambiguity associated with the CERES measurements in terms of constraining the heating and cooling of the atmospheric column by clouds, the introduction of extra measurements regarding the vertical distribution of clouds can be very valuable to the interpretation of TOA flux data. Visible and IR measurements are sensitive to cloud-top heights but are generally unable to resolve cloud structure below the cloud-top. The following figure presents a simulation of the IR spectral signature associated with different cloud configurations given the same cloud-top. It indicates that, similar to CERES instrument measurements, nadir-

viewing passive measurements cannot unambiguously describe how different cloud configurations contribute to the measured cloud spectral signatures.
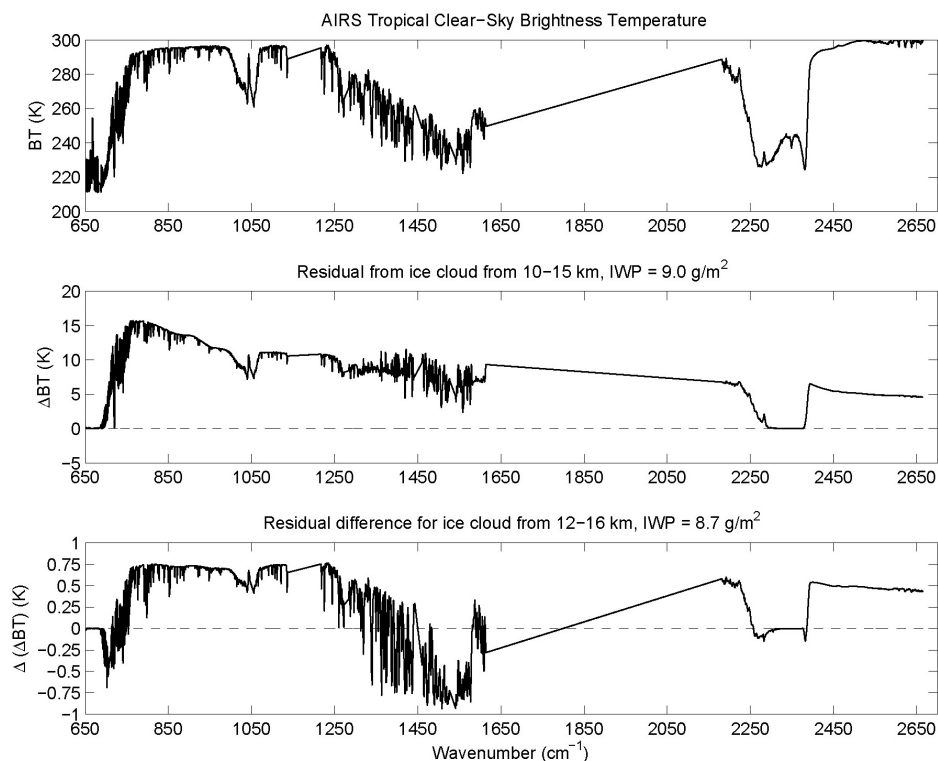
Figure 6.3: Top panel: Clear-sky spectrum associated with a Tropical Model Atmosphere [*Anderson et al.*, 1986]. Middle panel: spectral signature (residual) associated with a cirrus cloud from 10–15 km with an integrated IWP of 90 g/m², D_e = 22.5 μm. Difference in residual associated with a cirrus cloud from 12–15 km with an integrated IWP of 90 g/m², D_e = 22.5 μm.

This figure shows that passive infrared hyperspectral measurements such as those from the Atmospheric Infrared Sounder (AIRS) [*Aumann et al.*, 2003] are exquisitely sensitive to the presence of cirrus clouds. Nevertheless, it is much more difficult to discern different types of cirrus clouds. The spectral signatures from a 5-km-thick cirrus cloud and from a 3-km-thick cirrus cloud of similar values for the Integrated Ice Water Path are nearly identical.

On the other hand, limb-sounding measurements in microwave spectral regions with low cloud optical depth can potentially characterize the vertical distribution of upper-tropospheric clouds. The Upper Atmosphere Research Satellite (UARS), operating from 1991–2005, contained an earlier-generation Microwave Limb Sounder instrument [*Barath*, 1993] which

operated through mid-1994. This instrument measured in three bands: 63, 183, and 205 GHz and was sensitive to temperature and various gaseous species relevant to stratospheric ozone. More recently, the Microwave Limb Sounder (MLS) aboard the Aura platform became operational. Aura MLS is a more-advanced instrument that utilizes passive microwave spectroscopic measurements [*Waters et al*., 2006] and has sensitivity to the vertical distribution of ice clouds because it contains measurements that provide differential sensitivity both to scenes with low cloud optical depth and to scenes with high cloud optical depth. If utilized properly, these measurements, coupled with broadband flux data, may offer insight into the relative contribution of high clouds and low clouds to the observed CRE from CERES.

This chapter will begin with an overview of the MLS measurement approach and continue with a brief discussion of the retrieval of upper-tropospheric ice water content from radiance data. Next, we will describe the CERES data and how CRE is determined from such measurements. Subsequently, this chapter will analyze the contribution to the CRE from upper-tropospheric ice clouds and will compare those results with similar fields derived from forecast analysis models.

6.3   MLS Data Overview

The MLS instrument has been taking data from orbit aboard the Aura platform since July 2004 and measures radiances centered around 5 spectral bands in the vicinity of 118, 190, 240, 640, and 2520 GHz. Several channels per spectral band at approximately 5 GHz spacing record data with a limb-scan oriented along-track. Data are recorded above 215 hPa with a vertical resolution of better than 3 km. Along-track resolution is approximately 500 km with a cross-track footprint of 5 km. More advanced product versions claim a spatial resolution footprint of 3 km X 300 km X 7 km. Measurements at 118 and 2520 GHz are polarization sensitive, while the

radiometers for the other bands are double-sideband receivers, meaning they are insensitive to the polarization of the signal. These measurements lead to about two dozen standard products over the course of normal operations, including radical species. These products have led to a greatly increased understanding of upper-tropospheric and lower-stratospheric processes. The below figure depicts high-resolution radiances over the MLS spectral bands along with the instrument's channel coverage:
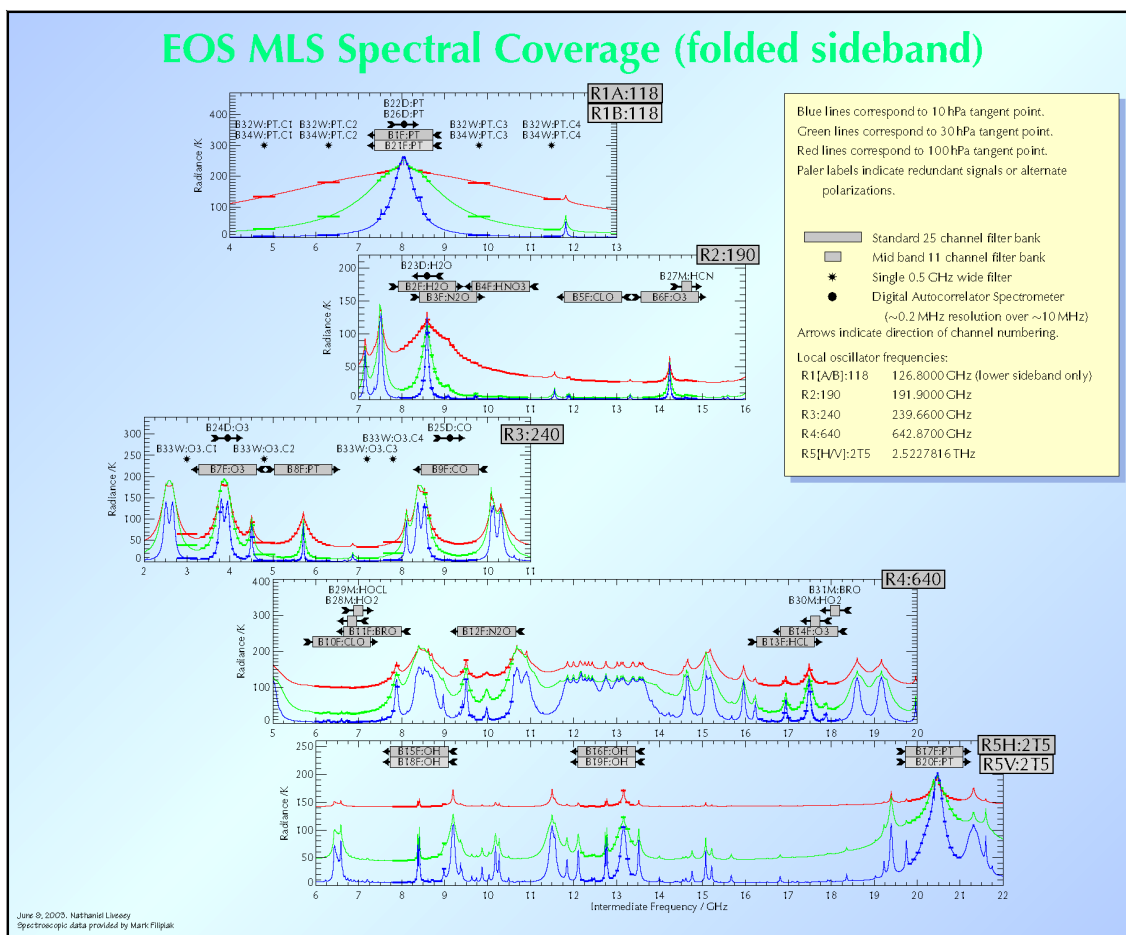
Figure 6.4: Depiction of folded-sideband high-resolution radiances at several tangent heights in the 5 spectral bands over which the MLS instrument measures. Diagram from http://mls.jpl.nasa.gov/images/folded-big.png

While the MLS instrument was primarily designed to characterize gaseous stratospheric constituents, one of the most scientifically interesting results generated from the instrument's

measurements is the Ice Water Content (IWC) product. As described by *Wu et al*. [2006], this

product is derived from a combination of radiance data from the MLS spectral bands with most of

the information coming from the window channels in the 240 GHz band. Some extra information

is derived from the 118 GHz and the 2.5 THz because they are sensitive to the polarization signal

from clouds. The figure below provides a cartoon of the MLS data measurement technique for

the IWC product.
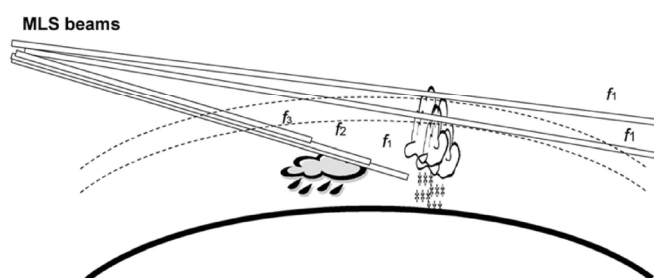
Figure 6.5: Schematic of cloud IWC observations derived from limb-viewing geometry from *Wu et al*. [2006]. At pressures above 215 mbar, IWC observations are derived from single-channel radiances in window channels.

The IWC product is derived by first retrieving the temperature and gaseous quantities from the

measurements and then utilizing the discrepancies in window-channel radiance between the clear-

sky forward model calculations [*Read et al*., 2006] and the measured radiance data to produce

cloud-induced radiance values (*Tcir*). The *Tcir* values are then used with the cloudy-sky forward

model to estimate cloud IWC predicated on several assumptions that are discussed below. Figure

6.6 indicates that between 5 and 30 mg/m^3, the relationship between IWC and *Tcir* is very robust

and that IWC values of up to 50 mg/m^3 can be retrieved through this technique. The resulting

IWC product is reported at 215, 178, 147, 121, 100, 83, and 68 hPa. The data can be gridded on

monthly timescales with at 4° latitude by 8° longitude resolution to produce maps of vertically

resolved cloud ice-water content.
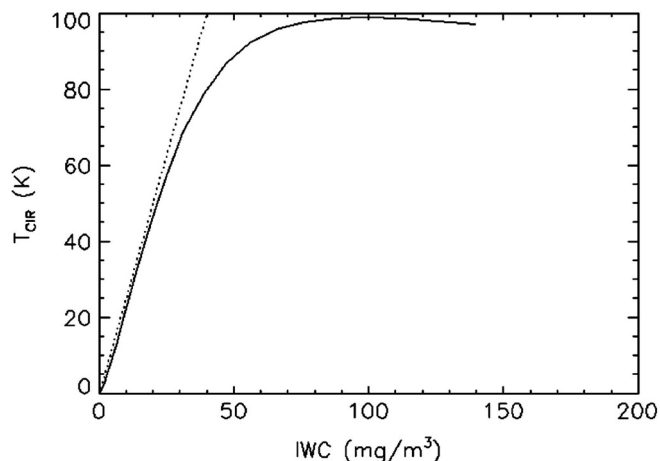
Figure 6.6: Solid line denotes sensitivity of MLS window channel brightness temperatures to cloud IWC. Dashed line indicates the fit line utilized in the retrievals. From *Wu et al.* [2006].

The following figure realizes the IWC vertical structure in a way that has not been achieved from previous remote sensing measurements.
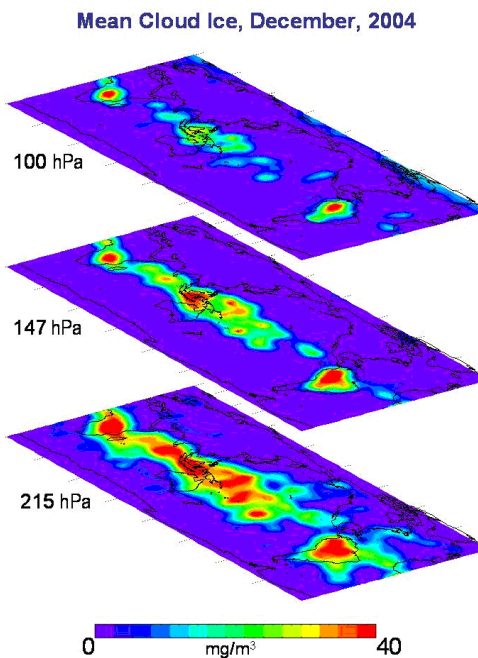
Figure 6.7: Monthly-mean IWC values at 4x5° resolution at several pressure levels for December 2004 retrieved from MLS, version 1.0. From http://mls.jpl.nasa.gov/products/iwc_product.php

Several features are indicated in this figure. First, the areas of the planet with strong convection

tend to produce high IWC values up to 147 hPa. Second, cloud ice extent outside of regions of

strong convection is sparse above 215 hPa. Furthermore, this figure gives an indication of the extent of cloud ice in the tropics and extra-tropics.

There are many sources of uncertainty in the derivation of the MLS IWC product, and several of the most significant sources arise from assumptions made in the retrieval process. First, there are radiance and forward model uncertainties. While the former is almost entirely random, the latter depends on the clear-sky gas retrievals, inducing a *Tcir* uncertainty of 2K at 100 hPa and 10K at 300 hPa which translates to 10–50% IWC product uncertainty. More systematic uncertainties are present in the assumptions utilized in the translation from *Tcir* to IWC. In particular, the ice particle size distribution and shape are mostly unconstrained by the retrieval, and variations in the IWC product may lead to uncertainties as large as a factor of 2. Finally, due to its viewing geometry, this IWC product covers an enormously large horizontal footprint, thereby thwarting standard validation efforts.

However, efforts by *Wu et al.* [2008] have explored how MLS data compare with estimates of cloud ice from other A-Train measurements, including MODIS [*Justice et al.*, 1998] and CloudSat [*Stephens et al.*, 2002]. These authors found that the MLS product is consistent to within 50% of results from other datasets, and assumptions regarding the particle size distribution within ice clouds contribute substantially to these discrepancies. Even with 50% nominal uncertainty in cloud ice, scientifically meaningful results can still be derived from the MLS IWC product. For example, *Li et al.* [2007] found that significant differences existed between the distribution of cloud ice fields from the ECMWF analysis product and the IWC distributions derived from the MLS measurements. The spatial patterns of this disagreement between the two characterizations of UT IWC suggested that the modeling of deep convection over equatorial land masses was deficient in the analysis calculations. Therefore, while caution must be exercised in the use of the MLS IWC product, it presents an unprecedented and scientifically valuable record of UT cloud layering.

6.4   CERES Data Overview

The Clouds and the Earth's Radiant Energy System (CERES) instrument [*Wielicki et al.*, 1996] is designed to measure the TOA energy balance through shortwave and longwave measurements. Several nearly identical instruments have been designed and flown on different platforms including the Tropical Rainfall Measuring Mission, TRMM, (1998–present), Terra (2000–present), and Aqua (2002–present). This system produces broadband radiance measurements and has a programmatic heritage from the Earth Radiation Budget Experiment (ERBE) suite of instruments [*Barkstrom et al.*, 1984] that dates back to 1984.

The Aqua platform, on which the newest CERES instrument operates, flies only a few minutes behind the Aura platform containing MLS, providing nearly temporally coincident measurements. The data processing algorithms for CERES [*Wielicki et al.*, 1998*; Young et al.*, 1998; *Loeb et al.*, 2003] derive several other higher-level products, including monthly-averaged TOA fluxes. As with many satellite instrument datasets, the details of the measurement are crucial to a proper interpretation.
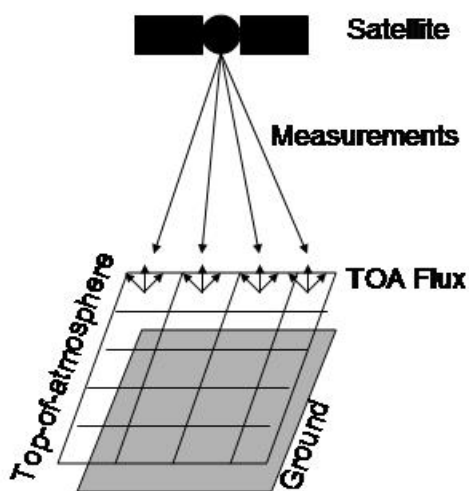
Figure 6.8: Cartoon detailing the mismatch between TOA flux and instrumental radiance measurements.

First, the conversion from the radiance values, which the instrument measures, to fluxes, which are desired for model-measurement comparison, is non-trivial. The cartoon in Figure 6.8 illustrates the nature of the complexity. Data processing algorithms are required to estimate TOA flux and necessitate the calculation of the angular distribution of TOA radiance for each footprint with a limited number of actual radiance measurements. Moreover, several of the CERES instruments support standard cross-track scanning along with rotating azimuthal plane scanning, and the latter method allows for more advanced estimation of the anisotropic nature of the TOA radiance [*Parkinson*, 2003]. Radiance anisotropy is conventionally parameterized and subjected to a scene-classification algorithm in order to derive top-of-atmosphere fluxes. The error associated with this conversion process is estimated to be approximately 5% globally, though it can be higher for certain types of cloud cover [*Loeb et al.*, 2004]. Another source of error in the CERES data processing algorithm arises because the temporal and spatial averaging of fluxes from the measurements requires careful consideration of the data sources. The radiance measurements view footprints in a sun-synchronous orbit and therefore have difficulty capturing the diurnal cycle of longwave and shortwave flux. Moreover, monthly-averaged fluxes are a product that is routinely produced by the CERES mission, and errors associated with this averaging process are approximately 6% in the SW and 0.5% in the LW [*Young et al.*, 1998]. Our analysis will primarily focus on the utilization of the ES-4 data product, a monthly-averaged SW and LW flux product that mimics the data produced by the ERBE instrument. The figures below illustrate the fluxes estimated for a typical month using the Aqua CERES instrument. In order to estimate the CRE from CERES data, we take the difference between all-sky fluxes and those derived from clear-sky conditions which are temporally averaged to yield monthly-averaged CRE values.
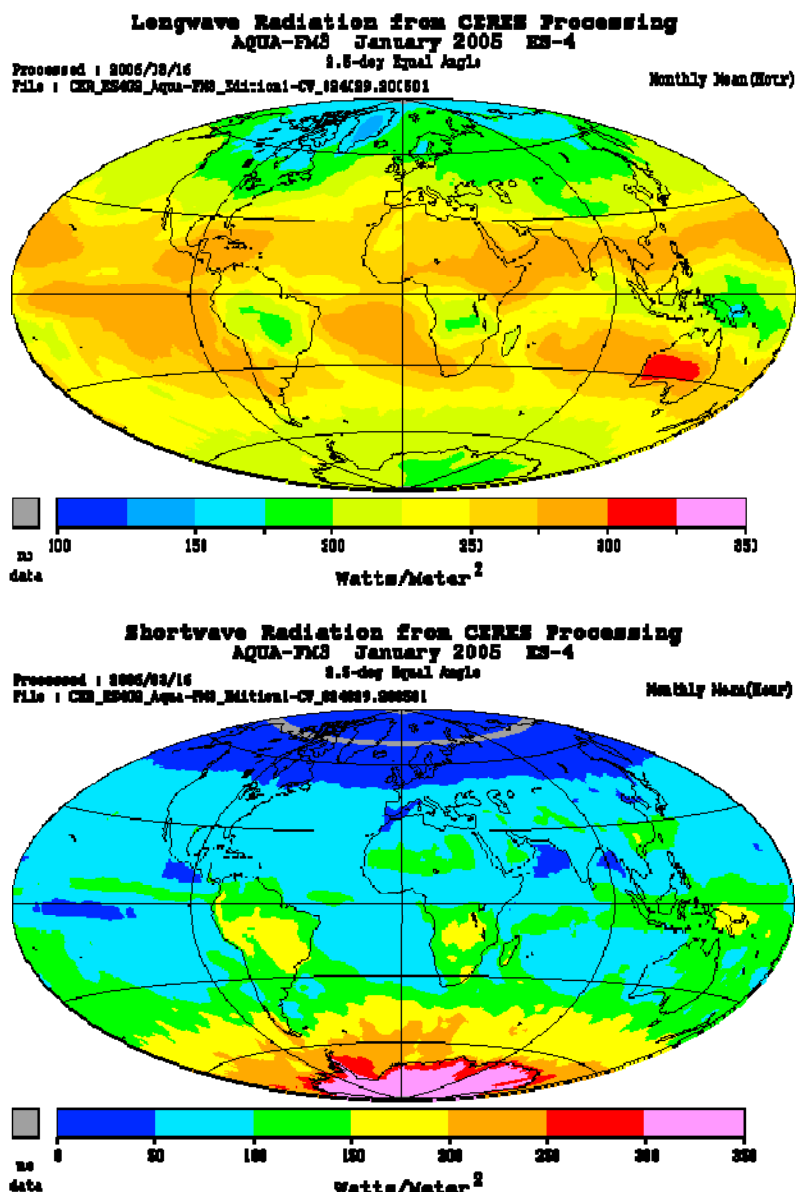
Figure 6.9: Longwave (top panel) and shortwave (top panel) monthly-averaged TOA flux derived from the Aqua CERES instrument in cross-track scanning mode.

6.5   UTC Radiative Effect

The purpose of this section is to provide an estimate of the contribution of upper tropospheric clouds to the cloud radiative effect observed by CERES. Because the MLS instrument data has sensitivity to UT clouds, it is reasonable to explore whether the IWC product provides insight into the CERES CRE product. Due to the limitations of the IWC retrieval, only

the radiative effect of clouds from 83 hPa to 215 hPa is considered. These clouds correspond to cirrus, cirrostratus, and deep convective clouds in the International Satellite Cloud Climatology Program (ISCCP) [*Rossow and Schiffer*, 1991] classification scheme. The radiative transfer model we use is RRTM [*Mlawer et al.*, 1997] which is a correlated-*k* distribution model [*Lacis and Oinas*, 1991] covering 16 contiguous bands in the longwave and 14 bands in the shortwave. The spectral extinction coefficient, the single-scattering albedo, and the asymmetry factor are parameterized in terms of the IWC and the effective ice crystal size (D_e). For D_e, we adopt the empirical formula for ice particle size distribution developed by *McFarquhar and Heymsfield* [1997] which is used in the MLS IWC forward model. Accordingly, D_e is computed as a function of MLS measured IWC and temperature. This treatment of ice particle size is consistent with the MLS IWC retrieval, but we recognize that the description of cloud microphysical properties is essential to the assessment of cloud radiative effect [*Stephens et al.*, 1990]. Several authors have noted that quantifying the radiative effects of clouds with horizontal spatial resolution that is much larger than the scale of the clouds requires the implementation of a cloud-overlap approximation to estimate the radiative effect of partial cloud coverage within the grid cell (e.g., [*Collins*, 2001]). Also, given the large horizontal footprint over which MLS makes measurements, it is reasonable to use a random overlap approximation in which the overlap of clouds between different vertical layers is randomly assigned.

Here we consider UT layer clouds and assume no clouds underneath (the "single-layer" case). This treatment has been a common practice to isolate the radiative effect of a certain type of clouds (e.g., [*Fu and Liou, 1993*; *Hartmann et al.*, 2001; *Fu et al.*, 2002]). However, the linearity of the contributions of liquid and ice clouds to the total cloud radiative effect must be considered. That is, we seek to address whether the presence of an underlying liquid cloud substantially mitigates the cloud radiative effect associated with an ice cloud. If it does not, then it is more straightforward to interpret the differences between CRE products derived from

CERES measurements and CRE calculations from MLS data alone. Figure 6.10 shows the

variation in CRE with UT IWP for several different cloud scenarios.
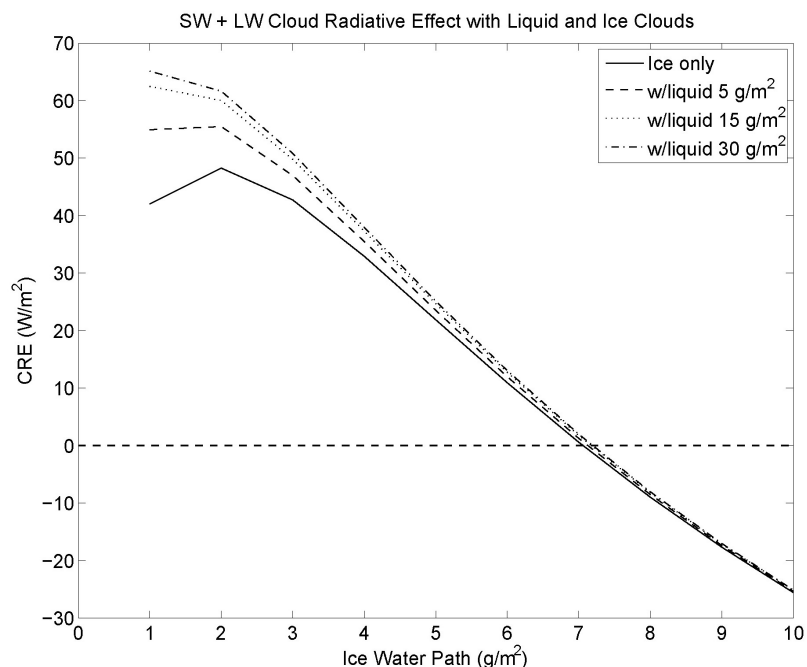
Figure 6.10: CRE vs. IWP (integrated from 68 to 215 hPa) for a uniformly distributed ice cloud (D_e = 30 μm) with varying liquid water path from 600 and 700 mbar (D_e = 6 μm).

This figure shows that the effect of different underlying liquid clouds is most significant at low

IWP values, and for IWP values of greater than 4 g/m^2, the presence of liquid clouds below an ice

cloud layer has very little impact on the CRE. The occurrence frequency of the MLS-retrieved

non-zero IWP for the month of January 2005 is depicted in Figure 6.11 and shows that

approximately 92% of the observations contained values with less than 4 g/m^2. From the results

in this histogram and from Figure 6.10, it can be concluded that the nonlinearity in the

contribution to CRE of liquid and ice clouds needs to be considered.

MLS−Derived IWP Histogram for January, 2005
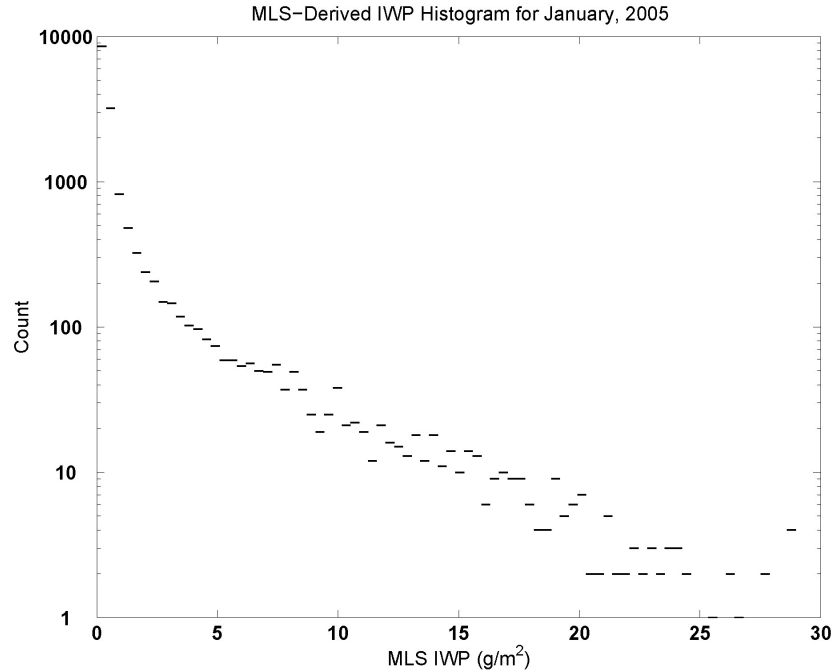
Figure 6.11: Histogram of IWP values (215 to 83 mbar) derived from MLS L2 v2 IWC products from January, 2005.

Consequently, it is first necessary to compute radiative fluxes using instantaneous UTC profiles along orbit tracks, rather than using averaged profiles over a certain area or period. The monthly mean CRE is then constructed by averaging all individual CREs for a certain 4x5° grid-point. We consider that each measurement footprint has fractional cloud coverage η which is determined by averaging the cloud fraction product of the AIRS instrument (spatial resolution ~ 45 km) concurrent with the MLS observation. Since the MLS measurement represents averaged IWC over the MLS FOV, the actual overcast IWC value is estimated as IWC/η. Thus, the radiative effect for each MLS measurement location is the following:

$$CRE_{NET}^{MLS} = \eta \left(CRE_{LW} + CRE_{SW} \right) \qquad . \qquad (6.4)$$

It is important to explore the impact of uncertainty in the MLS product and its large footprint on subsequent CRE calculations. In a sensitivity run, we add a correction factor of 0.2 to all CFR measurements to account for the effect of less opaque clouds being reported at a smaller fraction than derived from more sensitive instruments [*Kahn*, personal communication].

The "+0.2 CFR run" provides a rough estimate of the difference in cloud fraction from the AIRS effective cloud fraction to the true cloud fraction. The precise quantification of this error is under-way. We also test an extreme case by assuming that the UTC coverage for each MLS IWC FOV is 100% and that the AIRS CFR equals the cloud emissivity (the "overcast run"). These three sensitivity runs give a range of uncertainties in the UTC CRE values due to the estimate of cloud fractional coverage η. Using January 2005 as an example, we find the net UTC CRE is about 2.7 W/m^2 (warming) in the tropical average, with LW CRE being 4.7 W/m^2 and SW CRE being -2.0 W/m^2 in the "single-layer" case where η = AIRS CFR. Increasing η by 0.2 would increase the LW and SW CREs by 0.3 and 0.03 W/m^2, respectively, resulting in a stronger warming of 3.0 W/m^2 in the tropical average. The "overcast" run yields a significantly larger LW warming effect. The tropical-averaged net CRE becomes 17.6 W/m^2, with 21.4 W/m^2 LW CRE and -3.8 W/m^2 SW CRE. These estimates of net UTC CRE are approximately in the range of high cloud radiative effect calculated from models or obtained from observations.

Since UT IWC tends to increase along with the increase of SST, we conduct a set of sensitivity runs to investigate the change of CRE due to changes of IWC. We successively increase IWC values at each level equally over the tropics by 25% to 250%, while keeping CFR unchanged. For simplicity, the "single-layer" approach is used. Based on the previous calculations, the results obtained from the "single-layer" case is applicable to the "multi-layer" case, at least the sign and rough magnitude of UT CRE. Figure 6.13 shows that the tropical-mean net warming reaches its maximum when IWC is increased by 25%–50% from the current value. When IWP is increased by 50%, the net warming is 0.05 W/m^2 more than the standard run, with LW and SW effects both increasing by 0.7 W/m^2.
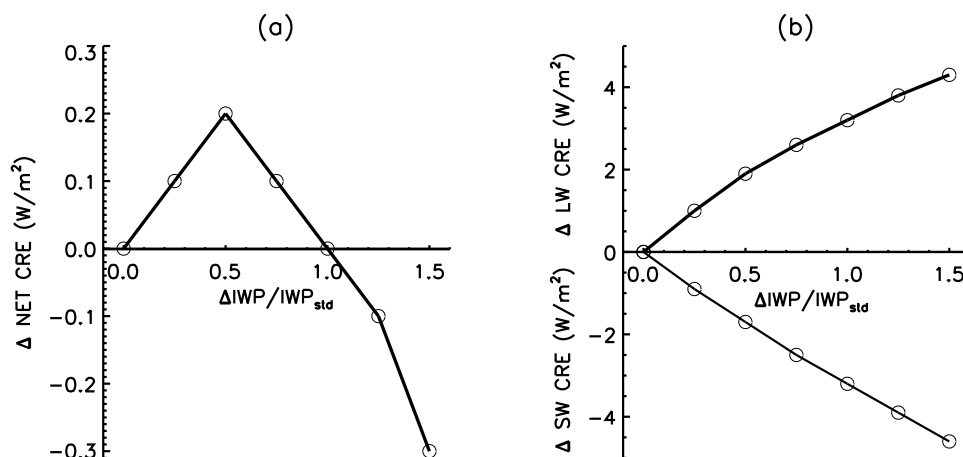
Figure 6.12: The difference of tropical-mean (a) net, (b) LW, and SW CRE (in W/m^2) between the runs with increased IWP and the standard run. All results are based on the January 2005 UT cloud profiles, assuming no low and middle clouds underneath.

Supposing that the rate of IWC increase with SST is 20% K^{-1}, the change of net CRE is about 0.02 W m^{-1} K^{-1}, while the separate changes of LW and SW CRE are larger. When IWC is increased more than 50%, the increase in SW cooling outweighs LW warming, causing the net CRE to decrease from its maximum value. When IWC is increased by 75%, the net CRE returns to approximately the same value as the standard run, although the changes in the LW and SW effects are both about 1.0 W/m^2 in the tropical average. A further increase of IWC yields net warming smaller than the standard run. However, it is unlikely the polarity of the net CRE would reverse sign given reasonable IWC changes for hypothetical SST changes within 5 K (corresponding to roughly doubled IWC change).

Figure 6.13 shows the monthly-averaged IWC product from MLS and ECMWF analysis. While the UT IWC fields from these two sources are not on the same vertical coordinate system, it is clear that the retrieved IWC values from MLS are larger than the ECMWF IWC values. This result is consistent with other findings [*Li et al.*, 2007] and suggests that there may be compensating factors within the forecast model in order to produce realistic OLR values. The resulting CRE from the two different IWC products can also be compared to determine the impact of this discrepancy in IWC on the contribution to the CRE.
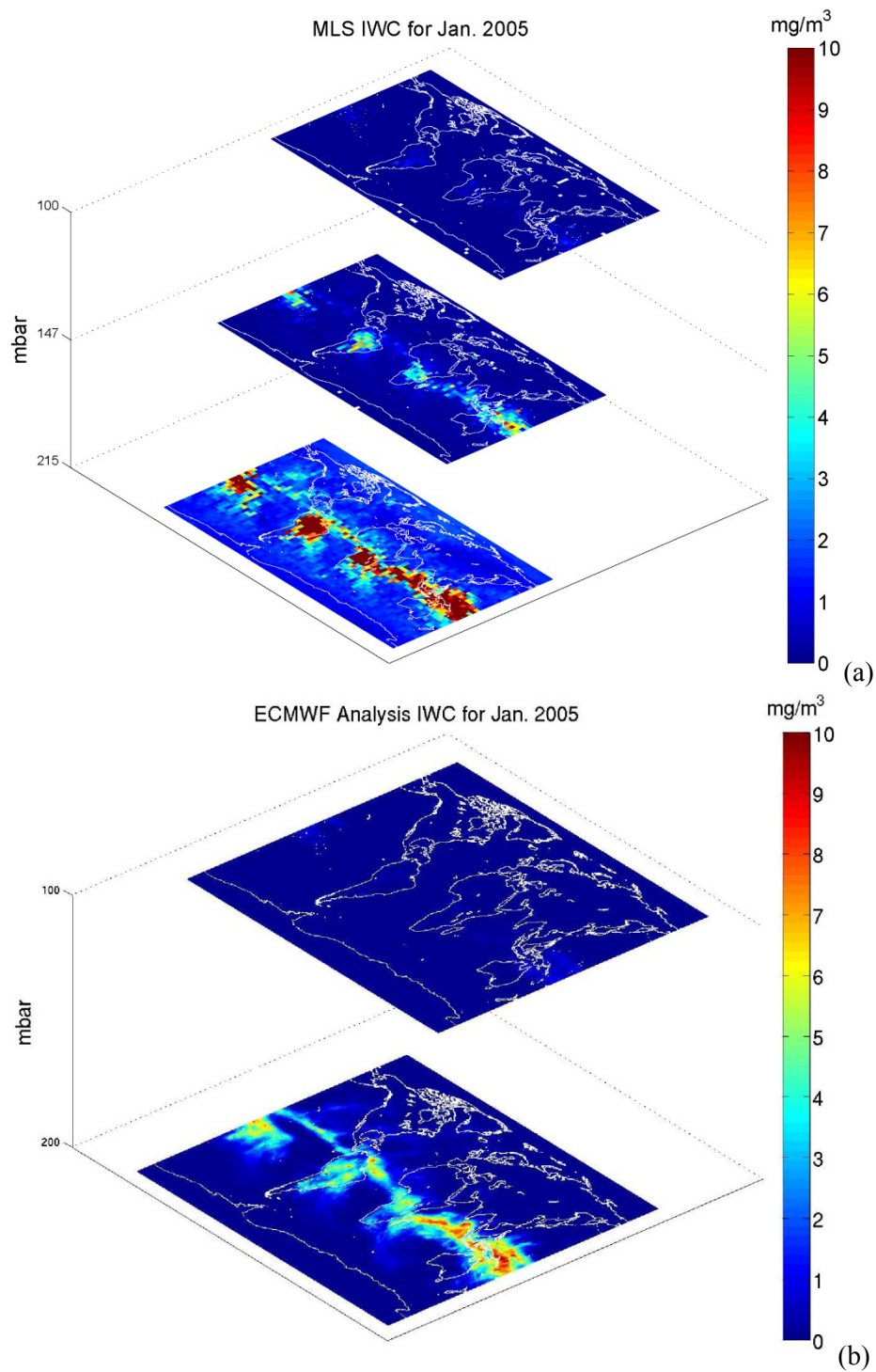
Figure 6.13: (a) Average IWC retrieved from MLS for Jan. 2005. (b) Average IWC from ECMWF analysis for January 2005.
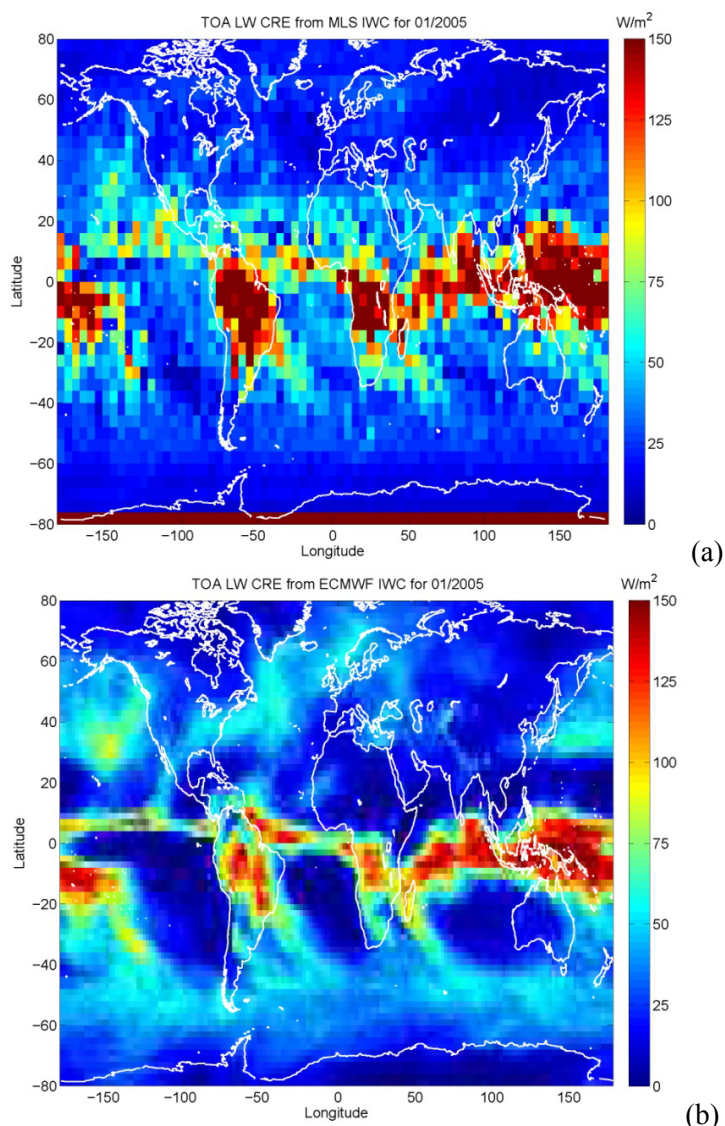
Figure 6.14: (a) Average CRE calculated from MLS IWC product for Jan. 2005. (b) Average CRE calculated from the ECMWF IWC product for Jan. 2005.

It is interesting to note that the LW CRE derived from the MLS and ECMWF IWC products is

actually significantly larger than the LW CRE derived from CERES measurements. The

principal reason for this is that the impact of underlying liquid clouds, which are not considered

in the LW CRE calculations from MLS and ECMWF, will mitigate the LW CRE caused by ice

clouds. However, the SW CRE is not influenced in the same manner as the LW CRE because the

latter's sensitivity to low clouds arises from the large temperature contrast between ice clouds and

surface emission, while shortwave radiative attenuation by ice clouds is not a strong function of underlying liquid clouds. From these results, it is clear that deriving information about the CRE from MLS IWC data is a difficult task without underlying liquid cloud information. Moreover, efforts to use CERES measurements to provide validation for the MLS IWC product are non-trivial as well.

Nevertheless, it may be possible to utilize integrated cloud-water path measurements from the AMSR-E instrument [*Kawanishi et al.*, 2003] to characterize the amount of ice-water clouds relative to liquid clouds over ocean surfaces. However, this technique will require a circumspect treatment of the two datasets.

6.6   Discussion

This chapter has explored the IWC product from the MLS instrument and how it may be used in a research capacity. The IWC product offers an unprecedented view of cloud ice profiles that can be compared to other conceptions of cloud ice, including that of the ECMWF analysis product. The ECMWF IWC product is consistently lower at all levels as compared with the MLS retrieved values of cloud ice. Corresponding to this discrepancy, there is a significant difference between the calculated CRE for the two IWC datasets. However, calculations of the CRE from the MLS IWC product should be approached cautiously, because it is difficult to account for underlying liquid clouds, especially for determining longwave CRE.

The advent of CloudSat [*Stephens et al.*, 2002] and CALIPSO [*Winker et al.*, 2003], will actively sense for hydrometeors and offer nadir observations of along-track cloud liquid and ice water content profiles. CloudSat in particular may lead to a much better picture, not only of cloud vertical distribution, but also of the contribution to the cloud radiative effect from various cloud types. Significant validation work is required for these active sounders and MLS retrievals

of cloud ice may assist in this endeavor. In the meantime, the MLS IWC product provides a

novel view of cloud ice even though the radiative effects of these clouds require information from

other A-Train datasets.

Chapter Seven. Heating and Cooling Rates from CloudSat.

7.1   Abstract

Determining the level of zero net radiative heating (Q_0^{net}) is critical to understanding parcel trajectory in the Tropical Tropopause Layer (TTL) and associated stratospheric hydration processes. Previous studies of the TTL radiative balance have focused on using radiosonde data, but remote sensing measurements from polar-orbiting satellites may provide the relevant horizontal and vertical information for assessing TTL solar heating and infrared cooling rates, especially across the Pacific Ocean. CloudSat provides considerable vertical information about the distribution of cloud properties relevant to heating rate analysis. The ability of CloudSat measurements and ancillary information to constrain Q_0^{net} is explored. We employ formal error propagation analysis for derived heating rate uncertainty given the CloudSat cloud property retrieval algorithms. Estimation of Q_0^{net} to within approximately 0.5 to 1 km is achievable with CloudSat, but it has a low-altitude bias because the radar is unable to detect thin cirrus. This can be remedied with the proper utilization of CALIPSO lidar backscatter information. Next, we explore the representativeness of non cross-track scanning active sounders in terms of capturing underlying Q_0^{net} distribution utilizing an orbital simulation with the GISS modelE dataset. In order to supplement CloudSat, we explore the ability of AIRS and AMSR-E to constrain Q_0^{net} and find that these passive sounders are useful where the cloud top height does not exceed 7 km. The spatial and temporal distribution of Q_0^{net} derived from CloudSat measurements is presented which, indicate the spatial distribution of this quantity with results that are generally in agreement with previous works.

7.2   Introduction

Stratospheric water vapor has been and continues to be the subject of scientific study due to its strong influence on the earth's radiation budget and its impact on catalytic ozone destruction. The observed values of stratospheric water vapor in the vicinity of the tropical tropopause (e.g., [*Webster et al.*, 1994; *Weinstock et al.*, 1994; *May*, 1998; *Paul et al.*, 2001; *Baer et al.*, 2002; *Vömel et al.*, 2007]) are significantly lower than would be expected from the Clausius-Clapeyron constraint imposed by the mean cold-point tropopause temperature [*Michelsen et al.*, 2000]. Discerning the relative roles of convection and radiation in the determination of the transport of water vapor from the troposphere to the stratosphere and observed trends therein remains an area of active scientific discussion. The tropical tropopause layer (TTL) is of particular importance to this discussion because it is thought to contribute substantially to stratospheric water vapor transport. Because there is very little latent heating above 12 km in the tropics, parcel vertical velocity and radiative heating are closely coupled in the TTL. In this region, net radiative heating is negative at lower altitudes due primarily to water vapor cooling, but is positive at higher altitudes due primarily to ozone heating. In between, there is a level (or levels) of zero net heating (denoted here and by others as Q_0^{NET}) which is the separation level that determines whether uplifted parcels ascend or descend. Determining the altitude of this level and characterizing its spatial and temporal variability are crucial to elucidating the relative strength of the mechanisms that control stratospheric H_2O transport.

The importance of the TTL has been recognized for some time as a mechanism for stratospheric control [*Holton et al.*, 1995] and was described in detail by *Highwood and Hoskins*, [1998] which qualitatively discussed the roles of convection and diabatic heating in determining stratosphere/troposphere transport. Subsequent work has focused on providing a detailed quantitative description of these and other possible processes. *Holton and Gettelman*, [2001] proposed that horizontal transport in the TTL, facilitated by long particle residence times, is

responsible for the observed excessive dehydration, and that the tropical Western Pacific Ocean exerts a disproportionate impact on this dehydration. However, *Sherwood and Dessler* [2001] presented a model that favored convection as a description of TTL H_2O transport. Later, *Sherwood et al*. [2003] found that active convection is a very significant process for governing parcel dehydration and the altitude and temperature of the tropical cold point tropopause.

Given the importance of radiative heating rates towards ultimately determining whether a parcel ascends or descends, several authors have analyzed heating rates from several different perspectives. The importance of radiative heating in the TTL and the differential heating associated with varying cloud configurations were described by *Hartmann et al*. [2001]. This work found that the vertical distribution of clouds may be key to the explanation of the observed stratospheric dehydration because the radiative influence of a cirrus cloud layer is dependent upon the convective cloud top height. The actual determination of Q_0^{NET} is a non-trivial process that has only recently been explored from a process perspective. *Gettelman et al*. [2004] broached the importance of a detailed evaluation of radiation balance in the TTL and used temperature and water vapor profiles from radiosondes to do so. This work found that Q_0^{NET} varied by about 500 meters from measurement to measurement. Additionally, *Corti et al*. [2005] determined vertical mass flux in the tropics from radiative heating rate calculations and found that it is a strong function of cloud cover. This paper, however, found that the transition from radiative cooling to heating occurs at lower altitudes where clouds are present, as compared to clear-sky cases, thereby contradicting the results of previous studies. Further work by *Gettelman and Birner* [2007] began the process of comparing TTL climatology and variability as determined through radiosonde observations with circulation model representation of TTL processes. They found that the large-scale mean state and variability of the TTL are well represented by the models despite heavily-parameterized cloud processes.

Heating rate profiles have also been determined at the Atmospheric Radiation Measurement (ARM) program's Tropical Western Pacific sites [*Stokes and Schwartz,* 1994]

using a combination of radiosonde and millimeter-wavelength cloud radar data [*McFarlane et al.*, 2007; *Mather et al.*, 2007]. The results were compared with those produced by the Community Atmosphere Model (CAM) model and it was found that CAM models capture some, but not all, of the heating rate variability. Also, *Fueglistaler and Fu* [2006] used European Centre for Medium-Range Weather Forecasting 40-year reanalysis (ECMWF ERA-40) trajectory analysis to understand the processes that control stratospheric water vapor variability and found reasonable agreement with assessments from satellite-based measurements. *Norton* [2001] analyzed longwave heating in the tropical lower stratosphere using ECMWF analyses. This work found that ozone IR heating displayed a high degree of variability and was anti-correlated with tropospheric cooling rates, suggesting the importance of upper-tropospheric clouds in governing heating rates near the TTL.

Most of the previous heating rate analyses have focused on utilizing radiosonde data or other limited spatial scale data to determine TTL properties, but satellite-based remote sensing measurements, if properly utilized, can introduce a much more-detailed spatial analysis of those quantities which are ultimately necessary for characterization of the Q_0^{NET} level. The availability of a new and unprecedented set of measurements from the NASA Earth Observing System A-Train Constellation [*Asrar and Dozier*, 1994], including AIRS [*Aumann et al.*, 2003] and CloudSat [*Stephens et al.*, 2002] may be able to reduce uncertainties in the determination of this level and provide a more spatially detailed analysis of TTL radiation balance. However, this approach will only be successful if the remote sensing measurements are evaluated within a retrieval framework that captures the true horizontal, vertical, and temporal variability in the TTL radiative balance.

In order to address the feasibility of applying remote sensing measurements to analyze the TTL radiation balance, we first present a description of several CloudSat products and discuss the estimation of their uncertainties. Next, determination of Q_0^{NET} from CloudSat and CALIPSO products is discussed, and the spatio-temporal distribution of Q_0^{NET} values derived from data

covering July 2006 to July 2007 is presented. Subsequently, the ability of passive sounding data

to constrain Q_0^{NET} is explored. Finally, orbital simulation experiments are performed to test the

representativeness of simulated along-track Q_0^{NET} sampling from CloudSat.

7.3   CloudSat Heating Rates

As part of the NASA Earth Observing System A-Train, the CloudSat satellite is a polar-

orbiting, sun-synchronous platform on which the CloudSat Profiling Radar measures along-track

radar reflectivity at 94 GHz with a minimum sensitivity of -31 dBz (see [*Meneghini and Kozu*,

1990] for an introductory discussion of space-borne cloud radar). Partial attenuation by

hydrometeors at this frequency allows for the characterization of cloud vertical distribution over a

broad range of observed cloud systems. Several mission products are derived from the radar

reflectivity at 240 meter vertical resolution and are directly relevant to a TTL radiative

heating/cooling analysis. The 2B-CWC-RO product, for example, contains cloud water content

profiles, and the 2B-FLXHR product provides radiative fluxes and heating rates consistent with

these water contents. However, due to potential uncertainties in these products, their nature must

be explored in the context of their ability to constrain radiative heating rates in the TTL.

The algorithms for generating 2B-CWC ice and liquid cloud products from radar

reflectivity measurements are described by *Austin* [2007] and are based on the works of *Benedetti*

et al. [2003] and *Austin et al*. [2001], respectively. Here, we make use of Release 04 of the radar-

only retrievals which only utilize radar reflectivity measurements and *a priori* data (refer to

http://www.cloudsat.cira.colostate.edu for details). The retrieval algorithm assumes that cloud

droplet distributions can be reasonably parameterized with a lognormal size distribution so that

droplet number count, effective radius, and geometric standard deviation are the 3 retrieval

targets. The retrieval also assumes that cloud droplets are sufficiently small so that they can be

effectively treated as Rayleigh scatterers, though this assumption is valid only for non-precipitating scenes. The cloud phase is determined by using ECMWF analysis information [*Rabier et al.*, 1998] for the observed scene, including temperature, water vapor, and ozone profiles. For those vertical bins when the temperature is less than -20 °C, ice cloud properties are retrieved, whereas for temperatures exceeding 0 °C, liquid cloud properties are retrieved. In between, both liquid and ice cloud properties are retrieved separately with scaling factors for the two phases which are a linear function of the temperature such that vertical bins at the upper altitudes of the transition zone are mostly ice and those at the lower altitudes are mostly liquid.

Optimal estimation theory [*Rodgers*, 2000] is employed to balance *a priori* knowledge of droplet number and effective radius profiles with that partially described by the measurements through a forward model. Empirical relationships between cloud water content, cloud effective radius, and geometric standard deviation as a function of temperature and pressure from aircraft campaigns are used as *a priori* constraints (e.g., [*McFarquhar and Heymsfield*, 1997]).

The current algorithm for generating fluxes and heating rates at 240 meter vertical resolution from CloudSat measurements and other ancillary products is described by *L'Ecuyer et al.* [2008]. Briefly: temperature, water vapor, ozone, cloud water content, and cloud effective radius profiles form the inputs to a broadband, two-stream, plane-parallel, doubling-adding radiative transfer model. Six shortwave and 12 longwave bands are utilized to produce net shortwave (0.2 to 4 μm) and longwave (4.55 to ∞ μm) fluxes and heating rates using a δ-Eddington and constant hemispheric approximation respectively. The subsequent analysis also makes use of an experimental fluxes and heating rate product derived from the combination of CloudSat and CALIPSO measurements. This new algorithm, that will likely form the basis of a new CloudSat 2B-FLXHR-LIDAR product in the near future, operates identically to the 2B-FLXHR approach, but the revised product also makes use of the CALIPSO vertical feature mask through CloudSat's GEOPROF-LIDAR product [*Mace*, 2007; *Marchand et al.*, 2007] to fill in thin high clouds and low clouds missed by CloudSat. The GEOPROF-LIDAR product is used to

define scenes where CloudSat misses high clouds. The raw CALIPSO backscatter observations are then used to determine the integrated optical depth of these clouds and their extinction using the molecular scattering above and below the cloud. This should fall off exponentially with height in the absence of a cloud. The extinction associated with the high clouds that CloudSat does not detect is generally independent of height, latitude, and season, and a representative effective radius (30 μm) and the mean ice water path (0.004 g/m^3) are assumed based on extinction observations from lidar data collected from the Canadian Network for the Detection of Atmospheric Change (http://www.candac.ca). While this approach is clearly approximate in nature, heating rate calculations derived in this manner should statistically capture the impact of these thin clouds quite well to first order (see [*Kay et al.*, 2008] for more details).

Parcels in the TTL experience a range of shortwave heating throughout the day which is a strong function of the incident solar zenith angle. Therefore, it is important to correct the shortwave heating rates produced by the CloudSat 2B-FLXHR and 2B-FLXHR-LIDAR products. For ascending track (daytime) measurements, the shortwave heating rates are calculated at approximately 1:30 pm local solar time. To account for diurnal variations, including no night-time heating, shortwave heating rates at all levels are multiplied by a correction factor of 0.39, which we determined yield diurnally averaged heating rates to within 5%.

It should be noted that some of the heating rate analysis and associated sensitivity tests presented in this paper do not directly utilize the radiative transfer code used to calculate the 2B-FLXHR. Rather, we use a slightly more-refined broadband radiative transfer model: RRTM [*Mlawer et al.*, 1997; *Clough et al.*, 2005]. The differences between the two codes are noticeable in some vertical regions. The codes utilize different water vapor continua models, which affect boundary layer longwave cooling: the 2B-FLXHR algorithm used CKD 2.1 [*Clough et al.*, 1989] whereas RRTM uses MT_CKD 1.0 [*Clough et al.*, 2005]. Also, different treatment of intermediate strength bands and overlap lead to discrepancies in heating and cooling rates in the middle stratosphere. In the mid-troposphere and upper troposphere lower stratosphere (UTLS)

regions, differences generally arise from the 2B-FLXHR treatment of cloud optical properties as grey. This stands in contrast to the treatment in RRTM which employs a wavelength-dependent parameterization for liquid clouds described by *Hu and Stamnes* [1993] and for ice clouds by *Fu et al.* [1997]. Potential differences in cloud overlap treatment do not have to be considered here because the CloudSat field-of-view is small enough that the overcast approximation is sufficient. Given the wide range of scenes examined here, differences in radiative transfer implementation are not expected to significantly alter the general conclusions reported below.

The current algorithm used to create CloudSat 2B-FLXHR products does not include error estimates on fluxes and heating rate products, though this can be accomplished through formal error propagation analysis [*Taylor et al.*, 1994; *Feldman et al.*, 2008]. Assuming that the variables relevant to heating rate calculations can be modeled as Gaussian, the uncertainty in the cooling rate profile is given by the following:

$$[\Delta\theta'(z)] = \sqrt{\sum_{i=1}^{n}\sum_{j=1}^{n}\frac{\partial\theta'(z)}{\partial x_i}\frac{\partial\theta'(z)}{\partial x_j}\text{cov}(x_i, x_j)} \qquad (7.1)$$

where $(x_1, \ldots x_i, \ldots x_j, \ldots, x_n)$ represent all of the atmospheric state inputs that are relevant to cooling rate profile calculations at each level, $\theta'(z)$ refers to the broadband cooling rate at height z, and cov refers to the covariance function. The relevant atmospheric state inputs include the T, H_2O, and O_3 profiles and the cloud water content and effective radius profiles. The T, H_2O, and O_3 profiles from the ECMWF analysis data are used in the 2B-FLXHR without error estimates, but it can be reasonably assumed that these data products will have difficulty estimating temperature to better than 1 K and water vapor and ozone to better than 10% vmr at each vertical bin. No information is provided to constrain the covariance of the T, H_2O, and O_3 profiles so that, especially under clear conditions, it may be necessary to calculate error bars assuming strong positive, zero, and strong negative covariance between different values of T, H_2O, and O_3 at different altitudes. Where clouds are present, heating rates are significantly

affected in those parts of the profile covered by clouds. Consequently, the uncertainties in cloud water content and cloud effective radius profiles retrieved from CloudSat generally dominate the error budget.

Shortwave and longwave heating rate uncertainties are estimated separately, and the net heating rate uncertainty is derived by combining the two uncertainty calculations using the following formula:

$$\Delta\theta'_{NET}(z) = \sqrt{(\Delta\theta'_{SW}(z))^2 + (\Delta\theta'_{LW}(z))^2} \qquad (7.2)$$

where $\Delta\theta'_{SW}(z)$ is the uncertainty in shortwave heating, $\Delta\theta'_{LW}(z)$ is the uncertainty in longwave cooling, and $\Delta\theta'_{NET}(z)$ is the uncertainty in the net heating. Given that the 2B-CWC-RO products regularly report uncertainties of 50% for cloud water content and cloud effective radius, the error estimate of in-cloud heating rates will be on the order of 50% of the calculated heating rate. In-cloud flux measurements in the course of validation experiments may be useful to govern the development of future CloudSat processing algorithms of 2B-FLXHR products. Figure 7.1a shows sample longwave cooling, shortwave heating, and net heating rate profiles produced by CloudSat through the 2B-FLXHR product, along with estimates of the uncertainty associated with these products based on temperature uncertainty of 1 K at each level and water vapor and ozone uncertainty of 10% of the volume mixing ratio at each level under clear-sky conditions. Figure 7.1b shows the same heating and cooling rate profiles where clouds are present and the estimated uncertainty is strongly affected by the reported CWC uncertainty at each level.

In order to provide a first-order check on the CloudSat 2B-FLXHR products, we perform a comparison between net heating rates produced from remote sensing analysis and those derived from comprehensive ground-based data at the Manus Island Tropical Western Pacific ARM site.
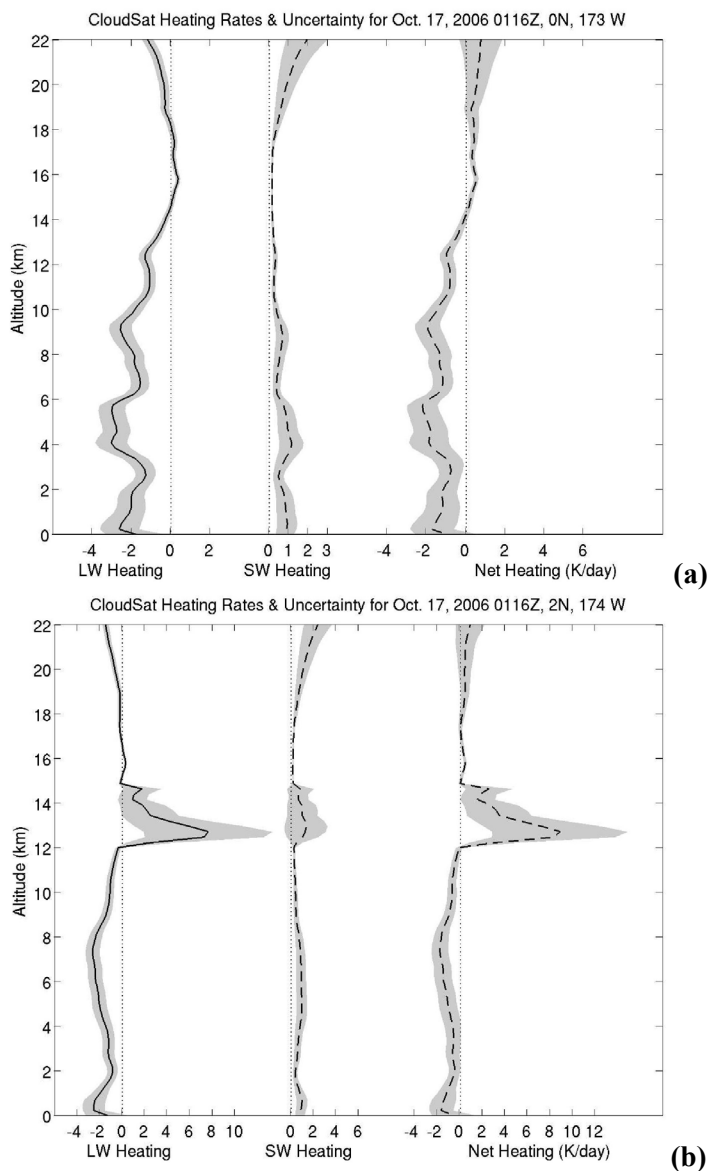
Figure 7.1:(a) Clear-sky longwave, shortwave, and net radiative heating rate profiles from the 2B-FLXHR product for the sample granule on Oct. 17, 2006 at 0116Z at 0N and 173W. Shaded gray indicates uncertainty estimate based on approximate ECMWF uncertainty estimates in T, H_2O, and O_3 profiles. (b) Same as (a) but for profile at 2N and 174W with a cirrus layer of cloud water path $\approx$ 15 g/m^2 at 14–16 km with cloud water content uncertainty from 2B-CWC-RO data.

Mcfarlane et al. [2007] present a comprehensive description of observed heating rates at the

Manus Island site (147.4 E, 2.0 S). Figure 7.2a shows the occurrence frequency of net heating

rate profiles in the vicinity of Manus Island from the CloudSat 2B-FLXHR product for July 2006

to July 2007. The color indicates occurrence frequency and the dashed black line shows the mean

net radiative heating rate profile. In the lower and middle troposphere, net heating rates are

strongly affected by the presence of clouds, and the probability distribution function (PDF) of net heating departs substantially from Gaussian. In fact, Figure 7.2a does not plot the net heating values that occur less than 1% of the time at a given altitude, yet these values clearly affect mean net heating between 6 and 13 km. In the upper troposphere, net heating rates are less affected by clouds and exhibit behavior that is qualitatively Gaussian.
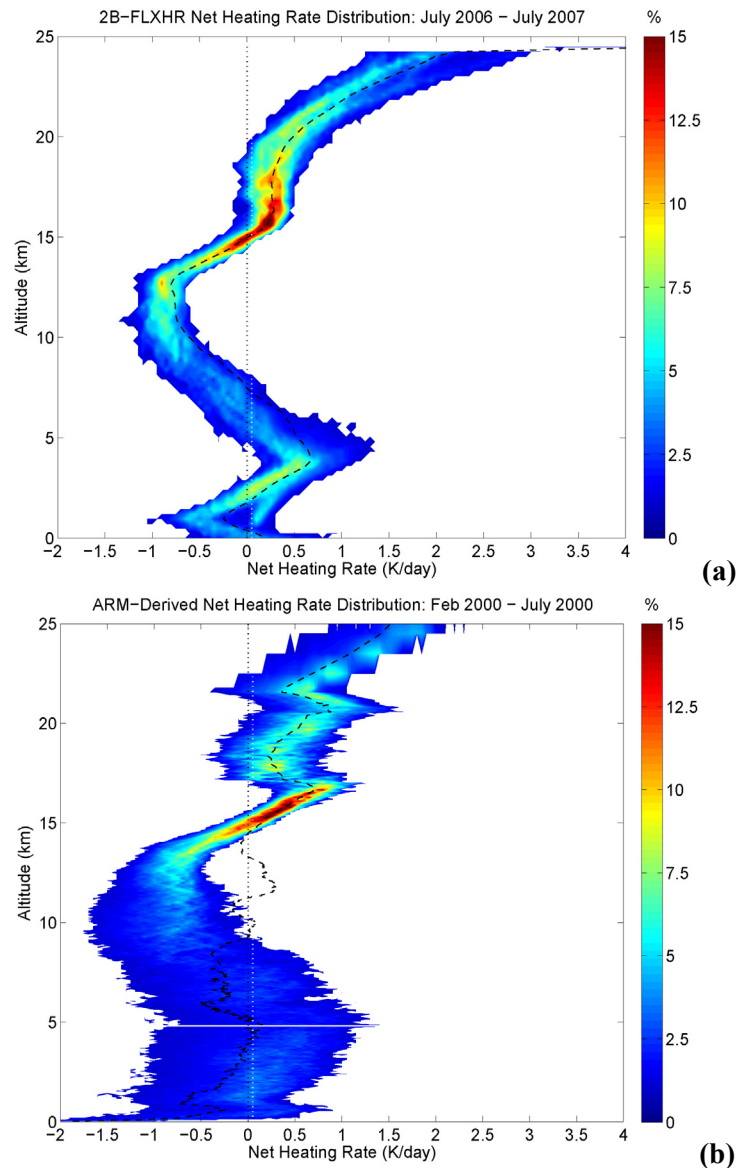
Figure 7.2: (a) Net heating rate profile frequency distribution derived from ascending (daytime) granules of CloudSat 2B-FLXHR data in the vicinity of Manus Island (the geographic region from 3S to 0N and 145E to 147 E) for July 2006 to July 2007 from 84 overpasses. Net heating rate values that occur with less than 1% frequency are excluded from the plot. Dashed black line indicates mean heating rate profile.

Figure 7.2b shows the same net heating rate distribution plot as determined by the methods described in *McFarlane et al.* [2007] from ground-based observations at the Manus Island site of the ARM program [*Stokes et al.*, 1994] for several months in 2000. This comparison is approximate and there are many caveats to the determination of heating rates from millimeter-wavelength radar returns, which are outlined in *Mather et al.* [2007]. Also, the comparison of ground- and satellite-based cloud radar measurements must be approached carefully. Nevertheless, the figure serves to show that particularly in the upper troposphere, the patterns of net heating rates derived from two disparate datasets show agreement.

7.4   Determination of Zero Net Heating

In the TTL, there is a transition from net radiative cooling to net radiative heating with increasing altitude, and Q_0^{NET} is located at a height of approximately 15 km. Because convective clouds rarely ascend into the TTL, heating rates generally change slowly with altitude at a rate of 0.1 K/day/km from around -0.5 K/day at the lower level of the TTL to around 0.2 K/day at the cold-point tropopause, which is approx. 2.5 km above the Q_0^{NET} level.

There are several atmospheric state quantities that contribute to the location of the Q_0^{NET} level. First, although water vapor dominates radiative cooling in the upper troposphere, H_2O emission efficiency decreases substantially above 13 km. Water vapor contributes to essentially all of the IR cooling in the TTL (CO_2 and O_3 produce IR heating), though water vapor variability contributes to only about 50% of net IR TTL heating variability. Second, the vertical temperature structure affects cooling from the CO_2 ν_2 band, while the O_3 profile details are important both for solar heating and IR cooling. Third, solar heating of CO_2, O_3, and H_2O is largely a function of zenith angle with higher zenith angles (maximum daily insolation) leading to lower Q_0^{NET} levels. Fourth, the presence of underlying clouds can impact Q_0^{NET} in many different ways, primarily by

modulating the CO_2 and O_3 infrared heating, and secondarily by affecting H_2O rotational band emission. Q_0^{NET} is affected by changes in shortwave heating arising from reflection from underlying cloud layers, but this effect is a second-order correction. Finally, where present, a cirrus layer in the TTL with underlying convective cloud-top height below 12 km will lead to net radiative heating while the same cirrus layer with a higher convective cloud-top height will have a net radiative cooling.

A typical clear-sky net radiative heating rate profile has radiative cooling due to water vapor in the lower and middle troposphere which transitions in the upper troposphere and stratosphere to radiative heating due to ozone. The transition region is often marked by a large number of oscillations in net heating about the zero line due to gravity waves. Meanwhile a typical cloudy-sky net radiative heating rate profile differs from the clear-sky case in that there is large radiative heating at the base and within clouds and strong cooling at the cloud top. Moreover, the presence of an underlying cloud slightly decreases the efficacy of cooling by water vapor in the upper troposphere and significantly decreases IR heating by ozone in the tropopause and lower stratosphere. Due to the latter effect, the Q_0^{NET} level is raised by a few kilometers by the presence of a cloud. The determination of the Q_0^{NET} level can be ambiguous given the number of oscillations in net heating near the zero-heating level. Nevertheless, the presence of clouds unambiguously diminishes the infrared heating from O_3, thereby leading to increased cooling at all layers between the cloud top and the level middle stratosphere.

The determination of the Q_0^{NET} level first requires a net heating rate profile. With this, we determine the Q_0^{NET} level as follows: beginning at 25 km, we test lower-altitude layers to find a layer where net radiative heating begins to increase. If the net heating associated with this layer is positive, then this layer is taken to represent the top of a heating rate oscillation. If the net heating associated with the layer is negative, the layer is selected as the bottom layer for Q_0^{NET} determination. A linear interpolation is performed to find the zero net heating level between the upper and lower levels of the net heating oscillation. Uncertainty in Q_0^{NET} determination for an

individual profile is assessed by adding one standard deviation to the net heating rate profile and recalculating Q_0^{NET}, and then doing the same after subtracting one standard deviation from the net heating rate profile. This process tends to overestimate the uncertainty in the Q_0^{NET} level but is practical and computationally-efficient.


(a)

(b)
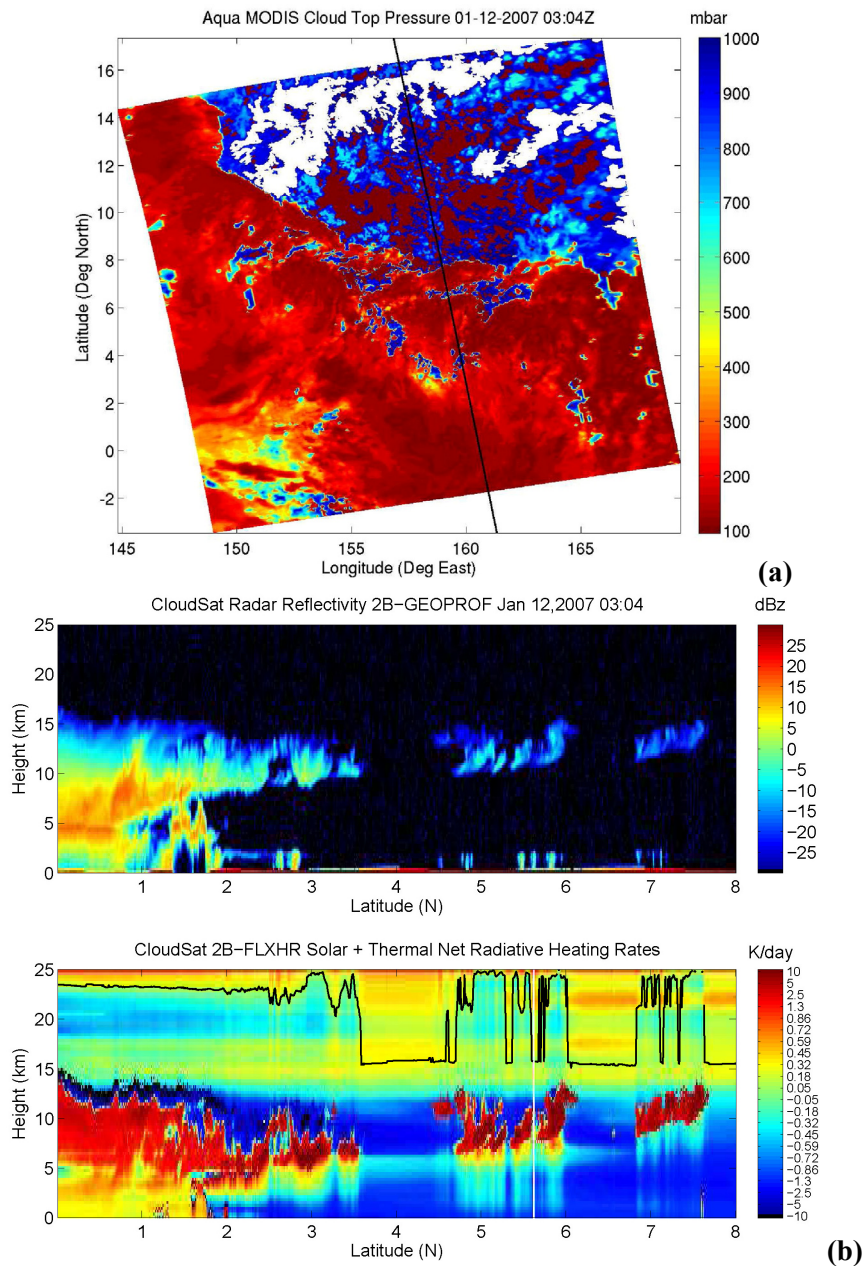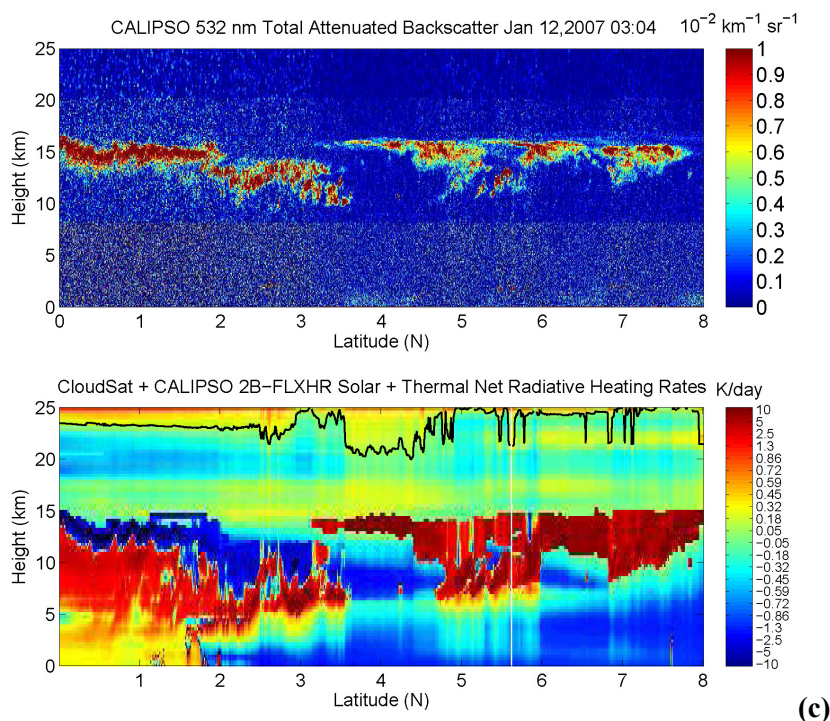
Figure 7.3: (a) MODIS Cloud Top Temperature granule for Jan. 12, 2007, at 0304Z from 0 to 10N and 145 to 165E with black line denoting ground footprint of the CloudSat and CALIPSO instruments. (b) Top-panel: CloudSat 2B-GEOPROF radar reflectivity for the curtain corresponding to the scene shown in (a). Bottom panel: diurnally-averaged net radiative heating rate profile curtains derived from the CloudSat 2B-FLXHR product. The overlaid black line indicates the estimation of the Q_0^{NET} level. (c) Top-panel: CALIPSO 532 nm total attenuated backscatter curtains corresponding to the scene shown in (a). Bottom panel: estimated diurnally-averaged net radiative heating rate profile curtains from the CloudSat 2B-FLXHR-LIDAR product. The overlaid black line indicates the estimation of the Q_0^{NET} level.

Figure 7.3a–c illustrates the along-track variability in Q_0^{NET} as determined by CloudSat. For reference purposes, Figure 7.3a shows the Cloud Top Height product from MODIS [*Platnick et al.*, 2003] with an overlay of the CloudSat and CALIPSO field-of-view. Figure 7.3b contains two panels: the top panel shows the CloudSat Radar Reflectivity for a sample granule from Jan. 12, 2007, at 0304Z. The bottom panel in Figure 7.3b shows the 2B-FLXHR net heating rate profiles for the granule.

There are a few missing profiles because the processing algorithm currently does not produce heating rate profiles where the CWC product contains null retrieval values. Nevertheless, where there are data, it can be seen that clouds affect net heating rate profiles: at the

base of a cloud deck, net radiative heating occurs, while significant net cooling occurs at cloud tops. Also, the panel shows the estimated location of Q_0^{NET}, which exhibits small variations from T, H_2O, and O_3 along-track variability but is dramatically elevated by the presence of clouds. Since CloudSat is unable to detect thin cirrus clouds, it is likely that measurements from this instrument will underestimate the Q_0^{NET} level. Merged CloudSat and CALIPSO cloud water content products will allow for TTL heating rate analysis with less systematic bias. Figure 7.3c shows similar curtains as Figure 7.3b but utilizes extra information provided by the CALIPSO instrument. The top panel shows CALIPSO's 532-nm total attenuated backscatter of the scene described in Figure 7.3b. Whereas the lidar measurements are sensitive to thin clouds, the measurements are unable to describe cloud vertical profiles for thick clouds. The bottom panel displays the 2B-FLXHR-LIDAR product for the scene. The ability to detect thin cirrus clouds clearly leads to increased upper-tropospheric heating and a higher Q_0^{NET} level.

Both Figures 7.3b and 7.3c depict the estimated altitude of the Q_0^{NET} level with a black line in the lower panel. For those scenes where CloudSat detects clouds, the two estimates of the Q_0^{NET} level are similar, but they differ substantially where CloudSat determines a clear-sky scene while CALIPSO detects overlying thin cirrus clouds.

It is necessary to address how well CloudSat observations and ancillary data constrain understanding of the Q_0^{NET} level. Figure 7.1a shows that given assumptions about the uncertainty in ECMWF analysis products, we find that clear-sky net heating can be known to within 0.1 K/day. Figure 7.4a shows the same plot as Figure 7.1a, focusing on the TTL and indicates that, for clear-sky conditions, the estimated uncertainty in the auxiliary ECMWF analysis fields produces a Q_0^{NET} level uncertainty of approximately ±0.3 km. The presence of a cloud, as seen in Figure 7.4b, significantly raises the Q_0^{NET} level to approximately 17.5 km. The cloud has also expanded the uncertainty in the Q_0^{NET} level to approximately ±0.5 km.
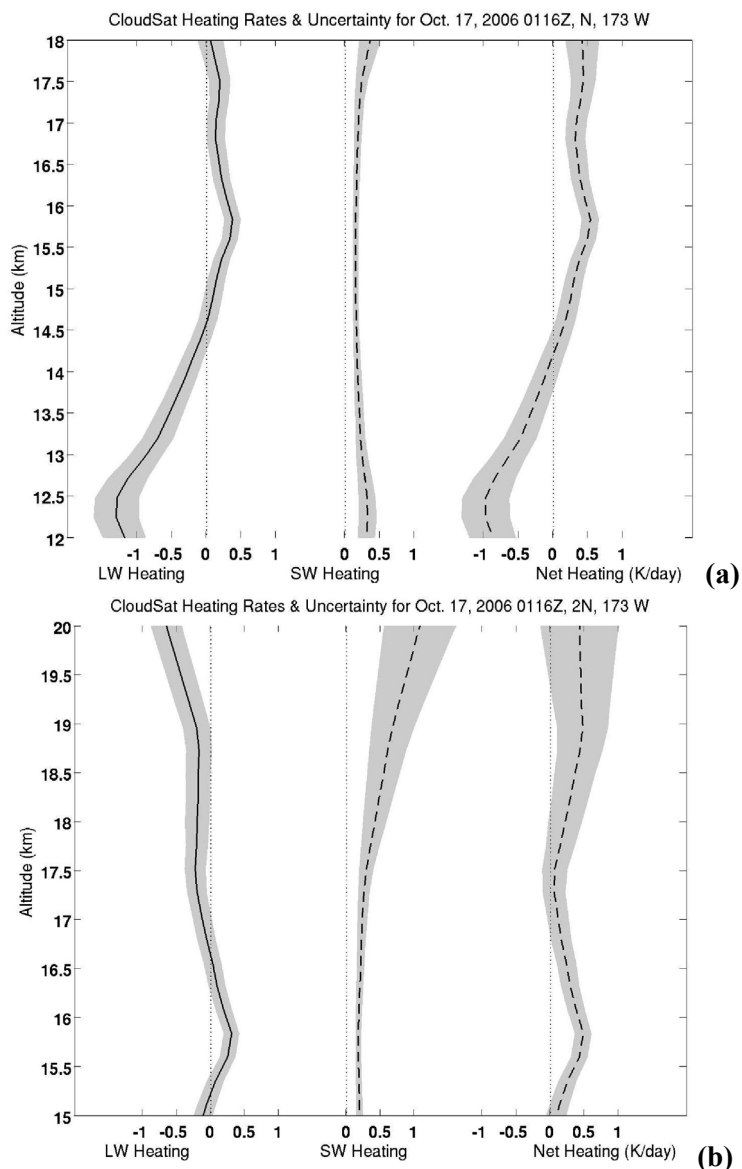
Figure 7.4: (a) Clear-sky longwave, shortwave, and net radiative heating rate profiles from the 2B-FLXHR product for the sample granule on Oct. 17, 2006, at 0116Z at 0N and 173W. Shaded gray indicates uncertainty estimate based on approximate ECMWF uncertainty estimates in T, H_2O, and O_3 profiles, and the Q_0^{NET} level is 14.5±0.3 km. (b) Same as (a) but for profile at 2N and 174W with a cirrus layer of cloud water path $\approx$ 15 g/m^2 at 14–16 km with cloud water content uncertainty from 2B-CWC-RO data. The Q_0^{NET} level is 17.5±0.5 km.

There is significant uncertainty associated with the retrieval of CWC profiles and consequently of net heating rate profiles in the vicinity of clouds. We seek to address the importance of CWC profile uncertainties in the determination of the Q_0^{NET} level. We assume that

the uncertainty in CWC is a constant percentage of the total CWC retrieval value for each layer.

Then, we vary the CWC value and determine the corresponding variance in the Q_0^{NET} level.
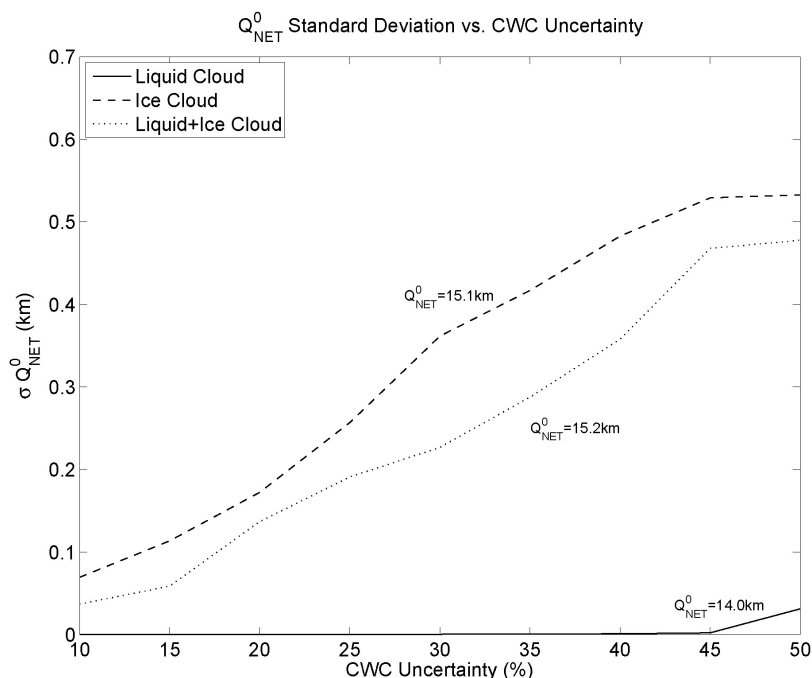
Figure 7.5: Standard deviation of Q_0^{NET} level as a function of cloud water content uncertainty for scenarios with an ice cloud from 10–12 km with R_e = 41.5 μm and IWC = 4.8 mg/m³, a liquid cloud 4–5 km with R_e = 6.2 μm and LWC=280 mg/m³, and a scenario with both such liquid and ice clouds overlapping.

Figure 7.5 shows the uncertainty in the Q_0^{NET} level as a function of the uncertainty in

CWC profiles for three different scenarios with an underlying Tropical Model Atmosphere: a 1-

km-thick liquid cloud spanning 4-5 km, a 2 km thick ice cloud spanning 10-12 km, and a 1-km-

thick liquid cloud spanning 4–5 km underlying a 2-km-thick ice cloud spanning 10–12 km. Even

with significant uncertainty in the liquid and ice water content values retrieved from CloudSat

measurements, the CWC approximation only contributes to an uncertainty in the Q_0^{NET} level of

approximately 0.5 km. Therefore, it is reasonable to conclude that the specification of cloud

profile information from CloudSat, even with large CWC retrieval uncertainty, is useful for

determining the Q_0^{NET} level.

7.5   Use of Passive Sounders

Given the wealth of instrumentation in the A-Train, it may be possible to supplement along-track information pertaining to Q_0^{NET} distribution from active sounders with cross-track information from passive sounders. For example, AIRS is a hyperspectral thermal IR sounder and AMSR-E [*Kawanishi et al.*, 2003] is a 6-channel passive microwave sounder. Both instruments reside aboard the polar-orbiting Aqua platform, which flies in close formation with the CloudSat platform. These instruments have nearly collocated ground footprints that have recorded measurements since mid-2002 with a retrieved-product spatial resolution of 45 km. Retrieval products from AIRS include T, H_2O, and O_3 profiles in addition to information on cloud top height (CTH). AMSR-E data processing algorithms generate a cloud water path (CWP) product over ocean scenes (i.e., *Huang et al.* [2006]). These standard L2 and L3 products may be utilized to derive information about the heating/cooling rate profile in most scenes. Although CloudSat and CALIPSO provide much greater vertical information, they are limited to nadir sounding with very limited pointing capability.

The issue of whether Q_0^{NET} can be determined adequately despite *a posteriori* uncertainties in T, H_2O, and O_3 profiles and, more importantly, the conspicuous lack of vertical cloud information needs to be addressed. The upper-bound on the contribution of clouds to Q_0^{NET} uncertainty can be determined by varying cloud water content distribution according to CTH and CWP constraints, while T,H_2O and O_3 errors can be incorporated according to section (2). For different CTH and CWP values, which can be well constrained by AIRS/AMSR-E jointly, we test to see the range in possible Q_0^{NET} associated with different cloud height distributions through Monte Carlo sampling using a Tropical Model Atmosphere. As seen in Figure 7.6, where CTH is less than 7 km, the specification of CWP and CTH is sufficient to constrain Q_0^{NET} to within

several hundred meters. Where CTH is greater than 7 km, further knowledge about the cloud

vertical distribution is necessary, except for cases with cloud water path is less than 0.2 kg/m^2.
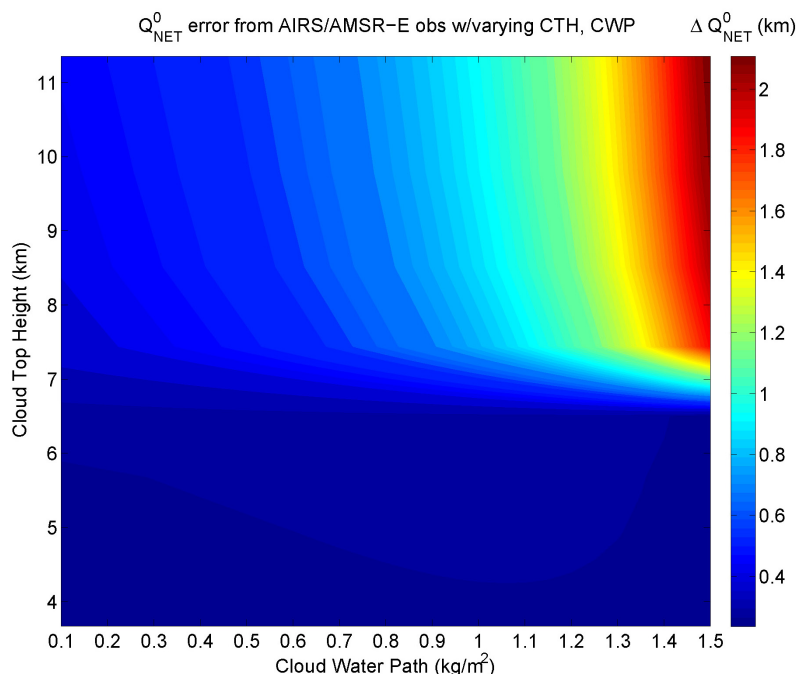
Figure 7.6: Uncertainty in Q_0^{NET} level where CWP and CTH are constrained by AIRS/AMSR-E measurements but vertical details of cloud water content distribution are allowed to vary below the cloud top.

Since there is significant cloud occurrence frequency above 7 km and the variations in

Q_0^{NET} are strongly affected by deep convective clouds, the current suite of passive sounders in the

A-Train are not likely to impart useful information towards understanding the spatial and

temporal distribution of Q_0^{NET}. Moreover, the CWP constraint by AMSR-E measurements is not

viable over land scenes, and this precludes comprehensive Q_0^{NET} spatial analysis.

7.6   Orbital Simulations

CloudSat provides a large amount of information content about heating rate profiles,

though only along its nadir ground track. The ability of CloudSat products to describe the true

two-dimensional distribution of Q_0^{NET} can be explored through orbital simulations. Here,

synthetic data are produced by using GISS modelE fields [*Schmidt et al.*, 2006]. The complete

provision of fields necessary to synthesize Q_0^{NET} maps allows one to test the question of whether

the limited spatial coverage attendant to CloudSat observations is sufficient to reproduce the

original spatial PDF of Q_0^{NET} that can be ascertained from the full dataset.

(a)

(b)
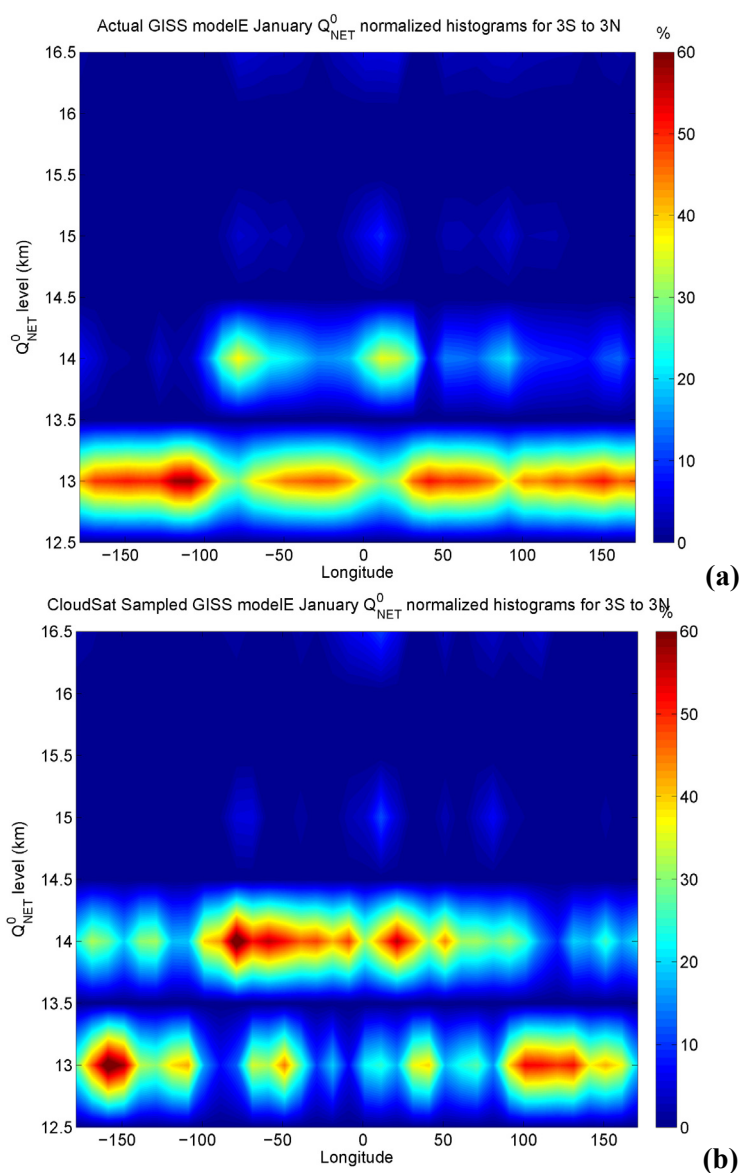
Figure 7.7: (a) Zonal variation in occurrence frequency of Q_0^{NET} level values derived from present-day atmospheric simulations using GISS ModelE data for a climatological January. (b) Same as (a) but data is derived by sub-sampling GISS ModelE fields per the CloudSat sampling pattern.

In order to accomplish the simulation, one month's worth of CloudSat footprints are interpolated to a 2.5 x 2.5 latitude/longitude grid. The data from the model fields corresponding to the nearest satellite footprint are input into a RRTM calculation from which Q_0^{NET} is estimated. The data subset is used to create maps of zonal occurrence frequency distribution of Q_0^{NET}. The distribution derived from the orbital coverage (assuming CloudSat is able to determine Q_0^{NET} perfectly) is compared to the underlying mean and standard deviation in Figure 7.5. These results, as seen in Figure 7.7, demonstrate that, on a monthly time-scale, CloudSat measurements are not quite sufficient for representing the underlying distribution of Q_0^{NET} and its variability, and the effects of under-sampling are apparent in the comparison. However, using 2–3 month datasets does allow for sufficient comparison, which implies that the effective temporal resolution of CloudSat data with respect to this analysis is 2–3 months.

7.7   CloudSat Zero Net Heating Distribution

Given the long residence times of parcels in the TTL (e.g., *Hartmann et al.* [2001]), it is important to characterize the spatial distribution of Q_0^{NET} values, because this distribution may describe which regions are having the most influence on stratospheric hydration. Although CloudSat 2B-FLXHR data has been released covering only 1.5 years, preliminary maps of the zonal Q_0^{NET} occurrence frequency can be produced.

A sample occurrence frequency for a geographic box surrounding Manus Island is shown in Figure 7.8 and indicates that Q_0^{NET} is most likely to be around 16 km. Strong convective events can push the level higher, though it is unlikely to be above 18 km. Figure 7.9 shows the zonal variation in Q_0^{NET} occurrence frequency in an equatorial band with several salient features. First, Q_0^{NET} values are generally higher for this period in the tropical western Pacific Ocean

(TWP), as compared to the tropical eastern Pacific Ocean (TEP), and this result is consistent with

findings of others regarding this level.
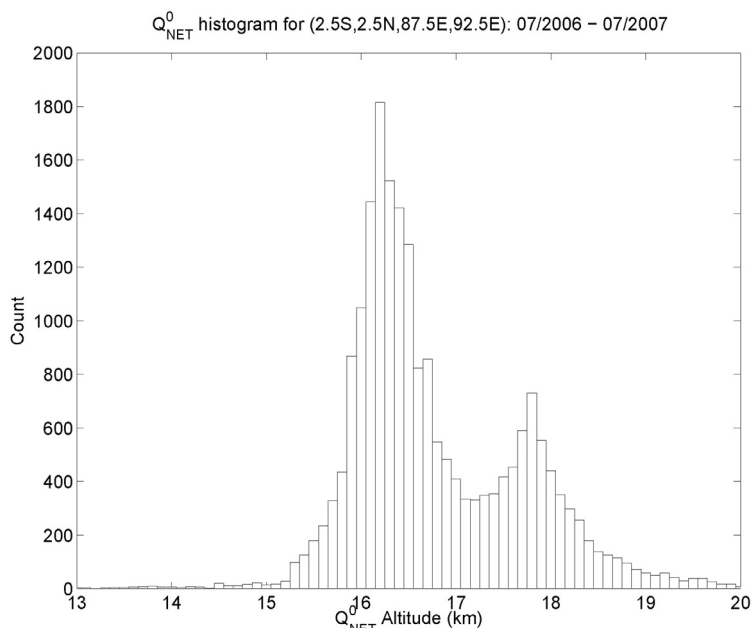
Figure 7.8: Histogram of Q_0^{NET} level values derived from CloudSat 2B-FLXHR products for July 2006 to July 2007 using daytime data in the vicinity of Manus Island (the geographic region from 3S to 0N and 145E to 147 E). The mean Q_0^{NET} value is 16.8 km.
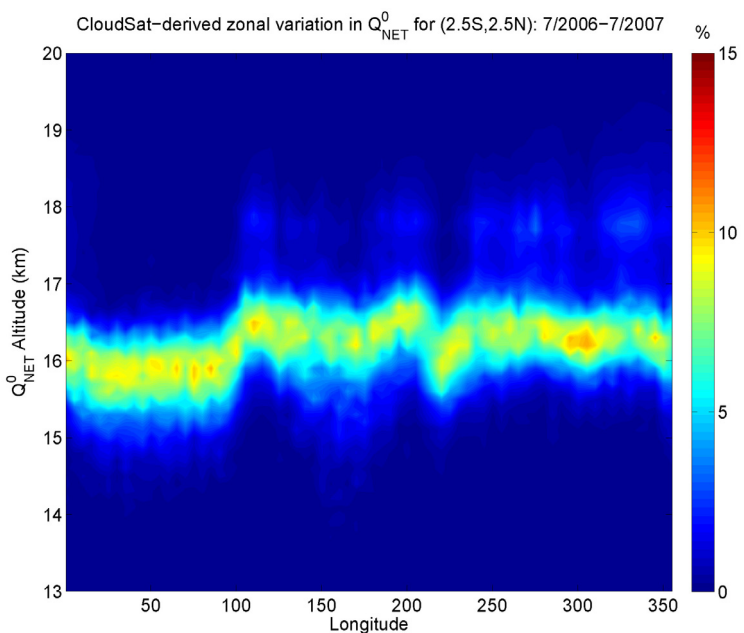

Figure 7.9: Zonal variation in occurrence frequency of Q_0^{NET} level values derived from CloudSat 2B-FLXHR data from July 2006 to July 2007 for 2.5S to 2.5N.

Second, there is a secondary maximum at 18 km specifically in the TWP associated with deep convection which can also be seen in Figure 7.2a. Finally, the distribution of Q_0^{NET} values is slightly broader in the TWP than in the TEP suggesting that strong convective processes are differentially affecting TWP and TEP TTL radiation balance.

Mean and standard deviation Q_0^{NET} maps can also be useful for determining the zonal and meridional variation in this quantity. Figures 7.10a and 7.10b show the spatial distribution of mean Q_0^{NET} values and their standard deviations for December 2006 to February 2007 (DJF), respectively, and the associated variation of these values. Figure 7.10a shows the equivalent results derived from the 2B-FLXHR product, while Figure 7.10b displays the results from the 2B-FLXHR-LIDAR product. At a resolution of 2.5 degrees, the seasonal mean TTL radiation balance derived from the two different datasets are generally in good agreement, although some minor differences are evident, particularly in regions of deep convection where the 2B-FLXHR product tends to underestimate the Q_0^{NET} level. More significantly, differences exist in the estimated standard deviation in Q_0^{NET}, where the 2B-FLXHR-LIDAR data indicate much larger variations throughout the tropics indicative of the greater variability introduced by thin cirrus that are not resolved by CloudSat.

Only some of the spatial and temporal Q_0^{NET} details derived from CloudSat data are described by the radiosonde dataset. Satellite-based remote sensing of TTL radiation balance has significant descriptive power over the equatorial Atlantic Ocean, the Indian Ocean, and the TEP. Still, where collocation occurs, Q_0^{NET} maps derived from CloudSat data agree with those derived from radiosonde observations (i.e., *Gettelman and Forster* [2002]). Ultimately, it is important to incorporate the remote sensing data on heating rates into a model of stratosphere-troposphere exchange to understand how data-driven knowledge of the level of zero radiative heating impacts understanding of the relative importance of different mechanisms for controlling stratosphere-troposphere exchange of water vapor.
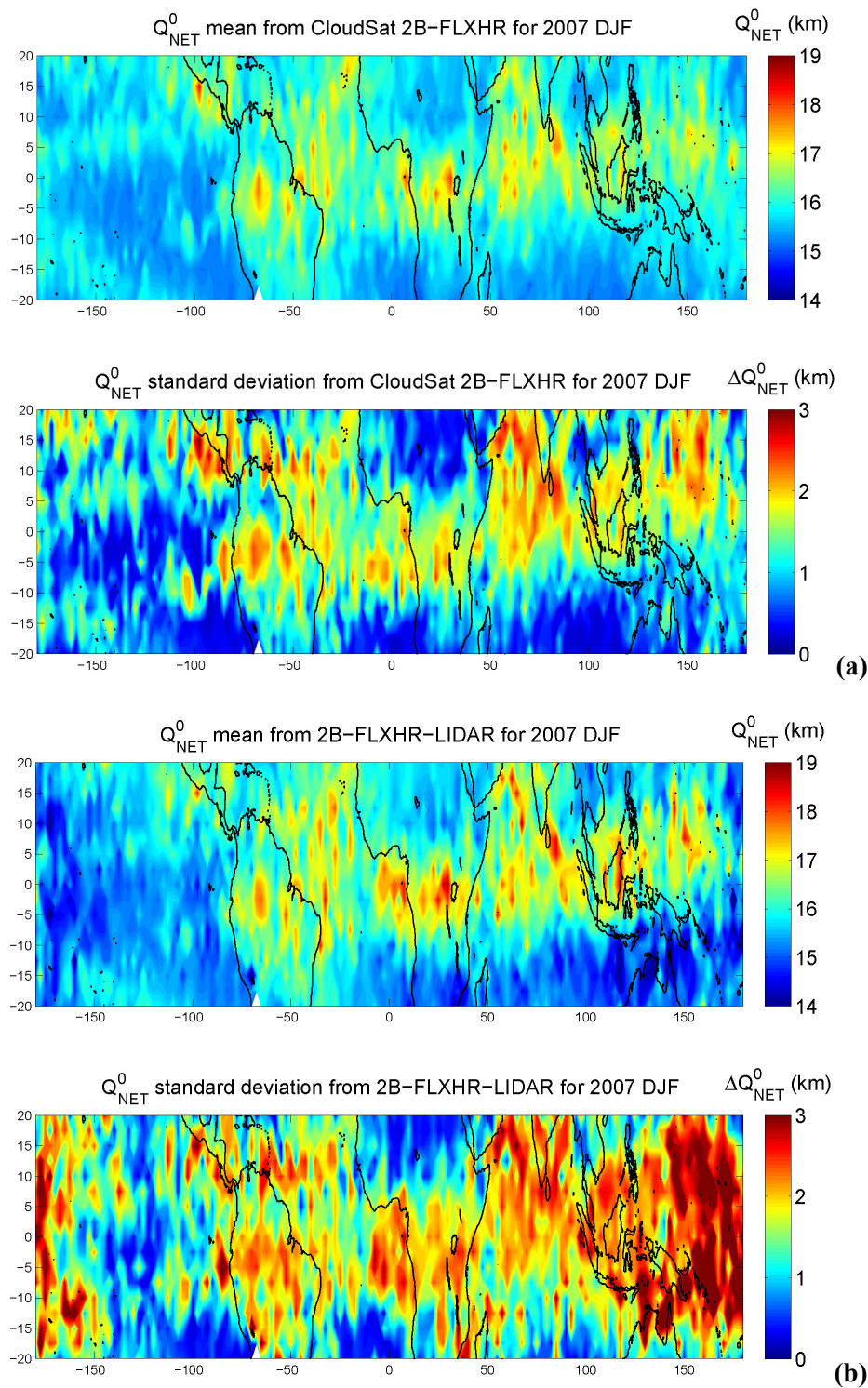
Figure 7.10: Monthly-mean and standard deviation Q_0^{NET} maps at 2.5 x 2.5° resolution derived from CloudSat 2B-FLXHR product results for (a) December 2006 to February 2007. (b) Same plot derived from 2B-FLXHR-LIDAR product results.

7.8   Conclusion

Active sounding of the vertical distribution of clouds from CloudSat introduces significant information for understanding vertical net heating rate profiles. Given ancillary information including temperature, water vapor, and ozone profiles from other instruments or forecast analyses, the spatial distribution of net heating rates can be described to within 0.1 K/day for clear-sky scenes. With CloudSat's retrieval of cloud properties, cloud heating rates are known to within several K/day, though the large uncertainties in the retrieval of cloud water content and effective radius currently renders instantaneous estimates of in-cloud heating rates difficult to resolve.

The longwave and shortwave fluxes and heating rate products have broad application to model-measurement comparisons and can be used directly to analyze the level of zero net radiative heating in the Tropical Tropopause Layer. This Q_0^{NET} level is a dividing line that determines parcel ascent or descent and should be well characterized in the course of discussions of the relative roles of different processes in hydrating the stratosphere. Given that passive remote sensing information can generally constrain the level of zero net heating where the cloud top height is less than 7 km, the introduction of active sounding information is very valuable towards Q_0^{NET} level analysis. We have analyzed one year's worth of CloudSat 2B-FLXHR products and derived information about the spatial and temporal distribution of the Q_0^{NET} level. The Q_0^{NET} differences between the 2B-FLXHR product and the 2B-FLXHR-LIDAR product for December 2006 through February 2007 are minor, and suggest that the usage of the CALIPSO lidar data is most important for the determination of the variability in the Q_0^{NET} level. The results also suggest that the effect of deep convective clouds on the radiative balance of the TTL is significant throughout the tropics. Further analysis will require integration of data-driven heating rate information into TTL models. The continued refinement of the 2B-FLXHR product

(including formal integration of the CALIPSO measurements), along with the increasing data volume will allow for a more thorough characterization of the Q_0^{NET} level.

The CloudSat 2B-FLXHR product contains data-driven heating rates and fluxes which will be scientifically meaningful to the extent that they can be validated. Using surface and top-of-atmosphere broadband flux measurements from CERES [*Wielicki et al.*, 1996] provides a first-order test of validity [*L'Ecuyer et al.*, 2008]. However, it would be useful first to analyze the CloudSat validation experiments (e.g., the CloudSat/CALIPSO Validation Experiment: see http://angler.larc.nasa.gov/ccvex/ for details) in terms of heating rates and fluxes, and second to consider the inclusion of *in situ* flux measurements (e.g., *Asano and Yoshida* [2004], *Mlynczak et al.* [2006a]) in such campaigns. Such data would allow for further CloudSat algorithm development, especially to address in-cloud heating rates, which are presently difficult to characterize with remote sensing measurements.

Chapter Eight. Far-Infrared Measurements.

8.1   Abstract

The far-infrared (15–100 µm) is extremely relevant to Earth's climate and new developments in observing technology hold promise that it will be measured directly and comprehensively from space in the near future. Recently, the Far Infrared Spectroscopy of the Troposphere (FIRST) instrument [*Mlynczak et al*., 2006b] has been built as a prototype FTS recording spectra from 5 to 200 µm. This provides a test-bed for the development of space-based far-infrared measurements in support of climate change monitoring, which is one of the goals of the planned CLimate Absolute Radiance and Refractivity Observatory (CLARREO) mission. We present a comparison of the retrieval capabilities of a notional space-based instrument of comparable performance to FIRST and the currently operational mid-infrared instrument AIRS under clear conditions. Synthetic temperature and water vapor profile retrievals are compared for tropical conditions, along with the relative ability of the retrievals from these two instruments to describe clear-sky cooling rate profiles. The information contained in clear-sky mid-IR spectra is found to be slightly less than that of far-IR spectra. Next, we explore the ability of mid-IR measurements to describe far-IR measurements in the presence of clouds. In general, mid-IR measurements can be used to extrapolate to the far-IR, though an error of several degrees Kelvin may be incurred for scenes where only thin cirrus are present in channels with weighting functions peaking at about two kilometers below the cloud base. Finally, a comparison of collocated spectra from FIRST test flights and several A-Train measurements is presented in the context of future climate monitoring objectives. This comparison indicates that far-infrared measurements are complementary to the other sets of A-Train instrumentation, but the dearth of space-like long-wavelength spectra suggests that more campaigns are warranted for understanding the additional information provided by the spectral region from 15–100 µm.

8.2   Introduction

A very substantial amount of the atmospheric greenhouse effect is accomplished through water vapor absorption in the far-infrared, and liquid and ice clouds significantly impact fluxes and heating rates throughout the atmospheric column. For most scenes, over 50% of outgoing longwave radiation is contained in far-infrared wavelengths. In spite of this, there are few global-scale hyperspectral measurements of this spectral region with the exception of data from the short-lived IRIS-D instrument [*Hanel et al.*, 1971] that measured from 4 to 25 μm. There are several datasets in the EOS A-Train [*Asrar and Dozier*, 1994] that may contain the information to infer processes relevant to far-IR radiative transfer, including high spatial-resolution passive radiometer data from MODIS [*Justice et al.*, 1998], visible/near-IR lidar measurements from CALIPSO [*Winker et al.*, 2003], mid-infrared passive spectra from AIRS [*Aumann et al.*, 2003], microwave passive measurements from AMSR-E [*Kawanishi et al.*, 2003] and MLS [*Waters et al.*, 2006], and active microwave sounding from CloudSat [*Stephens et al.*, 2002]. Meanwhile, the National Research Council Decadal Survey has recently recommended that NASA develop an absolute, spectrally resolved interferometer in support of the CLimate Absolute Radiance and Refractivity Observatory (CLARREO) mission [*Committee on Earth Science and Applications from Space: A Community Assessment and Strategy for the Future*, 2007]. Such an instrument has several requirements, including the measurement of mid-infrared spectra in addition to the measurement of a significant portion of the far-infrared spectrum (wavelengths between 15.4 and 50 μm) at high spectral resolution. Both broad coverage and high-spectral resolution have been deemed necessary mission specifications so that CLARREO can provide a calibration standard for climate change monitoring [*Anderson et al.*, 2004].

In support of future missions, research has been conducted regarding spectroscopic measurements in the far-infrared which will ultimately provide scientific justification for the

CLARREO mission. This research has touched on radiative transfer fundamentals, using FIR measurements to retrieve standard atmospheric state parameters, FIR analysis in the context of energy balance and middle-atmosphere heating rates, and finally instrumentation considerations at long wavelengths.

Far-IR radiative transfer calculations are pertinent to the CLARREO mission but have received less attention than other spectral regions that are currently measured by satellite instruments. Still, *Kratz et al.* [2005] reviewed the performance of several radiative transfer codes in benchmark cases and found radiometric agreement between codes with the same input values. Still, the results depend on line parameters and on which particular water vapor continuum model is used. Since many current radiative transfer codes utilize the MT-CKD model [*Clough et al.*, 2005], there is general agreement for clear-sky radiative transfer calculations. In terms of cloudy-sky radiative transfer, scattering properties of liquid clouds can be adequately described with Mie theory and are parameterized by *Hu and Stamnes* [1993]. *Yang et al.* [2005] published a detailed description of scattering and extinction coefficients and asymmetry parameters for various ice crystal habit distributions using the T-Matrix Method [*Mishchenko and Travis*, 1998]. This produces results with reasonable radiometric accuracy in the mid- and far-infrared.

Standard atmospheric state retrievals have conventionally utilized other spectral regions besides the FIR. However, the FIR may be useful because it contains a description of water vapor and clouds as they relate to fluxes and cooling rates. *Mertens* [2002] investigated the feasibility of retrieving water vapor profiles using far-infrared spectral measurements, and found that typical nadir sounding can have improved vertical resolution and performance using mid- and far-infrared measurements as compared to using mid-infrared measurements alone. For cloudy scenes, *Yang et al.* [2003] explored the spectral signature of cirrus clouds in the far-infrared and found that certain far-infrared channels are differentially sensitive to cloud effective radius and optical depth with a potential for improved performance over the usage of window-band (8–12 μm) channels for cloud characterization. In terms of addressing the error in trace gas retrievals

arising from cloud contamination, *Kulawik et al.* [2006] investigated how well standard retrieval products such as H_2O, O_3, and CO can be retrieved from the TES instrument in the presence of various types of clouds, finding that trace gas retrievals can be stable and well characterized for various types of cloudy scenes.

From a climate perspective, the water vapor feedback effect is dominated by rotational absorption lines in the far infrared, and the extent to which different cloud types modulate this feedback is one of the primary motivations for proposing widespread spectroscopic measurements covering the FIR. For clear-sky conditions, *Sinha and Harries* [1995; 1997] explored the importance of the far-infrared in determining the earth's longwave radiation budget and found that spectroscopic measurements of this spectral region were crucial to interpreting causes of clear-sky OLR variability. However, *Huang et al.* [2006] and *Huang et al.* [2007] found that AIRS mid-IR spectra can be used to diagnose sources of clear-sky OLR variability and differentiate model and measurement output. Also, *Mlynczak et al.* [2002] discussed the importance of far-infrared spectral measurements in the determination of water vapor and cirrus cloud radiative effects, though the extent to which FIR measurements are necessary to determine cloud radiative effect accurately has not been explored formally.

From an instrumentation perspective, far-infrared spectrometers have been developed on several platforms, though not all have been designed in the context of a climate-monitoring satellite mission. *Carli et al.* [1999] developed and successfully tested the Spectroscopy of the Atmosphere Using Far-Infrared Emission/Airborne (SAFIRE-A) instrument with coverage from 40–1000 μm. Also, *Johnson et al.* [1995] built FIRS-2, a limb-viewing, high-resolution far-infrared spectrometer for detecting minor stratospheric constituents. Recently, the Far-Infrared Spectroscopy of the Troposphere (FIRST) instrument [*Mlynczak et al.*, 2002; 2006b] has been developed as a prototype with favorable results from two separate balloon-borne test flights. Lessons learned from the FIRST instrument are directly relevant to the CLARREO mission, and this prototype offers an engineering and science test-bed for future mission development. From

an engineering perspective, the development of a prototype that compares favorably to other well calibrated mid-IR spectra lends confidence to the potential quality of far-IR data from space-based platforms. From a science perspective, the prototype can be flown so that its measurements can coincide with other satellite-based remote sensing data, and the spectral signature of clouds and water vapor in the far-IR can be compared with that in the mid-IR. This allows for a heuristic approach to determining the specific science (and therefore engineering) goals of a far-IR measurement campaign.

This chapter explores potential uses for the FIRST instrument and investigates multi-instrument far-IR analysis in the context of suite of A-Train measurements. First, we will explore the capabilities of a notional satellite-borne instrument that has comparable performance to FIRST in terms of spectral coverage, resolving power, and measurement error as they relate to the AIRS instrument. Temperature and water vapor synthetic retrievals are compared, and implications for cooling rates and OLR are presented. Next, the ability of the instruments to describe cloudy scenes is explored, followed by a discussion of the implications for understanding cloud radiative effect. Finally, results from the second test flight of the FIRST instrument are presented within a multi-instrument context, and some implications for CLARREO mission specification are considered.

For this chapter, we utilize several radiative transfer codes developed by AER, Inc. most of which are described by *Clough et al*. [2005]. These codes include the Line-by-Line Radiative Transfer Model (LBLRTM), version 11.1, for clear-sky radiance spectra, the Rapid Radiative Transfer Model (RRTM), version 3.01, for broadband flux and heating rate calculations, and the Code for Highly-Accelerated Radiative Transfer with Scattering (CHARTS) [*Moncet and Clough*, 1997], version 2.0, for calculating spectra with clouds. The instrument line shape (ILS) associated with the FIRST instrument is given by a sinc-function with a Hamming window, whereas the AIRS ILS is derived from after-launch instrument spectral response function characterization [*Gaiser et al.*, 2003].

8.3   FIRST Instrument Description

As part of the NASA Instrument Incubator Program, a passive high-spectral-resolution fariinfrared interferometer has been built, and lessons learned from this instrument will be directly applicable to CLARREO development. The FIRST instrument is a Fourier Transform Spectrometer that achieves spectral coverage ranging from 50 to 2000 cm^{-1} (wavelengths from 200 to 5 μm, respectively) with a nominal unapodized resolution of 0.643 cm^{-1}. Instrument noise, which is generally ≤ 1 K noise-equivalent brightness temperature and can be as low as 0.2K, is estimated through a two-point calibration with an ambient black-body and space view [*Mlynczak et al.*, 2006b]. The instrument contains 10 equivalent detectors for imaging capability, each having a 7.1 mrad IFOV with a full FOV of 37.7 x 37.7 mrad. The instrument scan-time is 1.4–8.5 seconds and the current instrument configuration does not provide for cross-track scanning or motion correction. FIRST has been the subject of two separate balloon-borne test flights from Ft. Sumner, New Mexico (34.5 N, 104 W), and several thousand spectra have been recorded from each flight. Recently, a second calibration blackbody has been added and the instrument has been configured for extensive ground-based operations.

As seen in Figure 8.1, actual FIRST and AIRS spectra show a large amount of commonality in the mid-infrared, where both record high-resolution, low signal-to-noise ratio measurements. However, the FIRST instrument records an additional set of measurements covering the water-vapor rotational lines. These may allow for improved characterizations of, in particular, the amount of upper-tropospheric water vapor, and the effects of clouds on water vapor emission lines and how they interact to affect OLR and heating rates.
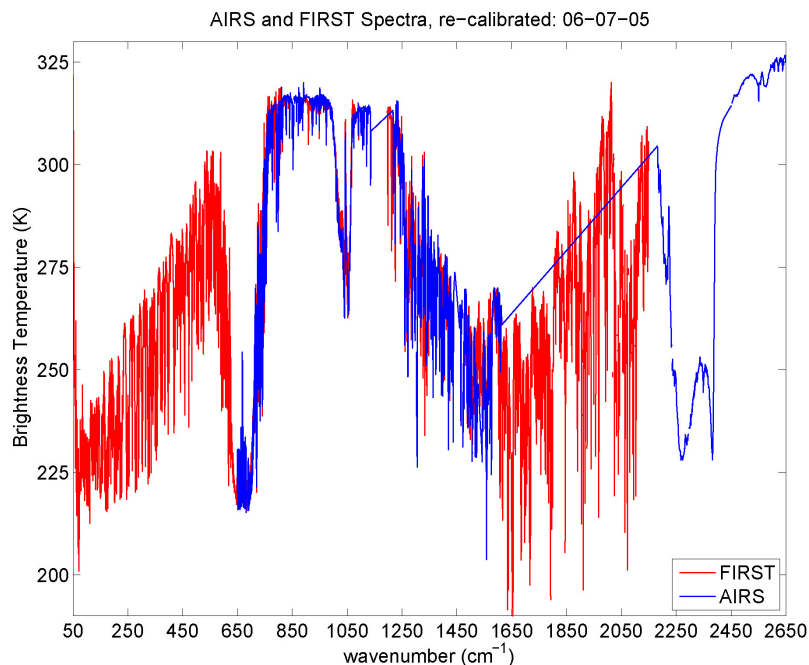
Figure 8.1: Brightness temperature spectra from collocated AIRS and FIRST (version 1.0 calibration) measurements during the test flight on June 7, 2005, at Ft. Sumner, New Mexico (34.5 N, 104.3 W).

From a remote-sensing platform, far-infrared measurements are generally difficult to achieve, but the absence of far-infrared measurements in a comprehensive terrestrial measurement program such as the A-Train is conspicuous. In fact, it warrants formal analysis in terms of the error incurred by the effects of retrieved products on the far-infrared, where they are essential for atmospheric energetic analysis. Therefore, it is important to compare the capabilities of the current generation of mid-IR spectrometers with the proposed new generation of far-IR spectrometers.

8.4 Clear-Sky Retrieval Comparison

For this section, we evaluate the ability of a notional instrument that is comparable to FIRST in terms of spectral coverage, resolving power, and measurement error to retrieve temperature and water vapor profiles (hereafter called "notional FIRST") in light of the

performance of existing mid-infrared satellite-borne spectrometers such as AIRS. This comparison is achieved through the use of synthetic retrievals in which we contrast the T and H_2O profile retrievals derived from synthetic measurements with noise to the actual T and H_2O profiles that underlie the measurements. Also, since the synthetic retrieval starts with a T and H_2O profile that is erroneous, this approach tests the sensitivity of the retrieval to incorrect *a priori* assumptions. Many of the aspects of this approach to retrieval system design are described by *Rodgers*, [2000].

While many advanced retrieval algorithms exist for processing radiance measurements into T and H_2O profiles, we analyze the relative ability of AIRS and notional FIRST using a linear Bayesian update that allows for straightforward characterization of posterior retrieval statistics and retrieval vertical resolution. Accordingly, the atmospheric state that is retrieved is a balance of *a priori* constraints with a state suggested by the difference between the measurement and the synthetic measurement corresponding to the *a priori* state. The relative weights given to the two factors controlling the retrieval output is determined by the estimated uncertainty in the *a priori* state and the measurement. Accordingly, it can be shown [*Rodgers*, 2000] that the retrieved atmospheric state update is given by:

$$\hat{\mathbf{x}} = \mathbf{x}_a + \left(\mathbf{K}^T \mathbf{S}_\varepsilon^{-1} \mathbf{K} + \mathbf{S}_a^{-1}\right)\left(\mathbf{K}^T \mathbf{S}_\varepsilon^{-1}\left[\mathbf{y} - \mathbf{y}_a\right]\right) \qquad (8.1)$$

where $\hat{\mathbf{x}}$ is the retrieved atmospheric state (in this case a concatenation of the T and H_2O profiles), $\mathbf{x}_a$ is the *a priori* state, $\mathbf{S}_\varepsilon$ is the measurement covariance matrix, $\mathbf{y}$ is the radiance measurement vector, $\mathbf{y}_a$ is the radiance determined by inputting the *a priori* atmospheric state into a radiative transfer model, *-1* and *T* refer to the inverse and transpose operators respectively, and $\mathbf{K}$ is the weighting function matrix given by:

$$K(i,j) = \frac{\partial y_i}{\partial x_j} \qquad . \qquad (8.2)$$

According to this formulation, the *a posteriori* covariance matrix is given by the following:

$$\hat{\mathbf{S}} = \left(\mathbf{K}^T \mathbf{S}_\varepsilon^{-1} \mathbf{K} + \mathbf{S}_a^{-1} \right)^{-1} \qquad . \qquad (8.3)$$

The averaging kernel matrix denotes the sensitivity of the retrieval to narrow vertical perturbations and is closely related to retrieval vertical resolution and is given by:

$$\mathbf{A} = \left(\mathbf{K}^T \mathbf{S}_\varepsilon^{-1} \mathbf{K} + \mathbf{S}_a^{-1} \right)^{-1} \mathbf{S}_\varepsilon^{-1} \mathbf{K} \qquad . \qquad (8.4)$$

For the synthetic retrieval test, the *a priori* covariance of the temperature, water vapor, and ozone profiles is assumed to be based on a first-order autoregressive process such that adjacent level errors are correlated [*Rodgers*, 2000]. Off-diagonal components are given by:

$$\text{cov}(x_i, x_j) = \sigma(x_i)\sigma(x_j)\exp\left(-\frac{|z_i - z_j|}{H} \right) \qquad . \qquad (8.5)$$

The synthetic retrieval is implemented by first starting at the "true" atmospheric state (in this case the Tropical Model Atmosphere [*Anderson et al.*, 1986]) and using the forward model to produce a corresponding radiance spectrum. The synthetic measurement is then produced by perturbing the elements of the radiance measurement by normally distributed values corresponding to the measurement covariance matrix. The *a priori* state is derived by randomly perturbing elements of the T and H_2O profiles while still respecting the presumed covariance between the atmospheric state parameters at different levels. The *a priori* radiance is calculated by inputting the *a priori* atmospheric state into the forward model. The results of a synthetic notional FIRST and AIRS T and H_2O profile retrieval comparison are shown in Figure 8.2. It is expected that the notional FIRST instrument will be more sensitive to upper-tropospheric water vapor given its spectral coverage, and the retrieval results in Figure 8.2 bear this out.
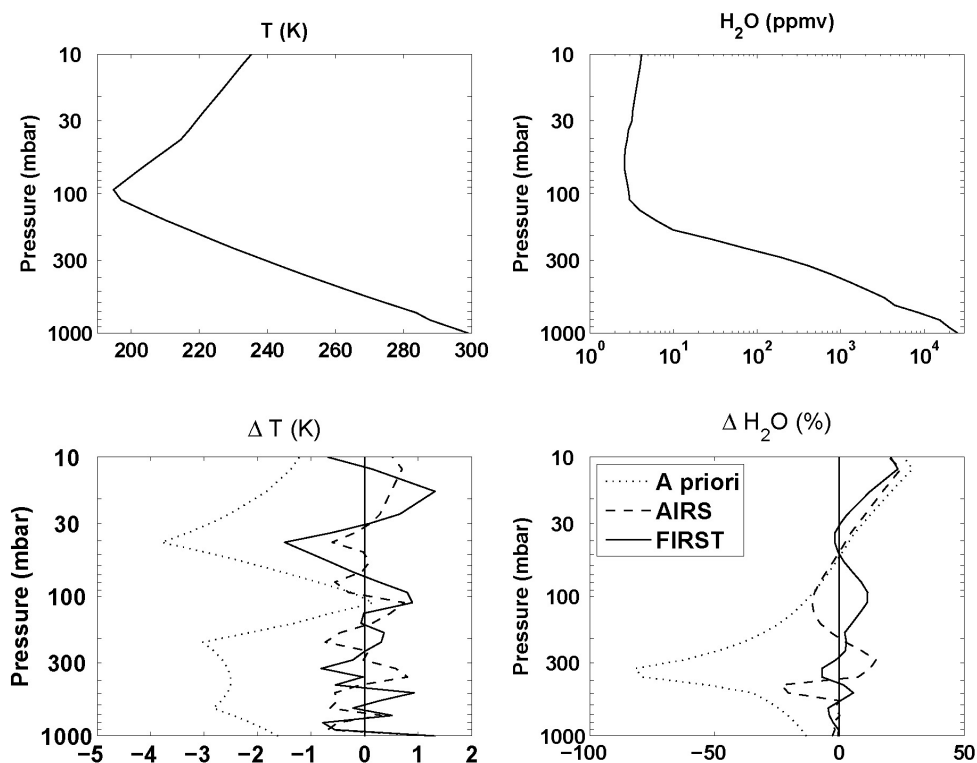
Figure 8.2: Top two panels denote the T and H_2O profiles for the Tropical Model Atmosphere Bottom three panels depict synthetic retrieval difference between true and *a priori* (dotted), and true and retrieved profiles of T and H_2O for the AIRS (dashed) and notional FIRST (solid) instruments.

The radiance residual spectra also are instructive in terms of understanding the results of the retrieval in measurement space, and we present the synthetic residuals in Figure 8.3. For clarity, the residuals are translated about the zero line with a dashed black line indicating zero difference between model and synthetic measurement. Major differences between the prior and posterior residuals indicate in general the stability of the retrieval method. The posterior residual shows little structure and is centered about the zero-residual line. Subtle differences between the residual of the notional FIRST spectrum derived from the retrieval using the AIRS measurement (FIRST post w/AIRS) and the residual associated with a retrieval using the notional FIRST spectrum (FIRST post) can be seen near 100 cm^{-1} and are revealed in terms of the retrieval power of upper-tropospheric water vapor.
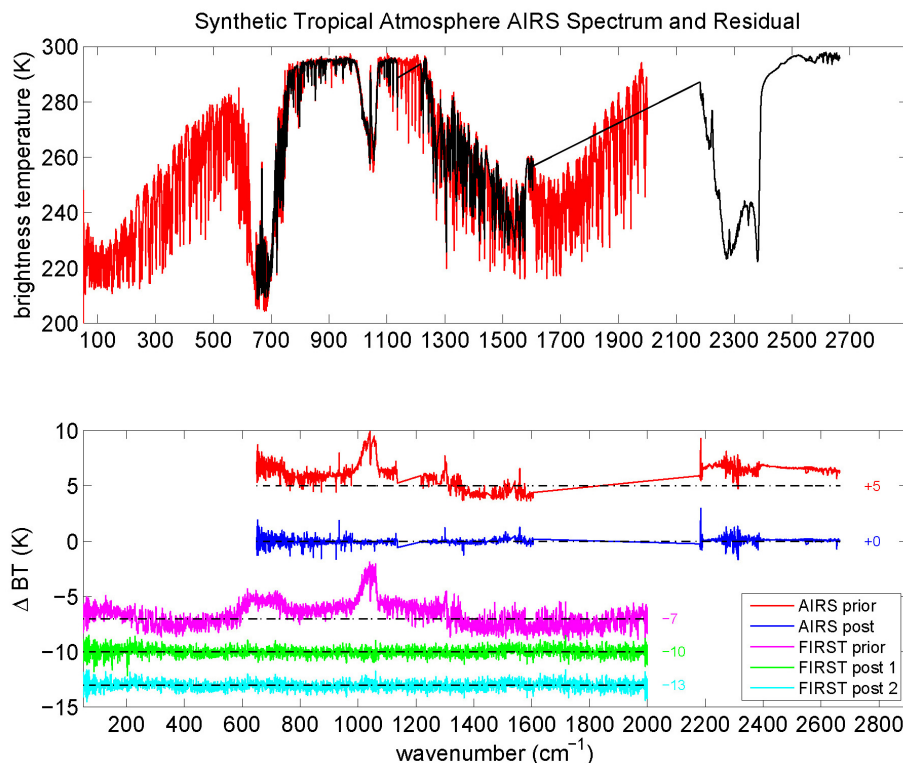
Figure 8.3: Upper panel shows synthetic brightness temperature spectra for a Tropical Model Atmosphere for the AIRS (black) and notional FIRST instruments (red). Lower panel: prior and posterior residuals (measured-model) for a synthetic simultaneous retrieval of T, H_2O, and O_3 profiles, translated on the y-axis by amounts indicated at right. The zero residual lines are indicated in dashed black.

The difference between the two notional FIRST residual lines is useful in that it reveals the extent to which extra information in the far-IR measurements relates to the quantities of interest such as T and H_2O profiles.

Averaging kernel matrices are presented in Figure 8.4 in a manner that emphasizes where the retrievals perform well and, conversely, where the *a priori* information must be utilized. We show the individual level T and H_2O normalized averaging kernels which, for a perfect retrieval, would be δ-functions centered on the one-to-one line. The spread (red or blue colors) about this line along the y-axis is clearly shown in the figure, implying that the retrieval has limited sensitivity in that region. Given the broad response of weighting functions to atmospheric perturbations, the retrieval has difficulty resolving profile perturbations fully, though thermal sounder retrievals generally operate well in the free troposphere where thermal contrast is large.

The performance of temperature retrievals using the notional FIRST and AIRS instruments are similar, while those with respect to upper-tropospheric and lower-stratospheric water vapor differ sharply.
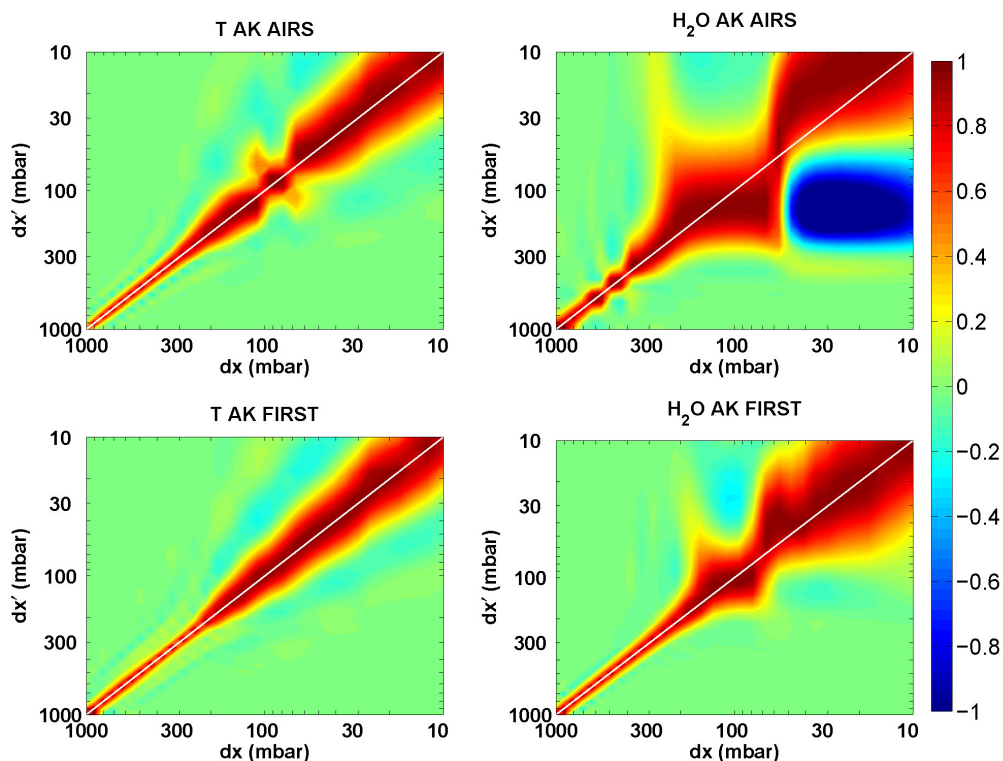

Figure 8.4: Level-normalized T and H_2O averaging kernels for AIRS and notional FIRST when observing the Tropical Model Atmosphere. The x-axis denotes the perturbation level and the y-axis denotes the response of the retrieval to the perturbation.

Another central question is to what extent remote-sensing measurements may be able to constrain thermal infrared cooling rates and outgoing longwave radiation. Cooling rates represent the influence that the distribution of absorbing species such as CO_2, H_2O, and O_3 have on the radiative energy exchange between layers of the atmosphere. They are ubiquitously calculated in the course of climate and weather model calculations, and can have a strong direct impact on upper-troposphere and stratosphere circulations. What is generally not presented is the variability in the cooling rate profile as determined by the propagation of uncertainty in the temperature, water vapor, and ozone profiles onto broadband cooling rates (CO_2 variability is very small and

has a negligible impact on CO_2 cooling rate variability). Formal error propagation analysis

[*Taylor*, 1994; *Feldman et al*., 2008] allows for the estimation of uncertainty in broadband

cooling rate profiles which is straightforward for clear-sky scenes. Cooling rate uncertainty is

given by the following formula:

$$\left[\Delta\dot{\theta}(z)\right] = \sqrt{\sum_{i=1}^{n}\sum_{j=1}^{n}\frac{\partial\dot{\theta}(z)}{\partial x_i}\frac{\partial\dot{\theta}(z)}{\partial x_j}\mathrm{cov}\left(x_i, x_j\right)} \tag{8.6}$$

where $\left(x_1,\ldots x_i,\ldots x_j,\ldots,x_n\right)$ represent all of the atmospheric state inputs that are relevant to

cooling rate profile calculations at each level, $\dot{\theta}(z)$ refers to the broadband cooling rate at height

z , and cov refers to the covariance function. The atmospheric state inputs are assumed to have

Gaussian distributions. The *a priori* covariance of the T, H_2O, and O_3 profiles is assumed to be

based on Eq. (8.5) and is also assumed to be block-diagonal. The *a posteriori* cooling rate profile

uncertainty is derived from the *a posteriori* T, H_2O, and O_3 covariance matrices from the AIRS or

notional FIRST instrument models.

Figure 8.5 shows that the introduction of a measurement only slightly reduces the

uncertainty in cooling in the ν_2 band of CO_2 and the ν_3 band of O_3, due to broad stratospheric

weighting functions in those bands. Though not appreciably different from the AIRS instrument,

the notional FIRST instrument significantly reduces uncertainties in the cooling rates at most

atmospheric levels as compared with *a priori*, with particularly notable performance in terms of

constraining water vapor rotational band cooling.

The total IR cooling rate uncertainty after a measurement is approximately 0.1 K/day in

the troposphere and 0.2 K/day in the lower and middle-stratosphere, increasing to nearly 0.4

K/day at the stratopause. The comparable retrieval performance for the two instruments in terms

of T and H_2O profiles leads predictably to comparable performance in constraining cooling rate
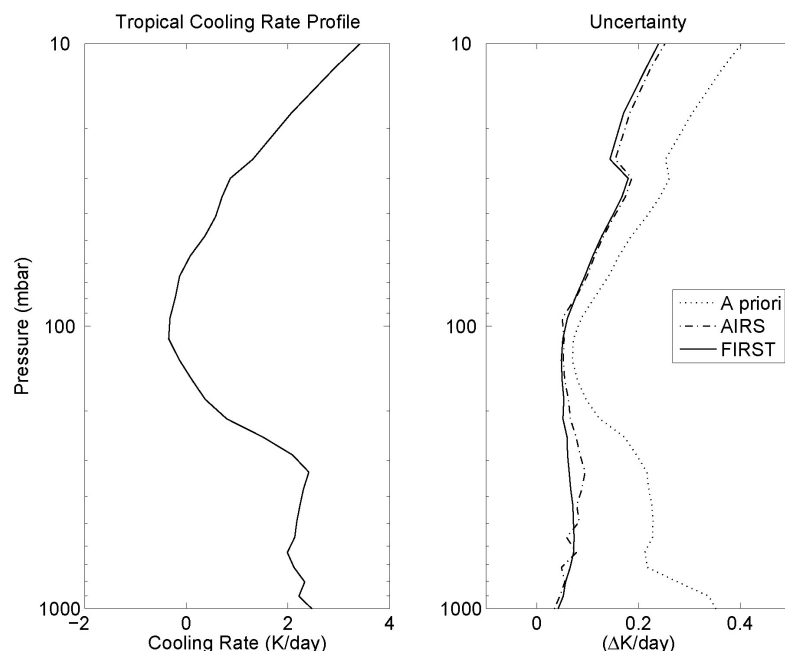
profiles.

Figure 8.5: Left panel: Tropical Model Atmosphere clear-sky total IR cooling rate profile; right panel: *a priori* (dotted line) and *a posteriori* uncertainty after AIRS (dashed line) and notional FIRST (solid line) measurements.

The improved upper-tropospheric H_2O retrieval power for the notional FIRST instrument may allow for a decrease in uncertainty of 0.05 K/day in the cooling rate profile around 200 mbar. For clear conditions, the results of this retrieval comparison are consistent with the findings of *Mertens* [2002], and emphasize that for FIR spectra the increased number of measurements of water vapor through the rotational lines imparts increased information about upper tropospheric water vapor.

8.5 Mid- and Far-Infrared Cloud Analysis

Where clouds are present, the extent to which mid-IR spectra can be used to recreate far-IR spectra is an open question that deserves close scientific scrutiny. Measurements from the CERES instrument provide a broadband view of the effect of clouds on the infrared, but since the spectral coverage of 5–100 μm is so broad, this instrument's data provides minimal insight into

the causes of OLR variability and the nature of the underlying cooling rates, all of which are important for evaluating the strength of climate models. Given the ubiquity of cloud cover and the fact that climate models must provide a comprehensive assessment of radiative transfer in the far-IR including clouds, it is important to understand the skill with which data from the current array of A-Train spectrometer measurements can be extrapolated to the far-IR, and how well the current spectra can impart information on cooling rate profiles for non-clear-sky scenes. Unfortunately, where clouds are present, the extrapolation of mid-IR spectra to the far-IR is made considerably more complicated relative to the clear-sky extrapolation, because the information in the cloudy spectra regarding the constituents needed to calculate OLR is obscured by one or more layers of generally optically thick clouds. Consequently, the approach used in the previous section, in which standard atmospheric constituent retrievals are used to explore the extra information in the far-IR spectra as compared to the mid-IR spectra, is less feasible for cloudy conditions. A simultaneous retrieval of T, H_2O, and O_3 profiles along with cloud microphysical property profile retrievals is reasonable for cases where cloud optical thickness is low but is difficult to formulate where cloud optical depth is high and there is no information regarding atmospheric constituents below the cloud deck.

However, synthetic tests will allow for the development of methods to translate the information in the mid-IR regarding cloud cover to the far-IR. For this analysis, the optical properties of clouds depend on their microphysical composition, and we employ a simple and straightforward parameterization for liquid clouds [*Hu and Stamnes*, 1993] and ice clouds [*Fu et al.*, 1997] based on cloud water content (CWC) and cloud effective radius (CER) to derive absorption, extinction, and asymmetry parameters from which cloud reflectance and transmittance functions are derived. Given these cloud optical properties, it is possible to formulate an expression for the radiance observed at the top-of-atmosphere which is necessary to understand the similarities and differences in response of the mid- and far-IR channels to the

presence of clouds. We utilize the following equation for IR channel radiance reaching the

detector as expressed by *Wei et al.* [2004]:

$$I_\nu^{obs} = I_\nu^1 T_\nu^u T_\nu^c + \left(1 - R_\nu^c - T_\nu^c\right) B_\nu^c T_\nu^u + I_\nu^2 + I_\nu^3 R_\nu^c T_\nu^u \qquad (8.7)$$

where I_ν^{obs} is the observed radiance for a certain channel ν, I_ν^1 is the radiation from the

atmosphere reaching the cloud's lower boundary, T_ν^u is the transmittance between the cloud top

and the observer, T_ν^c is the transmittance through the cloud, R_ν^c is the cloud reflectance, B_ν^c is

the Planck emission for the cloud, I_ν^2 is the atmospheric radiation from above the cloud top, and

I_ν^3 is the atmospheric downwelling radiation above the cloud top. The cloud reflectance and

transmittance functions can be formulated using the doubling-adding method [*van de Hulst*, 1963;

Twomey et al., 1966] or the discrete ordinate method [*Stamnes et al.*, 1988]. Where the cloud is

optically thin, the 1st and/or 3rd terms on the RHS of Eq. (8.7) dominate the observed radiance. If

the cloud is optically thick at a level where T_ν^u is small, the 3rd term of the RHS of Eq. (8.7) will

dominate the observation. However, if the atmosphere is largely transparent from the cloud top

to the observer, the measurement will be dominated by the 2nd term in the equation. The 4th term

generally contributes a small amount to the observation. We will generally focus on the cases of

10 μm optical depth less than 10 because these cases are less-dominated by the 2nd term of the

RHS, and it is expected to be most difficult to address cloud and water vapor interactions where

several of the terms of the RHS of Eq. (8.7) are of equal magnitude.

One view that allows for the characterization of mid- and far-IR response to the presence

of clouds is shown in Figure 8.6a–b. Figure 8.6a shows the brightness temperature spectral

residual for the notional FIRST instrument associated with a 1-km-thick liquid cloud layer with

cloud top height (CTH) of 5 km for a Tropical Model Atmosphere. The cloud water content

(CWC) of this layer is 20 mg/m^3 and the cloud effective radius (CER) is 5.89 μm. Figure 8.6b

indicates a rearrangement of the results in Figure 8.6a by sorting channels according to brightness temperature and denoting mid- and far-IR channels separately.
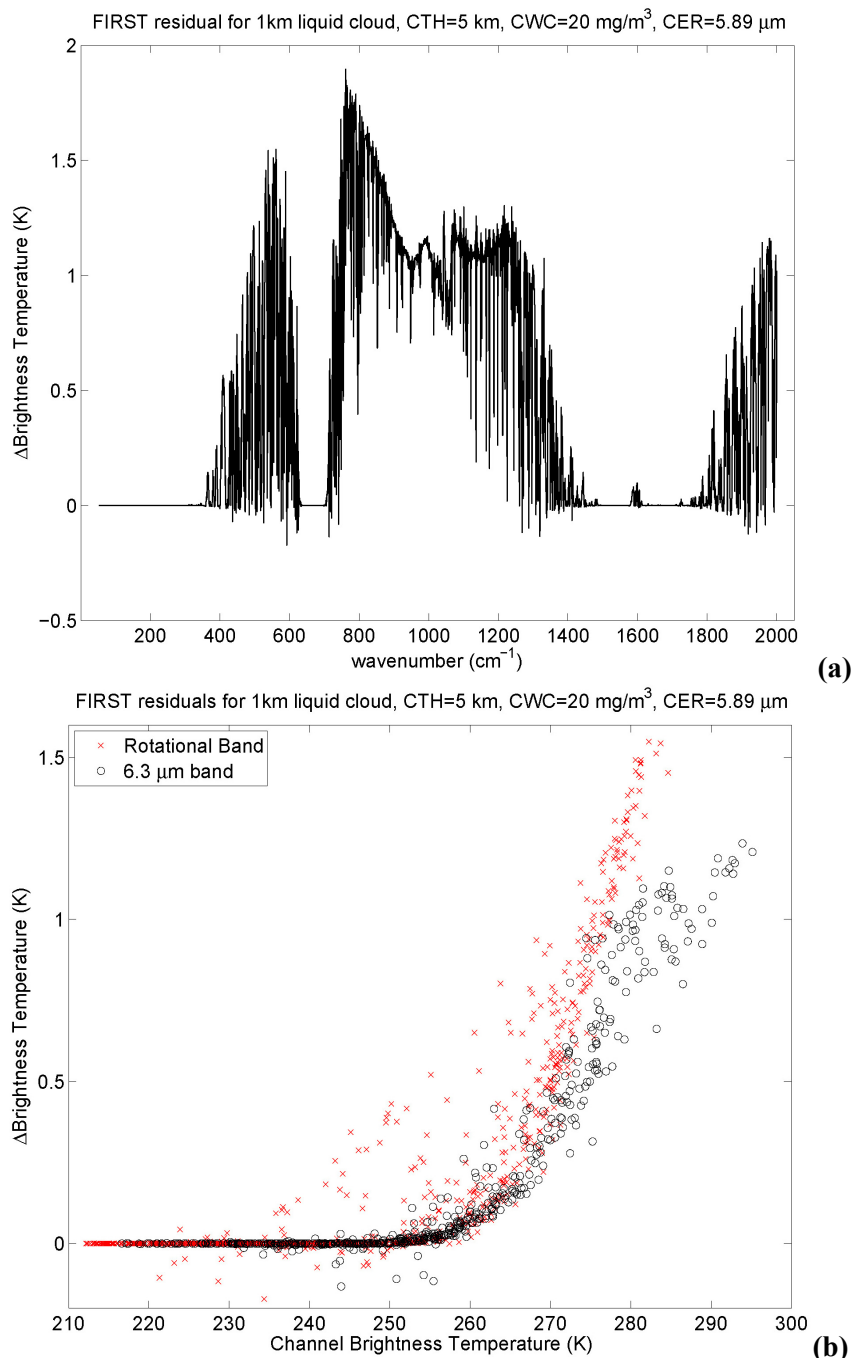

Figure 8.6: (a) Spectral signature of a 1-km-thick liquid cloud where CTH = 5 km, CWC = 20 mg/m³, and CER = 5.89 μm for the notional FIRST instrument under Tropical conditions. (b) Scatterplot of brightness temperature residual associated with inclusion of the cloud layer vs. clear-sky brightness temperature for far-IR (black o's) and mid-IR (red x's) channels.

In this figure, several prominent features can be seen: most of the channels with brightness temperature below 260 K have very limited response to the presence of the cloud, because those channels' weighting functions have very limited sensitivity to atmospheric conditions at or below 5km. For channels with brightness temperature between 260 and 290K, the cloud layer has an appreciable influence on the observation. There is clearly differential sensitivity between mid- and far-IR channels due to differences in cloud optical properties between and mid- and far-IR. It is possible to parameterize the response of mid-IR channels relative to far-IR channels, though some error will be incurred at the level of at least 0.5K.

In Figure 8.7a, the brightness temperature spectral residual is shown for a Tropical Model Atmosphere for a 2-km-thick ice cloud with a CTH of 10 km, a CWC of 2.4 mg/m^3, and a CER of 20.75 μm. Similar to Figure 8.6b, that information is rearranged in Figure 8.7b to mid- and far-IR brightness temperature residuals as a function of clear-sky brightness temperature for those notional FIRST channels covering the 6.3 μm H_2O band (1240 to 1613 cm^{-1}) and those covering the rotational H_2O band (50 to 630 cm^{-1}). This figure shows that for tropical conditions, the mid- and far-IR channels with brightness temperatures ranging from 220 to 250 K exhibit a similar response to the presence of a cirrus cloud. Since the weighting functions for these channels peak in the upper troposphere, most clouds will only have a slight impact on these channels, and extrapolation of these channels from the mid-IR to the far-IR is particularly amenable to parameterization. Meanwhile, those channels in the mid- and far-IR with a brightness temperature in excess of 270 K are quite sensitive to the presence of clouds. Here, we can see that 6.3 μm channels have a lower brightness temperature residual than the rotational band channels. The primary reason for this is that in the far-IR, these channels lie between 16 and 24 μm, and the ice extinction coefficient is greater at these wavelengths than at 6.3 μm.
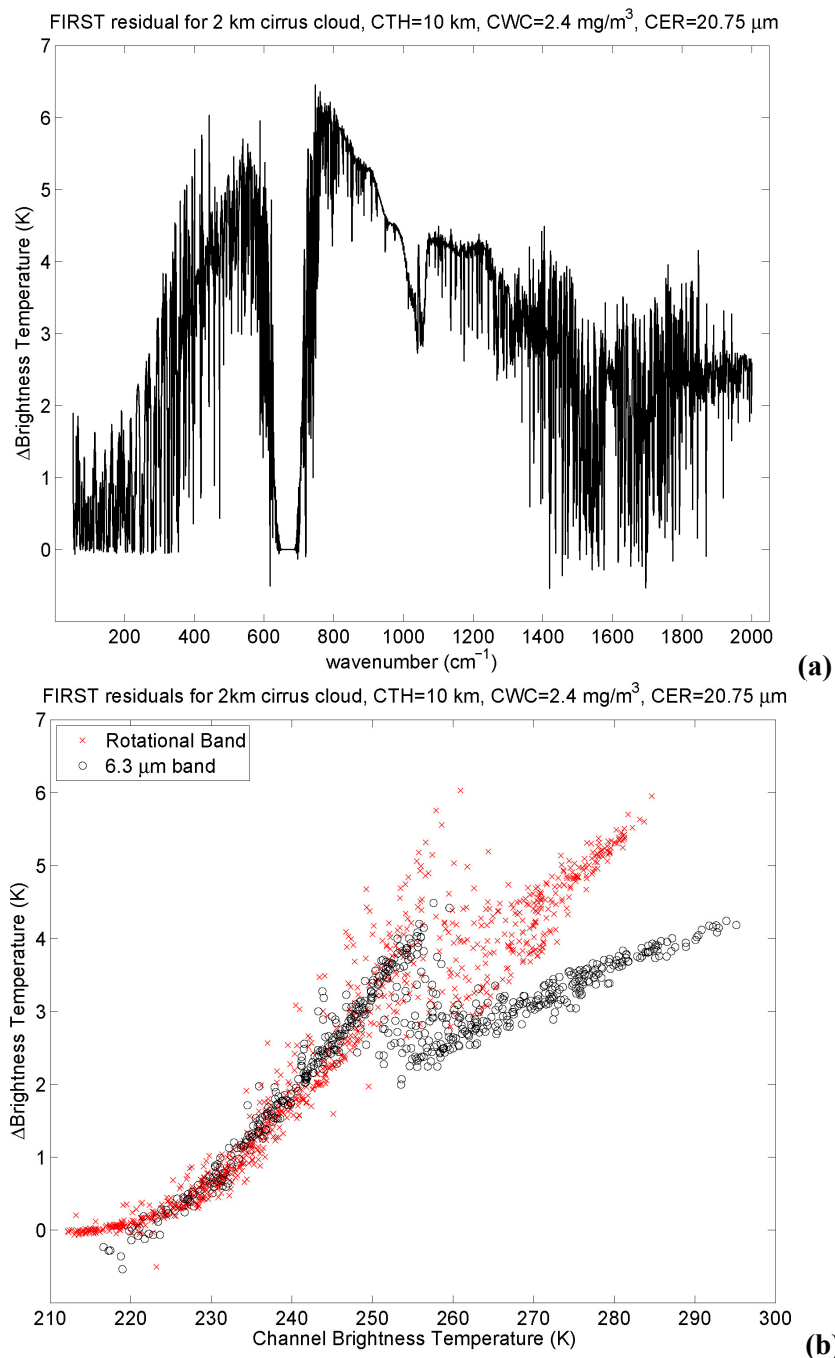
Figure 8.7: Same as Figure 8.6a–b except that the plots relate to a 2-km-thick ice cloud where CTH = 10 km, CWC = 4.8 mg/m³, and CER = 20.75 μm, again under Tropical conditions.

However, the relative difference in mid- and far-IR residuals of channels with clear-sky

brightness temperature in excess of 270K is a function of cloud effective radius.   Figure 8.8 gives

an indication of how well mid-IR predictors will work for far-IR channels with clear-sky

brightness temperatures greater than 270K. This graph gives an indication of the relationship between knowledge of cloud effective radius and how-well these far-IR channels can be predicted given mid-IR measurements.
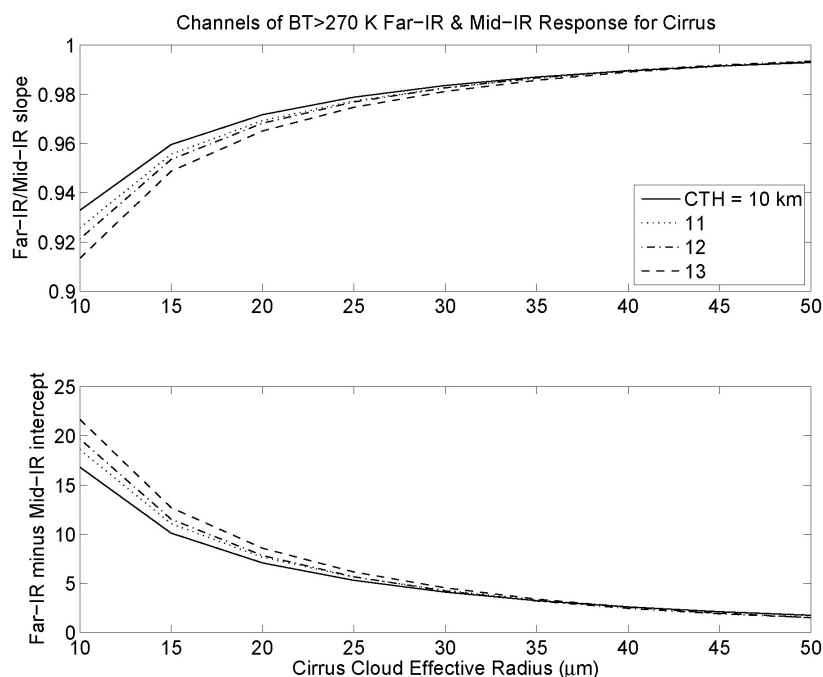
Figure 8.8: Slope-intercept relationships between mid-IR and far-IR channels with clear-sky brightness temperature greater than 270 K for varying CTH and CER.

The more problematic set of far-IR channels involves those with brightness temperatures between 250 and 270 K. For these channels, the cirrus cloud is emitting at or near the altitude from which water vapor is emitting, and the wavelength-dependence of cloud optical properties confounds easy parameterization.

The parameterization analysis described above is reasonable for tropical conditions but may not hold for other mid-latitude or polar conditions. Similar to Figures 8.6a–b, Figures 8.9a–b illustrate the relationship between mid- and far-IR channels in the Sub-Arctic Winter Model Atmosphere. Again, those channels with weighting functions peaking above the top of the cirrus cloud (between 220 and 225K) will be affected almost identically in the mid- and far-IR.
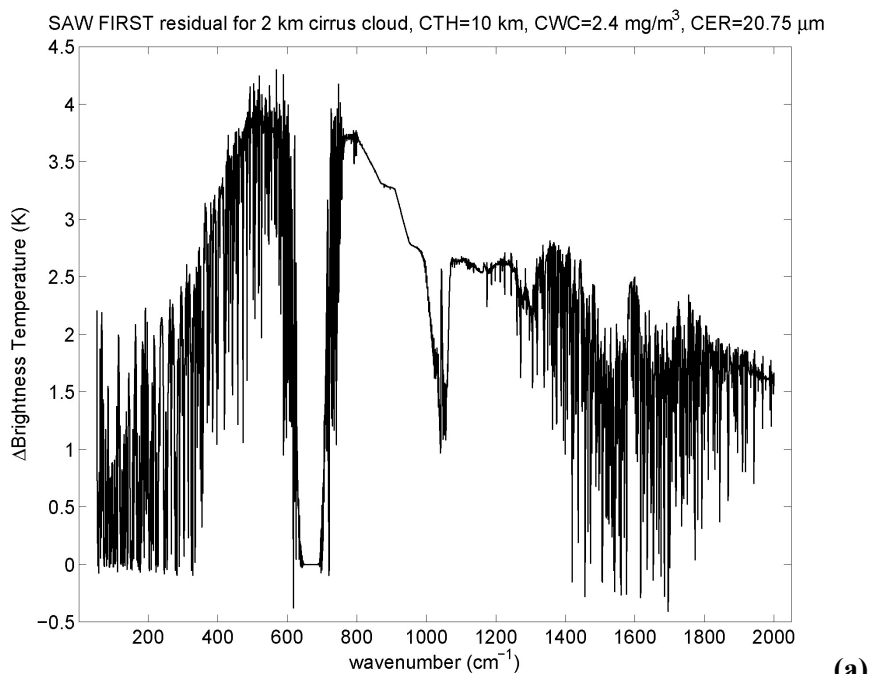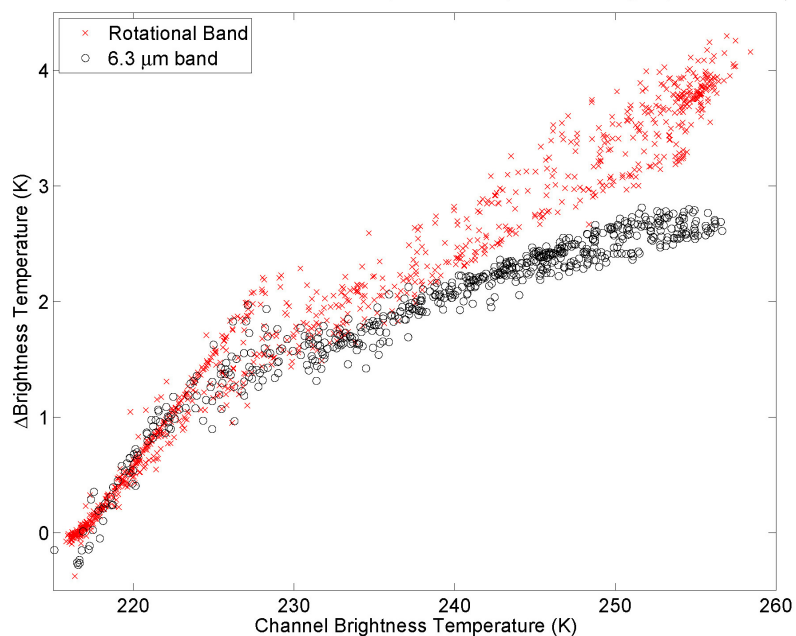
Figure 8.9: Same as Figure 8.7a–b except that the plots relate to a 2-km-thick ice cloud where CTH = 10 km, CWC = 4.8 mg/m³, and CER = 20.75 μm, again under Sub-Arctic Winter conditions.

Those channels with brightness temperatures between 235 and 255K will be affected

differentially in the mid- and far-IR, but this difference can be parameterized coarsely through

cloud top height and cloud effective radius. Mid- and far-IR channels between 225 and 235K

will be difficult to parameterize, though the parameterization will be able to predict far-IR

channels to within 1K.

(a)

(b)
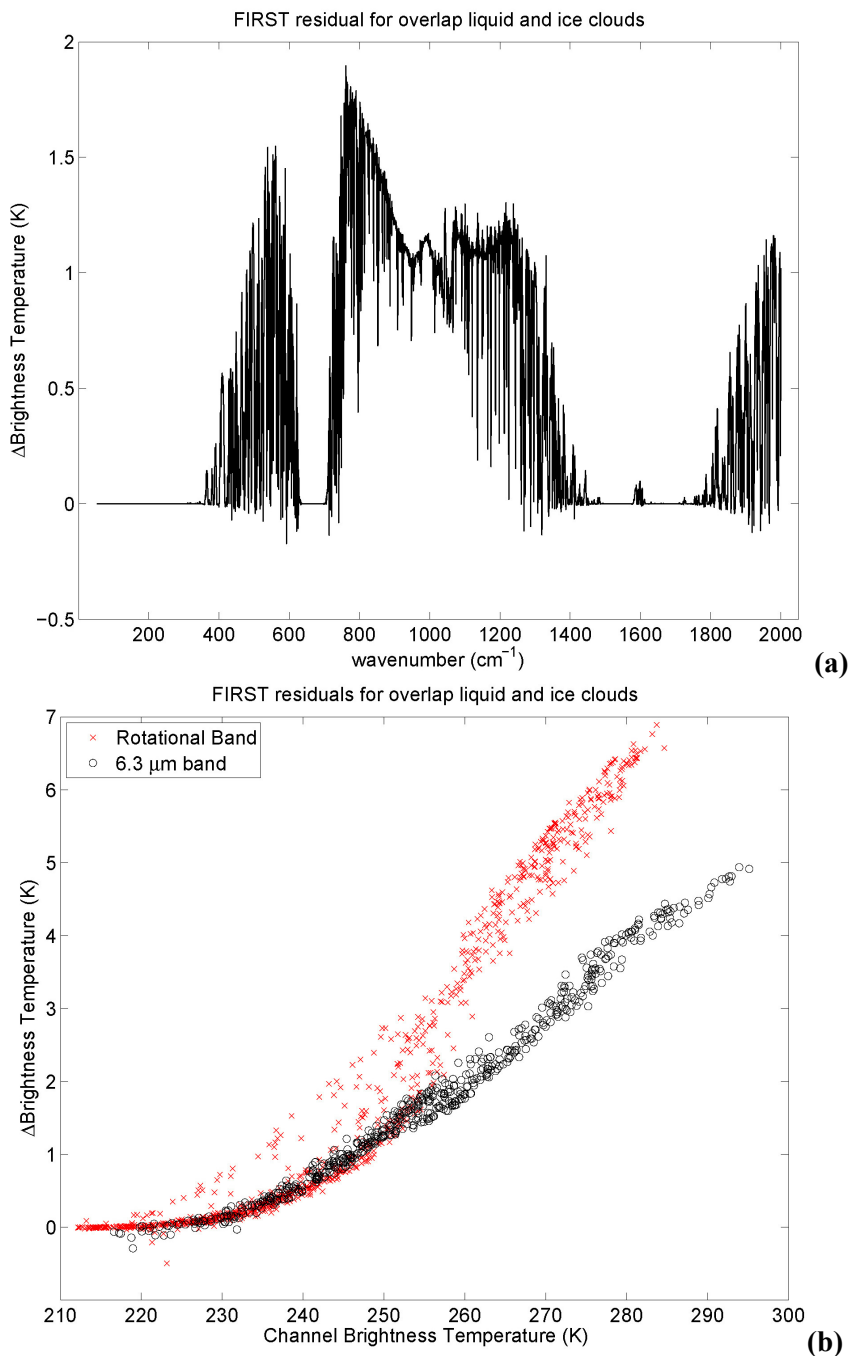
Figure 8.10: Same as Figure 8.6a–b except that the plots relate to a cloud-overlap scenario with a 1-km-thick liquid cloud where CTH= 5 km, CWC = 20 mg/m^3, and CER = 5.89 μm below a 2-km-thick ice cloud where CTH = 10 km, CWC = 4.8 mg/m^3, and CER = 20.75 μm, again under Tropical conditions.

For cases where liquid clouds underlie ice clouds, parameterization of mid- and far-IR cloud response can be fairly straightforward. Figure 8.10a–b is similar to Figure 8.6a–b except that for this case, we include a 1-km-thick liquid cloud layer with CTH = 5 km, CWC = 20 mg/m^3, CER = 5.89 μm using a Tropical Model Atmosphere. Also included is a 2-km-thick ice cloud with a CTH of 10 km, a CWC of 2.4 mg/m^3, and a CER of 20.75 μm. For channels below 230 K, there is very little response by mid- or far-IR channels. However, between 230 and 290 K, the mid- and far-IR channel response can be parameterized linearly.

If the mid-IR spectra can be used to extrapolate the far-IR spectra well, it is feasible to recreate the OLR using mid-IR spectra. The AIRS data processing schedule outputs total-sky and clear-sky OLR currently as a Level 3 product (see *Mehta and Susskind* [1999] for details) but the data are only available where AIRS produces a valid set of retrieval products. The AIRS retrieval algorithm systematically does not produce retrieval results for scenes with extensive and/or optically thick cloud cover, and so the OLR L3 product tends to be biased high. A parameterized treatment of mid- and far-IR channels will not suffer this high bias because it does not rely on the retrieval algorithm but rather uses only channel radiance measurements.

Final and open-ended questions pertain to mid- and far-IR heating rate determination from remote sensing measurements, and whether mid-IR data can be used to determine heating rates in the presence of clouds. Heating rates can vary dramatically at cloud interfaces and within clouds due to the abrupt change in inter-layer transmittance. Where optically thick cloud cover exists, substantial uncertainty in the T, H_2O, O_3, and other cloud profiles below the cloud top impedes any understanding of heating rates below clouds. However, the determination of heating rates in the presence of optically thin cloud cover is well-posed and feasible. The details of how the determination of mid- and far-IR spectra differentially describe heating rate profiles will require an extensive application of information theory concepts and will be left to future research. This analysis is essential for climate-measurement comparison efforts, especially in light of CLARREO.

It is necessary to discuss several caveats to the extrapolation of mid-IR measurements to the far-IR in the presence of clouds. To begin with, it should be noted that this analysis uses notional FIRST mid-IR channels to extrapolate to the far-IR, though in practice, it is more reasonable to use existing operational spectrometer data such as AIRS to extrapolate to the far-IR. AIRS has a different spectral response function as compared to notional FIRST, but the response of the 6.3 μm channels to the presence of cloud cover is essentially identical in character for the 2 instruments. Also, since the T, H_2O, and O_3 profiles will not be known exactly *a priori*, there may be some additional error incurred in the above extrapolation. Finally, a parameterization such as this one or, for example, the one developed by *Huang et al*. [2007], may be expedient in the absence of comprehensive far-IR measurements. However, the work here and by others to extrapolate the mid-IR to the far-IR should not be taken as a full-fledged replacement of actual spectral measurements or the interactions of clouds and water vapor in the far-IR. At the very least, the FIRST instrument should be used to verify the far-IR values predicted from any parameterization.

8.6   Test Flight Results

On September 18, 2006, the FIRST instrument was subjected to a balloon test flight and several thousand spectra were recorded over Ft. Sumner, NM (34.5 N, 104.3 W). Similar to the previous test flight conducted on June 7, 2005 (see *Mlynczak et al*. [2006b] for details), this experiment was coordinated with the overflight of several EOS A-Train platforms, including Aqua and Aura. Since CALIPSO and CloudSat were launched in April 2006, the second FIRST test flight benefitted from active sounding data that was nearly collocated. Additionally, the first-light spectra from the 2005 test flight occurred during exceptionally cloudless conditions, whereas shallow stratocumulus clouds were present for the second test flight.
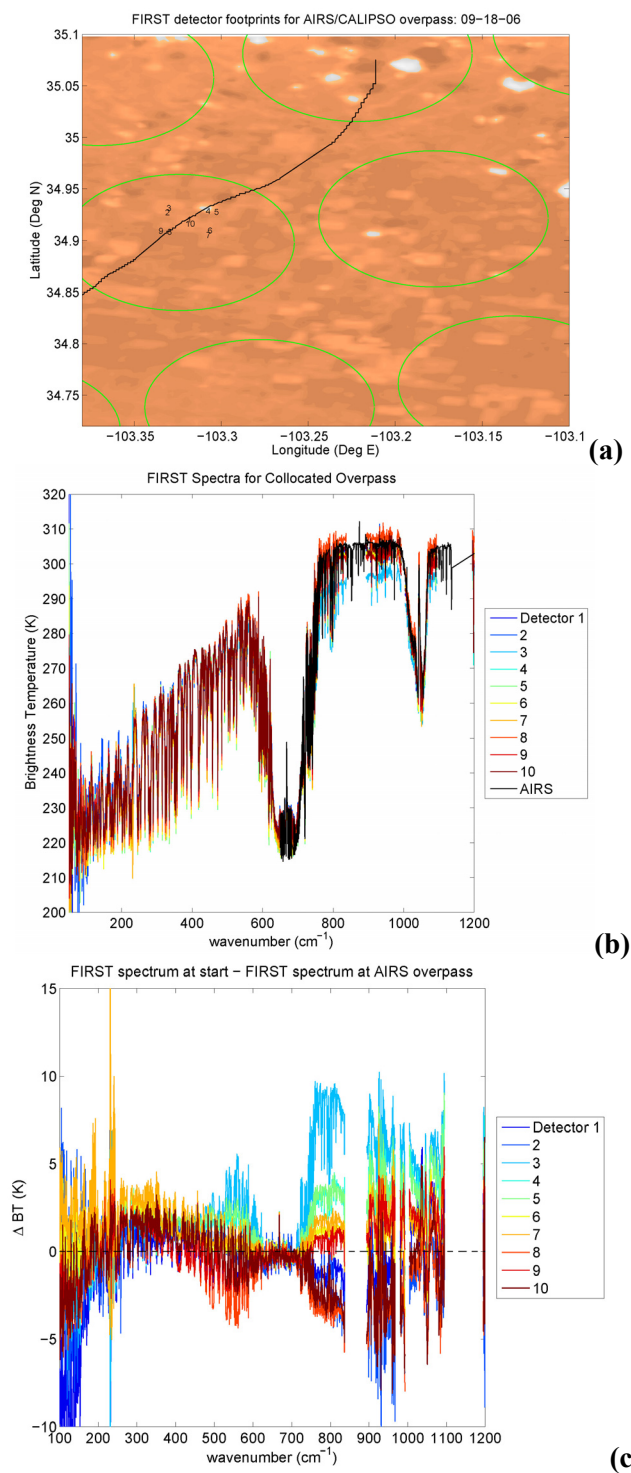
Figure 8.11: (a) Aqua MODIS RGB imagery for FIRST test flight September 18, 2006, at Ft. Sumner, NM. The green circles indicate AIRS footprints, the black line indicates FIRST balloon trajectory with black numbers indicating footprint location at Aqua overpass. (b) Spectra from the 10 FIRST detectors superimposed with the AIRS overpass spectrum. (c) Difference between FIRST spectra at start of flight (clear conditions) and at time of AIRS overpass (broken cloud cover). The zero residual line is indicated in dashed black.

Figure 8.11a shows the collocation of Aqua-MODIS imagery, AIRS footprints, and FIRST detectors. The RGB composite Aqua-MODIS 250-meter resolution imagery shows stratocumulus cloud features which cover the field of view of some but not all of the FIRST detectors, whereas the AIRS footprint is much larger than the clouds. In Figure 8.11b, the brightness temperature spectra of the 10 FIRST detectors are plotted in addition to the AIRS spectra and show a similar character to each other. The spectral residuals associated with the AIRS overpass are produced from the difference between the spectrum measured by each detector at the start of the test flight recording (clear conditions) and that measured at overpass. During this test flight, inter-detector discrepancies were approximately 1 K and were mostly time independent, allowing for meaningful cloud residual spectrum determination. As seen in Figure 8.11c, FIRST detector 4 in particular shows a spectral residual that is consistent with a cloud located at approximately 5 km with a cloud-water content of 80 mg/m^3.

While the CloudSat and CALIPSO footprints did not coincide directly with the FIRST footprint, they were within 200 km of the balloon, and all instruments sampled clouds that probably arose from the same meteorological conditions. In Figure 8.12a, the radar reflectivity (2B-GEOPROF) from CloudSat shows no detectable cloud cover, but the CALIPSO 1064 nm attenuation at latitude 35–36 N shown in Figure 8.12b indicate thin clouds at around 5 km, though the processing algorithms for the CALIPSO lidar information do not currently allow for a detailed description of the cloud water content or effective radius.

For the initial stages of understanding the spectra produced by the FIRST instrument, it is important to establish radiometric agreement between different instruments in the mid-IR, and between measurements and what radiative transfer models predict for far-IR spectra.
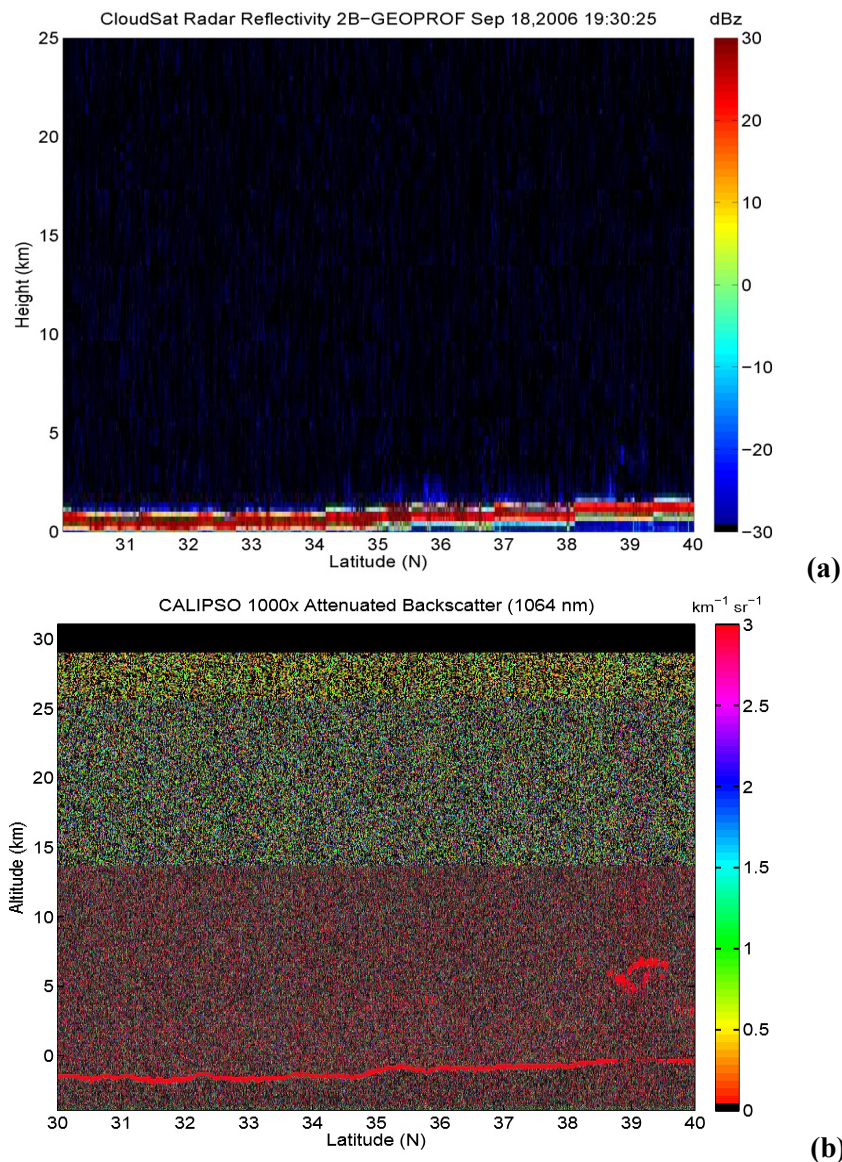
Figure 8.12: (a) CloudSat Radar Reflectivity nearly-collocated with FIRST test flight on September 18, 2006. (b) CALISPO 1064 nm Attenuated Backscatter nearly-collocated with the FIRST test flight on September 18, 2006.

Once this is accomplished, one can be more confident in data derived from extended measurement campaigns. Spectra can be gathered over a period ranging from several weeks to months from a ground-based site and compared to radiative transfer calculations derived from analysis fields and climate models to determine discrepancies of spectroscopy. Given that systematic spectroscopic errors are routinely discovered with the advent of comprehensive

measurements of a new spectral region, it is likely that an extended set of far-IR measurements will indicate the strengths and weaknesses in the current treatment of this part of the spectrum.

8.7   Discussion

The far-infrared (15–100 μm) portion of the spectrum is currently not measured directly by earth-observing hyperspectral satellite instruments, so the effect of water vapor and clouds on atmospheric energetics is inferred from other spectral regions. Under clear-sky conditions, information contained in mid-IR spectroscopy is only slightly inferior to that contained in mid- and far-IR measurements. Nevertheless, for comprehensive studies of water vapor between 100 and 300 mbar, we find that far-IR spectra may be useful. Upper-tropospheric water vapor in this region has a strong influence on the greenhouse effect, but any scientific advantage with FIR measurements can only be realized with high signal-to-noise ratio below 200 cm^{-1}.

The effect of clouds on the far-IR is much less determined by mid-IR spectra, however. The difference in cloud optical properties between the mid- and far-IR leads to a differential response between channels with the same clear-sky weighting functions in the two wavelength regions, necessitating the development of a parameterization to extrapolate mid-IR information to far-IR channels. For cloud cover including optically thin liquid clouds and liquid clouds underlying optically thin ice clouds, most far-IR channels exhibit similar behavior to mid-IR channels, especially when the cloud residual brightness temperature signal is plotted against clear-sky brightness temperature. For cases where only a thin ice cloud is present, however, it will be difficult to develop simple parameterizations for channels with clear-sky brightness temperature of 250–270K. The information content of mid- and far-IR relative to heating rate profiles has been established for clear-sky conditions, but is a subject that deserves close scientific scrutiny for cloudy conditions.

Finally, we present a multi-instrument analysis of several FIRST test flight spectra from September 18, 2006. Passive spectral measurements from AIRS and 250-meter imagery from MODIS are included with active sounding measurements from CALIPSO and CloudSat. The combined set of measurements allows for a characterization of the FIRST spectra for scenes with small amounts of stratocumulus clouds. While radiometric analysis of FIRST data from flight- and ground-based datasets is ongoing and will be reported in future work, the agreement between several different measurements lends credence to the accurate characterization of the scene. More far-IR spectra supported by A-Train measurements would be useful for understanding the strengths and deficiencies of mid-IR spectra in the determination of the far-IR for scenes with more diverse cloud cover. Ultimately, an instrument with FIR capabilities must be tested within an orbital simulation framework to determine how well mid-IR spectra can constrain the far-IR radiative interaction between clouds and water vapor.

Chapter Nine. Implications and Challenges.

9.1   Introduction

This research has explored several topics related to the remote sensing of fluxes and heating and cooling rates from satellite-borne instrumentation. However, this work is merely a foray into a much larger set of work that may be possible with the current generation of satellite instrumentation, or with the future generation that is currently in the scoping phase. This chapter will discuss future avenues of research that are tractable, and will also address challenges for the understanding of radiative fluxes and heating and cooling rates. These challenges can be broadly divided into two categories: measurement retrieval methods and model-measurement comparisons. First, measurement approaches from space will have limited sensitivity to fluxes and heating rates for certain scenes. Further work is required for the implementation of methods for the proper utilization of the EOS A-Train measurements for the analysis of these quantities. Second, significant work is warranted for the development of proper methods for the comparison of fluxes and heating and cooling rates calculated in models and those derived from measurements.

9.2   Frontier of Remote Sensing of Heating and Cooling Rates

The current instrumentation suite from the NASA Earth Observing System A-Train [*Asrar and Dozier*, 1994] provides a very diverse set of measurements. However, the analysis of this voluminous set of measurements with respect to heating and cooling rates has not matured as of this writing. Indeed, because the quality of many of the datasets exceeded the mission science requirements, it has become feasible to perform scientific research using the data in novel ways,

one of which is the characterization of heating and cooling rate profiles from the measurement suite.

It is possible to describe heating and cooling rates from passive satellite-borne spectrometers throughout the troposphere and stratosphere in clear-sky cases, and also from a tropospheric cloud-optical depth of around one into the stratosphere for scenes with clouds present. The determination of in-cloud heating and cooling rates is essentially unconstrained by passive measurements but is moderately well constrained by current cloud-radar measurements, especially with respect to cloud boundaries. Some of the difficulty in using radar measurements can be attributed to the fact that the heating and cooling rates are effectively sensitive to the second moment of the size distribution, while the signal measured by cloud-profiling radar such as CloudSat is determined by the sixth moment of the size distribution [*Mather et al.*, 2007]. The coincidence of lidar measurements on CALIPSO may allow for a refined picture of radiative heating and cooling within thin clouds, but, as of this writing, the retrieval of meaningful cloud products from the total attenuated backscatter at 532nm and 1064 nm and depolarization ratio profiles [*Vaughan et al.*, 2004] are not mature. The development of CloudSat and CALIPSO products and comprehensive validation efforts (including *in situ* flux measurements) are necessary in order to have confidence in the heating and cooling rate products. Indeed, a few efforts have been undertaken to attempt radiation closure analyses whereby fluxes are measured throughout the column to look for model deficiencies, but the *in situ* measurement of fluxes is a highly non-trivial task [*Valero et al.*, 1996].

From a remote-sensing perspective, heating/cooling rates below clouds are very difficult to constrain because top-of-atmosphere measurements at most wavelengths are insensitive to the atmospheric state parameters that are necessary for calculating heating/cooling rate profiles. Efforts to retrieve heating and cooling rate values will benefit from the presence of comprehensive measurements at the ARM sites [*Stokes and Schwartz*, 1994] which are able to

constrain heating rates in the lower troposphere similar to the combined ability of CloudSat and CALIPSO in the upper troposphere.

9.3   Problems Amenable to Heating Rate Analysis

There are many potential avenues for future research directed towards understanding radiative heating and cooling rates using remote-sensing measurements. An example of scientifically relevant analysis of heating and cooling rates to determine energy balance within the Tropical Tropopause Layer was discussed in some detail in Chapter 7. This shows how it may be possible to utilize remote sensing data to understand subtle transport processes that are controlled by radiative heating and cooling.

There are many other possibilities for analysis of remote sensing data with respect to heating and cooling rate profiles. As of the writing of this thesis, there are several open questions in the scientific community regarding the control that radiative processes exert on observed circulation patterns. First, it has been hypothesized that rotational-band water vapor cooling exerts a strong control on cirrus detrainment from convective cloud anvils [*Hartmann and Larson*, 2002]. This so-called Fixed-Anvil Temperature (FAT) hypothesis has been the subject of a large amount of scientific discussion and is thought to be invariant under climate change scenarios. The current set of A-Train measurements from AIRS, CloudSat, and CALIPSO would be able to describe convective cloud scenes, water vapor, and cirrus detrainment, and the cooling rates in the upper troposphere as described by these measurements would provide a real-world test of this hypothesis. Moreover, future development of far-IR monitoring missions such as CLARREO may allow for a direct characterization of the rotational band processes that may be influencing the hypothesized control on anvil detrainment.

Second, some of the dynamical aspects of cloud formation and dissolution described by *Houze* [1994] indicate that an important role is played by radiation in the maintenance of cloud structure over the cloud lifetime. It may be useful to examine the details of cloud radiative heating and cooling to determine whether radiative subsidence and uplifting as derived from measurements lead to cloud dynamical evolution that agrees with model calculations.

Finally, while radiative heating and cooling rates are not the dominant mechanisms in the determination of stratospheric circulation, they do exert significant control over the residual circulation in the stratosphere. Studies such as those described by *Pierce et al.* [1993] offer a path of analysis for the interaction of dynamics and radiation during sudden stratospheric warming events. Analysis of heating and cooling rates derived from measurements can provide a more-detailed look at the balance of processes governing these events.

## 9.4   Comparison of Heating Rates in Models and Measurements
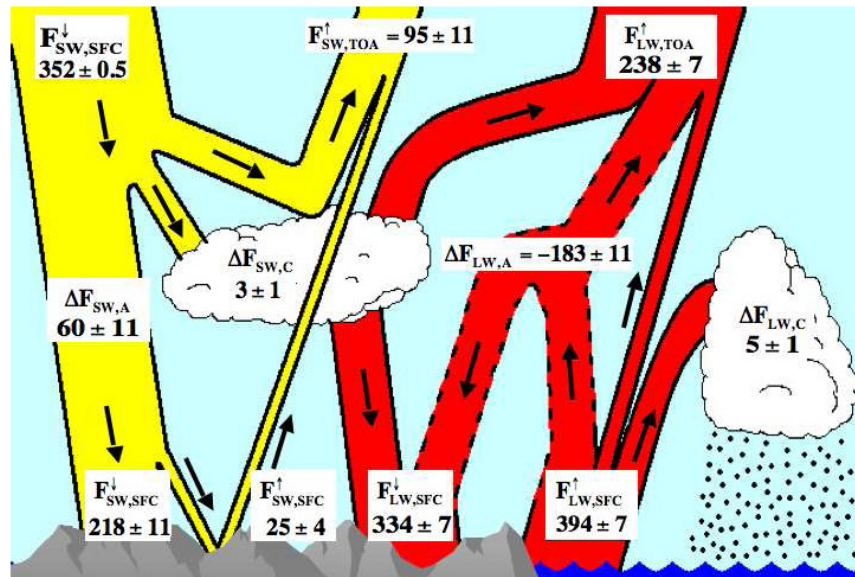
Figure 9.1: From *L'Ecuyer et al.* [2008]. Annual mean radiation budget for the Earth from 82° N to 82° S derived from the CloudSat 2B-FLXHR product from September 2006 to August 2007. Contribution to atmospheric radiative heating from clear skies are represented by $\Delta F_{SW/LW,A}$ and those due to clouds are represented by $\Delta F_{SW/LW,C}$.
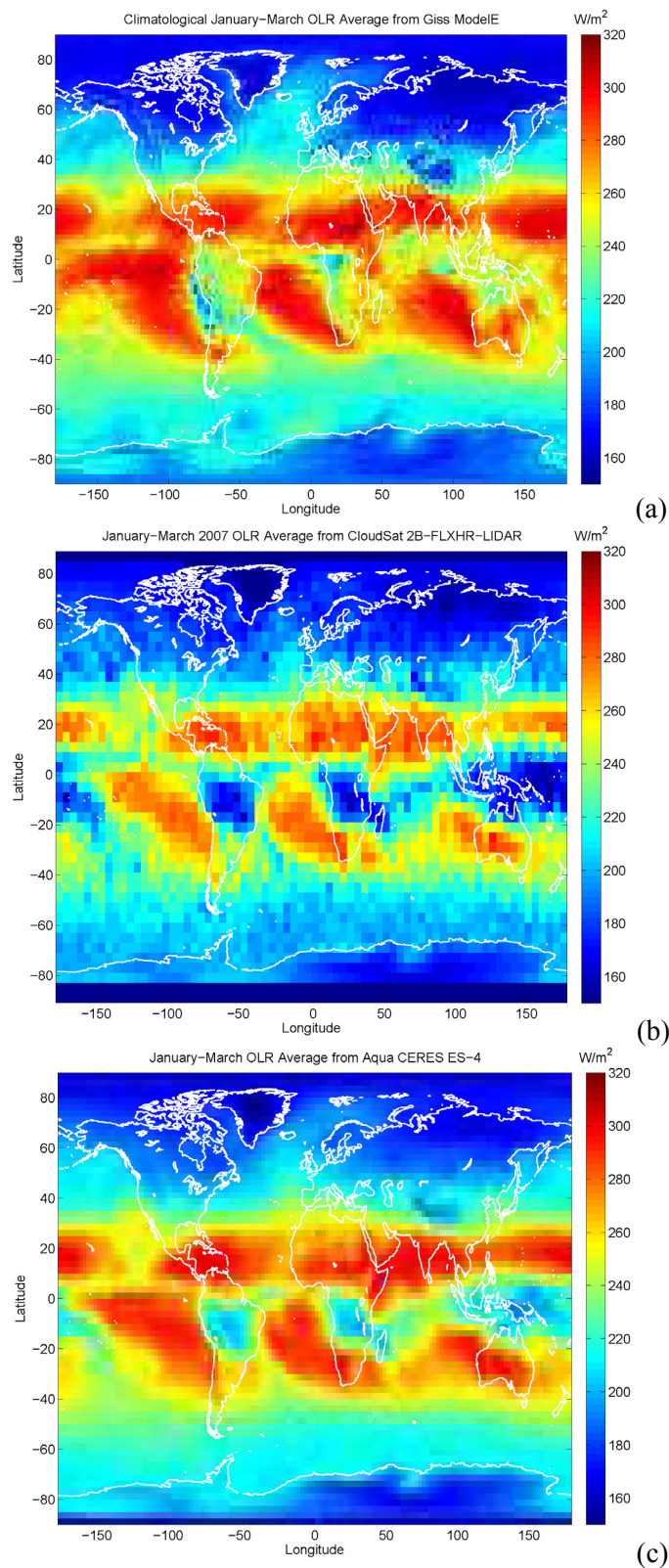
Figure 9.2: (a) Mean Outgoing Longwave Radiation from the GISS ModelE OLR for a climatological January –March (b) OLR derived from CloudSat 2B-FLXHR-LIDAR product for January–March 2007. (c) OLR from Aqua CERES for January–March 2007.

One of the outstanding issues associated with this research is the establishment of methods for the comparison of heating/cooling rates derived from measurements with those calculated in the course of model runs. For example, initial estimates of the radiative energy balance have been derived from CloudSat data, and a significant amount of information can be gained by comparing the figures shown in Figure 1.3 with those estimated in Figure 9.1. Whereas the top-of-atmosphere solar and thermal fluxes are very similar to those derived from other missions (i.e., [*Barkstrom et al.*, 1984; *Wielicki et al.*, 1996]), the estimates of surface fluxes differ rather substantially between the former and latter figures. Also, estimates of the distribution of radiative energy exchange within the atmosphere from measurements such as CloudSat are novel.

While CloudSat and CALIPSO measurements coupled with ECMWF analysis products can allow for the determination of OLR and heating and cooling rates, it is important to compare these values with those calculated in models. An example of this can be seen in Figure 9.2 which first shows the OLR associated with the GISS ModelE [*Schmidt et al.*, 2006] run of a climatological period covering January–March. Also shown are the CloudSat-derived OLR from the 2B-FLXHR-LIDAR product (see *L'Ecuyer et al.* [2008] for details) from January–March, 2007, and the Aqua CERES ES-4 OLR measurements for that same time period.

Several different features can be seen in the OLR comparison: first, sub-tropical OLR values generally agree among CloudSat/CALIPSO, CERES, and GISS ModelE. Second, the influence of convection on OLR in the GISS model generally agrees qualitatively with the CERES measurement, with some difficulties in the regions of the strongest convection in the equatorial tropics. Finally, the description of the cloud radiative effect associated with tropical convection from CloudSat/CALIPSO tends to be overestimated as compared to the CERES measurement suite.
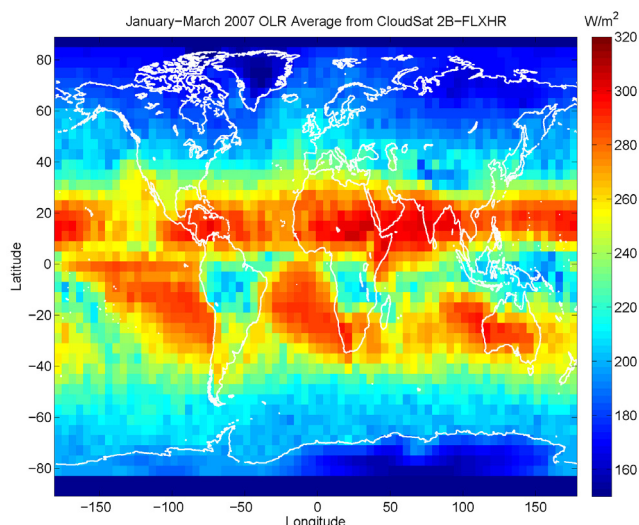
Figure 9.3: OLR derived from CloudSat 2B-FLXHR product for January–March 2007.

However, some of the discrepancies between CERES and the 2B-FLXHR-LIDAR product can be
attributed to the simplified treatment of thin cirrus clouds. Figure 9.3 shows the OLR product
from the 2B-FLXHR (without the estimates of thin-cloud properties from lidar). The agreement
between CERES measurements and CloudSat 2B-FLXHR products is considerably improved
over Figure 9.2b, suggesting that the algorithm for combining CloudSat and CALIPSO data may
benefit from refinement. However, as has been previously discussed, the production of similar
OLR values from measurements and models is a necessary but not a sufficient condition for
determining whether a model is treating the radiative budget of the scene appropriately.

Figure 9.4 compares the zonally averaged cooling rate profiles derived from CloudSat
over the same period of time described by the 2B-FLXHR and 2B-FLXHR-LIDAR products.
Figure 9.4a shows several interesting features, including lower-stratospheric IR heating from
ozone (regions of blue) and tropospheric cooling from water vapor (regions of green and yellow).
It also shows the influence of clouds on cooling rates in the tropical mid troposphere due to
convective clouds, and in the mid-latitude lower troposphere due to stratus clouds.
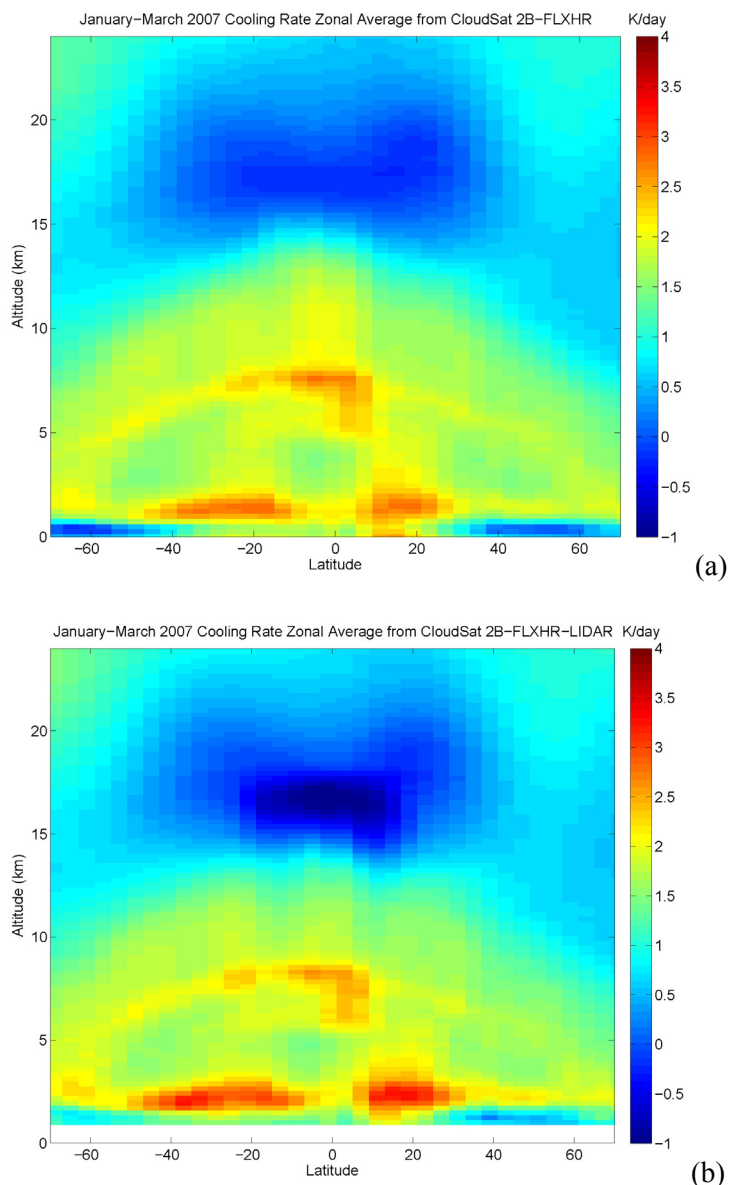
Figure 9.4: (a) Zonally averaged cooling rate profile contour map for January–March 2007 derived from the CloudSat 2B-FLXHR product. (b) Same as (a) but depicting results from the 2B-FLXHR-LIDAR product.

There are some subtle differences between the top and bottom panels of Figure 9.4, and a zeroeth-order estimate of the impact of optically thin clouds on cooling rate profiles can be attained from these differences. These results, though preliminary, suggest that mid-tropospheric cooling at most latitudes is well described by the A-Train, but that there is some remaining uncertainty in the characterization of cooling rates in the low-latitude stratosphere and the boundary layer at most latitudes.

Meanwhile, the characterization of cooling rates in the models shows a considerably different pattern. The following figure shows zonal average cooling rate profiles calculated from a GISS ModelE control run that produces the OLR fields shown in Figure 9.2a.
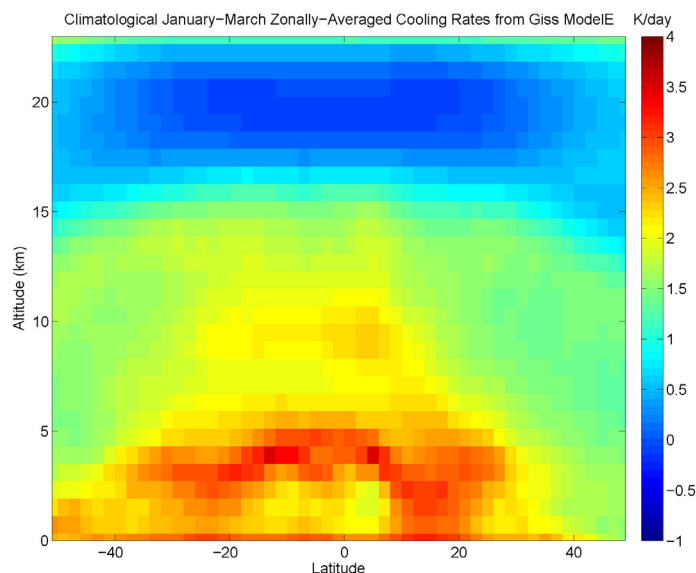

Figure 9.5: Zonally averaged cooling rate profile contour map from GISS ModelE results for a climatological January–March.

There are several notable differences between the cooling rates derived from measurements and those produced by the GISS model, despite qualitative agreement in OLR. The model produces substantial lower-tropospheric cooling rates that gradually decrease with altitude. Also, lower-stratospheric IR heating is slightly lower in the model, as compared to the CloudSat product.

One of the principal benefits of a comparison between heating rates derived from measurements and those calculated in models is that the comparison is on a lower dimension, as opposed to the separate comparisons of temperature, water vapor, ozone, and cloud fields. Moreover, the values of heating and cooling rates are directly relevant to (and calculated by) climate models. They are also much more specific than the comparisons of broadband top-of-atmosphere albedo and outgoing longwave radiation (i.e., Figure 6.2).

The determination of appropriate comparison methods depends on the specific goals of the comparison. For exploratory analysis of measurement and model heating/cooling rates, comparing mean heating and cooling rates or a relatively straightforward multivariate analysis of variance may be sufficient to make a determination about the statistical significance of whether two isolated heating/cooling rate profiles are similar.

One of the most important goals of research devoted to the understanding of heating/cooling rate profiles is the determination of whether the balance of different energy exchange processes is being adequately represented by model calculations at large grid footprints. Therefore, it may be necessary to understand not just radiative energy exchange, but also the latent heat budget. The latter information can be determined by precipitation measurements where they exist. For this the Tropical Rainfall Measuring Mission (TRMM) [*Kummerow et al.*, 1998] provides a decade-long set of precipitation data in the tropics. Also, the Advanced Microwave Scanning Radiometer [*Kawanishi et al.*, 2003] provides column-integrated precipitation retrievals over oceans which may be useful for assessing measurement and model energy balance. Unfortunately, other estimates of global precipitation (i.e., the Global Precipitation Climatology Project [*Adler et al.*, 2003]) are spatially sparse.

9.5   Challenges for Future Analysis and Observing Systems

The scientific community has attained a much greater understanding of the Earth-atmosphere system as a result of model development and satellite-based measurement system implementation. This understanding has been used to motivate serious policy discussions with respect to climate change among both the public and policy-makers. However, at the same time, the community has been unable to make substantial progress in reducing the uncertainty in climate forecast predictions for the next 50–100 years. Such continued uncertainty has partially

thwarted a cohesive climate change policy and suggests that the current organization of research efforts in the field of climate prediction may require new directions. It would be fruitful for the diverse community of measurement specialists and modeling experts to work more in tandem to focus their considerable intellectual, computational, and engineering capabilities on the elucidation of climate feedbacks. Moreover, if the dire consequences of climate change are realized, policy makers will have an urgent need for robust scientific recommendations regarding this topic, and the scientific community should be prepared to adopt a dramatically more central role in climate change policy.

The new generation of satellite missions recommended by the Decadal Survey of the Space Studies Board of the National Research Council, plus the realization of the capabilities of the current generation of A-Train instrumentation, promise to provide a foundation for moving forward in the establishment of a coherent set of measurements. Such measurements can be utilized on a large scale with models in support of integrated climate feedback studies. One can hope that the research in this thesis will facilitate more scientific studies that integrate measurements and models in a manner that will ultimately be of social relevance.

Appendix A. Cooling Rate Retrieval Derivation.

Remote sensing measurements provide information about quantities that are relevant to the calculation of cooling rate profiles, so it is reasonable to conclude that there is a functional relationship between these measurements and cooling rate profiles. This relationship will be explored in some detail in this Appendix, following the work of *Liou and Xue* [1988].

The derivation of retrieval of cooling rate profiles from top-of-atmosphere (TOA) spectra begins by establishing a relationship between atmospheric cooling rates and measured spectra. The cooling rate profile for a specific set of wavenumbers is a function of height and is given by:

$$\theta'_{\bar{v}}(z) = \frac{1}{C_p \rho(z)} \frac{dF_{\bar{v}}(z)}{dz}$$
(A.1)

where $\theta'_{\bar{v}}(z)$ is the cooling rate and $F_{\bar{v}}(z)$ is the net flux over a set of wavenumbers $\bar{v}$, C_p is the specific heat at constant pressure, and $\rho(z)$ is the atmospheric density. By ansatz, a kernel function can be introduced that relates the cooling rate to the TOA measurement, and that kernel function is given by:

$$K_v(z) = C_p \rho(z) T_v(z, \infty, \mu = 0)$$
(A.2)

where $T_v(z, \infty, \mu = 0)$ is the monochromatic transmittance between height z and the top-of-atmosphere at viewing zenith angle cosine μ. When the quantity of interest is convolved with the kernel function, a measurement functional is produced which is given by:

$$f_v = \int_0^\infty K_v(z) \theta'_{\bar{v}}(z) dz$$
.
(A.3)

Given the formulation for the net flux is derived from integrating the equation of radiative transfer over altitude and angle, and the flux divergence follows from a differentiation of net flux

with respect to the height coordinate, the following expression describes clear-sky flux

divergence without a loss of generality:

$$
\frac{dF_{\bar{v}}(z)}{dz} = \begin{cases}
2\pi B_{\bar{v}}\left(\theta_{surf}\right)\int_0^1 \frac{\partial}{\partial z}\left(T_{\bar{v}}\left(\frac{z}{\mu}\right)\right)\mu d\mu + \\[2mm]
2\pi\int_0^1 \mu d\mu\left\{\int_0^z B_{\bar{v}}\left(\theta(z')\right)\frac{\partial}{\partial z}\left(T_{\bar{v}}\left(\frac{z-z'}{\mu}\right)\right) + B_{\bar{v}}\left(\theta(z)\right)\frac{d}{dz}\left(T_{\bar{v}}\left(\frac{z-z'}{\mu}\right)\right)dz'\right\} - \\[2mm]
2\pi\int_0^1 \mu d\mu\left\{\int_z^\infty B_{\bar{v}}\left(\theta(z')\right)\frac{\partial}{\partial z}\left(T_{\bar{v}}\left(\frac{z'-z}{\mu}\right)\right) + B_{\bar{v}}\left(\theta(z)\right)\frac{d}{dz}\left(T_{\bar{v}}\left(\frac{z'-z}{\mu}\right)\right)dz'\right\}
\end{cases} \quad \text{(A.4)}
$$

In order to establish a functional relationship between cooling rates and remote sensing

measurements, a simplified band model can be illustrative. The random model [*Goody*, 1952] as

modified by *Möller and Raschke* [1964] expresses the transmittance as a function of absorber

amount for narrow spectral bands:

$$
T_v(\eta,\mu) = \exp\left[-\frac{a\sigma_v\eta}{\mu}\left(1+\frac{b\sigma_v\eta}{\mu}\right)^{1/2}\right] \quad \text{(A.5)}
$$

where a and b are band-specific coefficients, σ_v is the monochromatic absorption coefficient,

and η is the absorber path length given by:

$$
\eta = u\left(\frac{p}{p_{surf}}\right)^n \quad \text{(A.6)}
$$

where u is the optical path, p is the pressure at level of interest, and p_{surf} is the surface

pressure. In the weak-line limit, the transmission function reduces to the following expression:

$$
T_v\left(\frac{\eta}{\mu}\right) = \exp\left(-\frac{a\sigma_v\eta}{\mu}\right) \quad . \quad \text{(A.7)}
$$

The convolution of the weighting function in Eq. (A.2) with the flux divergence profile produces the following expression:

$$f_v = \int_0^\infty \exp\left(-\frac{a\sigma_v\eta}{\mu}\right)\frac{dF(\eta)}{d\eta}d\eta \tag{A.8}$$

where f_v is the measurement functional. The task then is to determine the relationship between the expression in Eq. (A.8) and TOA radiance measurements. By inserting Eq. (A.4) into the RHS of Eq. (A.8), the following expression is achieved:

$$f_v = \begin{cases} 2\pi(a\sigma)^2 \int_0^{\eta_1} \exp\left(-\frac{a\sigma_v\eta}{\mu}\right)\left\{\int_\eta^{\eta_1} B(\eta')\int_0^1 \exp\left(-\frac{a\sigma(\eta'-\eta)}{\mu'}\right)\frac{d\mu'}{\mu'}d\eta'\right\}d\eta + \\ 2\pi(a\sigma)^2 \int_0^{\eta_1} \exp\left(-\frac{a\sigma_v\eta}{\mu}\right)\left\{\int_0^\eta B(\eta')\int_0^1 \exp\left(-\frac{a\sigma(\eta-\eta')}{\mu'}\right)\frac{d\mu'}{\mu'}d\eta'\right\}d\eta + \\ 2\pi(a\sigma)B(\eta_1)\int_0^{\eta_1} \exp\left(-\frac{a\sigma_v\eta}{\mu}\right)\int_0^1 \exp\left(-\frac{a\sigma(\eta-\eta')}{\mu'}\right)d\mu'd\eta - \\ 4\pi(a\sigma)\int_0^{\eta_1} B(\eta)\exp\left(-\frac{a\sigma_v\eta}{\mu}\right)d\eta \end{cases} \tag{A.9}$$

These terms must be evaluated separately. By exchanging the order of integration for the first term of the RHS of Eq. (A.9), we find that:

$$\int_0^\infty \int_0^1 \exp\left(-\frac{a\sigma_v\eta'}{\mu}\right)\frac{d\mu'/\mu'}{l\left(1/\chi_v^2 - 1/\mu'\right)}d\eta' =$$
$$\int_0^\infty \exp\left(-\frac{a\sigma_v\eta'}{\bar{\mu}}\right)d\eta'\frac{\chi_v}{\sigma}\ln\left(1-\frac{1}{\chi_v}\right) \tag{A.10}$$

where $\chi_v = \frac{\sigma}{\sigma_v}\mu$. Integration of the LHS of Eq. (A.10) though the use of the Mean Value Theorem leads to a different RHS from that of Eq. (A.10), and since the forms of integration must yield identical answers, it can be shown that:

$$\int_0^\infty \int_0^1 \exp\left(-\frac{a\sigma_v \eta'}{\mu}\right) \frac{d\mu'/\mu'}{\sigma\left(1/\chi_i^2 - 1/\mu'\right)} d\eta' = \frac{\overline{\mu}\chi_v}{al^2} \ln\left(1 - \frac{1}{\chi_v}\right) \tag{A.11}$$

where

$$\overline{\mu} = \frac{1 + \chi_v \ln\left(1 - \frac{1}{\chi_v}\right)}{\ln\left(1 - \frac{1}{\chi_v}\right)} \qquad . \tag{A.12}$$

Moreover, since the emergent TOA spectral radiance can be expressed as

$$I_v(\mu) = \frac{a\sigma_v}{\mu} \int_0^{\eta_1} B_v(\eta') \exp\left(-\frac{a\sigma_v \eta'}{\mu}\right) d\eta' \qquad . \tag{A.13}$$

A very similar expression can be formulated for the TOA radiance over the entire band. Since Planck emission is nearly a constant function of wavenumber over the band of interest, it can be shown that the first term on the RHS of Eq. (A.9) can also be described by:

$$2\pi\chi_v \ln\left(1 - \frac{1}{\chi_v}\right) \left(\overline{\mu} I(\overline{\mu}) - \chi_v I_v(\mu)\right) \qquad . \tag{A.14}$$

Similar procedures can be followed for the second term on the RHS of Eq. (A.9) which yields the following expression:

$$2\pi\chi_v^2 \ln\left(1 + \frac{1}{\chi_v}\right) I_v(\mu) \qquad . \tag{A.15}$$

The third term of the RHS of Eq. (A.9) can be derived by performing integration analytically with respect to η. The result is a negative exponential function with η_{surf} as its primary argument. For large optical paths, this term approaches zero. The final term on the RHS of Eq. (A.9) can be related directly to Eq. (A.13) and we can show that it can be described as

$$-4\pi\chi_i I_i(\mu) \qquad . \tag{A.16}$$

Therefore, the resulting expression for Eq. (A.9) becomes

$$
f_v = I(\bar{\mu}) 2\pi \chi_v \left[1 + \chi_v \ln\left(1 - \frac{1}{\chi_v} \right) \right] +
$$
$$
I_v(\mu) 2\pi \chi_v \left\{ \chi_v \left[\ln\left(1 + \frac{1}{\chi_v} \right) - \ln\left(1 - \frac{1}{\chi_v} \right) \right] - 2 \right\}
$$

(A.17)

This expression can also be applied to strong lines in a similar manner as described above to show that:

$$
f_v = \begin{cases} I_{\bar{v}}(\bar{\mu}) * 4\pi \chi_v^{1/2} \left[\dfrac{1}{3} + \dfrac{1}{2} \chi_v^{1/2} + \chi_v + \chi_v^{3/2} \ln\left(1 - \chi_v^{-1/2} \right) \right] + \\ I_v * 4\pi \chi_v \left\{ \chi_v \ln \dfrac{\left(1 + \chi_v^{-1/2} \right)}{\left(1 - \chi_v^{-1/2} \right)} - 2 \chi_v^{1/2} - \dfrac{3}{8} \right\} \end{cases}
$$

(A.18)

where $\bar{\mu}$ can be represented by the following:

$$
\bar{\mu} = \frac{\frac{1}{3} + \frac{1}{2} \chi_v^{1/2} + \chi_v + \chi_v^{3/2} \ln\left(1 - \chi_v^{-1/2} \right)}{\frac{1}{2} + \chi_v^{1/2} + \chi_v \ln\left(1 - \chi_v^{-1/2} \right)}
$$

(A.19)

Therefore, these results present a set of expressions relating measured TOA radiance with the convolution of the band cooling rate profile with the kernel function. Inverse theory methods can be applied so that TOA spectral radiance measurements at several viewing angles can be used to retrieve the cooling rate profile over the band.

References.

Abramowitz, M., and I. A. Stegun (1964), *Handbook of Mathematical Functions*, National Institute of Standards and Technology, Gaithersburg, Maryland.

Ackerman, T. P., et al. (1988), Heating Rates in Tropical Anvils, *Journal of the Atmospheric Sciences*, *45*, 1606–1623.

Adler, R. F., et al. (2003), The version-2 global precipitation climatology project (GPCP) monthly precipitation analysis (1979–present), *Journal of Hydrometeorology*, *4*, 1147–1167.

Allan, R. P., and M. A. Ringer (2002), Influence of dynamics on the changes in tropical cloud radiative forcing during the 1998 El Nino, *Journal of Climate*, *15*, 1979–1986.

Anderson, G. P., S. A. Clough, F. X. Kneizys, J. H. Chetwynd, E. P. Shettle (1986), AFGL atmospheric constituent profiles (0–120 km). *AFGL-TR_86-0110,* Hanscom AFB, MA.

Anderson, J. G., et al. (2004), Absolute, spectrally-resolved, thermal radiance: a benchmark for climate monitoring from space, *Journal of Quantitative Spectroscopy & Radiative Transfer*, *85*, 367–383.

Andersson, E., et al. (1994), Use of Cloud-Cleared Radiances in 3-Dimensional 4-Dimensional Variational Data Assimilation, *Quarterly Journal of the Royal Meteorological Society*, *120*, 627–653.

Asano, S., and Y. Yoshida (2004), Development of a radiometer-sonde for simultaneously measuring the downward and upward broadband fluxes of shortwave and longwave radiation, *Journal of the Meteorological Society of Japan*, *82*, 623–637.

Asrar, G., and J. Dozier (1994), *EOS: Science Strategy for the Earth Observing System*, 128 pp., American Institute of Physics, Melville, New York.

Aumann, H. H., et al. (2003), AIRS/AMSU/HSB on the aqua mission: Design, science objectives, data products, and processing systems, *IEEE Transactions on Geoscience and Remote Sensing*, *41*, 253–264.

Aumann, H. H., et al. (2005), AIRS hyper-spectral measurements for climate research: Carbon dioxide and nitrous oxide effects, *Geophysical Research Letters*, *32*.

Austin, R. T., and G. L. Stephens (2001), Retrieval of stratus cloud microphysical parameters using millimeter-wave radar and visible optical depth in preparation for CloudSat – 1. Algorithm formulation, *Journal of Geophysical Research-Atmospheres*, *106*, 28233–28242.

Austin, R. T. (2007), Level 2B Radar-only Cloud Water Content (2B-CWC-RO) Process Description Document, http://www.cloudsat.cira.colostate.edu/ICD/2B-CWC/2B-CWC-RO_PD_5.1.pdf .

AVE (2005), AURA Validation Data Center (http://avdc.gsfc.nasa.gov), NASA, Greenbelt, MD.

Baer, F., N. Arsky, J. J. Charney, and R. G. Ellingson (1996), Intercomparison of heating rates generated by global climate model longwave radiation codes, *Journal of Geophysical Research-Atmospheres*, 101(D21), 26589–26603.

Baer, D. S., et al. (2002), Sensitive absorption measurements in the near-infrared region using off-axis integrated-cavity-output spectroscopy, *Applied Physics B-Lasers and Optics*, *75*, 261–265.

Barath, F. T. (1993), The Upper-Atmosphere Research Satellite Microwave Limb Sounder Instrument, *Journal of Geophysical Research-Atmospheres*, *98*, 10751–10762.

Barkstrom, B. R. (1984), The Earth Radiation Budget Experiment (ERBE), *Bulletin of the American Meteorological Society*, *65*, 1170–1185.

Barnet, C. D., S. Datta, and L. Strow (2003), Trace Gas measurements from the Atmospheric Infrared Sounder (AIRS), *Optical Remote Sensing*, OSA Technical Digest, paper OWB2.

Beer, R., T. A. Glavich, and D. M. Rider (2001), Tropospheric emission spectrometer for the Earth Observing System's Aura satellite, *Applied Optics,* 40, 2356–2367.

Beer, R., K. Bowman, et al. (2004), Tropospheric Emission Spectrometer (TES) Level 2 Algorithm Theoretical Basis Document, http://tes.jpl.nasa.gov/docsLinks/DOCUMENTS/TES.ATBD.L2.V1.99.v10.pdf

Benedetti, A., et al. (2003), Ice cloud microphysics retrievals from millimeter radar and visible optical depth using an estimation theory approach, *Journal of Geophysical Research-Atmospheres*, *108*.

Berg, B. A. (2004), *Markov Chain Monte Carlo Simulations and Their Statistical Analysis*, 380 pp., World Scientific, Singapore.

Berk, A., et al. (1989), MODTRAN: A moderate resolution model for LOWTRAN 7, 38 pp, AFGL, Bedford, MA.

Bergman, J. W., and H.H. Hendon (1998), Calculating monthly radiative fluxes and heating rates from monthly cloud observations, *Journal of the Atmospheric Sciences, 55*, 3471–3491.

Carli, B., and J. H. Park (1988), Simultaneous Measurement of Minor Stratospheric Constituents with Emission Far-Infrared Spectroscopy, *Journal of Geophysical Research-Atmospheres*, *93*, 3851–3865.

Cess, R. D., et al. (1991), Determining Surface Solar Absorption from Broad-Band Satellite Measurements for Clear Skies – Comparison with Surface Measurements, *Journal of Climate*, *4*, 236–247.

Cess, R. D., et al. (2001), The influence of the 1998 El Nino upon cloud-radiative forcing over the Pacific warm pool, *Journal of Climate*, *14*, 2129–2137.

Chalon, G., et al. (2001), IASI: An Advanced Sounder for Operational Meteorology, paper presented at Proceedings of the 52nd Congress of the IAF, Toulouse, France, 1–5 Oct., 2001.

Chang, L. H., et al. (2003), Clouds and the Earth's Radiant Energy System Data Management System Draft ES-8 Collection Guide, R3.4, 77 pp, NASA Langley Research Center, Hampton, Va.

Chen, T., et al. (2000), Sensitivity of atmospheric radiative heating rate profiles to variations of cloud layer overlap, *Journal of Climate*, *13*, 2941–2959.

Clough, S. A., et al. (1989), Line shape and water vapor continuum, *Atmospheric Research*, *23*, 229–241.

Clough, S. A., M. J. Iacono, and J. L. Moncet (1992), Line-by-line calculation of atmospheric fluxes and cooling rates: Application to water vapor, *Journal of Geophysical Research*, 97(D14), 15761–15785, 10.1029/92JD01419.

Clough, S.A., and M.J. Iacono (1995), Line-by-line calculations of atmospheric fluxes and cooling rates II: Application to carbon dioxide, ozone, methane, nitrous oxide, and the halocarbons, *Journal of Geophysical Research,* 100, 16,519–16,535.

Clough, S.A., M. W. Shephard, E. Mlawer, J. S. Delamere, M. Iacono, K. Cady-Pereira, S. Boukabara, and P. D. Brown (2005), Atmospheric radiative transfer modeling: a summary of the AER codes, *Journal of Quantitative Spectroscopy & Radiative Transfer*, *91* (2), 233–244.

Collins, W. D. (2001), Parameterization of generalized cloud overlap for radiative calculations in general circulation models, *Journal of the Atmospheric Sciences*, *58*, 3224–3242.

Collins, W. D., et al. (2006), Radiative forcing by well-mixed greenhouse gases: Estimates from climate models in the Intergovernmental Panel on Climate Change (IPCC) Fourth Assessment Report (AR4), *Journal of Geophysical Research-Atmospheres*, *111*.

Committee on Earth Science and Applications from Space: A Community Assessment and Strategy for the Future, N. R. C. (2007), *Earth Science and Applications from Space: National Imperatives for the Next Decade and Beyond*, National Academies Press, Washington, D. C.

Cooper, S. J., et al. (2006), Objective assessment of the information content of visible and infrared radiance measurements for cloud microphysical property retrievals over the global oceans. Part II: Ice clouds, *Journal of Applied Meteorology and Climatology*, *45*, 42–62.

Corti, T., et al. (2005), Mean radiative energy balance and vertical mass fluxes in the equatorial upper troposphere and lower stratosphere, *Geophysical Research Letters*, *32*.

Courtier, P., et al. (1994), A Strategy for Operational Implementation of 4d-Var, Using an Incremental Approach, *Quarterly Journal of the Royal Meteorological Society*, *120*, 1367–1387.

Courtier, P., et al. (1998), The ECMWF implementation of three-dimensional variational assimilation (3D-Var). I: Formulation, *Quarterly Journal of the Royal Meteorological Society*, *124*, 1783–1807.

Darnell, W. L., et al. (1983), Downward Longwave Radiation at the Surface from Satellite Measurements, *Journal of Climate and Applied Meteorology*, *22*, 1956–1960.

DeGroot, M. H. (1970), *Optimal Statistical Decisions*, 505 pp., McGraw-Hill Book Company, New York City.

Dongarra, J., et al. (2006), *Applied Parallel Computing*, 563–572 pp., Springer, Berlin.

Ellingson, R. G., and Y. Fouquart (1991), The Intercomparison of Radiation Codes in Climate Models – an Overview, *Journal of Geophysical Research-Atmospheres*, *96*, 8925–8927.

Ellis, J. S., and T. H. V. Haar (1976), Zonal average earth radiation budget measurements from satellites for climate studies, 57 pp, Colorado State University, Fort Collins, CO.

Feldman D. R., K. N. Liou, Y. L. Yung, D. C. Tobin, A. Berk (2006), Direct retrieval of stratospheric CO_2 infrared cooling rate profiles from AIRS data, *Geophysical Research Letters* 33, L11803.

Feldman, D. R., et al. (2008), On the Information Content of the Thermal Infrared Cooling Rate Profile from Satellite Instrument Measurements, *Journal of Geophysical Research-Atmospheres*, (*accepted)*.

Fisher, R. A. (1925), Theory of Statistical Estimation, *Proceedings of the Cambridge Philosophical Society*, 22, 700–725.

Fu, Q., and K. N. Liou (1993), Parameterization of the Radiative Properties of Cirrus Clouds, *Journal of the Atmospheric Sciences*, *50*, 2008–2025.

Fu, Q., et al. (1997), Multiple scattering parameterization in thermal infrared radiative transfer, *Journal of the Atmospheric Sciences*, *54*, 2799–2812.

Fu, Q., et al. (2007), Identifying the top of the tropical tropopause layer from vertical mass flux analysis and CALIPSO lidar cloud observations, *Geophysical Research Letters*, *34*.

Fu, R., et al. (1992), Cirrus-Cloud Thermostat for Tropical Sea-Surface Temperatures Tested Using Satellite Data, *Nature*, *358*, 394–397.

Fueglistaler, S., and Q. Fu (2006), Impact of clouds on radiative heating rates in the tropical lower stratosphere, *Journal of Geophysical Research-Atmospheres*, 111.

Gaiser, S. L., H. H. Aumann, L.L. Strow, S. Hannon, and M. Weiler (2003), In-flight Spectral Calibration of the Atmospheric Infrared Sounder, *IEEE Transactions on Geoscience and Remote Sensing*, 41, 287–297.

Gelman, A., et al. (2004), *Bayesian Data Analysis*, 2nd ed., 668 pp., Chapman and Hall, Boca Raton, Florida.

Geman, S., and D. Geman (1984), Stochastic Relaxation, Gibbs Distributions, and the Bayesian Restoration of Images, *IEEE Transactions on Pattern Analysis and Machine Intelligence*, *6*, 721–741.

Gettelman, A., and P. M. D. Forster (2002), A climatology of the tropical tropopause layer, *Journal of the Meteorological Society of Japan*, *80*, 911–924.

Gettelman A., P. M. de F. Forster, M. Fujiwara, Q. Fu, H. Vömel, L. K. Gohar, C. Johanson, and M. Ammerman (2004), Radiation balance of the tropical tropopause layer, *Journal of Geophysical Research*, 109, D07103, doi:10.1029/2003JD004190.

Gettelman, A., and T. Birner (2007), Insights on Tropical Tropopause Layer Processes using Global Models, *Journal of Geophysical Research-Atmospheres*, *In Press*.

Goody, R. M. (1952), A Statistical Model for Water-Vapour Absorption, *Quarterly Journal of the Royal Meteorological Society*, *78*, 165–169.

Goody, R. M., and Y. L. Yung (1989), *Atmospheric Radiation Theoretical Basis*, 519 pp., Oxford University Press, New York.

Gupta, S. K., et al. (1999), A climatology of surface radiation budget derived from satellite data, *Journal of Climate*, *12*, 2691–2710.

Hanel, R. A., B. Schlachman, D. Rogers, and D. Vanous (1971), Nimbus 4 Michelson interferometer, *Applied Optics.* 10, 1376–1382.

Hansen, J. E. (1971), Multiple Scattering of Polarized Light in Planetary Atmospheres .1. Doubling Method, *Journal of the Atmospheric Sciences*, *28*, 120–125.

Hansen, P. C. (1994), Regularization Tools: A Matlab Package for Analysis and Solution of Discrete Ill-Posed Problems, *Numerical Algorithms*, *6*, 1–35.

Harrison, E. F., et al. (1990), Seasonal-Variation of Cloud Radiative Forcing Derived from the Earth Radiation Budget Experiment, *Journal of Geophysical Research-Atmospheres*, *95*, 18687–18703.

Hartmann, D. L., J. R. Holton, and Q. Fu (2001), The heat balance of the tropical tropopause, cirrus, and stratospheric dehydration, *Geophysical Research Letters*, 28(10), 1969–1972, 10.1029/2000GL012833, 2001.

Hartmann, D. L., and K. Larson (2002), An important constraint on tropical cloud – climate feedback, *Geophysical Research Letters*, *29*.

Hicke, J., et al. (1999), Lower stratospheric radiative heating rates and sensitivities calculated from Antarctic balloon observations, *Journal of Geophysical Research-Atmospheres*, *104*, 9293–9308.

Highwood, E. J., and B. J. Hoskins (1998), The tropical tropopause, *Quarterly Journal of the Royal Meteorological Society*, *124*, 1579–1604.

Holton, J. R., and A. Gettelman (2001), Horizontal transport and the dehydration of the stratosphere, *Geophysical Research Letters*, *28*, 2799–2802.

Holton, J. R., et al. (1995), Stratosphere-Troposphere Exchange, *Reviews of Geophysics*, *33*, 403–439.

Houze, R. A. (1994), *Cloud Dynamics*, 573 pp., Academic Press, Burlington, MA.

Hu, Y. X., and K. Stamnes (1993), An Accurate Parameterization of the Radiative Properties of Water Clouds Suitable for Use in Climate Models, *Journal of Climate*, *6*, 728–742.

Huang, J. P., et al. (2006), Determination of ice water path in ice-over-water cloud systems using combined MODIS and AMSR-E measurements, *Geophysical Research Letters*, *33*.

Huang, X. L., et al. (2006), Quantification of the source of errors in AM2 simulated tropical clear-sky outgoing longwave radiation, *Journal of Geophysical Research-Atmospheres*, *111*.

Huang, Y., and V. Ramaswamy (2007), Effect of the temperature dependence of gas absorption in climate feedback, *Journal of Geophysical Research-Atmospheres*, *112*.

Huffman, A. C., et al. (1998), The Retrieval of Radiative Heating Rates in Cloudy Atmospheres: Test Cases Using ARM CART and IOP Data Results, paper presented at *Proceedings of the Eighth Atmospheric Radiation Measurement (ARM) Science Team Meeting*, Tucson, Arizona.

Iacono, M. J., E. J. Mlawer, S. A. Clough, and J. J. Morcrette (2000), Impact of an improved longwave radiation model, RRTM, on the energy budget and thermodynamic properties of the NCAR community climate model, CCM3, *Journal of Geophysical Research*, 105(D11), 14873–14890, 10.1029/2000JD900091.

IPCC, 2007: *Climate Change 2007: The Physical Science Basis. Contribution of Working Group I to the Fourth Assessment Report of the Intergovernmental Panel on Climate Change* [Solomon,

S., D. Qin, M. Manning, Z. Chen, M. Marquis, K.B. Averyt, M. Tignor and H.L. Miller (eds.)]. Cambridge University Press, Cambridge, United Kingdom and New York, NY, USA, 996 pp.

Jeffreys, H., and B. S. Jeffreys (1988), *Methods of Mathematical Physics*, 3rd ed., 718 pp., Cambridge University Press, Cambridge, England.

Johnson, D. G., et al. (1995), Smithsonian Stratospheric Far-Infrared Spectrometer and Data Reduction System, *Journal of Geophysical Research-Atmospheres*, *100*, 3091–3106.

Justice, C. O., et al. (1998), The Moderate Resolution Imaging Spectroradiometer (MODIS): Land remote sensing for global change research, *IEEE Transactions on Geoscience and Remote Sensing*, *36*, 1228–1249.

Kawanishi, T., et al. (2003), The Advanced Microwave Scanning Radiometer for the Earth Observing System (AMSR-E), NASDA's contribution to the EOS for global energy and water cycle studies, *IEEE Transactions on Geoscience and Remote Sensing*, *41*, 184–194.

Kay, J. E., et al. (2007), The contribution of cloud radiation anomalies to the 2007 Arctic sea ice extent minimum, *Geophysical Research Letters*, (*submitted*).

Kiehl, J. T., and S. Solomon (1986), On the Radiative Balance of the Stratosphere, *Journal of the Atmospheric Sciences*, *43* (14), 1525–1534.

Kiehl, J. T., and K. E. Trenberth (1997), Earth's annual global mean energy budget, *Bulletin of the American Meteorological Society*, *78*, 197–208.

Kratz, D. P., et al. (2005), An inter-comparison of far-infrared line-by-line radiative transfer models, *Journal of Quantitative Spectroscopy & Radiative Transfer*, *90*, 323–341.

Kulawik, S. S., et al. (2006), Implementation of cloud retrievals for Tropospheric Emission Spectrometer (TES) atmospheric retrievals: part 1. Description and characterization of errors on trace gas retrievals, *Journal of Geophysical Research-Atmospheres*, *111*.

Kummerow, C., et al. (1998), The Tropical Rainfall Measuring Mission (TRMM) sensor package, *Journal of Atmospheric and Oceanic Technology*, *15*, 809–817.

Lacis, A. A., and V. Oinas (1991), A Description of the Correlated Kappa-Distribution Method for Modeling Nongray Gaseous Absorption, Thermal Emission, and Multiple-Scattering in Vertically Inhomogeneous Atmospheres, *Journal of Geophysical Research-Atmospheres*, *96*, 9027–9063.

L'Ecuyer, T.S. (2001) *Uncertainties in Space-Based Estimates of Clouds and Precipitation: Implications for Deriving Global Diabatic Heating.* Ph.D. Thesis in Atmospheric Science, Colorado State University.

L'Ecuyer, T. S., et al. (2006), Objective assessment of the information content of visible and infrared radiance measurements for cloud microphysical property retrievals over the global oceans. Part I: Liquid clouds, *Journal of Applied Meteorology and Climatology*, *45*, 20–41.

L'Ecuyer, T. S. (2007), Level 2 Fluxes and Heating Rates Product Process Description and Interface Control Document, 21 pp, Cooperative Institute for Research in the Atmosphere, Fort Collins, Colorado.

L'Ecuyer, T. S., et al. (2008), The Impact of Clouds on the Atmospheric Radiation Budget in the R04 CloudSat Fluxes and Heating Rates Dataset, *Journal of Geophysical Research-Atmospheres*, (*in press)*.

Li, J., et al. (2005), Retrieval of cloud microphysical properties from MODIS and AIRS, *Journal of Applied Meteorology*, 44, 1526–1543.

Li, J. L., et al. (2007), Assessing consistency between EOS MLS and ECMWF analyzed and forecast estimates of cloud ice, *Geophysical Research Letters*, *34*.

Liou, K. N. (1974), Analytic 2-Stream and 4-Stream Solutions for Radiative-Transfer, *Journal of the Atmospheric Sciences*, *31*, 1473–1475.

Liou, K. N. (1980), *An Introduction to Atmospheric Radiation*, 392 pp., Academic Press, Burlington, MA.

Liou, K. N. (2002), *An Introduction to Atmospheric Radiation*, 2nd ed., 583 pp., Academic Press, San Diego, CA.

Liou, K. N., Y.K. Xue, (1988), Exploration of the remote sounding of infrared cooling rates due to water-vapor, *Meteorology and Atmospheric Physics*, 38(3), 131–139.

Loeb, N. G., et al. (2005), Angular distribution models for top-of-atmosphere radiative flux estimation from the Clouds and the Earth's Radiant Energy System instrument on the Terra satellite. Part I: Methodology, *Journal of Atmospheric and Oceanic Technology*, *22*, 338–351.

Loeb, N. G. (2003), Angular distribution models for top-of-atmosphere radiative flux estimation from the Clouds and the Earth's Radiant Energy System instrument on the Tropical Rainfall Measuring Mission satellite. Part II: Validation, *Journal of Applied Meteorology*, *42*, 1748–1769.

Lorenc, A. C. (1986), Analysis-Methods for Numerical Weather Prediction, *Quarterly Journal of the Royal Meteorological Society*, *112*, 1177–1194.

Mace, G. G. (2007), Global hydrometeor occurrence as observed by CloudSat: Initial observations from summer 2006, *Geophysical Research Letters*, *34*.

Mace, G. G. (2007), The Vertical Structure of Cloud Radiative Forcing at the ACRF SGP Revealed by 8 Years of Continuous Measurements, *Journal of Climate* (*accepted*).

Marchand, R., et al. (2007), Hydrometeor Detection using Cloudsat – an earth orbiting 94 GHz Cloud Radar, *Journal of Oceanic and Atmsopheric Technology (submitted)*.

Mather, J. H., et al. (2007), Cloud properties and associated radiative heating rates in the tropical western Pacific, *Journal of Geophysical Research-Atmospheres*, *112*.

May, R. D. (1998), Open-path, near-infrared tunable diode laser spectrometer for atmospheric measurements of H_2O, *Journal of Geophysical Research-Atmospheres*, *103*, 19161–19172.

McFarlane, S.A., J. H. Mather, and T. P. Ackerman (2007), Analysis of tropical radiative heating profiles: A comparison of models and observations, *Journal of Geophysical Research-Atmospheres, 112*, D14128, doi:10.1029/2006JD008290.

McFarquhar, G. M., and A. J. Heymsfield (1997), Parameterization of tropical cirrus ice crystal size distributions and implications for radiative transfer: Results from CEPEX, *Journal of the Atmospheric Sciences*, *54*, 2187–2200.

Mehta, A., and J. Susskind (1999), Outgoing longwave radiation from the TOVS Pathfinder Path A data set, *Journal of Geophysical Research-Atmospheres*, *104*, 12193–12212.

Meneghini, R., and T. Kozu (1990), *Spaceborne Weather Radar*, 208 pp., Artech House, Boston, MA.

Mertens, C. J. (2002), Feasibility of retrieving upper tropospheric water vapor from observations of far-infrared radiation, *Proceedings of the SPIE*, *4485*, 191–201.

Michelsen, H. A., et al. (2000), Features and trends in Atmospheric Trace Molecule Spectroscopy (ATMOS) version 3 stratospheric water vapor and methane measurements, *Journal of Geophysical Research-Atmospheres*, *105*, 22713–22724.

Mie, G. (1908), Articles on the optical characteristics of turbid tubes, especially colloidal metal solutions, *Annalen Der Physik*, *25*, 377–445.

Milman, A. S. (1999), *Mathematical Principles of Remote Sensing: Making Inferences from Noisy Data*, 406 pp., Sleeping Bear Press, Chelsea, MI.

Mishchenko, M. I., and L. D. Travis (1998), Capabilities and limitations of a current FORTRAN implementation of the T-matrix method for randomly oriented, rotationally symmetric scatterers, *Journal of Quantitative Spectroscopy & Radiative Transfer*, *60*, 309–324.

Mishchenko, M. I. (2006), Maxwell's equations, radiative transfer, and coherent backscattering: A general perspective, *Journal of Quantitative Spectroscopy & Radiative Transfer*, *101*, 540–555.

Mlawer, E. J., S. J. Taubman, P. D. Brown, M. J. Iacono, S. A. Clough (1997), Radiative transfer for inhomogeneous atmospheres: RRTM, a validated correlated-k model for the longwave, *Journal of Geophysical Research*, 102(D14), 16663–16682, 10.1029/97JD00237.

Mlawer, E.J., S. A. Clough, D. C. Tobin (2003), The MT_CKD Water Vapor Continuum: A Revised Perspective Including Collision Induced Effects, *Atmospheric Science from Space using Fourier Transform Spectrometry 10th Conference*, Bad Wildbad, Germany.

Mlynczak, M. G., C. J. Mertens, R. R. Garcia, R. W. Portmann (1999), A detailed evaluation of the stratospheric heat budget 2. Global radiation balance and diabatic circulations, *Journal of Geophysical Research*, 104(D6), 6039–6066, 10.1029/1998JD200099.

Mlynczak, M. G., et al. (2002), Far-infrared: a frontier in remote sensing of Earth's climate and energy balance, *Proceedings of the SPIE*, *4485*, 150–158.

Mlynczak, M. G. and D. G. Johnson, (2006a), INFLAME: In-situ net flux within the atmosphere of the Earth, *EOS Trans. AGU 87*(52), Fall Meet. Suppl., Abstract IN23B-04.

Mlynczak, M. G., et al. (2006b), First light from the Far-Infrared Spectroscopy of the Troposphere (FIRST) instrument, *Geophysical Research Letters*, 33, L07704, doi:10.1029/2005GL025114.

Moncet, J. L., and S. A. Clough (1997), Accelerated monochromatic radiative transfer for scattering atmospheres: Application of a new model to spectral radiance observations, *Journal of Geophysical Research-Atmospheres*, *102*, 21853–21866.

Morcrette, J.J. (1990), Impact of Changes to the Radiation Transfer Parameterizations Plus Cloud Optical Properties in the ECMWF Model, *Monthly Weather Review 118*, 847–873.

Norton, W. A. (2001), Longwave heating of the tropical lower stratosphere, *Geophysical Research Letters*, *28*, 3653–3656.

Palacios, M. B., and M. F. J. Steel (2006), Non-Gaussian Bayesian Geostatistical Modeling, *Journal of the American Statistical Association*, 101, 604–618.

Pagano, T. S., et al. (2003), Prelaunch and in-flight radiometric calibration of the Atmospheric Infrared Sounder (AIRS), *IEEE Transactions on Geoscience and Remote Sensing*, *41*, 265–273.

Parkinson, C. L. (2003), Aqua: An earth-observing satellite mission to examine water and other climate variables, *IEEE Transactions on Geoscience and Remote Sensing*, *41*, 173–183.

Paul, J. B., et al. (2001), Ultrasensitive absorption spectroscopy with a high-finesse optical cavity and off-axis alignment, *Applied Optics*, *40*, 4904–4910.

Pierce, R. B., et al. (1993), The Interaction of Radiative and Dynamical Processes During a Simulated Sudden Stratospheric Warming, *Journal of the Atmospheric Sciences*, *50*, 3829–3851.

Platnick, S., et al. (2003), The MODIS cloud products: Algorithms and examples from Terra, *IEEE Transactions on Geoscience and Remote Sensing*, *41*, 459–473.

Posselt, D.J., T. S. L'Ecuyer, G. L. Stephens (2006), Nonlinear Non-Gaussian Parameter Estimation Using Markov Chain Monte Carlo Methods, *EOS Trans. AGU*, 87(52), Fall Meet. Suppl., Abstract A31A-0867.

Qu, Y. N., et al. (2001), Ozone profile retrieval from satellite observation using high spectral resolution infrared sounding instrument, *Advances in Atmospheric Sciences*, 18, 959–971.

Rabier, F., et al. (1998), Extended assimilation and forecast experiments with a four-dimensional variational assimilation system, *Quarterly Journal of the Royal Meteorological Society*, *124*, 1861–1887.

Randall, D. A. (2000), *General Circulation Model Development*, 1st ed., 807 pp., Academic Press, Burlington, MA.

Randel, W. J., et al. (2001), Seasonal variation of water vapor in the lower stratosphere observed in Halogen Occultation Experiment data, *Journal of Geophysical Research-Atmospheres*, *106*, 14313–14325.

Randel, W. J., et al. (2006), Decreases in stratospheric water vapor after 2001: Links to changes in the tropical tropopause and the Brewer-Dobson circulation, *Journal of Geophysical Research-Atmospheres*, *111*.

Read, W. G., et al. (2006), The clear-sky unpolarized forward model for the EOS Aura Microwave Limb Sounder (MLS), *IEEE Transactions on Geoscience and Remote Sensing*, *44*, 1367–1379.

Revercomb, H. (1998), Recent Results from Two New Aircraft-Based Fourier-Transform Interferometers, in *ASSFTS Conference*, Toulouse, France.

Rodgers, C. D. (2000), *Inverse Methods for Atmospheric Sounding: Theory and Practice*, 238 pp., World Scientific, London, England.

Rossow, W. B., and R. A. Schiffer (1991), Isccp Cloud Data Products, *Bulletin of the American Meteorological Society*, *72*, 2–20.

Rothman, L. S., et al. (2005), The HITRAN 2004 molecular spectroscopic database, *Journal of Quantitative Spectroscopy & Radiative Transfer*, *96*, 139–204.

Schmidt, G. A., et al. (2006), Present-day atmospheric simulations using GISS ModelE: Comparison to in situ, satellite, and reanalysis data, *Journal of Climate*, *19*, 153–192.

Schuster, A. (1905), Radiation through a foggy atmosphere, *Astrophysical Journal*, *21*, 1–22.

Shannon, C. E. (1948), A Mathematical Theory of Communication, *Bell System Technical Journal*, *27*, 379–423.

Sherwood, S. C., and A. E. Dessler (2001), A model for transport across the tropical tropopause, *Journal of the Atmospheric Sciences*, 58, 765–779.

Sherwood, S. C., et al. (2003), Convective impact on temperatures observed near the tropical tropopause, *Journal of the Atmospheric Sciences*, *60*, 1847–1856.

Sinha, A., and J. E. Harries (1995), Water-Vapor and Greenhouse Trapping – the Role of Far-Infrared Absorption, *Geophysical Research Letters*, *22*, 2147–2150.

Sinha, A., and J. E. Harries (1997), The earth's clear-sky radiation budget and water vapor absorption in the far infrared, *Journal of Climate*, *10*, 1601–1614.

Slingo, A., and J. M. Slingo (1988), The Response of a General-Circulation Model to Cloud Longwave Radiative Forcing .1. Introduction and Initial Experiments, *Quarterly Journal of the Royal Meteorological Society*, *114*, 1027–1062.

Stamnes, K., et al. (1988), Numerically Stable Algorithm for Discrete-Ordinate-Method Radiative-Transfer in Multiple-Scattering and Emitting Layered Media, *Applied Optics*, *27*, 2502–2509.

Stephens, G. L. (1990), The Relevance of the Microphysical and Radiative Properties of Cirrus Clouds to Climate and Climatic Feedback, *Journal of the Atmospheric Sciences*, *47*, 1742–1753.

Stephens, G. L., et al. (2002), The Cloudsat mission and the A-Train – A new dimension of space-based observations of clouds and precipitation, *Bulletin of the American Meteorological Society*, 83, 1771–1790.

Stokes, G. M., and S. E. Schwartz (1994), The Atmospheric Radiation Measurement (ARM) Program – Programmatic Background and Design of the Cloud and Radiation Test-Bed, *Bulletin of the American Meteorological Society*, 75, 1201–1221.

Strow, L. L., et al. (2003), Prelaunch spectral calibration of the Atmospheric Infrared Sounder (AIRS), *IEEE Transactions on Geoscience and Remote Sensing*, 41, 274–286.

Strutt, J. W. (1899), On the Transmission of Light Through an Atmosphere Containing Small Particles in Suspension, and On the Origin of the Blue of the Sky, *Philosophical Magazine*, 47, 375–384.

Susskind, J., et al. (2003), Retrieval of atmospheric and surface parameters from AIRS/AMSU/HSB data in the presence of clouds, *IEEE Transactions on Geoscience and Remote Sensing*, 41, 390–409.

Susskind, J., et al. (2006), Accuracy of geophysical parameters derived from Atmospheric Infrared Sounder/Advanced Microwave Sounding Unit as a function of fractional cloud cover, *Journal of Geophysical Research-Atmospheres*, 111.

Tarantola, A. (2005), *Inverse Problem Theory and Methods for Model Parameter Estimation*, Society of Industrial and Applied Mathematics, Philadelphia, PA.

Taylor, B.N. and C.E. Kuyatt (1994), *Guidelines for Evaluating and Expressing the Uncertainty of NIST Measurement Results*, NIST Technical Note 1297, http://www.physics.nist.gov/Pubs/guidelines/contents.html .

Taylor, P. K. (2000), Intercomparison and Validation of Ocean-Atmosphere Energy Flux Fields, 307 pp, Joint WCRP/SCOR Working Group on Air-Sea fluxes.

Thuburn, J., and G. C. Craig (2002), On the temperature structure of the tropical substratosphere, *Journal of Geophysical Research-Atmospheres*, *107*.

Tikhonov, A. N. (1963), Solution of Incorrectly Formulated Problems and Regularization Method, *Doklady Akademii Nauk Sssr*, *151*, 501–504.

Tipping, R. H., and Q. Ma (1995), Theory of the Water-Vapor Continuum and Validations, *Atmospheric Research*, *36*, 69–94.

Trenberth, K. E. (1992), *Climate System Modeling*, 818 pp., Cambridge University Press, Cambridge, England.

Twomey, S. (1963), On Numerical Solution of Fredholm Integral Equations of First Kind by Inversion of Linear System Produced by Quadrature, *Journal of the Acm*, *10*, 97–101.

Twomey, S. (1966), Matrix Methods for Multiple-Scattering Problems, *Journal of the Atmospheric Sciences*, *23*, 289–298.

Twomey, S., et al. (1967), Light Scattering by Cloud Layers, *Journal of the Atmospheric Sciences*, *24*, 70–79.

Twomey, S. (1977), *Introduction to the Mathematics of Inversion in Remote Sensing and Indirect Measurements*, Elsevier Scientific Publishing Company, Amsterdam, NY.

Uppala, S. M., et al. (2005), The ERA-40 re-analysis, *Quarterly Journal of the Royal Meteorological Society*, 131, 2961–3012.

Valero, F. P. J., et al. (1982), Radiative Flux Measurements in the Troposphere, *Applied Optics*, *21*, 831–838.

Valero, F. P. J., et al. (1996), Determination of clear-sky radiative flux profiles, heating Rates and optical depths using unmanned aerospace vehicles as a platform, *Journal of Atmospheric and Oceanic Technology*, *13*, 1024–1030.

van de Hulst, H. C. (1963), *A New Look at Multiple Scattering*, NASA Goddard Institute for Space Studies, New York.

Vaughan, M., et al. (2004), Fully automated analysis of space-based lidar data: an overview of the CALIPSO retrieval algorithms and data products, *Proceedings of the SPIE*, *5575*, 16–30.

Verlinde, J., et al. (2007), The mixed-phase Arctic cloud experiment, *Bulletin of the American Meteorological Society*, *88*, 205–221.

Vömel, H., et al. (2007), Accuracy of tropospheric and stratospheric water vapor measurements by the cryogenic frost point hygrometer: Instrumental details and observations, *Journal of Geophysical Research-Atmospheres*, *112*.

Wallace, J. M., and P. V. Hobbs (1977), *Atmospheric Science: An Introductory Survey*, 1st ed., 467 pp., Academic Press, Burlington, MA.

Waters, J. W., et al. (2006), The Earth Observing System Microwave Limb Sounder (EOS MLS) on the Aura satellite, *IEEE Transactions on Geoscience and Remote Sensing*, *44*, 1075–1092.

Webster, C. R., et al. (1994), Aircraft (ER-2) Laser Infrared-Absorption Spectrometer (ALIAS) for in-Situ Stratospheric Measurements of HCl, N_2O, CH_4, NO_2, and HNO_3, *Applied Optics*, *33*, 454–472.

Wei, H. L., et al. (2004), Retrieval of semitransparent ice cloud optical thickness from atmospheric infrared sounder (AIRS) measurements, *IEEE Transactions on Geoscience and Remote Sensing*, *42*, 2254–2267.

Weinstock, E. M., et al. (1994), New Fast-Response Photofragment Fluorescence Hygrometer for Use on the NASA ER-2 and the Perseus Remotely Piloted Aircraft, *Review of Scientific Instruments*, *65*, 3544–3554.

Weisz, E., et al. (2007), Comparison of AIRS, MODIS, CloudSat and CALIPSO cloud top height retrievals, *Geophysical Research Letters*, *34*.

Wielicki, B. A., et al. (1996), Clouds and the earth's radiant energy system (CERES): An earth observing system experiment, *Bulletin of the American Meteorological Society*, *77*, 853–868.

Winker, D. M., J. Pelon, M. P. McCormick (2003), The CALIPSO mission: Spaceborne lidar for observation of aerosols and clouds. *Proceedings of the SPIE*, 4893, 1–11.

Wu, D. L., et al. (2006), EOS MLS cloud ice measurements and cloudy-sky radiative transfer model, *IEEE Transactions on Geoscience and Remote Sensing*, *44*, 1156–1165.

Wu, D. L., et al. (2008), Validation of the Aura MLS Cloud Ice Water Content (IWC) Measurements, *Journal of Geophysical Research-Atmospheres (in press)*.

Yang, P., et al. (2003), Spectral signature of ice clouds in the far-infrared region: Single-scattering calculations and radiative sensitivity study, *Journal of Geophysical Research-Atmospheres*, *108*.

Yang, P., et al. (2005), Scattering and absorption property database for nonspherical ice particles in the near- through far-infrared spectral region, *Applied Optics*, *44*, 5512–5523.

Young, D. F., et al. (1998), Temporal interpolation methods for the Clouds and the Earth's Radiant Energy system (CERES) experiment, *Journal of Applied Meteorology*, *37*, 572–590.

Zhang, Y. C., W.B. Rossow, and A.A. Lacis (1995), Calculation of surface and top of atmosphere radiative fluxes from physical quantities based on ISCCP data sets 1. Method and sensitivity to input data uncertainties. *Journal of Geophysical Research-Atmospheres*, 100(D1): 1149–1165.

Zhang, Y.C, W.B. Rossow, A. A. Lacis, V. Oinas, and M. I. Mishchenko (2004), Calculation of radiative fluxes from the surface to top of atmosphere based on ISCCP and other global data sets: Refinements of the radiative transfer model and the input data, *Journal of Geophysical Research-Atmospheres, 109*, D19105, doi:10.1029/2003JD004457.

Index.

About the Author.

Daniel Feldman was born in August 1980 in Portland, Oregon. He attended school there and graduated from Woodrow Wilson High School in 1998 as co-valedictorian. He then attended the Massachusetts Institute of Technology and graduated there in 2002 with a Bachelor's of Science in Environmental Engineering Science and a double minor in Earth, Atmosphere and Planetary Sciences and Latin American Studies. In 2004, he received a Master's of Science in Environmental Science and Engineering from the California Institute of Technology. His interests include environmental science, alternative energies, emerging technologies, and running.